Universität Bremen

Thamires Canuto de Almeida e Silva

Polymer-derived SiOC Ceramics as New Electrode Materials for Microbial Fuel Cell Applications

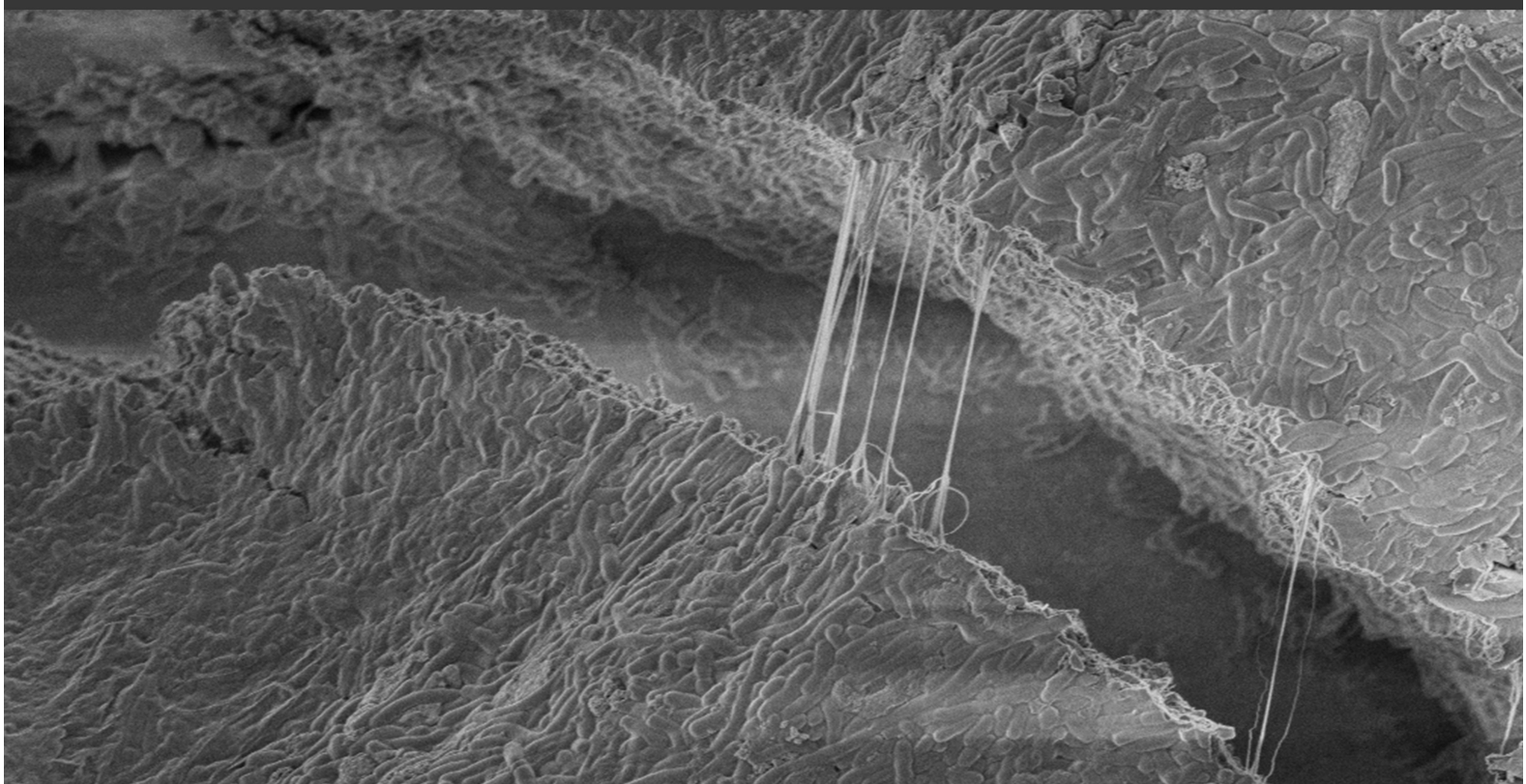

Polymer-abgeleitete SiOC-Keramiken als neue Elektrodenmaterialien für Anwendungen in mikrobiellen Brennstoffzellen

---

Polymer-derived SiOC Ceramics as New Electrode Materials for Microbial Fuel Cell Applications

Vom Fachbereich Produktionstechnik

der

UNIVERSITÄT BREMEN

zur Erlangung des Grades

Doktor-Ingenieur

genehmigte

Dissertation

von

Thamires Canuto de Almeida e Silva

Gutachter:

Prof. Dr.-Ing. Kurosch Rezwan, Universität Bremen

Prof. Dr.-Ing. Sven Kerzenmacher, Universität Bremen

Tag der mündlichen Prüfung: 08.05.2020

To my family and those who were part of this memorable journey.

My 4-years Ph.D. journey in Germany could not have been accomplished without the contribution of essential characters, therefore I would like to start this thesis by expressing my gratitude to all of them.

Firstly, I would like to thank the Brazilian National Council for Scientific and Technological Development (CNPq) for the financial support provided to this work through the Science without Borders program within the process number 232484/2014-7. I would like to thank Prof. Dr.-Ing. Kurosch Rezwan for the supervision and opportunity given to me to carry out this work in the Advanced Ceramics group at the University of Bremen. I also would like to extend my acknowledgments to my advisor Dr. Michaela Wilhelm for kindly incorporating me to the PDC group and for all her guidance, trust and encouragement dedicated to my work. Furthermore, I thank my second reviewer Prof. Dr.-Ing. Sven Kerzenmacher for taking part in the last step of this journey.

I further extend my gratitude to the collaborators from other institutions for elevating the quality of this work. Starting with Prof. Dr. Makarand Madhao Ghangrekar (Indian Institute of Technology Kharagpur, India) and Dr. Kaido Tammeveski (University of Tartu, Estonia), I thank for our fruitful scientific and cultural discussions in Bremen, Tartu and Kharagpur, during the 3 years of INNO INDIGO project. To Dr. Manuel Simões (University of Porto, Portugal) for his helpful experience with biofilms and finally to Falk Harnisch (Helmholtz-Zentrum für Umweltforschung Leipzig, Germany) for his cooperative expertise in bioelectrochemical systems. Also, a special thanks to Gourav Dhar (Kharagpur), Marek Mooste (Tartu) and Dr. Rodrigo Quejigo (Leipzig) for the shared knowledge in the experimental part. I extend my acknowledgments to the research training group GRK 1860 Micro-, meso- and macroporous Nonmetallic Materials: Fundamental and Applications (MIMENIMA) for the additional financial support provided to research stays/conferences and to the scientific inputs during progress reports and workshops.

I also would like to thank my supervised students Luiz Pedro Carvalho, James Ziemah, Viviane Kettermann, Fernanda Tavares, Samuel Elkes, Lisa Tölle and Katrin Hoffmann for the engagement and hard work in contributing with this work. I further extend my acknowledgments to Tina Kühn, Christian Ellenberg, Cristian Nuortila and Gabriela Berger for the technical and administrative support.

I extend my gratitude to my multicultural working colleagues and friends, which I will try to thank accordingly to the chronological order in which they took part in this journey. Starting from Dr. Renato Almeida, (which accompanied me since my internship time in Ceramics until

the final stages of the Ph.D.) I thank for his decisive answer to my email, to his wise veteran advices and all the shared moments outside the lab. Moving to my officemates, I would like to thank Dr. Daniel Carmona for making things lighter with his treasured sense of humor and friendship. To Vignesh Ahilan for contributing to my research progress, discussing MFC, electrochemical and life-related topics and also to his company in congresses and studies abroad. Recently, to Leticya Coelho for sharing not only the office with me but sunflowers and her friendship too. Furthermore, I would like to thank the PDC group members Dr. Prabu Moni, Dr. Silvia Abarca, Daniel Schumacher, Natália Fontão and Dr. Sarabjeet Kaur for the scientific discussions and contributions. Also, a special thanks to the sandwich members Dr. Heloísa Pimenta and Dr. Rafael Nishihora for their Brazilian scientific support, friendship and shared gastronomic moments on the weekend. A special thanks to Reshma Kadam, which started her Ph.D. journey at the same time as mine and became one of my best friends and family here. I am especially grateful to her heartfelt support, her friendship and priceless moments that we could share during this journey (from Kaffeepausen to dips in icy waters in Finland). I also thank Joeri Smits for his smiles in the hallway and our scientific/funny conversations.

I also would like to express my gratitude to the students from UFSC, which are nowadays official engineers and good friends, Carolina Silvério, Jéssica Mainardi, Eloisa Marcon, André Trajano, Lucas Reibnitz, Marina Zilli, Marcelo Rech, Raul Back, Paola Giuline, Viviane Kettermann, Isadora Deschamps, Luca Mazzafero and Lukas Butzke. I thank them for all memorable moments in La Viva, every Fridays, daily kicker sessions, cooking sessions, funny lunches in Mensa, birthdays/Christmas celebrations and also for being part of some of my best trips in Europe. I especially thank them too, to always remind me how far I've come and keep cheering for me from wherever they are now. Lately, to more gifts from UFSC, I thank again Natália and Leticya for their friendship and emotional support in the final stages and Ana Luiza Fiates, Pedro Braun, Gustavo Hamann, Lucas Ferrari for being part of all my kind of farewells events. I extend my gratitude to the flatmates which I had during this time in Bremen, Feli, Anna and Lukas. I thank for all the motivational support that I used to receive when I got home, also for the cooking experiments, kebabs, wine evenings and outdoor (day/night) activities which we used to have. I also would like to thank my Brazilian friends Raphaela Ronchi and Thaís Paganini for the long-distance indispensable support and for including Bremen on their itinerary to spend a special weekend with me.

Finally, I would like to thank my parents Nailton and Salete and my sister Thatiane for encouraging me in all my journeys, for the unconditional love and emotional support given. I also thank God for always taking care of my path so that everything happens in its proper time.

Abstract

The increased demand for energy sources and solutions for global warming have required great efforts regarding the development and optimization of renewable energy devices. Among the available technologies, microbial fuel cells (MFCs) arise as a single system, wherein electricity is produced from the biomass using bacteria as biocatalyst, while the wastewater is treated. Traditional MFCs are composed of an anode chamber, where an electroactive biofilm is developed, and a cathode chamber, separated by an ion conducting membrane. The main reactions occur during the interaction of bacteria and electrode surfaces, therefore the anode has been considered as a fundamental component in an MFC. Furthermore, the oxygen reduction reaction (ORR), which takes place at the cathode is often limiting the performance as a result of its slow reaction kinetics. An ideal MFC anode material should enable the electron transfer with simultaneous microbial attachment, while cathode materials should have a high reduction potential. Thus far, mainly carbon-based electrode materials are applied in MFC. However, their electrochemical oxidative degradation and limited active reaction sites for microbial adhesion still restrict their use. In this work, silicon oxycarbide (SiOC)-based electrodes are synthesized targeting the development of cost-effective electrode materials to improve electrochemical performance in MFCs. The materials were prepared by the polymer-derived ceramics (PDCs) route, using poly(methyl silsesquioxane) and poly(methyl phenyl silsesquioxane) as precursors tailoring the properties by varying pyrolysis temperatures and incorporating conductive phases and further fillers. The influence of pyrolysis temperature and incorporation of conductive materials on functional properties and electrical conductivity was investigated and discussed along with first investigation of biofilm development on SiOC-based ceramic surfaces. Their applicability in MFC was investigated throughout several types of bioelectrochemical setups and compared with commercially available carbon materials. Maximum power density values varying from 30 to 211 mW m^{-2} were obtained, which showed a two to three-fold increase when compared to carbon felt, attributed to its porous structures and surfaces properties. In terms of wastewater treatment, chemical oxygen demand (COD) removal efficiency of about 85% was demonstrated. Additional studies revealed the correlation of performance with surface properties emphasizing hydrophilicity as major aspect followed by specific surface area. In addition, cobalt/nickel-containing SiOC-based nitrogen(N)-doped ceramic electrocatalysts were produced as a new class for the ORR and studied under acidic, neutral and alkaline conditions. The N-doped (Co)SiOC catalyst exhibited significantly higher ORR activity suggesting its promising applicability. Based on the properties and results

obtained, the proposed and investigated new class of SiOC-based porous materials have a high potential to be considered in MFC technology.

Zusammenfassung

Die gestiegene Nachfrage nach Energiequellen und die globale Erwärmung erforderten große Anstrengungen bei der Entwicklung und Optimierung von Prozessen zur Nutzung erneuerbarer Energien. Unter den verfügbaren Technologien treten mikrobielle Brennstoffzellen (MFCs) als ein einziges System hervor, bei dem aus im Abwasser verfügbarer Biomasse unter Verwendung von Bakterien als Biokatalysator Elektrizität erzeugt wird, während das Abwasser gleichzeitig gereingt wird. Herkömmliche MFCs bestehen aus einer Anodenkammer, in der ein elektroaktiver Biofilm aufgebaut wird, und einer Kathodenkammer, die durch eine ionenleitende Membran getrennt werden. Die Hauptreaktionen treten während der Wechselwirkung zwischen Bakterien und der Anodenoberflächen auf, weshalb die Anode als grundlegender Bestandteil einer MFC angesehen wird. Darüber hinaus schränkt die an der Kathode stattfindende Sauerstoffreduktionsreaktion (ORR) aufgrund ihrer langsamen Reaktionskinetik häufig die Leistung ein. Ein ideales MFC-Anodenmaterial sollte den Elektronentransfer bei gleichzeitiger mikrobieller Anlagerung ermöglichen, während Kathodenmaterialien ein hohes Reduktionspotential aufweisen sollten. Bisher werden in MFC hauptsächlich Elektrodenmaterialien auf Kohlenstoffbasis verwendet. Ihr elektrochemischer oxidativer Abbau und ihre begrenzten aktiven Reaktionsstellen für die mikrobielle Adhäsion beschränken jedoch immer noch ihren praktischen Einsatz. In dieser Arbeit wurden auf Siliziumoxycarbid (SiOC) basierende Elektroden synthetisiert, die auf die Entwicklung kostengünstiger Elektrodenmaterialien abzielen, um die elektrochemische Leistung in MFCs zu verbessern. Die Materialien wurden als Polymeren abgeleitete Keramiken (PDCs) hergestellt, wobei Poly (methylsilsesquioxan) und Poly (methylphenylsilsesquioxan) als Ausgangpolymere verwendet wurden, um die Eigenschaften durch Variation der Pyrolysetemperaturen und den Einbau leitfähiger Phasen und zusätzlicher Füllermaterialien anzupassen. Der Einfluss der Pyrolysetemperatur und des Einbaus leitfähiger Materialien auf die Funktionseigenschaften und die elektrische Leitfähigkeit wurde zusammen mit einer ersten Untersuchung der Biofilmentwicklung auf SiOC-basierten Keramikoberflächen diskutiert. Ihre Anwendbarkeit in MFCs wurde in verschiedenen Arten von bioelektrochemischen Aufbauten untersucht und mit im Handel erhältlichen Kohlenstoffmaterialien verglichen. Es wurden maximale Leistungsdichten zwischen 30 und 211 mW m^{-2} erhalten, die im Vergleich zum Kohlenstofffilz aufgrund ihrer porösen Strukturen und Oberflächeneigenschaften zwei- bis dreifach höhere Leistungsdichten zeigten. In Bezug auf die Abwasserbehandlung wurde ein Wirkungsgrad der Reduzierung des chemischen Sauerstoffbedarfs (CSB) von etwa 85% nachgewiesen. Zusätzliche Studien belegen die Korrelation der Leistung mit den

Oberflächeneigenschaften, wobei die Hydrophilie als Hauptaspekt gefolgt von der spezifischen Oberflächegrüßen hervorgehoben wird. Zusätzlich wurden Cobalt/Nickel-haltige SiOC-basierte Stickstoff (N) -dotierte keramische Elektrokatalysatoren als neue Klasse für die ORR hergestellt und unter sauren, neutralen und alkalischen Bedingungen untersucht. Der N-dotierte (Co) SiOC-Katalysator zeigte eine signifikant höhere ORR-Aktivität, was auf seine vielversprechende Anwendbarkeit hindeutet. Aufgrund der erhaltenen Eigenschaften und Ergebnisse weisen die vorgeschlagenen porösen Materialien auf SiOC-Basis ein hohes Potenzial auf, Einsatz in der MFC-Technologie zu finden.

List of Acronyms, Symbols and Abbreviations

3D	Three Dimensional
AAS	Atomic Absorption Spectrometer
AC	Alternating Current
AgCl/Ag	Silver-silver chloride
APTES	3-aminopropyl triethoxysilane
Ar	Argon
Az/Azo	Azodicarbonamide
BCNT	Bamboo-like carbon nanotube
BES	Bioelectrochemical Systems
BET	Brunauer-Emmett-Teller
BJH	Barrett–Joyner–Halenda
CB	Carbon Black
CE	Coulombic Efficiency
CE	Counter Electrode
CeO_2	Cerium(IV) oxide
CFU	Colony Forming Units
CH_4	Methane
CLSM	Confocal Laser Scanning Microscopy
CNTs	Carbon Nanotubes
CO	Carbon monoxide
Co	Cobalt
$Co(NO_3)_2$	Cobalt nitrate
CO_2	Carbon dioxide
$CoCl_2$	Cobalt(II) chloride
COD	Chemical Oxygen Demand
CoO	Cobalt(II) oxide
CoPc	Cobalt phthalocyanine
CoTMPP	Cobalt tetramethylphenylporphyrin
Cu	Copper
Cu_2O	Copper(I) oxide
CV	Cyclic Voltammetry
DC	Direct current
DCDA	Dicyandiamide

DVB	Divinylbenzene
EDX	Energy-dispersive X-ray
EIS	Electrochemical Impedance Spectroscopy
EPS	Extracellular Polymeric Substances
ESCA	Electron Spectroscopy for Chemical Analysis
Fe_2O_3	Iron(III) oxide
$FeCl_3$	Iron(III) chloride
FePc	Iron phthalocyanine
FESEM	Field Emission Scanning Electron Microscopy
FTO	Fluorine-doped Tin oxide
G	Graphene
GC	Glassy Carbon
GO	Graphene oxide
H_2SO_4	Sulfuric acid
H44	poly (methyl phenyl silsesquioxane)
Hg	Mercury
HRSEM	High-resolution Scanning Electron Microscope
IIT	Indian Institute of Technology
Imi	Imidazole
ITTC	Ice-templated Titanium-based ceramic
IUPAC	International Union of Pure and Applied Chemistry
IV	Current-voltage
K-L	Koutecky–Levich
KNO_3	Potassium nitrate
KOH	Potassium hydroxide
KS75	Graphite
LBL	Layer-by-layer
LSV	Linear Sweep Voltammetry
M-C	Metal-containing
MEMS	Micro-electro-mechanical Systems
MFC	Microbial Fuel Cell
MHB	Mueller–Hinton Broth
MK	poly (methyl silsesquioxane)
M-N-C	Metal-containing Nitrogen-doped Carbon

MnO_2	Manganese dioxide
Mo_2C	Molybdenum carbide
MOFs	Metal-organic Frameworks
$MoSi_2$	Molybdenum disilicide
N_2/N	Nitrogen
NaCl	Sodium chloride
$NaClO_4$	Sodium perchlorate
N-C	Nitrogen-doped Carbon
NER	Normalized Energy Recovery
NHE	Normal Hydrogen Electrode
Ni	Nickel
$NiCl_2$	Nickel(II) chloride
NiO	Nickel(II) oxide
OCV	Open Circuit Voltage
ORR	Oxygen Reduction Reaction
OV	Operating Voltage
PANI	Polyaniline
PBS	Phosphate Buffer Solution
PDAP	poly(2,6-diaminopyridine)
PDC	Polymer derived-ceramic
PEDOT	poly(3,4- ethylenedioxythiophene)
PEM	Proton Exchange Membrane
PHMS	Polyhydromethylsiloxane
PMPS	Polymethylphenyl siloxane
PMS	Polymethylsiloxane
PPS	Polyphenylsiloxane
Pt	Platinum
Pt/C	Platinum/Carbon
PVA	Polyvinyl alcohol
RDE	Rotating Disk Electrode
RHE	Reversible Hydrogen Electrode
SCE	Saturated Calomel Electrode
SEM	Scanning Electron Microscopy
SHE	Standard Hydrogen Electrode

Si_3N_4	Silicon nitride
SiC	Silicon carbide
SiO	Silicon monoxide
SiO	Silicon monoxide
SiOC	Silicon oxycarbide
SnO_2	Tin(IV) oxide
SOFC	Solid-oxide Fuel Cell
SS	Stainless Steel
SSA	Specific Surface Area
TEM	Transmission Electron Microscopy
TEOS	Tetraethyl orthosilicate
TiC	Titanium carbide
TiO_2	Titanium dioxide
TTCS	Tetravinyl cyclotetrasiloxane
UFZ	Helmholtz-Zentrum für Umweltforschung
V_2O_5-MFs	Vanadium pentoxide microflowers
WCA	Water Contact Angle
WE	Working Electrode
XPS	X-ray Photoelectron Spectroscopy
XRD	X-ray Diffraction
ZrO_2	Zirconium dioxide
θ	Contact angle
E	Potential
F	Faraday's constant
P	Confidence level
P	Power
Ra	Surface roughness
T	Temperature
V	Voltage
i/I	Current
j	Current density
n	Number of electrons
p/p^0	Relative pressure
Ω	Internal resistance

σ	Electrical conductivity
ω	Rotation rates

Table of Contents

Chapter I. Introduction and Aim of the Work 1
1.1 Introduction 1
1.2 Aim of the Work and Approach 2
1.3 Thesis Overview 3
Chapter II. State of the Art 5
2.1 Microbial Fuel Cells (MFCs)-Fundamentals 5
2.1.1 Basic Concepts and Electrochemical Principles 6
2.1.2 Components of Microbial Fuel Cells 8
2.1.2.1 Anode 9
2.1.2.2 Cathode 11
2.1.2.3 Membrane 12
2.1.3 Electrode Materials Used in MFCs 13
2.1.4 Ceramic Composite Electrode Materials Applied in MFCs 19
2.2 Polymer-derived Silicon Oxycarbide (SiOC) Ceramics 24
2.2.1 General Background 25
2.2.2 Silicon Oxycarbide (SiOC) Ceramics 29
2.2.3 SiOC-derived Ceramics Materials in Electrochemical Applications and as Catalysts 34
Chapter III. Experimental Section 40
Preparation and Characterization of SiOC Ceramics 40
3.1 Preparation of SiOC Ceramic Electrode Materials 40
3.1.1 Manufacturing of SiOC Electrode Materials 40
3.1.1.1 Materials 40
3.1.1.2 Tape-cast SiOC Electrode Materials 41
3.1.1.3 Sandwiched SiOC-carbon-based Composite Electrode Materials 43
3.1.2 Manufacturing of SiOC Pristine and Nitrogen-doped Electrocatalyst Materials 44
3.2 Characterization Techniques for Structural and Surface Properties 46
3.2.1 Scanning Electron Microscopy 46
3.2.2 Nitrogen Adsorption 47
3.2.3 Mercury Intrusion Porosimetry 50
3.2.4 X-ray Diffraction 51
3.2.5 X-ray Photoelectron Spectroscopy 51
3.2.6 Surface Characteristics Characterization 53
3.2.6.1 Vapor Adsorption 53
3.2.6.2 Surface Contact Angle 53
3.2.7 Chemical Stability Test 54
3.2.8 Biofilm Assays 55

3.3 Electrochemical Characterization 56
3.3.1 Electrochemical Impedance Spectroscopy 56
3.3.2 Cyclic Voltammetry 57
3.3.3 Linear Sweep Voltammetry 59
3.3.4 Rotating Disk Electrode 60
3.4 Bioelectrochemical Characterization 63
3.4.1 BES Configuration 63
3.4.1.1 Aqueous Cathode Clayware-based MFC 63
3.4.1.2 Two-chambered MFC 64
3.4.1.3 Three-electrode Setup 65
3.4.2 Electrochemical Measurements and Analysis 66
Chapter IV. Functional Properties of Tape-cast SiOC-based Porous Ceramic Electrode Materials 68
4.1 Macrostructure and Surface Characterization 68
4.2 Electrical Properties 75
4.3 Chemical Stability 79
4.4 Biofilm Development 80
Chapter V. Application of SiOC-based Polymer derived-ceramic Porous Anodes in Microbial Fuel Cells 83
5.1 Tape-cast SiOC-based Anode Materials 83
5.1.1 Electrical Performance of MFC 86
5.1.2 Wastewater Treatment in MFC 89
5.1.3 Biofilm on Anode Surfaces 90
5.2 Sandwiched SiOC-carbon-based Composite Anode Materials 92
5.2.1 Surface and Electrical Characterization 92
5.2.2 MFC Performance and Wastewater Treatment 98
5.3 The Impact of SiOC-based Porous Anode Materials Properties on Current Generation in BES 100
Chapter VI. Polymer-derived Co/Ni–SiOC(N) Ceramic Electrocatalysts for Oxygen Reduction Reaction in Fuel Cells 103
6.1 Physical Characterization of SiOC(N)-based Electrocatalysts 103
6.2 ORR Studies in Alkaline, Neutral and Acid Media 110
6.2.1 Cyclic Voltammetry and Linear Sweep Voltammetry Studies 110
6.2.2 RDE Studies of ORR and Koutecky–Levich Analysis 112
6.3 The ORR Activity of the PDC-Co–N Catalyst 115
6.4 The MFC Performance of PDC-Co-N Catalyst 119
Chapter VII. Conclusion 120
Chapter VIII. Outlook 123

Chapter IX. References **125**
Appendix **141**
List of Supervised Students **156**
Curriculum Vitae **157**
List of Publications **159**
List of Presentations and Research Stays **160**

Chapter I. Introduction and Aim of the Work

1.1 Introduction

Two major problems that humanity is now facing are environmental pollution and the energy crisis. Microbial fuel cells (MFCs) arise as a single bioelectrochemical system (BES), wherein electricity is produced from the biomass using bacteria as biocatalyst, while the wastewater is treated [1].

The electricity generation occurs through the oxidation of organic matter present in the wastewater, and the release of electrons which are transferred to the anode due to the growth of exoelectrogenic bacteria on the anode surface. The electrons flow through an external circuit reaching the cathode, thus producing an electric current. Subsequently, the electrons combine with oxygen molecules, which act as a terminal electron acceptor, and with protons that were diffused through a proton exchange membrane [2, 3]. The oxygen reduction reaction (ORR), which takes place at the cathode, frequently limits the performance as a result of its slow reaction kinetics [4], demanding the use of an electrocatalyst. Furthermore, the interaction of bacteria with the anode surface, the resistance of electron flow, and substrate oxidation essentially depend on the properties of anode materials. Therefore, the anode is the defining element that can critically affect the overall performance of an MFC [5-7].

In general, an ideal anode material should have good electrical conductivity, biocompatibility, large surface area, chemical stability, sufficient mechanical strength, and low costs [8]. The most reported anode materials used in MFCs are the traditional carbon-based materials, such as carbon cloth and felt, carbon brush, carbon rod and granular activated carbon [6]. However, their inherently hydrophobic character and limited active reaction sites restrict microbial adhesion and biofilm formation. Additionally, the surface fouling of the material due to microbial secretion during the operation of MFC may cause the loss of anode functionality and, as a result, compromise the power output [9-11]. Different from anodes, cathode materials should have a high reduction potential and have the ability to easily capture protons [8].

From this perspective, there have been great efforts in the development of novel electrode materials that could provide better surface characteristics for biofilm formation and improved electron transfer. Other properties such as optimized porous structure to accommodate bacteria cells and maintain the access of nutrients through the pores, and long-term stability, are also highly desirable and investigated earlier [5, 8, 12]. Recently, studies concerning the use of ceramics in MFCs have been increased. This class of materials fulfils the aforementioned properties, due to the adjustment of porosity, thickness, density, chemical

stability, as well as the low cost of these materials [13]. Most of the investigations in MFCs, related to the use of ceramics, have been focusing on proton exchange membranes and reactor design [14, 15]. Nevertheless, a few researchers have reported the applicability of ceramics as electrode materials [12, 16, 17], mainly due to the non-conductive aspect of ceramics.

To address this problem, an attractive way to produce electron conducting porous ceramics is investigated based on the approach of polymer-derived ceramics (PDCs) route through polysiloxanes, where chemical and physical properties can be varied according to the molecular precursor, filler incorporation and pyrolysis conditions, generating silicon oxycarbide (SiOC)-based ceramics [18-20]. The tailorable properties in these materials, such as specific surface area and surface characteristics, feasibility of incorporation of conductive phases [21, 22] and metal nanoparticles in a SiOC support [23], have attracted interests for electrochemical applications as electrocatalysts [24], sensors [25] and as electrode materials in lithium-ion batteries and supercapacitors [21, 26], but not yet explored for applications in bioelectrochemical systems.

1.2 Aim of the Work and Approach

Focus on the need of new electrode materials development, novel porous SiOC-ceramic electrodes and electrocatalysts based on poly(silsesquioxanes) were developed in the present study. SiOC-based materials were produced in order to fulfil the aforementioned requirements targeting its potential upcoming application as alternative BES electrodes to the traditional carbon-based materials. The produced materials were characterized in terms of structural and electrical properties, as well as biocompatibility, in means of bacterial adhesion. The applicability of the developed materials was further investigated by evaluating the BES performance compared to commercially available carbon-based materials. In addition, the applicability of the SiOC-based electrocatalysts as a new class of catalysts for the ORR was for the first time investigated and extended to studies under acidic, neutral, and alkaline conditions.

To achieve the above mentioned aim and requirements, the following approaches were adopted for electrode and electrocatalyst materials, respectively.

- SiOC-based electrode materials

As starting materials, commercial poly(methyl silsesquioxane) and poly(methyl phenyl silsesquioxane) were used as polymer-to-ceramic precursors and synthesized by tape-casting technique. The functional properties were adjusted by varying pyrolysis temperatures and incorporating conductive phases like carbon fillers and metal-based conductive materials.

Pyrolysis was conducted under argon and N_2 atmosphere with varying temperatures of 500–1500 °C and six types of conductive materials were incorporated. In addition, the functional properties were also compared to carbon felt, a usual electrode applied in BES. Furthermore, a study regarding 3D-strucutres was carried out with a synthesized composite composed by PDC and carbon felt layers in a sandwich structure. The composites were developed in order to improve electron transport, prevent carbon felt corrosion and adjustment in porosity by varying pyrolysis conditions of the PDC layers. Pyrolysis were carried out under nitrogen and argon environment from temperatures between 1000 to 1500 °C. Additionally, the developed structure also intended to facilitate the wire connection of the electrode in the setup through the flexible carbon felt part.

- SiOC(N)-based electrocatalyst materials

As starting materials, commercial poly(methyl silsesquioxane) and poly(methyl phenyl silsesquioxane) were similarly used as polymer-to-ceramic precursors and combined with graphite as a carbon source for a sufficient electrical conductivity. Besides, metal salts were used as precursors for metal (Co/Ni) nanoparticle formation. Pyrolysis was conducted, in a first step, under N_2 atmosphere at 1000 °C resulting in fine powder material. The synthesis included nitrogen doping of SiOC-based materials with dicyandiamide (DCDA) and a second pyrolysis step under N_2 atmosphere at 800 °C. In addition, the ORR activity was also compared to commercial Pt/C.

- SiOC-based materials as electrode in BES setups

To investigate the applicability of the produced materials as parts of BES, MFC setups and a three-reactor BES were applied. The experiments were initiated during research visits at the Indian Institute of Technology (Kharagpur, India) and Zentrum für Umweltforschung (Leipzig, Germany), respectively.

1.3 Thesis Overview

This thesis is divided into nine chapters starting from the general introduction of the topic and target aims. In Chapter 2, the concept and components of MFCs are presented along with the background of silicon oxycarbide (SiOC) ceramics and its applications. This chapter encloses the topics related to basic concepts and electrochemical principles of MFCs as well as a review of previous carbon-based and ceramic electrode materials applied in this research area. The uses of SiOC-derived ceramics materials in electrochemical applications and as catalysts are likewise given. Chapter 3 describes the preparation steps used in the manufacturing of

SiOC-based electrode and electrocatalyst materials with an overview of the characterization methods used in this thesis. In this chapter, BES setups designs, operating conditions, and electrochemical characterization methods used to characterize the performance of the produced materials are likewise included. Chapter 4 address the characterization and discussion of the functional properties concerning the tape-cast SiOC-based electrode materials described in Chapter III. Properties regarding structural and electrical characteristics as well as biocompatibility, in means of bacterial adhesion, are considered for bioengineering applications as BES. Chapter 5 focus on the evaluation of BES performance regarding the SiOC electrode materials described in Chapter III. The BES performance is discussed through current and power densities as well as chemical oxygen demand (COD) removal determining the wastewater treatment efficiency. Chapter 6 contains the characterization of physical properties concerning the Co/Ni-SiOC(N) electrocatalyst materials described in Chapter III, along with ORR studies in alkaline, neutral and acid media. Furthermore, the ORR activity of the PDC-Co–N catalyst is highlighted and its MFC performance is also included. Lastly, Chapter 7 and 8 summarize the findings of the work and future perspectives, respectively, followed by the references (Chapter 9). The main outcomes of this work were published elsewhere, and are adapted within the thesis accompanied with additional unpublished results. This thesis also contains an Appendix section providing supporting information and the curriculum vitae of the doctoral candidate followed by lists of student projects, publications, presentations and research stays.

Chapter II. State of the Art

In this chapter, the concept and components of MFCs are presented along with the background of silicon oxycarbide (SiOC) ceramics and its applications. The literature review focuses on several key parameters that influence MFCs performance as well as some of the traditional and novel classes of materials studied as electrodes in this technology. In addition, SiOC ceramics processing and their use in electrochemical applications are included.

2.1 Microbial Fuel Cells (MFCs)-Fundamentals

Microbial fuel cell (MFC) is a prospective bioelectrochemical system (BES) wherein electricity is produced from the biomass using bacteria as biocatalyst, while the biodegradation of organic matters or wastes takes place [27]. Simple molecules, such as carbohydrates and proteins, can be used in an MFC for energy production. Moreover, even complex organic matter present in animal, human and food-processing waste can be treated [28]. Apart from wastewater treatment and bioenergy production, MFCs have also been applied as biosensors and desalination processes [29, 30].

The earliest idea of utilizing microbes to generate electricity was demonstrated and attributed to Potter in 1911 [31], but very few advances were achieved in this field even 55 years later [32]. With the development of other alternatives sources of energy, such as solar photovoltaic systems, MFCs suffered a setback. In the 1990s, studies about this topic [33-35] started to progress again, due to the concern about global energy production and environmental damage. In the last decade, numerous research papers on MFCs advancement have been published providing a better understanding of electron transfer mechanisms and reporting novel classes of materials and MFC designs with suitable and improved features for this technology [6].

Even though the biological aspect adds another level of complexity compared to conventional fuel cells, MFCs present advantages such as clean production process and products, mild operation conditions, alternative less expensive catalyst (microorganisms as biocatalysts) and extensive diversity fuel availability (wastewater and sludge) [33, 34].

At present, commercially MFCs are not available on a large-scale due to limitations as low-efficiency electron transport from bacteria to electrode surfaces, high costs of separators and cathode catalysts, stability and fouling issues during long-term operation [36]. The progress of MFC has considerable started only a decade ago and is a constantly expanding attractive

platform to study microbial interaction with solid surfaces with the potential to advance through engineering innovation.

2.1.1 Basic Concepts and Electrochemical Principles

MFCs is an innovative strategy wherein electricity is produced from biomass using bacteria, while the wastewater is treated in a single system. Traditional MFCs are composed by an anode and a cathode separated by a proton exchange membrane (PEM) [33]. Figure 1 presents a basic design of a two-chambered MFC often used in laboratory studies.

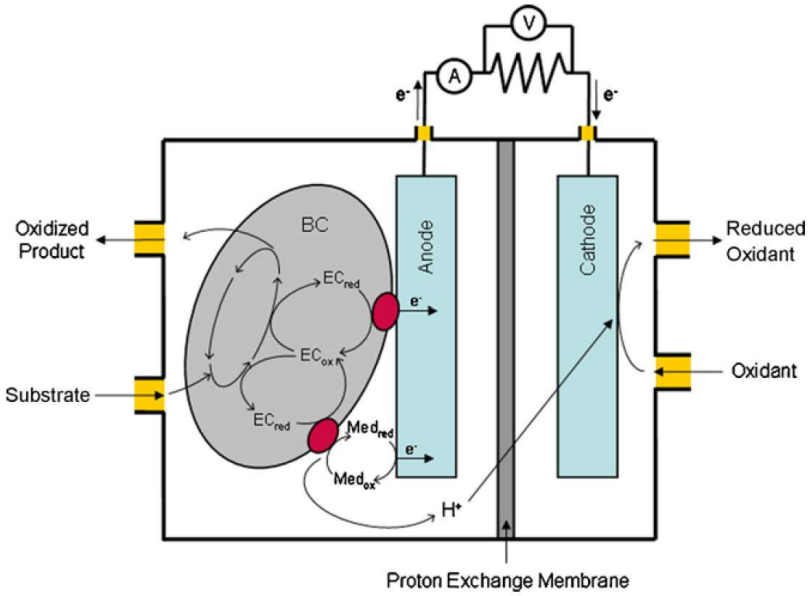

Figure 1. Schematic representation of a two-chambered MFC design. Adapted from [37].

The mechanism of current generations starts in the anodic chamber, with the acclimatization of the microorganisms and oxidation process of the organic substrate with electrons and protons release. Throughout the process, an electroactive biofilm is formed on the electrode surface, where directed or mediated electron transfer mechanisms take place [38]. The electrons transferred to the anode are transported to the cathode via an external electrical connection, producing energy [39]. The protons produced during substrate oxidation are transferred to the cathode compartment through the PEM. The protons and electrons react at the cathode surface, which is normally coated with a catalyst to improve oxygen reduction reaction (ORR), with an electron acceptor. Typically, oxygen is used as an electron acceptor and water is formed [33, 38].

The overall reaction in MFCs is the oxidation of the substrate to carbon dioxide and water with associated electricity production as a by-product. The electrode reactions are divided into anodic and cathodic reactions, as following using acetate as an example [39].

Anodic reaction:

$CH_3COO^- + 2\ H_2O \rightarrow 2\ CO_2 + 7H^+ + 8e^-$

Cathodic reaction:

$O_2 + 4e^- + 4H^+ \rightarrow 2\ H_2O$

Overall cell reaction:

$CH3COO^- + O_2 + 8e^- + 8H^+ \rightarrow 2\ CO_2 + 2H_2O + 7H^+ + 8e^-$

The performance of the MFCs is affected by various factors such as microbial community, substrates used, cell design and selected operating conditions as well as materials variety and electrode surface properties [40, 41].

To determine and evaluate the MFC performance theoretical principles and electrical variables are taking into account in MFC studies. As in any electrochemical system, voltage and current are the initial variables of concern, followed by electrode potentials. Voltage meters and data acquisition systems are used to measure cell voltage across an external resistor, while reference electrodes are applied in the determination of anode or cathode potentials [42]. Potentiostats are also applied in order to study the electrochemical response of an electrode to specific imposed conditions and is usually operated in a three-electrode-setup [43]. Current is calculated from Ohm's law, whereas power is determined as the product of current and voltage. Successively, power and current are often either normalized to the anode projected surface area ($A\ m^{-2}$, $W\ m^{-2}$) or reactor volume ($W\ m^{-3}$). When polarization curves are recorded and the power density plotted as a function of current density, the maximum value of the curve is taken and considered as a performance indicator. Internal resistance values of the MFC are also obtained from the slope of the polarization curve [42].

In terms of wastewater treatment efficiency, the performance is usually investigated considering the chemical oxygen demand (COD) removal rate [44]. This parameter relates the difference between the COD concentration present in the influent and effluent, after a certain feed cycle. With the change in COD (Δ_{COD}), Coulombic efficiency (CE) can also be obtained to determine the conversion of organics into electrical charge. Recently, normalized energy

recovery (NER) has also been included to correlate energy recovery in MFCs with technical viability [45].

The biofilm structure in MFCs is typically investigated by imaging methods such as light microscopy, scanning electron microscopy (SEM), confocal laser scanning microscopy (CLSM) and epifluorescence [46]. For biofilm composition, analytical methods to measure extracellular polymeric substances (EPS) components are used. Additionally, microbial electron transfer mechanisms are studied by means of electrochemical impedance spectroscopy (EIS) and cyclic voltammetry (CV) analysis.

A more detailed description of the electrochemical characterization and associated equations, procedures and methods used in this work are presented in Chapter III.

2.1.2 Components of Microbial Fuel Cells

A typical MFC consists of an anodic chamber and a cathodic chamber separated by a PEM. Two basic types of configuration, which differs in a number of chambers, are built according to two-chamber MFC (Figure 2a-b) and single-chamber MFC (Figure 2c-d) architectures [47, 48]. For the latter, anode and cathode are placed in a single compartment, with an air-based cathode configuration that works using the oxygen from the atmosphere. Membrane-less MFCs are also considered as low-cost approach (Figure 2d) [47, 48]. Regarding operation mode, MFCs can be operated in three different modes; batch, fed-batch and continuous mode [5]. The main challenge is to design and select materials which increase power density in a cost-effective way.

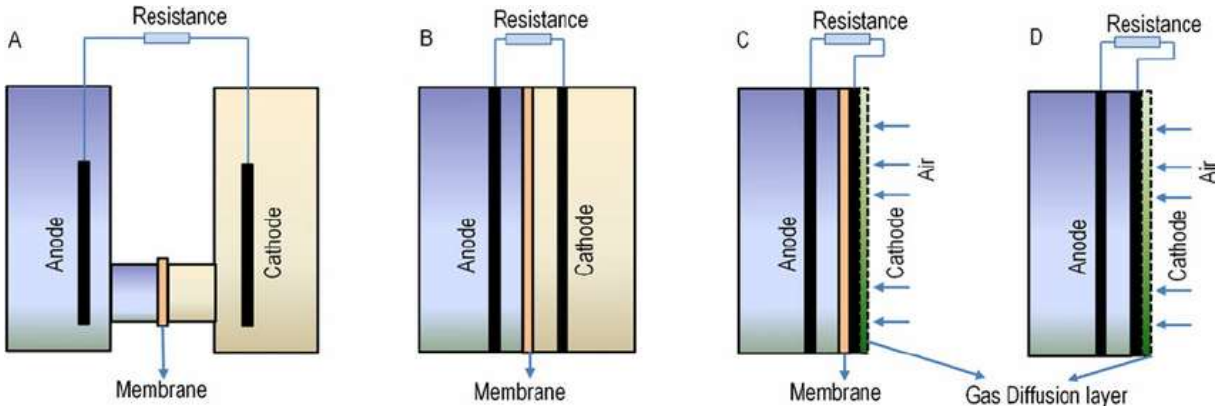

Figure 2. Types of MFCS used in studies: (a) H-shaped two-chamber system, (b) Cube-shaped two-chamber reactor, (c) Single-chamber air–cathode reactor with membrane electron assembly, (d) Membrane-less air–cathode reactor. Adapted from [48].

Although the anode and cathode have different functions during the MFC operation, they share common properties such as conductivity, porosity and surface area, durability and stability as well as costs and availability [49]. Furthermore, biocompatible nature is mainly preferable for anode materials while catalytic active sites for the ORR are desirable in cathode materials.

2.1.2.1 Anode

The choice of anode materials can affect substrate oxidation, bacterial attachment, and electron transfer rate. Therefore, it is considered a defining element that can critically affect the overall performance of an MFC [50].

An ideal anode should exhibit good electrical conductivity, creating low resistance in the conductance of released electrons [49]. An optimized porous structure to accommodate bacteria cells and maintain the access of nutrients through the pores is also highly desirable and investigated [5]. Besides, the anode surface characteristics will influence the interactions between electroactive microorganisms and biofilm formation.

The mechanisms for the conversion of organic substrates into electricity through bacteria are divided in indirect oxidation of organic substrates through biofilm (Figure 3a–c) and direct oxidation of secondary metabolites from bacteria (Figure 3d) [51]. Furthermore, three types of electron transfer mechanisms from bacteria to the anode through a biofilm have been identified in MFCs: direct electron transfer by direct contact between the outer membrane of the bacteria and the surface of the anode (Figure 3a), via extracellular conductive connections called conductive pili or bacterial nanowires (Figure 3b), and indirect electron transfer through mediators (electron shuttle) (Figure 3c) [6, 51]. However, in the current state of knowledge, it is impossible to separate the electron transfer mechanisms involved in studies of mixed species biofilms [6].

The development of a biofilm is a complex multi-step process which leads to the formation of a microbial community adhered to the surface [52]. The electrochemically-active biofilms developed on the anode surface play a vital role in the power output of the electricity generation in MFC. Mostly, the electroactivity of these biofilms is related to the presence of specific bacterial strains (*Geobacter sulfurreducens, Rhodoferax ferrireducens, Shewanella sp.*, etc.) which are able to exchange electrons with solid substrata (i.e. electrodes) also with some producing their own redox mediators [6].

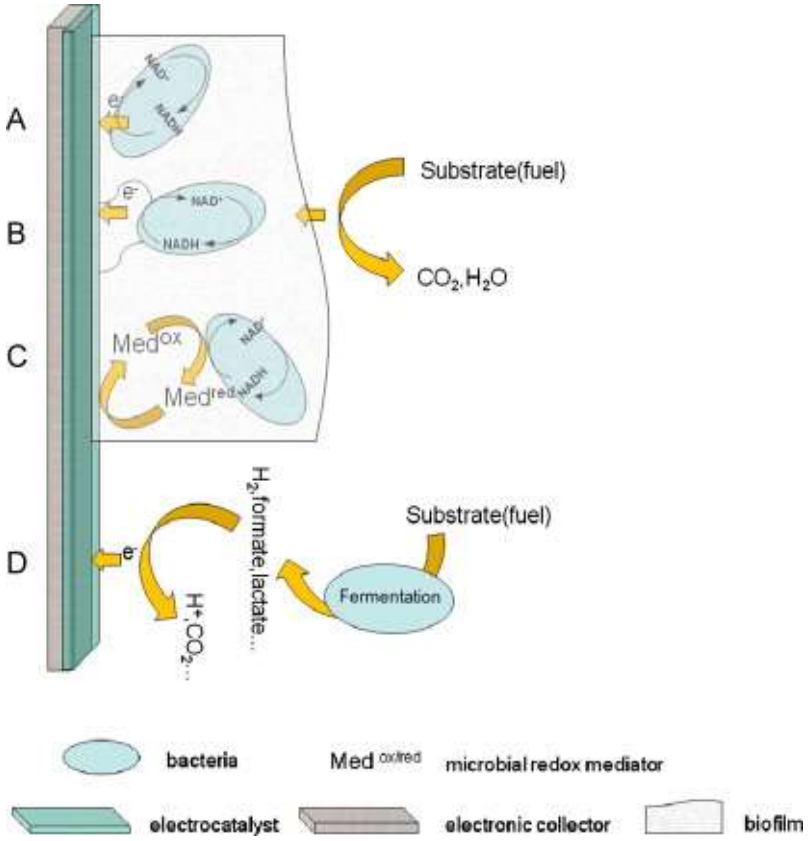

Figure 3. Identified electron-transfer mechanism in MFCs: electron transfer via (A) bacteria cell-membrane, (B) electrically conductive nanowires, (C) conductive matrix of microbial redox mediators, and (D) oxidation of reduced secondary metabolites. Adapted from [51].

To enhance biocompatibility between electrode and bacteria, properties such as surface charges, hydrophobicity, roughness, topography, and configuration are considered from the nano to macrometer level (Figure 4) [53, 54]. Additional features as scalability for larger sizes, easy production, low production costs, appropriate mechanical strength and chemical stability are also desirable [8].

For instance, surface chemistry can impact the microbe–electrode interactions while hydrophilicity, generally promote faster bacterial adhesion. With regard to surface charges and biofilm formation, positively charged surfaces are more favourable due to interaction with the negatively charged surface of most of the bacteria. Further, the topographic features such as nano-roughness, can provide more anchoring points for bacteria enhancing bacterial adhesion. When the microscale is considered, 3D porous materials offer larger surface areas with respect to their volume, maximizing current production with reduced mass transfer limitations [53].

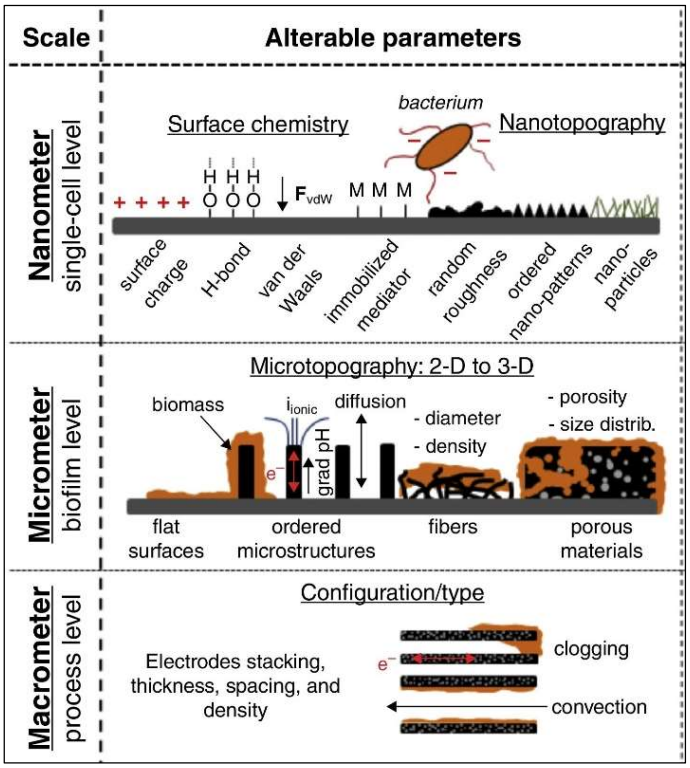

Figure 4. An overview of impact of material surfaces (chemistry and topography) in BES. Adapted from [53].

2.1.2.2 Cathode

At cathode chamber, the electrons, protons, and oxygen meet at the catalyst and react with each other following the ORR, with the function of the electrocatalyst to accelerate the reaction. For this reaction a conductive surface, water and air has to be present in the cathode chamber. The requirement of a balanced three-phase interface (solid, air and water), makes the cathode chamber one challenging aspect on the construction of an MFC [55].

As for anodes, conductive surfaces with sufficient mechanical and chemical stability are needed [49]. In terms of porosity, open pores can influence oxygen transport to the catalyst for the ORR. Different from anodes, cathode materials should have a high reduction potential and the ability to easily capture protons [8].

Generally, catalysts can be incorporated to the carbonaceous or metallic-based materials described to improve the ORR that takes place at the cathodes. The ORR is a multi-step reaction, where oxygen can be directly reduced to water via a $4e^-$ pathway or a two-step $2e^-$ pathway, forming hydrogen peroxide as an intermediate product in alkaline solutions as following [4, 56].

$O_2 + 2H_2O + 4e^- \rightarrow OH^-$

$O_2 + H_2O + 2e^- \rightarrow OH^- + HO_2^-$

Suitable electrocatalysts should support either the $4e^-$ or $2 \times 2e^-$ pathway with minimal production of subproducts, to avoid degradation of fuel cell components and restricted efficiency [56]. Likewise, the ORR catalysts in MFC must be tolerant to poisoning due to the contact with wastewater (single-chamber designs), resistant to biofouling and able to restore catalytic activity after cleaning [57].

Besides oxygen, the electron acceptor most commonly used in the cathode, several aqueous catholyte such as potassium ferricyanide or permanganate are also efficient electron acceptors applied in MFCs. However, their costs, the need for frequent replacement and their potential to be harmful to the environment, limit their use [47].

2.1.2.3 Membrane

Even though membranes are not essential for MFCs, it is mainly used to separate liquids present in the cathode and anode chamber, while inhibiting the presence of oxygen in the anode chamber. In addition, considering that the membrane should be permeable, it provides an environment for efficient transport of protons from the anode to the cathode. Besides, it can also be used to avoid unwanted subtracts from one chamber to another, loss of substrate and biofouling at the cathode chamber [47, 58].

Further, advantages of using an MFC without a membrane are low costs in the production and high system performance, due to the decrease of the internal resistance [58].

Polymers, ceramics, and composites are the classes of materials used as membranes in MFCs. Examples of particular materials often used as membrane are Nafion, Zirfon, Ultrex, clayware and sulfonated polymer [13, 47].

2.1.3 Electrode Materials Used in MFCs

In general, carbon-based, metal-based and composite materials are the three main types of electrode materials used in MFCs [53]. The common use of carbon-based materials can be attributed to the low cost, good conductivity, biological inertness, stability and catalytic activity [36]. Among carbon-based materials, carbon: cloth, brush, rod, mesh, veil, paper, felt are used as well as granular activated carbon, granular graphite, carbonized cardboard, graphite plate and reticulated vitreous carbon (Figure 5a-l), varying between planar and three-dimensional (3-D) materials [6]. As metal-based materials, stainless steel (SS) (plate, mesh and scrubber form) (Figure 5m-o) and silver, nickel, copper, gold and titanium as sheet and plate form (Figure 5p-t) were already investigated [6]. Advantages of metal-based anodes are the high conductivity and their high mechanical strength.

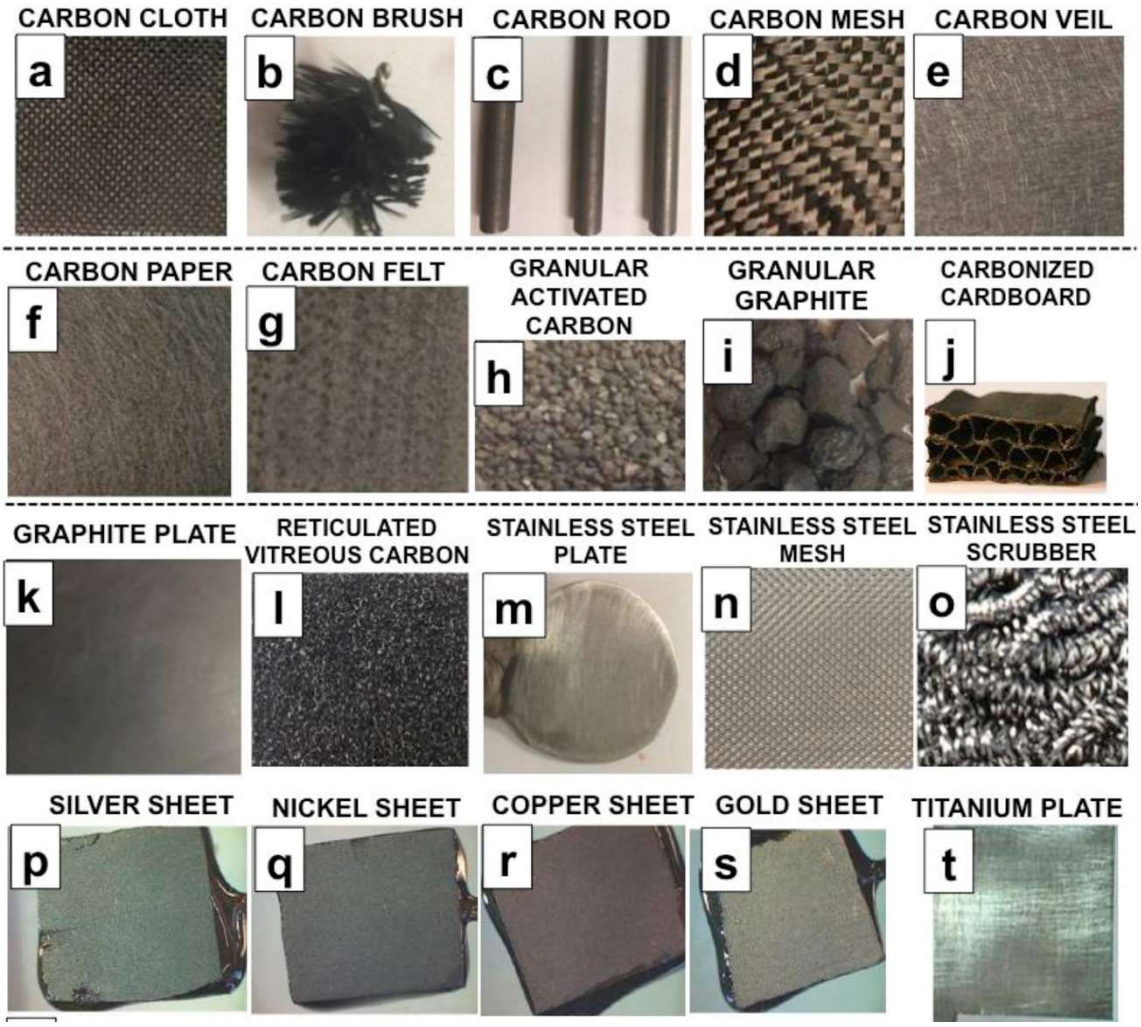

Figure 5. Digital photographs of types of electrode materials: carbon cloth (a), carbon brush (b), carbon rod (c), carbon mesh (d), carbon veil (e), carbon paper (f), carbon felt (g), granular activated carbon (h), granular graphite (i), carbonized cardboard (j), graphite plate (k),

reticulated vitreous carbon (l), stainless steel plate (m), stainless steel mesh (n), stainless steel scrubber (o), silver sheet (p), nickel sheet (q), copper sheet (r), gold sheet (s), titanium plate (t). Adapted from [6].

Carbon felt (Figure 5g) is one of the carbonaceous material used very often as anode material in MFCs due to its electrical conductivity and flexibility. The work of Cha et al. [59] described an investigation of the effect of electrode material on performance using different sets of electrodes consisting of carbon cloth and graphite felt. Among four MFCs with different electrode materials, the MFC with graphite felt as anode and cathode showed the highest power density of 16.7 W m^{-3}, attributed to the superior attachment of the biofilm [59]. Carbon brushes (Figure 5b) are also heavily used as anodes on MFC investigations aiming the increase of accessible surface area and decrease in costs. The work of Logan et al. [60] highlighted the highest power density (2400 mW m^{-2}), normalized by cathode projected area, achieved by an air-cathode system in the earliest investigations with carbon brushes. The work of Chen et al. [61] describes one additional interesting low-cost carbonized cardboard material (Figure 5j), composed by a single wall corrugated cardboard from recycled paper. Projected current density ranging from 70 A m^{-2} to 390 A m^{-2} could be obtained as resulting performance [61]. Despite the commonly reported antimicrobial activity of silver and cooper, the work of Baudler et al. [62] demonstrated electrochemical active biofilms on these surfaces, with anodic current densities of 1.1 mA cm^{-2} and 1.5 mA cm^{-2}, respectively. The findings of this study increased the prospect of metals as electrode in BES.

However, properties such as inherently hydrophobic character and limited active binding sites restricting microbial adhesion and biofilm formation, as well as low electron conductivity and mechanical strength (for some varieties) limits the use of carbon-based electrodes [10, 53]. Regarding metal electrodes, their high costs, biocompatibility and stability concerns still hold back the operative potential window [53, 62].

In reality, it is difficult to choose a material, which completely fulfills the desirable requirements of electrodes in MFCs. Nevertheless, to improve the properties of the anode materials, surface modifications and composite materials are used as alternative approaches to increase power density. Regarding surface modifications, nanostructures such as carbon nanotubes (CNTs) and graphene and conductive polymers, are incorporated into the structures [10]. One of the goals of the modifications is the provision of functional groups on the anode surface. Positively charged functional groups at the anode surface enable the interaction between the negatively charged bacteria cell wall [63] via electrostatic interactions [53].

Several modifications on carbon or stainless steel anodes with CNTs were investigated with the aim of changing the surface structure [64-66]. Nano-roughness provides anchoring points for bacteria which facilitate the adherence to the surface [53]. CNTs enhance the surface area by creating a more 3-D like topology and therefore enlarging the accessible surface area as well as improving hydrophilicity for bacteria attachment as discussed in [65-67]. On the other hand, the operational costs in MFCs are also elevated with CNT-incorporation making its large scale application unfavorable [10]. Graphene has also been considered in MFCs due to the capability of improving electronic conductivity, specific surface area and mechanical strength [68]. For instance, coating the surface of SS-felt with CNTs and graphene in the work of Hou et al. [69] dramatically enhanced the anodic biofilm formation and thus the bioelectrocatalysis on SS felt, which was associated to the larger surface area for reaction, interfacial transport and biocompatible interface.

In terms of conductive polymers, for instance, polyaniline (PANI), poly(3,4-ethylenedioxythiophene) (PEDOT) or polypyrrole have been used as a coating or combined with carbon-based materials to improve the hydrophilicity of the surface and the interactions with the bacteria [10]. The work of Cui et al. [63] presented a PANI/graphite felt CNT modified electrode with improved electrical conductivity, accessible surface area, and hydrophilicity, when compared to graphite felt bare electrode. Liu et al. [70] incorporated PEDOT on carbon cloth electrode, resulting in an increase of redox-active centers and reduced anodic resistance. Poly pyrrole was first *in situ* polymerized on CNT then deposited on carbon felt electrode in the study of Roh and Woo [71], decreasing the anodic resistance. In addition, polypyrrole deposited on SS surfaces improved corrosion resistance [72]. Even though polymers are conductive, biocompatible and relatively cheap, the shrink-swell capacity and its stability often limit their use [73].

Modifications with nanocomposites of metal oxides semiconductors of titanium (Ti), manganese (Mn) and iron (Fe) were experimented in order to improve the conductivity of the anode or generate active centers for interactions with the bacteria [10]. The positive effect in MFC performance by the use of TiO_2 with carbon-based materials was described in the works of Yin et al. [74] and Tang et al. [75]. TiO_2 contents of 200 mg/0.2 g of activated carbon and 0.5 g/piece of loofah sponge were used at the start, respectively. The improved performance was attributed to the contact area of the 3-D structure developed (Figure 6) and biocompatible surfaces for interfacial bacterial electron exchange, with [74, 75]. Carbon paper electrode modified with Fe_3O_4-CNT (0.07 to 2.52 g Fe_3O_4/0.1 g CNT) and carbon cloth coated with Fe_2O_3 (C/Fe_2O_3 loading of 1 mg cm^{-2}) were reported in [76] and [77]. As a result, a favorable improved

environment for bacterial growth and enhance in extracellular electron transfer were presented [76, 77].

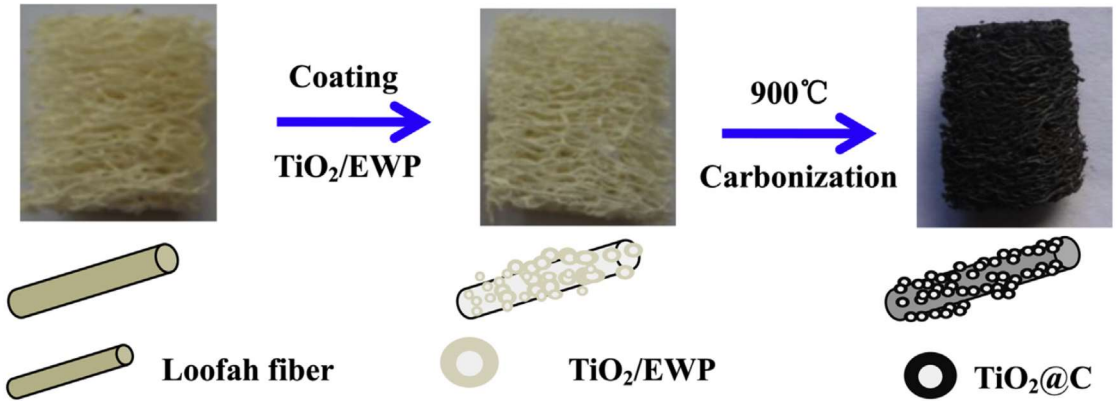

Figure 6. Schematic illustration of the preparation of the loofah sponge electrode with capacitive layer composed of TiO_2 and egg white protein (EWP)-derived carbon. Adapted from [75].

Focusing on cathode materials, enzymes, microbes or abiotic catalysts are used to facilitate the ORR reaction in MFCs [6]. Regarding abiotic catalysts, they are mainly grouped according to the presence/absence of platinum (Pt) and presence/absence of non-precious metal catalysts. These groups are Pt-based (with $4e^-$ transfer mechanism), carbonaceous-based (metal-free, with $2e^-$ transfer mechanism) and nonprecious metal catalysts-based (with $2e^-$ or $2x2e^-$ or $4e^-$ transfer mechanisms) [6]. Even though Pt-based have been by far the most used in the cathode, due to its high cost and long-term operation stability issues several nonprecious ones have been developed [6, 56]. Proposed alternatives to ORR electrocatalysts to address Pt-based material issues can be additionally divided into carbonaceous-based, transition metal-containing (M-C) and/or nitrogen-doped carbon (M–N–C or N–C) materials [78-80]. Activated carbon, graphene, carbon nanotubes, carbon nanofibers and carbon black are generally applied in MFCs as carbonaceous materials, while for M-N-C materials, Mn, Fe, Co, Ni are usually the metals (M) considered [6].

The use of Pt-based catalysts could improve electrical power generation from 0.02 to 0.097 mW in previous work of Oh et al. [81]. However, not only cost limitations but also the stability of Pt towards components of wastewater hinders its use for the large-scale operation of MFCs [82]. Pt alloys with transition metals were used as an attempt to replace Pt-containing materials due to increase in d-band vacancy promoting its electroactivity towards ORR [57, 82].

Considering the low costs and relatively stable performance, carbonaceous-based cathodes are also investigated to replace Pt-based materials. Among the varieties, activated carbon is one of the most used for ORR in MFCs [6]. Watson et al. [83] and Ahn et al. [84] reported that chemistry and porosity significantly affect the overall performance. A positive impact in performance was also observed by Zhang et al. [85] when the conductivity of activated carbon was increased through the addition of carbon black.

In addition, nitrogen doping approach was also described to enhance the ORR catalysis function of carbonaceous materials (N-C) [82]. The outcome is related to positive charges adjacent to C atoms which favor the oxygen adsorption and O-O bond breaking [57, 86]. Works of He et al. [87] and Feng et al. [88] demonstrated N-doped CNTs and N-doped mesoporous graphene outperforming the Pt/C-MFCs in terms of power production. By means of the M-C materials, activated carbon was doped by non-stoichiometric Fe_3O_4 in the work of Fu et al. [89], resulting in a maximum power density 83% higher than the bare activated carbon, with a 4-electron pathway mechanism. Chen et al. [90] reported a MnO_2/CNT coated-stainless steel mesh cathode with improved electron transfer number and maximum power density comparable to a Pt/C MFC. MnO_2 was similarly *in situ* reduced on graphene in [91] significantly increasing the power density from 1470 mW m^{-2} (pure MnO_2) to 2083 mW m^{-2}, which was also 22% higher than the MFC with Pt/C. However, since the synthesis of M-graphene catalysts consists of two-steps (reduction of graphene oxide and metals incorporation), may not always be practical for MFC applications [57].

As a combination of M-C and N-C catalysts types, CoNi alloy particles were encapsulated at the end of CNTs and N-doped graphene filled the internal cavities of bamboo-like CNT hybrid (Figure 7) [92]. When tested in MFCs, the developed cathode catalysts yielded an average current density of 6.7 A m^{-2}, slightly lower than that of Pt/C, but with an estimated cost 200 times lower than Pt/C [92].

M-N-C materials refer to a wide range of materials with metal cations coordinated with nitrogen functional groups in carbonaceous matrixes [57]. Whilst the catalytic activity of the metal centers play an important role in the ORR, the different nitrogen and carbon precursors affect the surface chemistry of the prepared catalysts and therefore also influencing the catalytic performance [6].

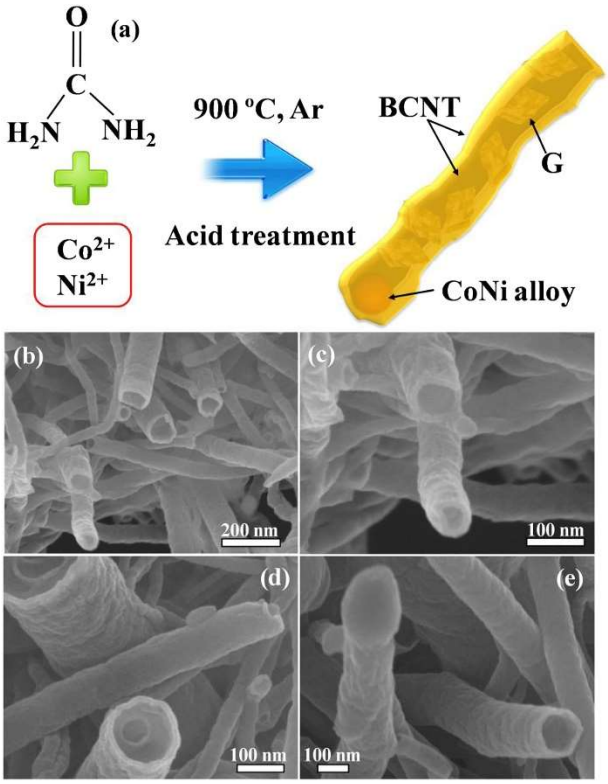

Figure 7. (a) Schematic illustration for the synthesis process of the cathode catalysts and its FESEM images (b–e) at different magnifications. Adapted from [92].

Metal macrocyles, a class of M-N-C complexes, are one of the alternative cathode catalysts applied in MFCs. For instance, the use of pyrolyzed iron phthalocyanine (FePc) in the work of [93], revealed a current density comparable to Pt/C in acidic medium. The approach of Co macrocycles started more than a decade ago [94] and with further improvements, deposited cobalt tetramethylphenylporphyrin (CoTMPP) and FePc on CNTs produced a maximum power density of 751 mW m^{-2}, which was 1.5 higher than that with Pt/C [95]. Li et al. [96] combined non-pyrolyzed binuclear CoPc with CoO and NiO and could achieve power densities (368 mW m^{-2} and 450 mW m^{-2}, respectively) comparable to MFC with Pt/C (450 mW m^{-2}).

Other precursors as polymers, simple organic compounds and metal-organic frameworks (MOFs) can also be used to form metal-N_x/C active sites [57]. Zhao et al. [97] combined Co and Fe salts with poly(2,6-diaminopyridine) (PDAP) and pyrolyzed at 700 °C under NH_3 atmosphere (Figure 8). A maximum power density of 1.2 W m^{-2} was achieved, which was 2.2 times higher than that with MFC-Pt/C being accounted to the abundance of Fe-N_x and Co-N_x centers [97].

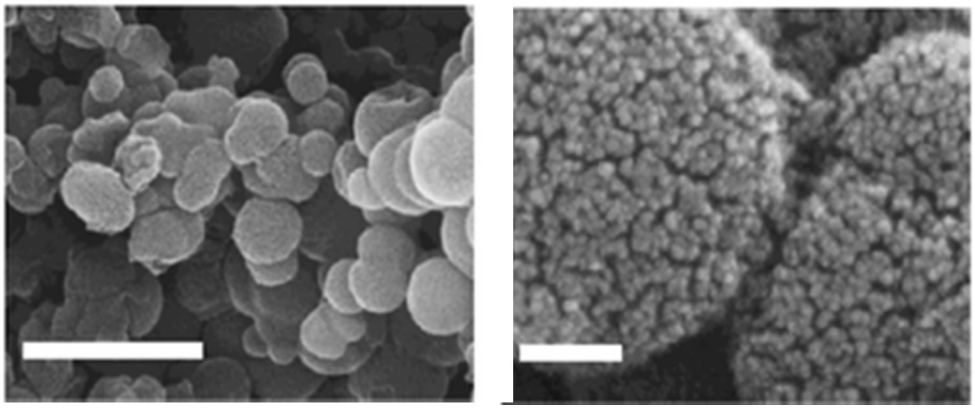

Figure 8. Surface morphology of CoFe-PDAP after pyrolysis in the presence of NH_3, Scale bars: 1 μm (left); 100 nm (right). Adapted from [97].

As organic compounds strategy, cyanamide was pyrolyzed with $FeCl_3$ in [98] forming a core-shell structured Fe-N-C nanorod. When the developed materials were tested in an MFC with two cathode chambers, a slightly higher power density (4.3 W m^{-3}) than for that chamber with Pt/C cathode was achieved. The application of pyrolyzed MOFs structures in MFC is fairly recent and have gained interest due to its high specific surface areas, tuneable microstructures and M-N-C sites [57]. In a recent study by Tang et al. [99], Co-MOF (ZIF-67) was pyrolyzed at 800 °C in the presence of $NiCl_2$. The Ni/Co-MOF-based material produced a 1.7 times higher maximum power density (4336 mW m^{-2}) than the MFC with Pt/C [99].

2.1.4 Ceramic Composite Electrode Materials Applied in MFCs

Ceramics were first applied in fuel cells, in a solid-oxide fuel cell (SOFC) type in 1937. Due to its appropriate thermal stability for SOFC conditions as well as adjustable porosity and permeability for electrode design, ceramics are the materials of choice [13]. The interest in the use of these features as functional elements of MFCs is progressing. An additional benefit is that ceramics are not toxic for microorganisms and are already applied in wastewater treatment systems as supports and filter materials [36]. Most of the investigations of ceramics in MFCs focus on their use in reactor design and as separators for proton exchange. Regarding their use as electrode materials, the prospects have not been highlighted often [36]. As described in the topic 2.1.3, the use of carbon materials has advanced further for MFCs. However, limitations of electrical activity and active binding sites for microbial adhesion still motivate the search for alternative materials that could provide better surface properties.

The tested ceramic anode materials in MFCs can be divided into conductive ceramic materials, ceramic as part of a composite and ceramic deposited on a conductive support [36]. As regards conductive ceramics, Thorne et al. [12] developed titanium oxide-based porous ceramic anodes covered with a conductive ceramic film of fluorine-doped tin oxide (FTO) shown in Figure 9. When tested in a photo-MFC setup, an increase of 16 times in power density was found compared with a carbon anode. The elevated performance was attributed to the effective biofilm growth on the ceramic surface [12].

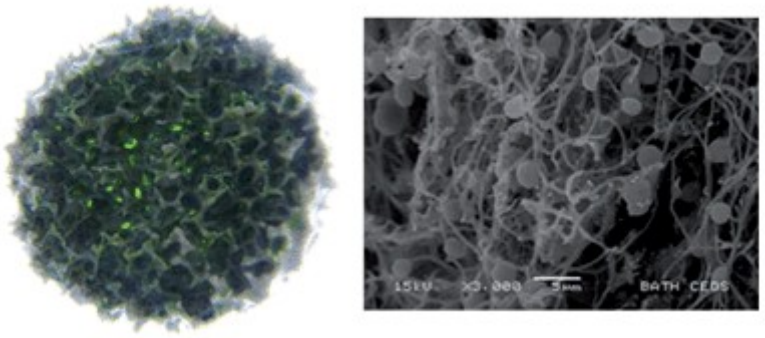

Figure 9. Porous FTO coated ceramic anode material covered with an algal biofilm and its internal algae growth. Adapted from [12].

Lately, attention was given to ceramic materials composed of transition metal carbides. A Mo_2C anode material demonstrated a maximum power density of 2.39 W m^{-3} in an MFC based on *Klebsiella pneumoniae*, which was higher compared with the value achieved by carbon felt (0.61 W m^{-3}) [100]. Further CV analysis confirmed that Mo_2C catalyzes the oxidation process of microbial fermentation and the direct electron transfer from bacteria to anode, working as an anodic catalyst [100].

Titanium suboxides (Ti_4O_7) has also been considered in the work of Massazza et al. [17] as an ice-templated titanium-based ceramic (ITTC) conducting 3D structure with 88% porosity (Figure 10). The anode material outperformed graphite in a bioelectrochemical reactor with *Geobacter sulfurreducens*. The achieved performance demonstrated the potential of ceramic materials when compared to the state-of-the-art available carbonaceous electrodes (Figure 10) [17].

For ceramic as part of a composite anode, four groups can be distinguished: transition or non-transition metal oxides combined with carbon, transition or non-transition metal oxides combined with conducting polymers, transition or non-transition metal oxides combined with carbon, conducting polymers and metal nanoparticles and finally, conducting polymers with carbon [36]. Due to the non-conductive aspect of ceramics, the function of electrical conductivity in the composites is mainly supported by the carbonaceous materials.

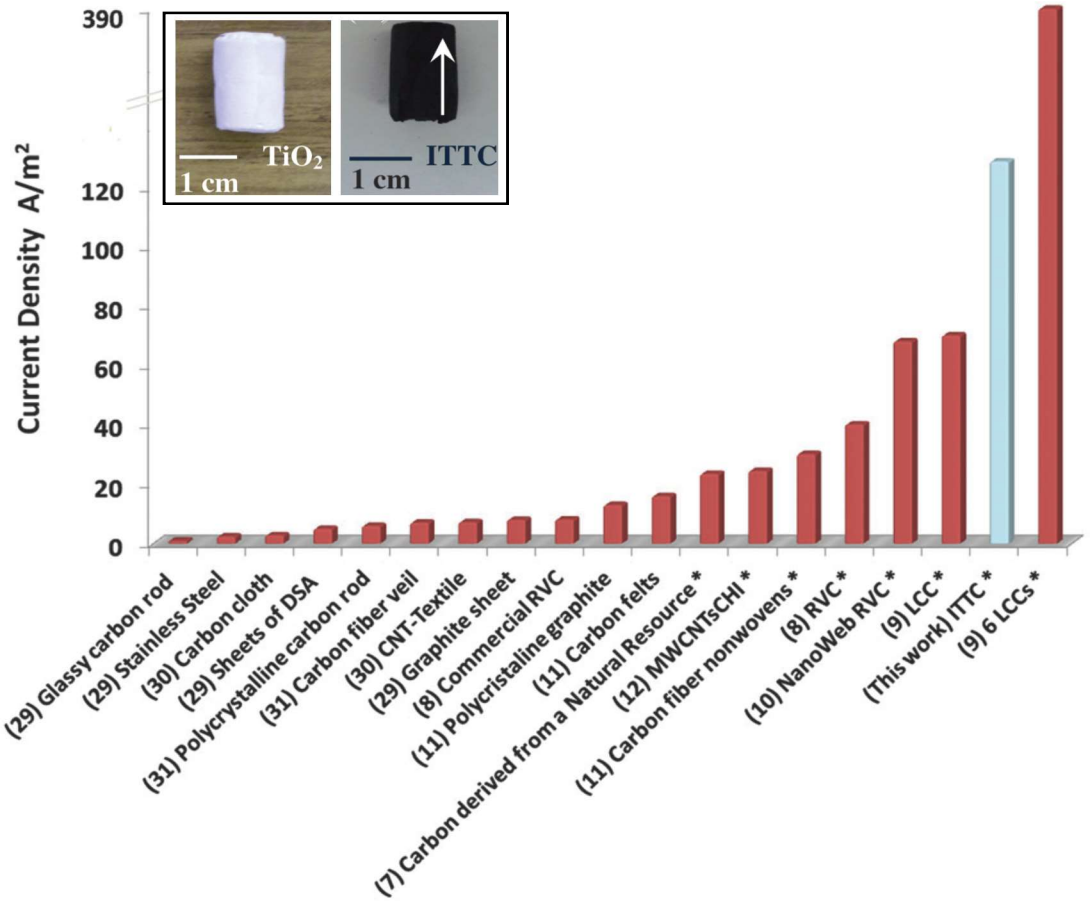

Figure 10. 3D TiO_2 porous scaffold, obtained ITTC electrode (top of the graph) and comparison of ITTC electrode performance with that of the current state-of-the-art electrodes. Adapted from [17].

Works of Mehdinia et al. [7, 101] described SnO_2 combined with multi-walled CNTs/glass carbon and graphene oxide/carbon fiber and its MFC performances in the presence of *Escherichia coli*, respectively. For the combination with nanotubes a maximum power density of 1421 W m^{-2} was achieved, while for graphene oxide, 1624 W m^{-2} was reached. The resulted performance was related to the large surface area of graphene oxide and CNTs enhancing charge transfer, biocompatibility and interactions between graphene and tin(IV) oxide [7, 101]. In addition, a PANI-mWO_3/carbon felt anode material demonstrated a maximum

power density of 0.98 W m^{-2} in MFCs performance tests with *Escherichia coli* [51]. Nano-CeO_2 was also used to modify the carbon felt anode in a work of Yin et al. [102] and an increase from 1.70 W m^{-2} to 2.94 W m^{-2} was observed in contrast with the unmodified anode. From additional CV analysis was inferred that the bioelectrochemical activity of exoelectrogens was promoted by nano-CeO_2 [102].

For ceramic materials deposited on conductive supports, Lv et al. [103] deposited ruthenium(IV) oxide on a carbon felt support achieving an increase of 16.7 times in power density when compared to the unmodified anode. The positive impact was related to the capability of ruthenium(IV) to be reduced and oxidized quickly contributing to effective electron transfer [103]. In the work of Chen et al. [104], a paste of manganese(IV) oxide and polypyrrole (MnO_2/PPy) was applied to carbon felt as coating and the anode was tested in a marine benthic MFC. An enhancement in power density of 2.2 times was attained by the modified anode when compared to unmodified carbon felt. The improvement in the output performance was associated with the fact that manganese(IV) oxide acts as an electron carrier and the additional facilitated electron transport given by the conducting polymer [104].

On an inverse way, non-conductive ceramic scaffolds (70% SiO_2/20% Al_2O_3) in the shape of Berl saddles, commonly used as support for bacteria immobilization in bioreactors, were covered with a thin carbon layer in [16] as a low-cost proposed anode material. A maximum power density of 130 mW m^{-2} was obtained, which is about 2–3 times higher than the values reported in the literature by commercial anode materials.

As cathode materials in MFCs, ceramics are either applied as support or regarding its catalytic functions. As an alternative to replace carbon, TiO_2 can be used as support for cathode catalysts (Pt), due to improved corrosion resistance and higher catalytic activity [36]. The work of Venkatesan and Dharmalingam [105] described TiO_2 supported metal catalysts (Pt/TiO_2, Pt–Fe/TiO_2), which were tested in MFC resulting in higher power densities (110.5 and 136.8 mW m^{-2}) compared to that of Pt/C (77 mW m^{-2}). Additional CV analysis demonstrated superior electrochemical stability of TiO_2 than carbon.

Considering the heat-treated materials possessing crystalline structure classified as ceramics, metal oxides of manganese, iron, cobalt, nickel, copper, vanadium and zirconium and composite materials are studied in MFCs [36]. MnO_2 are frequently used cathode catalysts and the work of Zhang et al. [106] reported three modifications of MnO_2 – α, β and γ-structures as an alternative cathodic catalyst to Pt. β-MnO_2 was tested in distinct MFC designs producing higher output power, with the maximum volumetric power density of 3773 ± 347 mW m^{-3}, accounted to its largest specific surface area [106]. In the work of Chen et al. [90] SS mesh was

coated with MnO_2/CNT and polymethylphenyl siloxane (PMPS) revealing a maximum power density of 2676 mW m^{-2} (normalized to the cathode surface area), with the additional feature of water-repellent gas-diffusion layer (due to PMPS coating) improving cathode performance. Vanadium pentoxide microflowers (V_2O_5-MFs) catalyst (Figure 11) were reported by Noori et al. [107] and compared with α-MnO_2 nanotubes (α-MnO2-NTs), resulting in the improved power density of 6.06 W m^{-3} related to the α-MnO_2-NT (5.5 W m^{-3}) material.

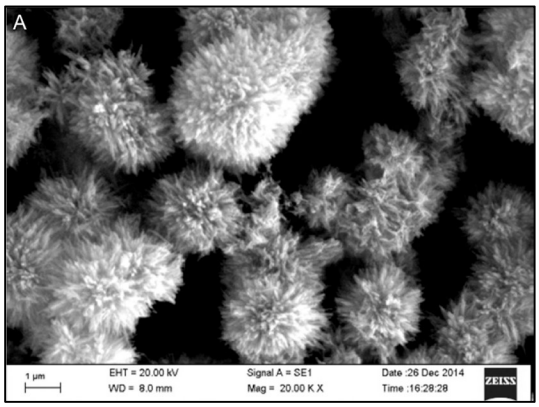

Figure 11. SEM micrograph showing the surface morphology of as-synthesized V_2O_5 catalysts with flower-like structure. Adapted from [107].

CoOx nanoparticles were incorporated on carbon in order to enhance the catalytic activity of cobalt phthalocyanine [108]. A maximum power density of 780 mW m^{-2} was reached during the MFC studies which were 50% higher than that without cobalt oxide [108]. Mecheri et al. [109] developed a carbon-supported ZrO_2 cathode which produced a maximum power density of 600 mW m^{-2} with a comparative cost of 15 times lower than Pt/C cathode. With regard to ceramic materials as biocathodes (using bacteria as catalysts for oxygen reduction), the use of ceramics has not been yet investigated [36].

From this perspective, there have been great efforts in the development of novel electrode materials that could provide better surface characteristics for biofilm formation and improved electron transfer. Other properties such as optimized porous structure to accommodate bacteria cells and maintain the access of nutrients through the pores, and long-term stability, are also highly desirable and investigated earlier [5, 8, 12]. Even though ceramic materials are potential candidates which are able to fulfil the aforementioned properties, most of the investigations focus on proton exchange membranes and reactor design [14, 15]. Therefore, there is still a broad field of research to be explored in terms of new classes of electron conducting porous ceramics in MFCs.

2.2 Polymer-derived Silicon Oxycarbide (SiOC) Ceramics

In order to meet the before mentioned requirements, polymer-derived ceramics (PDCs) could be seen as an appropriate class of materials for the new development of electrodes and membrane in MFC technology.

Polymer-derived ceramics are a rather new class of ceramics that can be synthesized via cross-linking and controlled thermal treatment (pyrolysis) of appropriate polymeric silicon-based precursors [110]. The first experiments regarding this synthesis strategy were made in the early 1960s by Aigner and Herbert [111] and Chantrell and Popper [112], which reported the production of non-oxide ceramics starting from molecular precursors [18]. However, just at the end of 1970s, significant progress occurred with the works of Yajima et al. [113, 114], demonstrating an organosilicon polymer suitable to be converted into a silicon carbide (SiC)-based fiber.

The transformation from polymer to ceramic provides ceramics with a polymer-like nanostructure and ceramic-like properties dependent on pyrolysis temperatures. The stated properties are influenced by the chemistry and architecture of the precursors, their processing route, and by the parameters used for their pyrolysis (heating rate, reactive or inert atmosphere, and dwelling time) and thus, can be adjusted to a huge extend [18, 110].

Silicon-based polymeric precursors (e.g., polymers based on a backbone of Si atoms containing also C, O, N, B and H atoms) are applied for the last 40 years in the production of various advanced ceramic components such as fibers, coatings, powder, infiltrated porous media and complex bulk parts [110, 115]. To generate these shaped ceramic parts, manufacturing processes such as plastic-forming techniques (e.g., fiber spinning, foaming, warm pressing, extrusion, injection molding or resin transfer molding) are used and represent an advantage over conventional (powder processing) procedures [115].

The relatively low cost of the precursors and the wide variety, the chemical composition not achievable by other techniques (polymers with a -Si-O- backbone converted into an amorphous SiOC (silicon oxycarbide) residue), low processing cost and exceptional thermo-mechanical and chemical properties obtained, makes the PDCs route an emerging chemical process for a relatively simple production of ceramic-based materials [18, 115].

2.2.1 General Background

Preceramic polymers consisting of oxygen-free inorganic/organometallic systems are used to provide non-oxide ceramics, which decompose according to the following equation [116].

polymers (s) → ceramics (s) + species (g)

A suitable preceramic polymer precursor consist of Si-based polymeric chains, and side chain functionalities, general represented in Figure 12 as monomeric unit. In the schematic representation, X is considered as the group of the polymer backbone (e.g. Si, CH_2, and O) whereas R^1 and R^2 are the substituents attached to silicon [18].

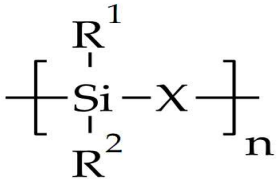

Figure 12. General representation of the molecular structure of preceramic organosilicon compounds. Adapted from [18].

The variation of X determines the class of the final polymer such as poly(organosilanes) for X=Si, poly(organocarbosilanes) for X=CH_2, poly(organosiloxanes) for X=O, poly(organosilazanes) for X=NH, and poly(organosilylcarbodiimides) for X=[N=C=N]. Nevertheless, since the variable atoms in the backbone can belong to more than one group, an even wider range of possible polymer composition must be considered, as schematized by Colombo et al. [18] (Figure 13).

By changing the functional groups R^1 and R^2, chemical, thermal, electronic or optical properties can be adjusted. R^1 and R^2 are generally composed by H or carbon-based (e.g. alkyl, aryl, etc.), which also influence the carbon content of the finally derived ceramic material (in non-oxidizing pyrolysis atmosphere) [18].

In addition, during the choice of preceramic polymers two requirements should be considered in order to attain an effective thermal decomposition process with a suitable ceramic yield. Firstly, a polymer with sufficiently high molecular weight should be taken, in order to avoid the volatilization of low molecular- weight components. Secondly, polymers with appropriate rheological properties and solubility (relevant for the shaping process), as well as

latent reactivity (i.e., the presence of functional groups) for any subsequent curing and cross-linking steps should be chosen [110, 117].

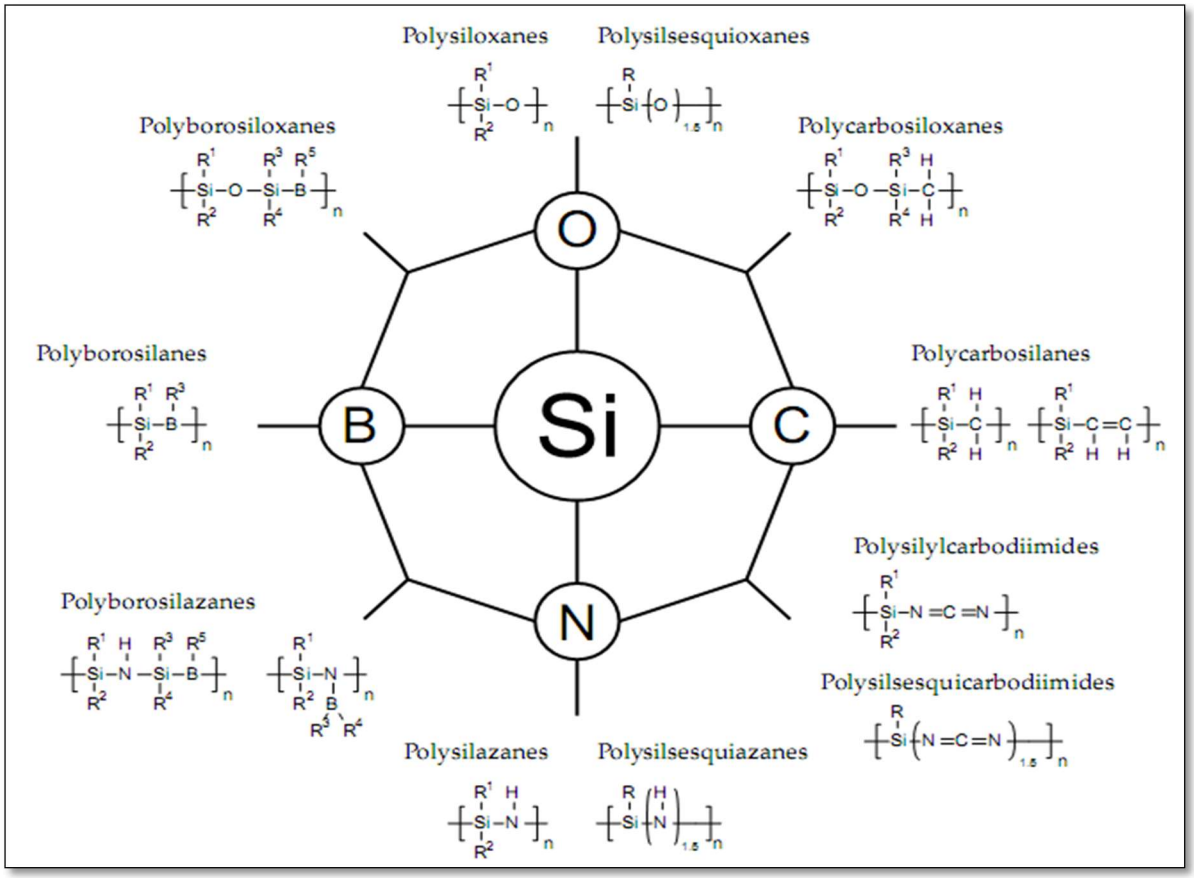

Figure 13. Main classes of Si-polymer as precursors for ceramics. Adapted from [18].

After polymerization, the processing route of PDCs consists of four steps: shaping, cross-linking, polymer-to-ceramic conversion and crystallization when desired, as represented in Figure 14. In each segment, the polymeric precursor undergoes different chemical reactions deepening on the temperature. Amorphous ceramics are obtained upon pyrolysis (temperatures ranging from 800 to 1400 °C), while subsequent annealing at high temperatures leads to (poly)crystalline materials [110, 117]. Moreover, stopping pyrolytic conversion of preceramic polymers at low pyrolysis temperatures (500 – 700 °C) allows the creation of hybrid ceramic (ceramers) materials with properties in between polymers and of ceramics [118].

The relatively low synthesis temperature of 1100 to 1400 °C for the production of PDCs is of economic interest, due to lower energy consumption in comparison with classical ceramic powder processing technology, which requires 1700 to 2000 °C to sinter covalent Si_3N_4 and SiC-based ceramics [18].

With regard to the polymer-to-ceramic transformation steps description, the initial shaping step consists of a fabrication of a green body with defined geometry and density. It also represents an advantageous aspect of PDCs route when compared with powder process techniques, since the precursors are in the polymeric state and can be subjected to a large variety of forming methods [18]. Moreover, the possibility of obtaining a machinable component prior to the polymer-to-ceramic conversion also allows a more precise shape control without the limitations related to ceramic brittleness and tool wear [119].

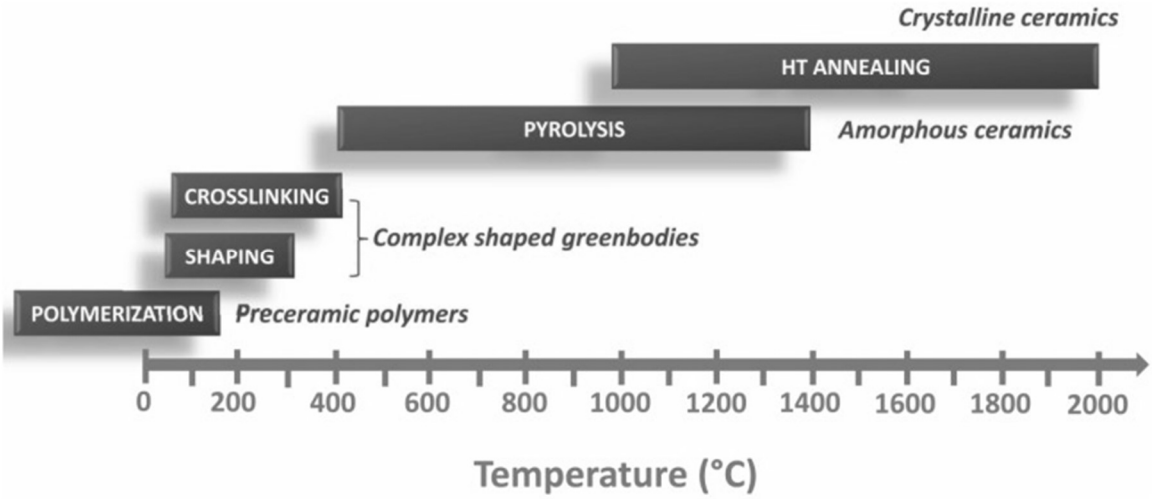

Figure 14. Polymer-to-ceramic transformation of preceramic polymers. Adapted from [117].

In addition to basic shaping technologies like pressing, tape casting, coating and injection molding, more advanced forming methods like rapid prototyping, extrusion, spin coating, and chemical vapor deposition can be used. Complex geometries can be produced by fibre drawing, infiltration of pre-formed scaffolds, joining/bonding, or lithographic techniques [18, 120].

The cross-linking process occurs at lower temperatures (up to 400 °C) with the precursors being converted into organic/inorganic materials. This stage prevents the loss of low molecular weight components of the polymer precursors as well as fragmentation processes during the pyrolysis process and by that increasing the ceramic yield [117]. During cross-linking, functional groups (e.g., Si–H, Si–OH, or Si-vinyl functionalities) are incorporated to enables the formation of a thermoset via condensation or addition which occur typically, below 200 ºC (thermal cross-linking). In addition, catalysts are applied in the interest of lowering the cross-linking temperature and often allows the cross-linking reactions to occur even during shaping [18]. According to the curing mechanism, a release of gaseous by-products, e.g. water or ethanol, can occur leading to the formation of unfavourable structures as trapped pores or

bubbles inside the polymeric material. By controlling this mechanism, it is possible to process either self-foaming polymers or achieve a dense, pore-free ceramic [121].

The last and probably the most important step within the PDC processing route is the polymer-to-ceramic conversion at high temperatures (600–1000 °C) producing totally inorganic, non-volatile amorphous covalent ceramics [117]. The most widely thermal process approach used for this conversion is oven pyrolysis, in which a flowing inert gas continuously removes the decomposition gases from the system [122].

The increase of temperature, starting from 300 °C leads to: structural rearrangements and radical reactions resulting in cleavage of chemical bonds (e.g. Si-H, Si-C and C-H), decomposition or elimination of organic moieties (e.g. methyl and phenyl groups) with simultaneous release of hydrogen and volatile hydrocarbons and the formation of an inorganic network [18, 23]. At temperatures above 1000 ºC, devitrification processes begin to occur leading to amorphous multiphase systems and, subsequently, to nucleation and the growth of nanocrystals. Additionally, phase-separation processes can lead to decomposition, usually accompanied by the release of gases such as CO, SiO (for SiOC-based systems), or N_2 (as for SiCN materials) while the ‘‘free’’ carbon phase is subjected to a graphitization process [18, 110].

Nevertheless, one drawback of PDC technology is the poor control of shrinkage and structural integrity as a consequence of the organic moieties decomposition and gas release. An alternative solution for the latter, is the use of inert and active fillers (Figure 15) [115].

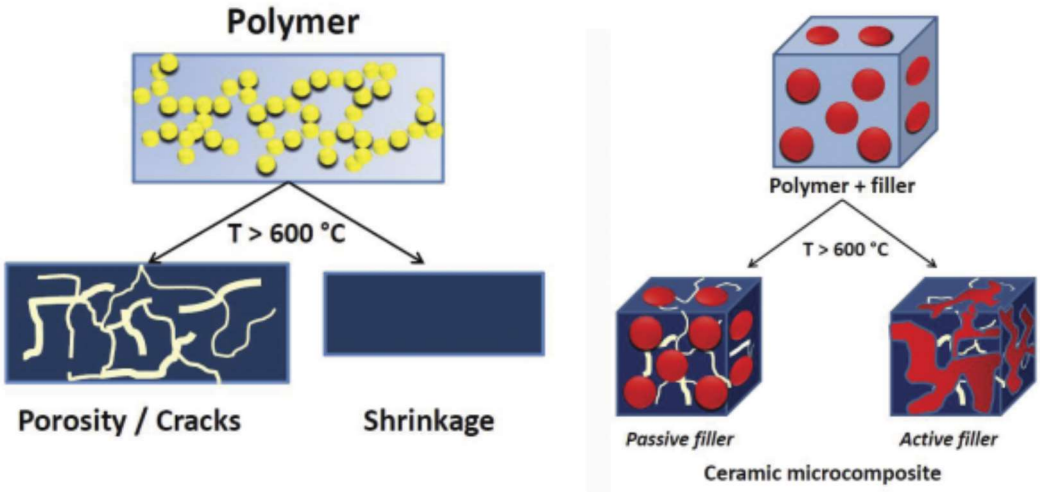

Figure 15. Processing and thermolysis of preceramic polymers containing fillers. Adapted from [18].

The inert fillers are ceramic particles which do not react with the ceramic residue, simply diluting the preceramic polymer, therefore decreasing the amount of gas generated and the associated volume shrinkage, reducing macroscopic cracks formation during processing. In contrast, active fillers, i.e., metallic or intermetallic powders react, during pyrolysis, with the ceramic residue reducing the amount of gas generated and the local gas pressure in the part, respectively, therefore enabling the fabrication of near-net shape, bulk, uncracked ceramic components [115, 123].

Functional fillers including particles, metallic powders, metal salts or fibers can be added to modify the design of the microstructures as well as certain properties, such as electrical conductivity or magnetic characteristics, likewise to tailor the coefficient of thermal expansion of the ceramic component [18].

2.2.2 Silicon Oxycarbide (SiOC) Ceramics

Silicon oxycarbide (SiOC) is an interesting system of PDCs where properties can be tailored by varying chemical composition and pyrolysis conditions. Suitable precursors used to produce SiOC-based ceramics are poly(organosiloxanes), which show excellent chemical and physical properties [18, 117]. Generally, they are represented as silicones and are usually inexpensive with great variety of derivatives commercially available. Polysiloxanes are normally synthesized through the reaction of chloro (organo) silanes with water [18].

Upon pyrolysis, cross-linked polysiloxanes are converted into SiOC glassy network. During the ceramization the release of hydrocarbons (mainly CH_4) and hydrogen takes place while redistribution reactions between Si–O, Si–C and Si–H bonds can additionally occur [124]. At the temperatures ranging from 400 to 600 °C, the evolution of low-molecular-weight silanes can arise leading to a decrease of the ceramic yield. At higher temperatures between 600 and 1000 °C, extensive cleavage processes of C-H, Si-C and Si-O bonds occur and furnish ceramic materials consisting of amorphous SiOC phase and residual free carbon [110, 117] .

In the work of Sorarù et al. [125] the pyrolysis kinetics for the conversion of polysilsesquioxane into SiOC demonstrated that evolution of hydrocarbons (methane) and hydrogen is the main mechanism for the removal of carbon during pyrolysis. Furthermore, the reaction rate was found to directly correlate to the amount of the remaining carbon sites. Thus, the nanostructure/architecture of the SiOC-derived ceramics relies on the configuration of the molecules in the cross-linked preceramic polymer [117, 125].

The cross-linked elastomers can accept relatively high extension without cracks when compared to polycarbosilane, polysilazane and polysilanes. This particular property is useful to shape the starting materials into desired forms by molding, casting, injection, impregnation or extrusion [126].

Processing strategies for producing polysiloxane-derived porous ceramics include replica, sacrificial template, direct foaming and reaction technique schematically presented in Figure 16. The replica, sacrificial template, and direct foaming techniques are related to the pore formation, and the reaction technique deals with the matrix [127].

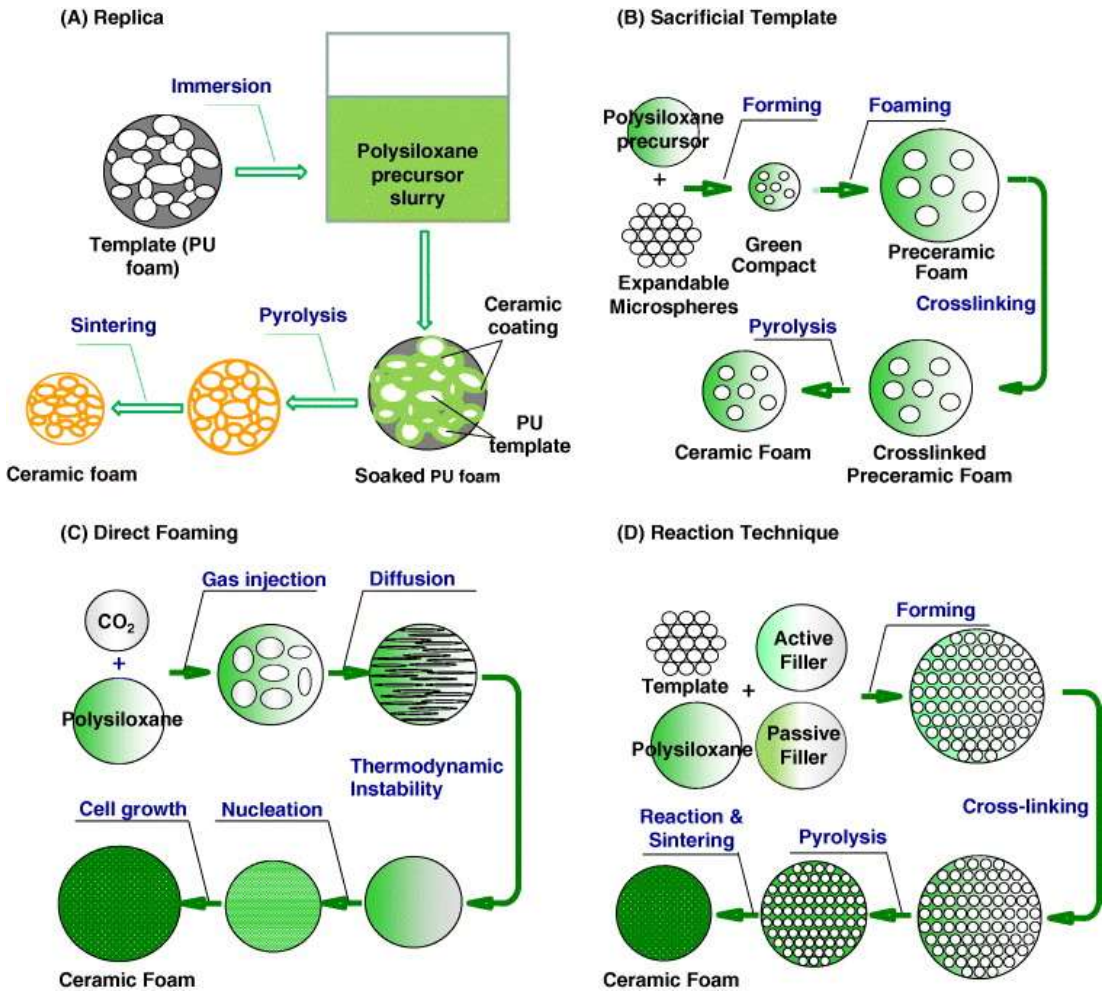

Figure 16. Scheme of processing strategies for the production of polysiloxane-derived porous ceramics: (A) replica, (B) sacrificial template, (C) direct foaming and (D) reaction technique. Adapted from [127].

Briefly, the replica method (Figure 16a) consists of a coated porous structure which decomposes during pyrolysis resulting in the same cell morphology as the original material. Open cells with cell size > 150 μm and porosity range of 85–96% is achieved by this method. The sacrificial template method (Figure 16b) starts with a homogeneously dispersed template in a precursor matrix, followed by extraction of the template material with subsequent pyrolysis and/or sintering generating the porous structure. Varying the type, volume fraction and size of the template, the porosity can be tailored from 20 to 90% and the pore size from 1 to 100 μm [127].

In direct foaming (Figure 16c), bubbles are generated in the polymeric precursor solution to create a stable foam structure which upon heating produces porous ceramics. Open and closed-cell structures with a wide range of cell dimensions and a wide range of porosity or relative density can be prepared with this easy and cheap technique [127]. Conversely, this method limits the production of materials with a narrow cell size distribution, and they often have an anisotropic structure [128]. Lastly, the reaction technique (Figure 16d) combined with previously discussed strategies can develop cellular or microcellular ceramics with open and interconnected open cells and tailored porosity from 11 to 95% [127].

The production of porous ceramics from polysiloxanes precursors offers advantages in terms of simple storage and processing methodology, low processing cost and low processing temperature (1000 – 1200 °C), excellent mechanical strength despite the amorphous phase, semiconduction, excellent oxidation and thermal shock resistance and easy control over porosity and other properties of the resultant ceramics [127].

Regarding the electrical properties of SiOC ceramics, the influence of the microstructure and carbon content was investigated by Cordelair and Greil [129]. For this, SiOC-derived materials from polymethylsiloxane (PMS) and polyphenylsiloxane (PPS), pyrolyzed in an inert atmosphere at 800-1500 ºC were considered. Thus, two temperature regimes could be distinguished in a first model (with respect to the carbon content in the ceramics, Figure 17):

- At low temperatures, a semiconductor behavior was identified that could be attributed to the tunneling processes of localized electrons (tunneling regimes).
- At higher temperatures, electron conduction was found to be induced by the formation of a percolation network of turbostratic carbon (percolation regime) [110, 129].

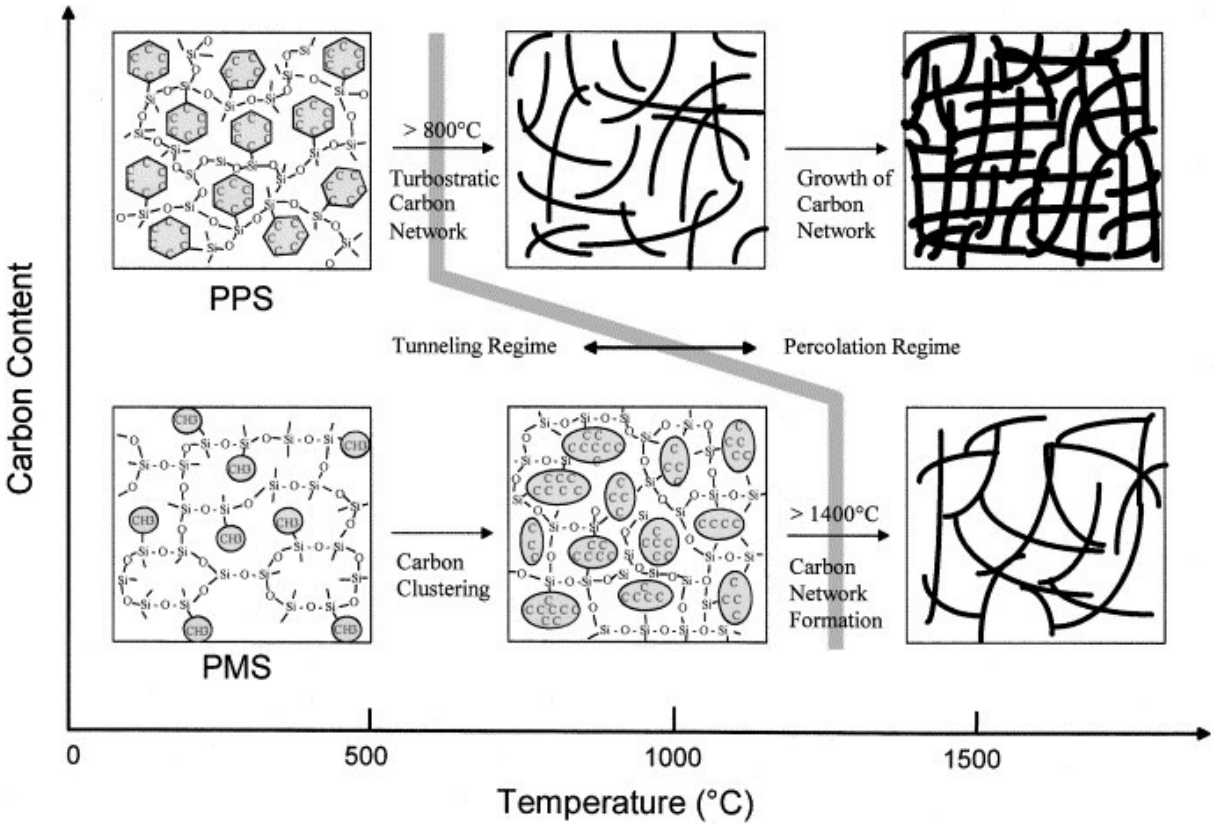

Figure 17. Model of carbon redistribution reactions during pyrolysis in (bottom) PMS and (top) PPS derived ceramic residue. Adapted from [129].

The addition of fillers can influence the electrical properties of the SiOC ceramics. Regarding positive effects of integration of conductive constituents on electrical conductivity of SiOC-based ceramics, Colombo et al. [130] reported the use of fillers such as $MoSi_2$, α-SiC and graphite in amounts up to 80 wt%, as well as, use of copper acetate (up to 80 wt%) and Cu_2O (up to 30 wt%) in SiOC ceramic foams and obtained values of electrical conductivity from 1.4×10^{-5} to 45.5 Ω^{-1} cm^{-1} at room temperature. By varying ratio of graphite, carbon black, and $MoSi_2$, Drillet et al. obtained conductivity in the range of 0.004–0.305 S cm^{-1} in SiOC-based air cathode [131]. The influence of carbon nanotubes and graphene oxide incorporation into a SiOC matrix (Figure 18a) was investigated by Moni et al. [22]. An increase in direct current (DC) conductivity by 3–4 orders of magnitude was found with incorporation of 5 wt% nanofilers (2.97×10^{-9} S cm^{-1}, 2.5×10^{-6} S cm^{-1}–5 wt% GO and 2.1×10^{-5} S cm^{-1}–5 wt% CNT) [22].

Cordelair and Greil [132] have reported a composite ceramics from polymethylsiloxane (NH 2100) loaded with $MoSi_2$ filler in the system Mo-Si-O-C with an increase of resistance from 0.05 to 560 Ω cm, at pyrolysis temperatures from 20 to 680°C, and a resistance lower than 10^{-3} Ω.cm above 1000 °C. The effect of carbon addition on the electrical properties of dense

SiOC ceramics was investigated by Kim et al. [133]. The electrical resistivities of 3.7 x 10^{-3}, 2.2 x 10^{-1} and 4.5 x 10^{-2} Ω cm were reported for an amount of carbon of 4, 8 and 16 (wt%), respectively. Lu et al. [134] prepared a carbon-enriched SiOC by pyrolysis of polyhydromethylsiloxane (PHMS) and divinylbenzene (DVB) and investigated the relationship between thermal stability and electrical conductivity, reporting an electrical conductivity from 2.58 S cm^{-1} at room temperature to 4.28 S cm^{-1} at 400 ºC.

In terms of metal-loaded polymer-derived ceramic materials, Scheffler et al. [135] investigated the influence of nickel on the structural evolution of the carbon phase. A decrease in electrical resistivity from 3 × 10^3 to 0.5 Ω cm was found when the filler-free samples and filler-loaded (1 wt% elemental Ni in the preceramic polymer matrix) pyrolyzed at 1000 °C were compared, respectively. Moreover, the formation of multiwall carbon nanotubes was observed within the pores (Figure 18b) [135].

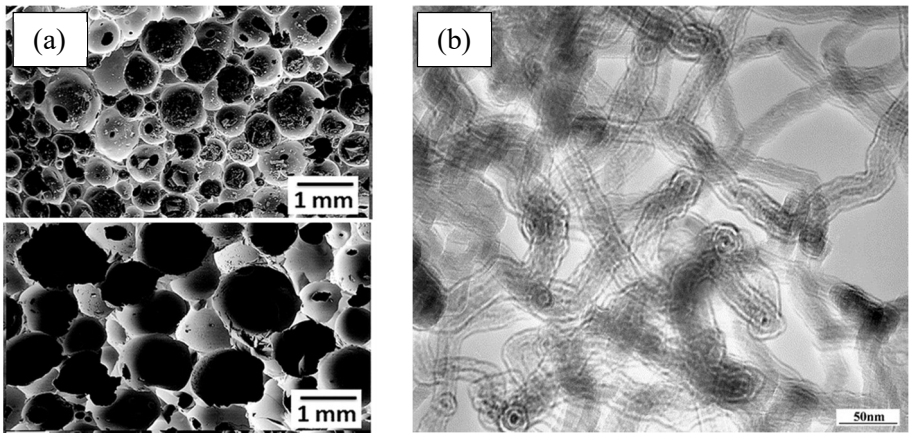

Figure 18. SEM images of pyrolyzed poly(methyl phenyl silsesquioxane) monoliths with 5wt% ratios of fillers (GO and MWCNT) (a), TEM image of multiwall CNTs in a pore, pyrolysis at 1000 °C (b). Adapted from [22] and [135].

Lu et al. [136] synthesized (SiOC)-TiC_xO_y composites based on PHMS and TiO_2 nanoparticles applying pyrolysis temperature between 1200 to 1400 °C under argon flow demonstrating electrical conductivities in the range of 0.0178 to 1.78 S cm^{-1} measured at room temperature (Figure 19). The increase in the conductivity with increasing pyrolysis temperatures was related to the increasing TiC formation and free carbon content [136].

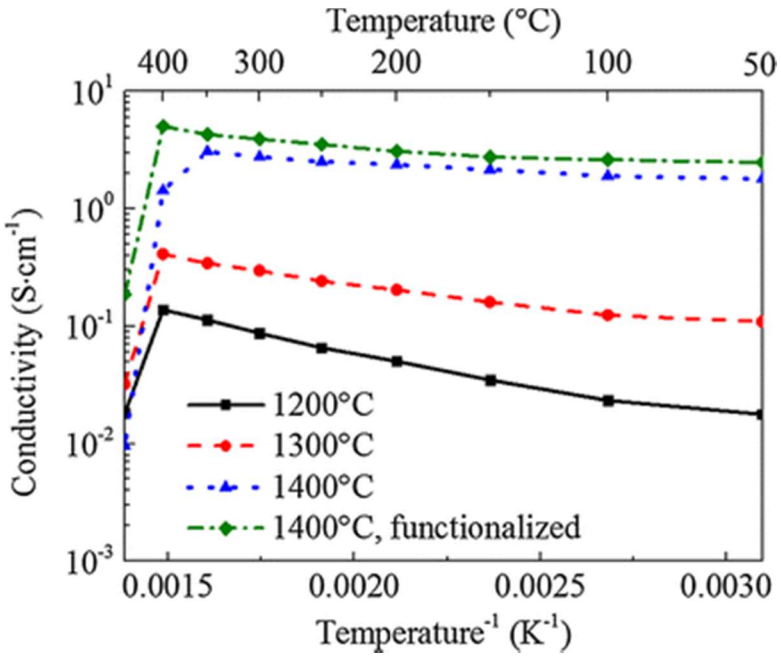

Figure 19. Conductivity change with the pyrolysis temperatures for the SiOC–TiC_xO_y composite at different pyrolysis temperatures. Adapted from [136].

2.2.3 SiOC-derived Ceramics Materials in Electrochemical Applications and as Catalysts

One alternative to improve performance and long-term applicability of electrodes in electrochemical applications is the use of porous ceramics electrodes. Porous electrodes are used to increase the surface area for charge transfer, thereby reducing the electrode overpotential, as well as to increase the charge storage capacity of capacitive electrochemical systems [137, 138]. Additionally, an optimized porous structure, to accommodate bacteria cells and maintain the access of nutrients through the pores in MFCs, is desirable [5, 12].

Due to outstanding features (described in 2.2.2), such as high chemical durability, semiconductor behavior, adjusted porosity, and surface characteristics, SiOC-derived ceramics are a promising class of new materials to address and improve the properties required for electrode materials and provide a porous structure [18, 20].

The tailorable properties in SiOC systems have already attracted interests for electrochemical applications, as electrode materials in lithium-ion batteries [21, 26, 139-141] and supercapacitors [21, 139, 142] and micro electro mechanical systems (MEMS) [143]. Furthermore, SiOC has been investigated as a metal-containing PDC catalyst in the CO oxidation reaction [144] and as an electrocatalyst under acidic conditions (0.1 M H_2SO_4) [24], in isopropyl alcohol conversion [145], CO_2 methanation and Fischer–Tropsch reaction [146].

Regarding lithium-ion batteries, Pradeep et al. [26] presented porous carbon-rich SiOC ceramic aerogels synthesized from a polyhydridomethyl siloxane (PHMS) cross-linked with divinylbenzene (DVB). The resulting pre-ceramic aerogels were then subjected to pyrolysis at 1000 ºC under argon atmosphere developing the desired SiOC aerogel (Figure 20).

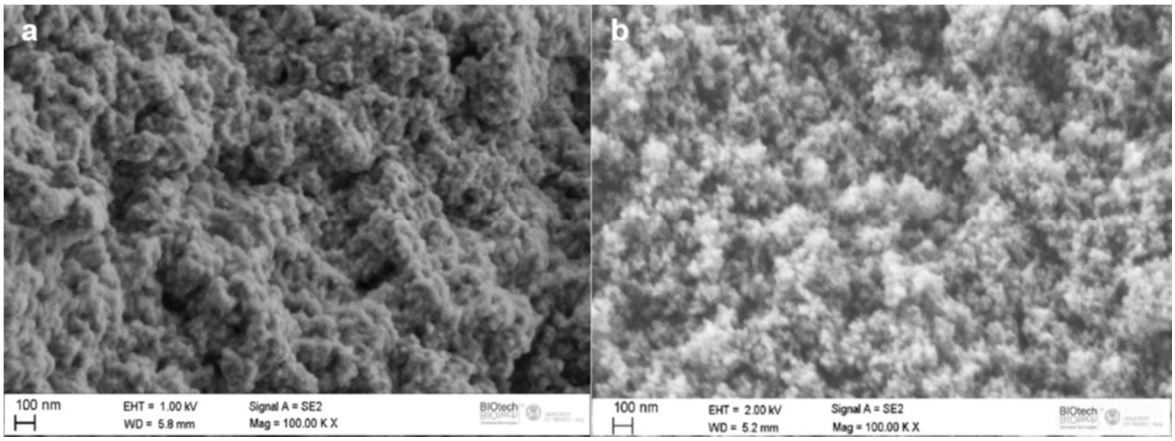

Figure 20. SEM images of SiOC aerogel material a) before pyrolysis and b) pyrolyzed at 1000 ºC. Adapted from [26].

The electrochemical performance demonstrated reversible lithium storage capacity as high as 650 mA h g^{-1} recovered at a faster rate of charge (360 mA g^{-1}). In addition, the specific capacity of more than 200 mA h g^{-1} was registered at a rate of 10 charge/10 discharge (3600mA g^{-1}), where most of the conventional electrodes, fails to give any capacities. The resulting performance was related to the porous nature of the carbon-rich ceramics which allows fast ionic transport and helps to accommodate the structural changes providing a stable performance during repeated lithiation/delithiation [26].

R. Bhandavat and G. Singh [140] demonstrated the synthesis and electrochemical performance of SiOC−CNT composites as a stable lithium intercalation material for secondary battery applications. The composite was prepared through controlled thermal decomposition of 1,3,5,7-tetramethyl 1,3,5,7-tetravinyl cyclotetrasiloxane (TTCS) precursor on carbon nanotubes surfaces that resulted in the formation of shell/core type ceramic SiOC−CNT architecture. The polymer-to-ceramics transformation occurred at 1000 ºC under argon atmosphere. The electrochemical performance revealed a charge capacity of 686 mA h g^{-1} even after 40 cycles, highlighting the improved chemical and mechanical stability of the composite [140].

As an application in lithium-ion batteries extended to supercapacitors, Kolathodi et al. [21] synthesized SiOC–graphene composite papers, relating a ceramic/reduced GO sandwich paper by intercalating liquid tetravinyl cyclotetrasiloxane (TTCS) between individual GO sheets during a layer-by-layer (LBL) vacuum filtration assembly process (Figure 21). The intercalated TTCS oligomers were converted to SiOC ceramic and simultaneously, GO was reduced to reduced graphene oxide (rGO) assembly process, through pyrolysis at 800 ºC under argon (Ar) atmosphere [21].

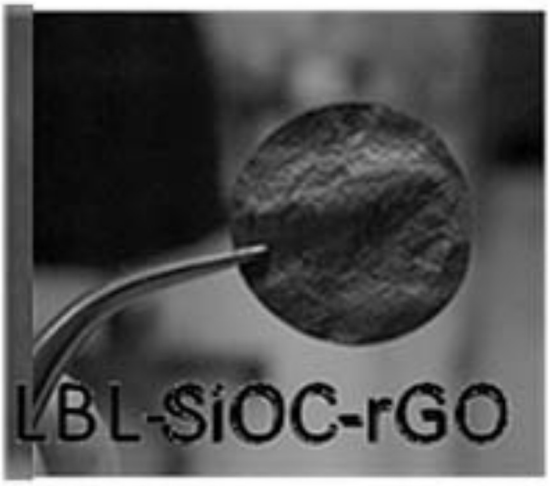

Figure 21. LBL-SiOC–rGO composite paper. Adapted from [21] .

Furthermore, the performance of the as-synthesized LBL-SiOC–rGO was compared with pyrolyzed polyvinyl alcohol on GO (PVA–rGO) paper electrode demonstrating that SiOC thin layers trapped between the graphene layers are critical to achieving high Li-charge capacity. As a result, a high reversible capacity of 750 mA h g^{-1} was achieved when used as an electrode for lithium-ion battery [21].

Moni et al. [142] also presented ceramic monoliths composed of polysiloxane microspheres sheathed by carbon allotropes (Graphene or MWCNT) and metal nanoparticles (Co and Ni) with hierarchical micro-/meso-/macroporous structures (Figure 22). The ceramic monoliths were prepared through the emulsion template route using poly (methyl phenyl silsesquioxane) (H44), 3-aminopropyl triethoxysilane (APTES), tetraethyl orthosilicate (TEOS) as the precursors. Pyrolysis at 600 ºC under nitrogen atmosphere was applied for the polymer to ceramic conversion. The materials were studied as electrode material for supercapacitors and additionally in CO_2 capture as pure physical adsorption process. A specific capacitance of 93 F/g at 2 mV s^{-1} in 0.5 M KOH electrolyte solution with a capacity retention of 88% after 50 cycles was achieved as an electrode material. Further, as a solid adsorbent, a

maximum CO_2 adsorption capacity of 2 mmol g^{-1} at 100 kPa equilibrium pressure and 303 K was shown [142].

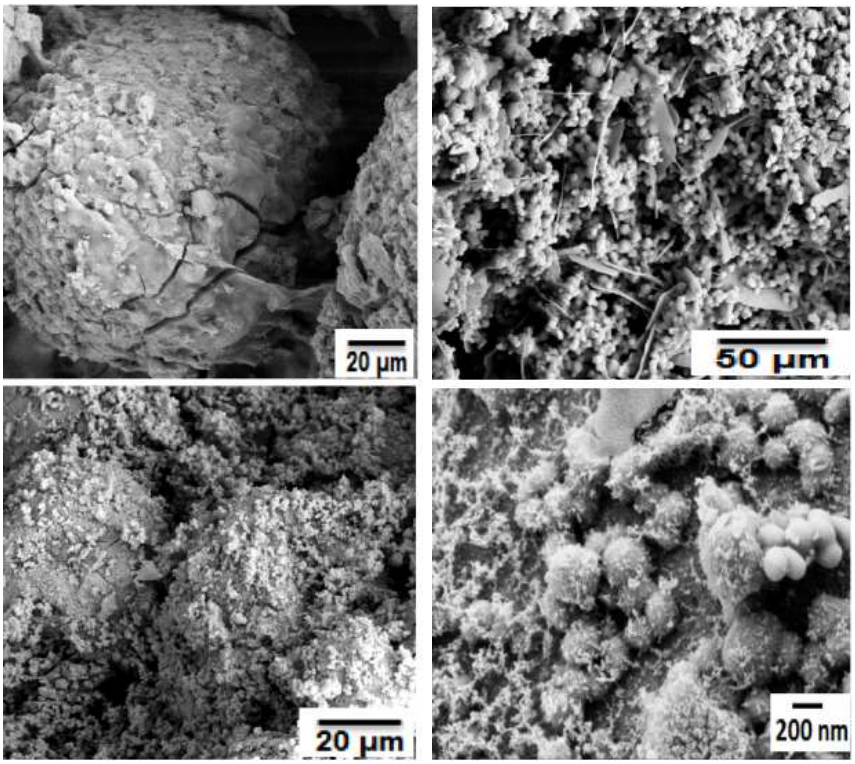

Figure 22. SEM images of pyrolyzed hybrid ceramic monoliths with different precursor ratios, containing GO (top row) and CNT (bottom row). Adapted from [142].

Moreover, the SiOC ceramics can be employed for micro-electro-mechanical systems (MEMS) as reported by Harshe et al. [143]. In this work, bulk Si–Al–O–C ceramics were produced by pyrolysis of poly(methylsilsesquioxane) which was cross-linked with a catalyst, or modified by the sol-gel-technique with an Al-containing alkoxide compound. Thermal treatment with temperature regime ranging from 1100 to 1700 °C was applied. The presence of Al in the SiOC matrix forms SiC and mullite and prevented micro cracking at elevated temperatures due to transient viscous sintering. Crack-free bulk and SiOC ceramic gears were obtained after pyrolysis of the green compact in argon atmosphere up to 1100 °C and suggested to fulfil the requirements for potential application in the field of MEMS [143].

Concerning SiOC-based catalysts, Adam et al. [144] synthesized Pt-containing hybrid ceramics by the pyrolytic conversion (500 ºC) of a methyl phenyl polysiloxane and latinic acid or a modified mixture containing in addition 3-aminopropyltriethoxysilane (APTES) as a complexing agent in an atmosphere of nitrogen (Figure 23). When tested in CO oxidation as a model reaction, it could be shown that the addition of APTES as a complexing agent is crucial to enhance the accessibility of the Pt particles (diameter: 1-10 nm) and the catalytic activity. CO conversions of 95% and 98%, could be achieved with high conversion rates beyond 75% [144].

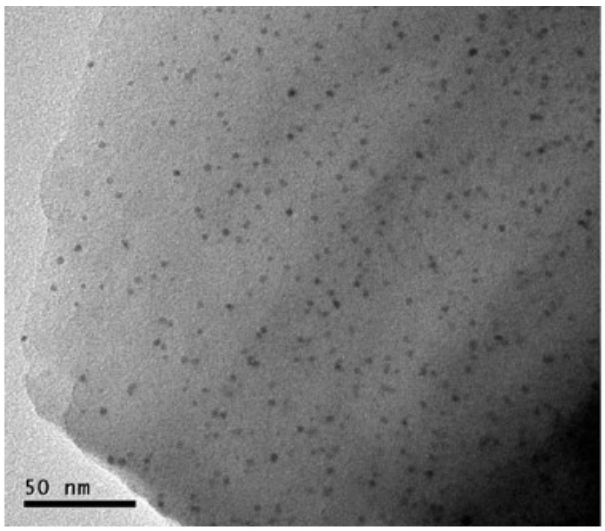

Figure 23. TEM image of Pt-containing hybrid ceramic pyrolyzed at 500 °C, with APTES: Pt ratio, HA8Pt1. Adapted from [144].

Besides, Pt nanoparticles in pyrolyzed siloxane matrices with additional carbon fillers were developed in [24] and tested for their use as electrocatalysts. As preceramic precursors, methylphenylpolysiloxane (H44) and a methylpolysiloxane (MK), as well as 3-aminopropyltriethoxysilane (APTES), were used and pyrolysis at 500 or 600 ºC was applied under nitrogen atmosphere. The electrochemical behavior of the siloxane-based electrocatalysts in contact with 0.1 M H_2SO_4 was studied by cyclic voltammetry and electrocatalytic activities were studied by CO adlayer oxidation. High electrochemically active surface areas with up to 50 m^2 g^{-1} Pt were obtained, which are comparable to carbon-based electrocatalysts.

Pt metallic particles were also dispersed in poly(vinylsiloxane) networks obtained by cross-linking of linear vinylsiloxane (D_2Vand V_3) polymers with hydrosiloxanes in the work of Wójcik-Bania et al. [145]. Pyrolysis of poly(vinylsiloxane) networks, performed at 1000 °C in argon atmosphere led to metallic Pt particles dispersed in SiCO ceramics (Figure 24). Catalytic

properties of the systems were investigated using isopropyl alcohol conversion as test reaction, exhibiting stable catalytic performance up to high temperatures (380 ºC) [145].

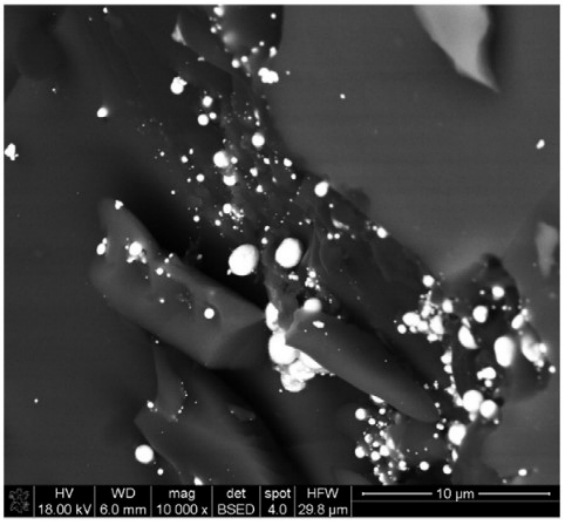

Figure 24. SEM image of $V_3(D_4^H)$Pt_P sample. Adapted from [145].

Lastly, with regard to Co and Ni as studied catalysts for Fischer–Tropsch synthesis and CO_2 methanation, Schubert et al. [146] used the synthesis route of Adam et al. [144] for the preparation of Ni- and Co-based ceramers. Pyrolysis temperatures between 400 and 600 °C were used to obtain catalysts with different surface hydrophilicities. A connection between the variation of the pyrolysis temperature on the material properties and the overall effect on the catalytic activity was investigated. The catalysts with the lowest tendency towards water adsorption showed the highest activity for CO_2 methanation, whereas the catalysts with smaller Co-particles showed a higher selectivity to hydrocarbons C_{5+} during Fischer–Tropsch synthesis also influenced in means of hydrophobicity.

Chapter III. Experimental Section

The following chapter presents the materials and preparation steps used in the manufacturing of SiOC-based electrode and electrocatalyst materials. A brief overview of the main measurement and characterization methods used in this thesis along with their related basic principles is also covered. The BES performance evaluation regarding setups designs, operating conditions, and electrochemical characterization methods are likewise included.

Parts of the following materials preparation description and characterization methods have been published in the Journal of Materials Science, 54 (2019) 6471–6487 (DOI: 10.1007/s10853-018-03309-3) [147], in Catalysis Science & Technology, 9 (2019) 854-866 (DOI: 10.1039/C8CY02207K) [148] and in Biochemical Engineering Journal 148 (2019) 29-36 (DOI: 10.1016/j.bej.2019.04.004) [149]. This chapter is also supplemented with added unpublished results.

Preparation and Characterization of SiOC Ceramics

3.1 Preparation of SiOC Ceramic Electrode Materials

3.1.1 Manufacturing of SiOC Electrode Materials

3.1.1.1 Materials

As starting materials, commercial poly(methyl silsesquioxane) (Silres® MK, Wacker Chemie AG) and poly(methyl phenyl silsesquioxane) (Silres® H44, Wacker Chemie AG) were used as preceramic polymer precursors. Based on previous works of the research group, graphite (KS75, IMERYL Graphite and Carbon) was added as first carbon-based conductive filler for increment of electrical conductivity and additives such as molybdenum disilicide ($MoSi_2$, abcr GmbH) and azodicarbonamide (Az, azodicarboxamide Sigma-Aldrich Co) were added in means of controlling shrinkage and inducing formation of pores, respectively [131]. In order to further increase electrical conductivity, an additional carbon-based conductive filler, carbon black (CB, Vulcan XC72 Cabot), was used. For the metal-containing electrode materials, metallic grids of copper (Cu, The Mesh Company Ltd) and stainless steel (SS, The Mesh Company Ltd) were integrated during the preparation of the samples. For the same purpose, cobalt and nickel chloride ($CoCl_2$ and $NiCl_2$, Alfa Aesar) were used as a metal source for the formation of metal particles within the PDC matrix. Xylene (Sigma-Aldrich Co) was

used as solvent in the preparation and imidazole (Imi, Alfa Aesar) was used as catalyst for the cross-linking process. For comparison purposes, a commercial carbon felt (CGT Carbon GmbH) was used in some of the characterizations.

3.1.1.2 Tape-cast SiOC Electrode Materials

The electrode preparation route is depicted in Figure 25 and starts by dissolving the precursors MK and H44 (in a weight ratio 1:1) in xylene followed by the dispersion of the additives ($MoSi_2$ and Az) and conductive fillers under stirring at room temperature. For the materials with metal particles, the metal salts ($CoCl_2$ and $NiCl_2$) were additionally used in the dispersion step. The amount of solvent was kept as low as possible to achieve a sufficient viscosity for further casting. The cross-linking process starts by adding the catalyst (Imi) into the mixture, which was kept under constant stirring for 20 min. After that, the materials were tape casted using a doctor blade with the gap set from 1.5 to 5 mm. For the materials with metallic grids (Cu and SS), the grids were integrated subsequently after to the tape-casting step. The tapes were then dried at room temperature for 24 h and cut in square shapes with dimensions varying between 10 x 10 x 1.5 mm and 50 x 50 x 5 mm.

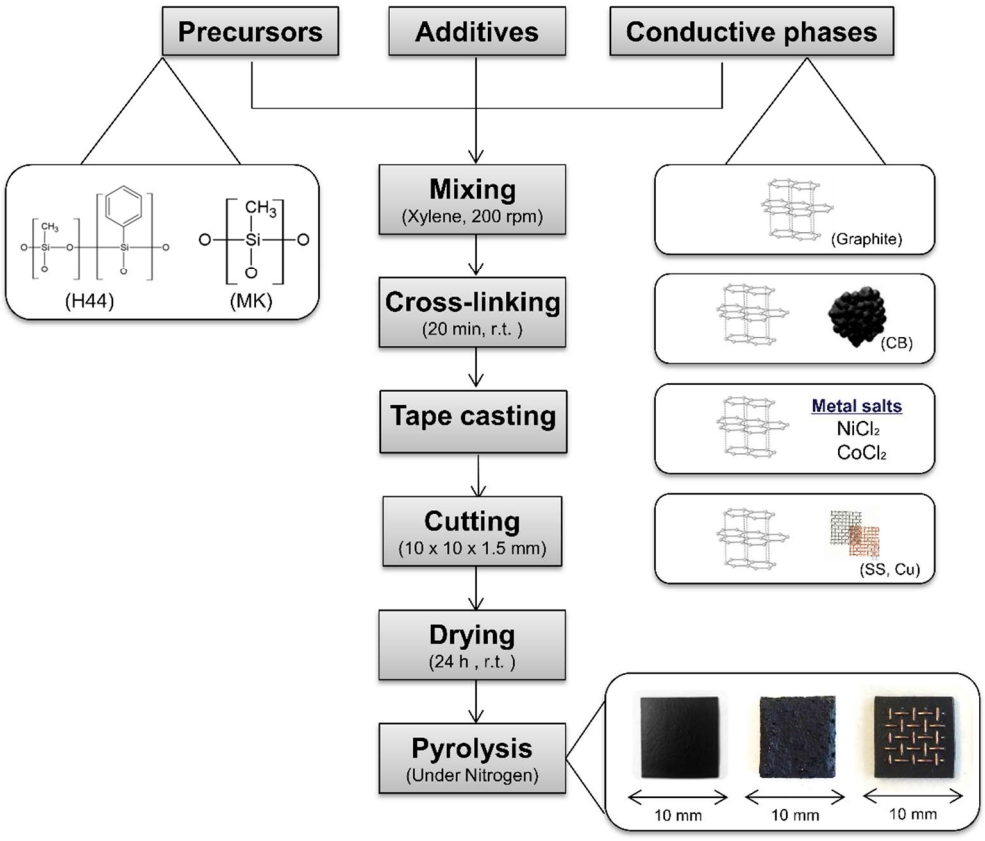

Figure 25. Processing route, materials and structure of the synthesized SiOC electrode materials. Adapted from [147].

The cross-linked tapes were pyrolyzed in order to convert the precursors into a hybrid ceramic or a ceramic material. The pyrolysis was performed under an N_2 atmosphere at temperatures between 500 and 1500 ºC, with the heating up of 120 K h^{-1} up to 100 ºC below the final temperature and 30 K h^{-1} to the final temperature, with a dwelling time of 4 h. A cooling rate of 120 K h^{-1} was applied to end the pyrolysis step. For the metal-containing/integrated electrode materials, only 1000 ºC was applied. The heat treatment was done in a pyrolysis oven (GERO Hochtemperaturöfen GmbH, Germany, max. temperature 1100 °C, gas: nitrogen).

The obtained SiOC-based materials were denoted with regard to the wt% of the polysiloxane (PS) and conductive solid components, in the total mass of the composition and the respective pyrolysis temperature used. For the materials with metallic grids, Cu and SS are indicated as the material variety but not considered as wt%. The denotation, composition of the materials and pyrolysis temperature applied are described in Table 1.

Table 1 Materials composition (wt%) of the cross-linked materials prepared and pyrolysis temperatures applied.

Materials denotation (wt%)	H44	MK	$MoSi_2$	KS75	CB	Az	Imi	Metal salt	Pyrolysis temperature (°C)
60PS-600	30.5	30.5	12.0	-	-	26.0	1.0	-	600
60PS-1000	30.5	30.5	12.0	-	-	26.0	1.0	-	1000
42PS-31G-500	21.1	21.1	8.4	30.8	-	17.7	0.9	-	500
42PS-31G-600	21.1	21.1	8.4	30.8	-	17.7	0.9	-	600
42PS-31G-1000	21.1	21.1	8.4	30.8	-	17.7	0.9	-	1000
42PS-31G-1200	21.1	21.1	8.4	30.8	-	17.7	0.9	-	1200
42PS-31G-1500	21.1	21.1	8.4	30.8	-	17.7	0.9	-	1500
40PS-30G-5CB-1000	20.0	20.0	8.0	29.2	5.0	17.0	0.8	-	1000
40PS-30G-5Co-1000	20.0	20.0	8.0	29.2	-	17.0	0.8	5.0	1000
42PS-30G-1Ni-1000	20.9	20.9	8.4	30.5	-	17.5	0.8	1.0	1000
40PS-30G-5Ni-1000	20.0	20.0	8.0	29.2	-	17.0	0.8	5.0	1000
42PS-31G-SS-1000	21.1	21.1	8.4	30.8	-	17.7	0.9	-	1000
42PS-31G-Cu-1000	21.1	21.1	8.4	30.8	-	17.7	0.9	-	1000

In Chapter V, the selected SiOC electrode materials synthesized are applied as anode materials and its MFC and BES performance is demonstrated and discussed. However, the denotation of the materials differs as follows.

Topic 5.1

- 42PS-31G-1000: PDC-Graphite
- 40PS-30G-5CB-1000: PDC-G-Carbon Black

- 42PS-30G-1Ni-1000: PDG-G-Nickel

Topic 5.3

- 42PS-31G-500: E1
- 42PS-31G-1000: E2
- 40PS-30G-5CB-1000: E3

Besides, a distinct commercial carbon felt (Panex 35, Zoltek Corporation) was used as anode control during the MFC performance tests (Topic 5.1).

3.1.1.3 Sandwiched SiOC-carbon-based Composite Electrode Materials

The composite structures were composed by one layer of carbon felt (CGT Carbon GmbH) and two layers of polymer-derived ceramics in a sandwich structure, as shown in Figure 26a. The materials and preparation of the PDC layers are identical to the SiOC electrode materials described in topic 3.1.1.1 and 3.1.1.2., with additional processing. After the tape-casting step, pieces of carbon felt (10 x 10, 25 x 25 and 40 x 5mm) were placed onto the PDC layer (as it is shown in Figure 26b) and the structure was dried for 12 hours. Then, another layer of PDC was prepared in equivalent means and combined with the previously prepared structure. The final sandwich structure is presented in Figure 26c.

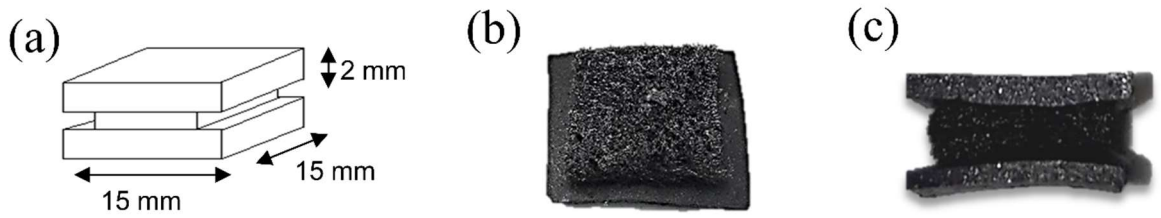

Figure 26. Sandwich structure proposal (a), first layer of PDC combined with carbon felt (b), composite sandwich structure (c).

For the SiOC-carbon-based composite structures, pyrolysis was performed under an N_2 and argon atmosphere at temperatures of 1000, 1300 and 1500 ºC, with the heating up of 120 K h^{-1} up to 100 ºC below the final temperature and 30 K h^{-1} to the final temperature, with a dwelling time of 4 h. A cooling rate of 120 K h^{-1} was applied to end the pyrolysis step. The heat treatment was done in a pyrolysis oven (GERO Hochtemperaturöfen GmbH, Germany, max.

temperature 1650 °C, gas: nitrogen and argon). The materials were denoted with regard to single materials (PDC and carbon felt) and composite structure as shown in Table 2. The composition of the PDC layers follows the one described in Table 1.

Table 2. Materials denotation.

PDC Nomenclature	Carbon felt Nomenclature	Composite Nomenclature
42PS-31G-1000-N_2	CF-1000-N_2	Sandwich-1000-N_2
42PS-31G-1300-N_2	CF-1300-N_2	Sandwich -1300-N_2
42PS-31G-1500-N_2	CF-1500-N_2	Sandwich -1500-N_2
42PS-31G-1000-Ar	CF-1000-Ar	Sandwich -1000-Ar
42PS-31G-1300-Ar	CF-1300-Ar	Sandwich -1300-Ar
42PS-31G-1500-Ar	CF-1500-Ar	Sandwich -1500-Ar

3.1.2 Manufacturing of SiOC Pristine and Nitrogen-doped Electrocatalyst Materials

The PDC-based materials were synthesized according to an adapted procedure used for conductive porous materials as well as hybrid materials containing metallic nanoparticles reported previously [131, 150]. Briefly, silicon resin poly(methyl silsesquioxane) (MK, Wacker Chemie AG) and poly(methyl phenyl silsesquioxane) (H44, Wacker Chemie AG) were used as preceramic precursors combined with graphite (KS75, IMERYL Graphite & Carbon) as a carbon source for a sufficient electrical conductivity. Additional fillers, such as molybdenum disilicide ($MoSi_2$, abcr GmbH) and azodicarboxamide (Azo, Sigma-Aldrich Co), were used for shrinkage control related to the polymer-to-ceramic conversion and pore formation, respectively. For the Co/Ni-containing materials, metal salts such as nickel chloride ($NiCl_2$, Alfa Aesar) and cobalt chloride ($CoCl_2$, Alfa Aesar) were used as precursors for metal nanoparticle formation. The powder materials were dissolved/dispersed under constant stirring at room temperature using xylene (Sigma-Aldrich) as a solvent.

A cross-linking step was initiated by the addition of the catalyst imidazole (Imi, Alfa Aesar) and stirring for 20 min. The mixture of reagents was then dried and the resultant materials were subjected to pyrolysis under a N_2 atmosphere. The heating up was performed with 120 K h^{-1} up to 900 °C and with 30 K h^{-1} up to 1000 °C, with a dwelling time of 4 h. With a cooling rate of 120 K h^{-1}, the pyrolysis ended. The heat treatment was done in a pyrolysis oven (GERO Hochtemperaturöfen GmbH, Germany, max. temperature 1100 °C, gas: nitrogen). The pyrolyzed materials were ground and sieved to particle sizes <300 µm. The resulting powders were further ball-milled (PM 400, Retsch) at 350 rpm min^{-1} for 4 h to produce a fine

powder. The obtained samples are denoted as PDC, PDC-Ni, and PDC-Co and their compositions are presented in Table 3.

Table 3 Composition of PDC-based electrocatalysts (wt%).

Catalyst material composition (wt%)	H44	MK	Graphite	$MoSi_2$	Azo	Imi	$Ni/CoCl_2$
PDC	21	21	31	8	18	1	-
PDC-Ni	20	20	29	8	17	1	5
PDC-Co	20	20	29	8	17	1	5

PDC, PDC-Ni and PDC-Co were doped with nitrogen using a previously optimized procedure [151]. As the nitrogen source, dicyandiamide (DCDA) was added in a weight ratio of 1 : 20 (DCDA : PDC, PDC-Ni or PDC-Co). Polyvinylpyrrolidone was used as a surface-active agent, in an amount of 1/10 of the corresponding PDC material. The mixture of reagents was transferred to a beaker containing 2-propanol (99.8%, Honeywell Riedel-de Haën) and sonicated for 2 h to achieve a homogeneous mixture. Subsequently, 2-propanol was evaporated in a vacuum at 60 °C. The material was collected in a quartz boat and pyrolyzed in a flowing N_2 atmosphere at 800 °C for 2 h using a heating rate of 10 °C min^{-1}. After pyrolysis, the furnace was slowly cooled to room temperature and the products were collected and weighed. The N-doped catalyst materials are marked with additional –N in the designation: PDC–N, PDC-Ni–N, PDC-Co–N.

3.2 Characterization Techniques for Structural and Surface Properties

3.2.1 Scanning Electron Microscopy

Scanning electron microscopy (SEM) is a common technique for material analysis. SEM is used to observe and study the surface topography, grain sizes, chemical composition of many materials with a higher resolution [152]. In MFCs research, this technique has been used in the interest of analyzing morphology, pore structure, biofilm layers, and internal bacterial colonization [8].

A SEM instrument is usually composed by an electron optical column, a scanning unit, a specimen chamber, detectors system and image view system. In an SEM, the images are produced by scanning the sample with a high-energy beam of electrons enabling information about a defined area on the sample. At the top of the microscopy, a beam of electrons is produced by an electron gun. The beam is accelerated over the sample surface under vacuum conditions and through electromagnetic fields and lenses. When the beam hits the sample, electrons interact with the sample producing secondary electrons, backscattered electrons, and characteristic X-rays with distinct information. Different detectors register the produced signals and convert them into a magnified image on a computer screen [152, 153].

A field emission SEM SUPRA 40-Carl (Zeiss, Germany) equipped with an energy-dispersive X-ray (EDX) XFlash 6|30 detector (Bruker) was used to analyze the surface morphology, porous structure and chemical composition of the resulting SiOC electrode and electrocatalysts materials.

For SEM observations regarding electrocatalysts materials described in topic 3.1.2, a high-resolution scanning electron microscope (HRSEM) (Helios NanoLab 600 (FEI Company) equipped with an EDX spectrometer analyzer (INCA Energy 350 (Oxford Instruments) was additionally used.

Concerning biofilm formation on the as-synthesized anode materials discussed in Chapter V, an optical microscope (Light Microscope Keyence Digital, Germany) and SEM (CAM SCAM, Cambridge Scanning) were applied for the examination after MFC operation. For this, the biofilm on the surfaces was first fixed in 2.5% glutaraldehyde for 60 min and subsequently dehydrated for 10 min in alcoholic solutions of 20, 40, 60, 80 and 100% ethanol. The materials were dried and gold coated (K550, Emitech SA, Versailles, France) for 20 s under an argon atmosphere for SEM observations.

3.2.2 Nitrogen Adsorption

Gas adsorption is of major importance for the characterization of a wide range of porous materials [154]. Of all the many gases and vapors, which could be used as adsorptive, nitrogen has remained universally important [155]. Nitrogen adsorption and desorption is a measurement technique, where gaseous nitrogen is adsorbed on a solid surface at very low temperatures (77 K) as recommended by the International Union of Pure and Applied Chemistry (IUPAC) [154]. This technique is employed for analysis of specific surface areas and for evaluation of the mesopore size distribution [154].

Volumetric methods are generally employed for measuring nitrogen isotherms at temperatures ~ 77 K, but gravimetric methods are also applied for studies at ambient temperature [154]. Considering the volumetric technique, a degassed sample is exposed to nitrogen gas at the temperature of liquid nitrogen (~77 K) at a series of precisely controlled pressures. During the measurement, the isotherm is usually constructed point-by-point by the admission and withdrawal of known amounts of gas, with adequate time allowed for equilibration at each point. Gas in pores with different diameters will condense at different pressures, obtaining the distribution of pores sizes of the sample [154, 156].

The adsorption isotherms are usually displayed in graphical form plotted with the adsorbed volume of nitrogen (273.15 K and 101.3 kPa) versus the equilibrium relative pressure (p/p^0), where p^0 is the vapor pressure of nitrogen at 77 K (p^0 = 101.3 kPa) [157]. Depending on the type of material, the obtained adsorption isotherms can be classified according to IUPAC into 6 different classes as shown in Figure 27.

The identification of the type of isotherm and hysteresis loop is considered to be a useful starting point in the characterization of a porous material [158]. Type I isotherms are typical for microporous solids having relatively small external surfaces as activated carbons, zeolites and certain porous oxides. For type II isotherm, normally is associated with a non-porous or macroporous adsorbent represented by unrestricted monolayer-multilayer adsorption. The type III isotherm is convex to the p/p^0 axis over its entire range. Isotherms of this type are not common, and in such cases, the adsorbate-adsorbate interactions play an important role. Type IV isotherm characterizes mesoporous adsorbents. As characteristic features of its type, a hysteresis loop associated with capillary condensation takes place in mesopores and the limiting uptake over a range of high p/p^0. The initial part of the isotherm is attributed to monolayer-multilayer adsorption since it follows the same path as the corresponding part of a Type II isotherm adsorbents [157].

Type V represents a weaker adsorbent-adsorbate interaction related to type III, is uncommon, but is obtained with certain porous adsorbents. The type VI isotherm represents stepwise multilayer adsorption on a uniform non-porous surface. Amongst the best examples of type VI isotherms are those obtained with argon or krypton on graphitized carbon blacks at liquid nitrogen temperature [157].

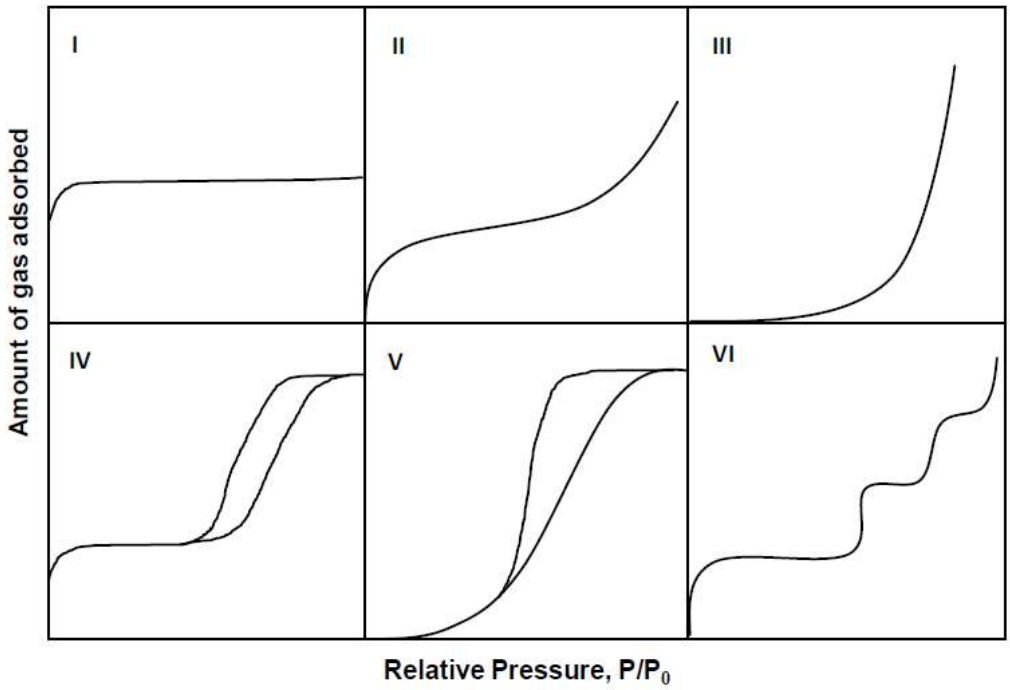

Figure 27. IUPAC classification of physisorption isotherms [157].

Hysteresis loops, which appear in the multilayer range of physisorption isotherms, are generally associated with the capillary condensation of mesopores [157]. The hysteresis loops exhibit a wide variety of shapes (as shown in Figure 28) and may differ depending on the pore geometry.

The type H1 loop exhibits parallel and nearly vertical branches and is often reported for materials that consisted of agglomerates or compacts of spherical particles arranged uniformly. Recently, it has also been related to materials with cylindrical pore geometry and a high degree of pore size uniformity. Type H2 has a triangular shape and a steep desorption branch, which is often considered to be a result of the presence of pores with narrow mouths (ink-bottle pores). In case of type H3 loops, which do not level off at relative pressures close to the saturation vapor pressure, materials comprised of aggregates (loose assemblages) of plate-like particles forming slit-like pores were reported. Type H4 loops feature parallel and almost horizontal branches and their occurrence has been attributed to adsorption-desorption in narrow slit-like

pores. Furthermore, H4 hysteresis loops may merely arise from the presence of large mesopores embedded in a matrix with pores of much smaller size [159].

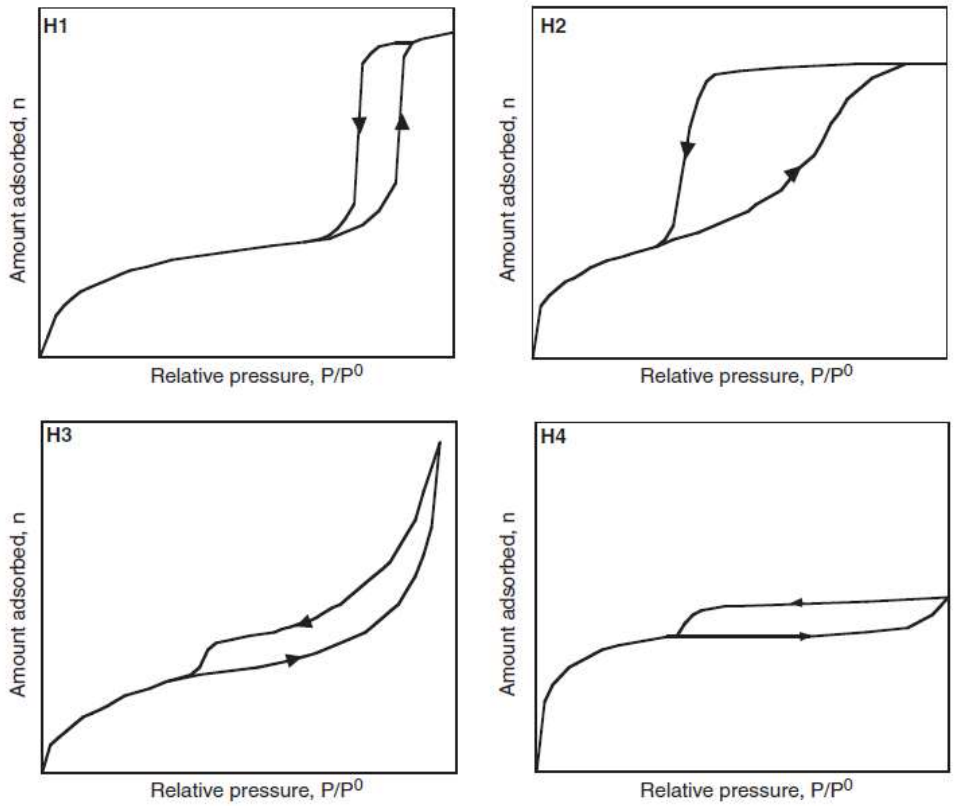

Figure 28. The four types of hysteresis loops identified by IUPAC. Adapted from [158].

The specific surface area of a solid is defined as the total surface area of a material per unit of mass ($m^2\ g^{-1}$) or volume ($m^2\ m^{-3}$ or m^{-1}). For determination of specific surface areas, Brunauer-Emmett-Teller (BET) method is usually applied to derive the surface area from physisorption isotherm data. For this purpose, the following BET equation is used [154, 160].

$$\frac{p}{n^a(p^0-p)} = \frac{1}{n_m^a C} + \frac{(C-1)}{n_m^a C}.\frac{p}{p^0}$$

where n^a is the amount adsorbed at the relative pressure p/p^0, n_m^a is the monolayer capacity and C is a constant, which is dependent on the isotherm shape.

In a BET plot, a linear relation is obtained when $p/n^a(p^0-p)$ is plotted against p/p^0. By this linear regression is possible to obtain the constant C, as well as the specific volume of one mono-layer n_m^a. Though, the range of linearity of the BET plot is always restricted to a limited part of the isotherm -usually not above $p/p^0 \sim 0.3$, and deviates from the linear line in the low or high-pressure range [154, 160].

With the obtained monolayer capacity and molecular cross-sectional area ($a_m = 0.162$ nm^2 at 77 K), BET surface area $A_s(BET)$ can be calculated according to the following equations [154, 157].

$$A_s(BET) = n_m^a \,.\, L \,.\, a_m$$
$$a_s(BET) = A_s(BET)/m$$

where $A_s(BET)$ and $a_s(BET)$ are the total and specific surface areas, respectively, of the adsorbent (of mass m) and L is the Avogadro constant [154, 157].

Pore sizes are characterized according to IUPAC notation as follows:

- micropores (< 2 nm)
- mesopores (from 2 to 50 nm)
- macropores (> 50 nm)

Micro–mesoporosities and BET specific surface area (SSA) were determined in this thesis by nitrogen adsorption isotherms measured at 77 K using Belsorp-mini (Bel Japan, Inc.) device. The materials were pre-treated at 120 ºC for 3 h under vacuum.

3.2.3 Mercury Intrusion Porosimetry

The mercury (Hg) intrusion porosimetry is a widely used technique for analyzing the pore size distribution of a porous material over a wide range of pore sizes [161]. Pores between about 500 µm and 3.5 nm in the meso-macroporous range can be investigated [162]. Both the inter-particle pores (between the individual particles) and the intra-particle pores (within the particle itself) can be characterized using this technique [163]. It provides reliable information about pore size/volume distribution, the total pore volume or porosity, bulk, and apparent density and specific surface for most porous materials, regardless of their nature and shape [162, 163].

The pore size distribution is determined through the introduction of a non-wetting liquid, with a contact angle higher than 90°, into the capillaries under pressure. On ceramics materials, Hg has a mean contact angle of 140° and is considered a non-wetting liquid [164].

Meso–macroporosities were determined in this thesis with analysis carried out in the equipment Mercury Porosimeter Pascal 140 and 440, POROTEC GmbH in the pressure range of 0.1 to 400 kPa with an accuracy of <0.25 %. Pieces of 0.5 to 1 cm were used for the characterization without any pre-treatment. The instrument employs a pressurized chamber to

force mercury to intrude into the voids in a porous substrate. As pressure is applied, mercury fills the larger pores first. As pressure increases, the filling proceeds to smaller and smaller pores. The relationship between the pressure and capillary diameter is described by the following Washburn equation:

$$p = \frac{-4\gamma \cos\theta}{d}$$

Where p = pressure, γ = surface tension of the liquid (0.48 N m^{-1}), θ = contact angle of the liquid (141.3°), and d = pore diameter. The pore size distribution is determined from the volume intruded at each pressure increment. Likewise, total porosity is determined from the total volume intruded [165, 166].

3.2.4 X-ray Diffraction

X-ray diffraction (XRD) patterns are the fingerprint of periodic atomic arrangements in each material. This technique is used in order to analyze the crystallinity of a material, providing information about the structures, phases, preferred crystal orientations, and other structural parameters, such as average grain size, crystallinity, strain, and crystal defects [167].

X-ray diffraction is produced by constructive interference of a monochromatic beam of X-rays scattered at specific angles from each set of lattice planes in a sample. The peak intensities are determined by the distribution of atoms within the lattice [167].

The phase structure of the SiOC electrocatalysts materials was identified on an Iso-Debyeflex SEIFERT diffractometer that uses a Bragg–Brentano geometry and Cu-Kα radiation with a wavelength of 0.154 nm at 40 kV and 40 mA. Data were recorded from 5 to 80° in 0.025° steps. For the N-doped materials, an additional XRD system (Bruker D8 Advance diffractometer) with Ni filtered Cu-Kα radiation, 0.6 mm (0.3°) wide parallel beam, two 2.5° Soller slits, and a LynxEye line detector was used. Data were recorded from 21 to 80° in 0.0149° steps.

3.2.5 X-ray Photoelectron Spectroscopy

X-ray photoelectron spectroscopy (XPS), also known as ESCA (electron spectroscopy for chemical analysis) is a surface analysis technique applied in the examination of surface chemistry of a material. Elemental composition, empirical formula, chemical state and electronic state of the elements within a material can be determined with XPS [168].

In XPS, the sample is illuminated with x-rays - monochromatic or unfiltered Al Kα or Mg Kα - causing photoelectrons to be emitted from the surface. The kinetic energy of these emitted electrons is typical for the element from which the photoelectron originated. The chemical state of an atom alters the binding energy of a photoelectron resulting in a change in the measured kinetic energy. From the binding energy and intensity of a photoelectron peak, the elemental identity, chemical state, and quantity of a detected element can be determined [169, 170].

In this thesis, XPS technique was applied in the characterization of the SiOC electrocatalysts materials described in topic 3.1.2. For the XPS measurements, 11 × 11 mm^2 plates of GC were coated with SiOC materials. The spectra were acquired with a SES-100 spectrometer at 200 eV pass energy. Survey spectra were acquired with 500 meV steps and core-level spectra with 100 meV steps. The excitation source used was a non-monochromatic Thermo XR3E2 dual anode X-ray gun. Mg (Kα at 1253.6 eV) at 300 W was used for PDC-Ni and Al (Kα at 1486.6 eV) at 400 W was used for all the other samples. The vacuum in the analysis chamber was below 10^{-9} torr at all times.

The N1s XPS peak was deconvoluted into 5 components [171, 172]: (i) pyridinic-N, (ii) amines/M–Nx, (iii) pyrrolic-N, (iv) graphitic-N, and (v) pyridine-N-oxides. The peak binding energy positions were found to be: (i) 398.0 eV, (ii) 399.2 eV, (iii) 400.7 eV, (iv) 402.7 eV and (v) 404.5 eV. The FWHM was constrained from 1 eV to 2 eV for peaks (i)–(iv) and 1 eV to 2.5 eV for peak (v). Peak positions were constrained: (i) 398.1–397.7 eV, (ii) 399.7–399.1 eV, (iii) 401.7–400.5 eV, (iv) 403–402.6 eV and (v) 403.8–405.8 eV. All peaks were assumed to be 70% Gaussian and 30% Lorentzian. A linear background was used for only PDC-Co; for all other peaks Shirley background was used. The software CasaXPS (2.3.18) was used for peak fitting.

3.2.6 Surface Characteristics Characterization

Different methods were used to characterize the surface characteristic of SiOC electrode materials within this thesis. Measurements of the maximal adsorption capacity for different vapors (n-heptane and water) conducted in simple storage experiments and water contact angle measurements were considered.

3.2.6.1 Vapor Adsorption

The hydrophilicity/hydrophobicity characteristics were analyzed by weighing 0.5 g of sample (particle size ≤ 300 µm) which was then dried for 24 h at 70 ºC. The dried specimens were stored into vessels, which were placed in closed Erlenmeyer flasks filled with water or n-heptane at room temperature and at equilibrium with its vapor phase. After 24 h, the materials in the adsorptive atmosphere were weighed again to determine the vapor uptake and maximal adsorption capacity [173]. With the values of BET-specific surface area acquired, the uptake was recalculated into adsorbed vapor mass per unit area (g m^{-2}).

3.2.6.2 Surface Contact Angle

Hydrophilicity and hydrophobicity are general terms introduced to describe relative affinity of solids to water spreading on their surfaces, while wettability can be related to unbalanced molecular interactions when materials are in contact [174]. Contact angle (θ) is, therefore, the measure of this unbalance of forces. In general, θ < 90° indicates that the solid surface is partially wetted by a liquid (for example water), associated with hydrophilic surfaces and water spreading. A completely wettable surface has a contact angle of 0. The contact angle θ > 90° indicates non-wetting, characterizing hydrophobic surfaces. The water drops tend to form „beads" on hydrophobic („water rejecting") solid surfaces [174]. Water spreading and formed drops are presented in Figure 29.

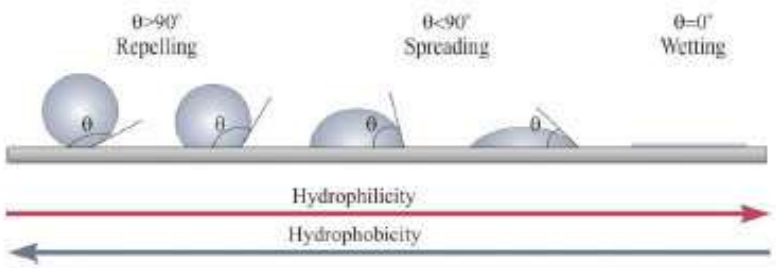

Figure 29. Water drop behavior and contact angle values at solid with distinct surface characteristics. Adapted from [174].

The main technique used to assess the contact angle of surfaces is the sessile drop. Contact angles can be determined through the setup shown in Figure 30, in which an image of a liquid droplet that sits on a solid (sessile drop) is captured. The image is subsequently analyzed in software using the tangents at the intersections of the drop outline and the baseline [175]. In addition, Young's equation is usually considered and describes wettability as the balance of interfacial interactions for a solid/fluid system as following:

$$\cos\theta = \frac{\gamma_{sf} - \gamma_{sf1}}{\gamma_{f1,2}}$$

where θ is the equilibrium (or Young's) contact angle, γ are interfacial (or surface) tensions, s refers to the solid phase, and f_1 and f_2 refer to the two fluid phases [176].

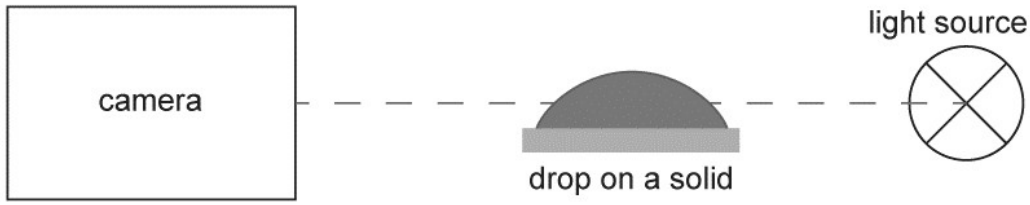

Figure 30. Schematic representation of the setup to measure the contact angle. Adapted from [175].

The surface wettability of the SiOC electrode materials was assessed by water contact angle measurements, carried out on a pendant drop tensiometer (OCA25, DataPhysics, Germany) at about 22 ºC. The surfaces were polished, cleaned and dried prior to the analysis.

3.2.7 Chemical Stability Test

The chemical stability was analyzed by the change of the dry weight of the materials placed in 30 ml of phosphate buffer solution (PBS, pH 7), at room temperature over a period of 4 weeks. The materials were previously placed in an oven at 70 ºC for 6 h, cooled and weighed. Every seventh day, the materials were then rinsed with distilled water, dried, weighed and immersed again in PBS solution.

3.2.8 Biofilm Assays

As model microorganism, a gram-negative bacterium *Escherichia coli* (CECT 434) and a gram-positive bacterium *Bacillus cereus* (a strain isolated from a biocide solution [177]) were used for the adhesion and biofilm experiments. The bacteria were chosen due to its biofilm forming ability [178, 179] likewise its applicability in BES [180-182]. The bacterial suspensions were grown overnight in Mueller–Hinton broth (MHB, Merck, VWR) at 30 °C and 120 rpm. The cells were centrifuged (3999 g, 15 min, 25 °C) and washed with saline solution. The concentration of the bacterial solution was adjusted to a final concentration of 1 x 10^8 colony forming units (CFU)/ml. Electrode materials with dimensions of 1 x 1 x 0.1 cm were first sterilized in UV exposure for 20 min (each surface). Then, were immersed in 1 ml of bacterial solution and incubated for 2 h (adhesion) and 24 h (biofilm formation) at 30 °C under constant stirring (120 rpm) in a 48-well microtiter plate (Corning), according to Malheiro et al. [183]. To evaluate the cell viability, after the defined periods the materials were vortexed in 5 ml (adhesion) and 9 ml (biofilm formation) of saline solution (0.85% NaCl) for 1 min to provide the detachment of the cells. After dilution, the detached cells were assessed in terms of CFU in Mueller–Hinton agar after 24 h of incubation at 30 °C. The counts were normalized to the exposed area of the material tested and expressed in CFU per cm^{-2}. Three independent experiments with replicates were performed for each bacterium/material.

Bacterial adhesion and biofilm formation data were analyzed using GraphPad Prism 7. The mean and standard deviation within samples were calculated in all cases. Because low sample numbers contributed to uneven variation, the nonparametric Kruskal–Wallis test was used. Statistical calculations were based on confidence level equal or higher than 95% ($P>0.05$ was considered statistically significant).

The experiments were carried out by a cooperation partner at the University of Porto, under supervision of Dr. Manuel Simões.

3.3 Electrochemical Characterization

3.3.1 Electrochemical Impedance Spectroscopy

Electrochemical Impedance Spectroscopy (EIS) is a relatively new and potent method of characterizing many of the electrical properties of materials and their interfaces with electronically conducting electrodes. It may be considered to investigate the dynamics of bound or mobile charge in the bulk or interfacial regions of any kind of solid or liquid material: ionic, semiconducting, mixed electronic-ionic and even dielectrics. EIS has been applied to study different corrosion processes, batteries and fuel cells for many years [184, 185]. In MFCs, EIS is applied to investigated electrochemical reactions that occur on electrodes as well as surface and materials properties [184].

In this thesis, EIS technique was applied in order to characterize electrical conductivity of the resulting SiOC electrode materials. Measurements of electrical conductivity were carried out according to Moni *et al.* [22]. The flat materials were placed between stainless steel blocking electrodes connected with an impedance analyzer (Impedance Measurement Unit IM6ex Zahner Electric), as shown in Figure 31. The measurements were performed in the frequency range of 1 MHz to 10 mHz with an AC amplitude of 10 mV at 25 °C.

Figure 31. Setup for EIS measurements.

The following electrochemical methods were only used to characterize the produced SiOC electrocatalysts materials (topic 3.1.2) within this thesis. The studies were carried by our cooperation partners at the University of Tartu under supervision of Dr. Kaido Tammeveski and with strong support of Marek Mooste.

3.3.2 Cyclic Voltammetry

Cyclic voltammetry (CV) is a powerful and popular electrochemical technique commonly employed to investigate the reduction and oxidation processes of molecular species. Additionally widely applied to study electron transfer-initiated chemical reactions in catalysis [186].

A schematic representation of an electrochemical cell used for a cyclic voltammetry experiment is presented in Figure 32. This setup is composed of three electrodes categorized as a working electrode (WE), the counter electrode (CE), and a reference electrode placed in an electrolyte solution. While the current flow between the working and counter electrodes, the reference electrode is used to accurately measure the applied potential relative to a stable reference reaction [186].

The working electrode carries out the electrochemical event of interest with a controlled applied potential as a function of the reference electrode potential. A reference is used as a reference point against which the potential of other electrodes can be measured in an electrochemical cell. The applied potential is thus typically reported as versus a specific reference. Commonly used reference electrodes in aqueous media include the saturated calomel electrode (SCE), standard hydrogen electrode (SHE), and the AgCl/Ag electrode [186].

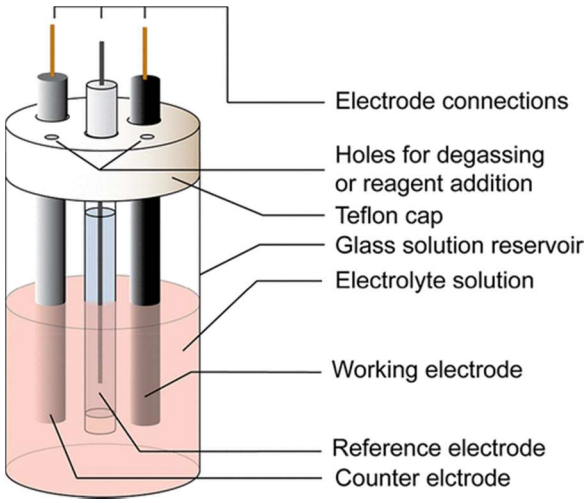

Figure 32. Schematic representation of an electrochemical cell for CV experiments. Adapted from [186].

To complete the electrical circuit, the counter electrode is used. Current is recorded as electrons flow between the WE and CE [186]. A platinum wire is typically used as a counter electrode, though carbon-based counter electrodes are also available [187].

Once the cell has been assembled and sparged of oxygen, the electrodes are connected to the potentiostat, and the experimental parameters are selected. Fundamental parameters are the potential window that will be scanned (defined by the initial, switching, and final potentials), the scan rate, and the number of segments/scans. The scan rate of the experiment controls how fast the applied potential is scanned [186]. The electrolyte, solvent, and nature of the working electrode all influence the potential window that can be used for a CV experiment [187].

The data generated from CV experiments are called cyclic voltammograms (Figure 33). In these diagrams, the x-axis represents a parameter that is imposed on the system, here the applied potential (E), while the y-axis is the response, here the resulting current (i) passed.

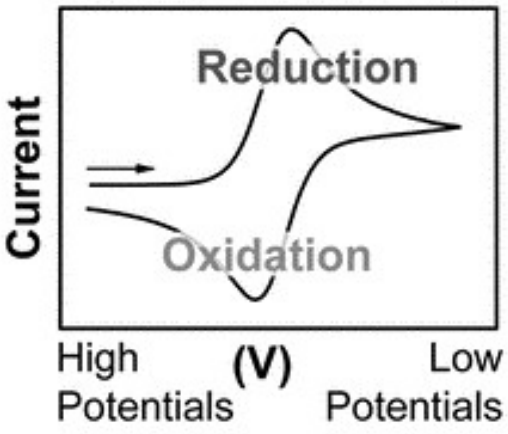

Figure 33. Cyclic voltammogram profile according to US convention. Adapted from [186].

This equilibrium between the studied species is normally described by the following Nernst equation.

$$E = E^0 + \frac{RT}{nF} ln \frac{(Ox)}{(Red)} = E^0 + 2.3026 \frac{RT}{nF} log_{10} \frac{(Ox)}{(Red)}$$

The Nernst equation relates the potential of an electrochemical cell (E) to the standard potential of a species (E^0) and the relative activities of the oxidized (Ox) and reduced (Red) analyte in the system at equilibrium. In the equation, F is Faraday's constant, R is the universal gas constant, n is the number of electrons, and T is the temperature [186].

3.3.3 Linear Sweep Voltammetry

In linear sweep voltammetry (LSV) a fixed potential range is employed and the voltage is scanned from a lower limit to an upper limit as shown in the diagrams below (Figure 34). On the contrary of CV, which the voltage is swept between two values at a fixed rate, with a reversed scan to the initial voltage [188].

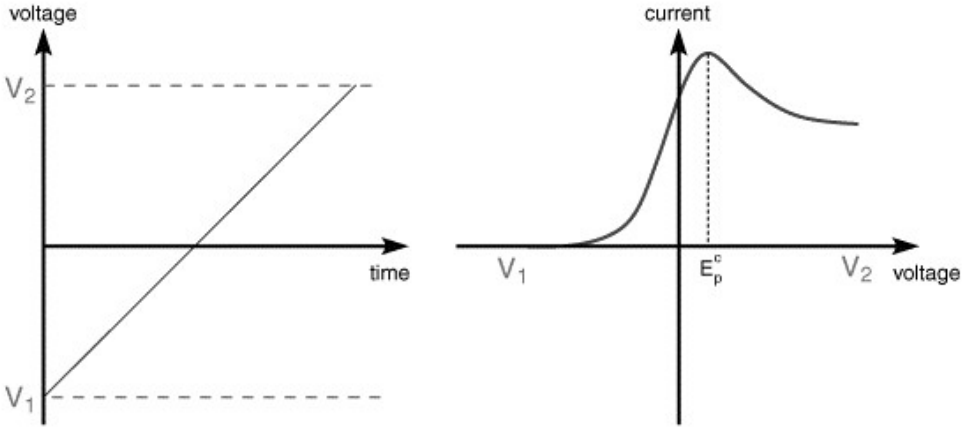

Figure 34. LSV voltammogram representation. Adapted from [188].

In LSV measurements the current response is plotted as a function of voltage. The scan begins from the left-hand side of the current/voltage plot where no current flows. As the voltage is swept further to the right (to more reductive values) a current begins to flow and eventually reaches a peak before dropping. To explain this behavior we need to consider the influence of voltage on the equilibrium established at the electrode surface [188].

The characteristics of the linear sweep voltammogram depend on a number of factors which includes [188]:

- The rate of the electron transfer reaction(s)
- The chemical reactivity of the electroactive species
- The voltage scan rate

To obtain the LSV voltammograms, the same electrochemical cell configuration described in the CV experiments is used. Furthermore, the Nernst equation is also considered to study the equilibrium electrochemistry.

3.3.4 Rotating Disk Electrode

Rotating disk electrode (RDE) technique has been widely used for research on electrode reaction mechanism and kinetics, particularly those of oxygen reduction reaction (ORR). RDE is a convective electrode system for which the diffusion-convection equation can be derived and used for measuring the steady-state electrochemical reaction [189].

For electrochemical measurements using RDE technique a conductive disk embedded in an inert insulating material, like any working electrode, is required. Generally these electrodes are made by glassy carbon (GC) or noble metals. For evaluating the activity of the ORR catalysts, the GC electrode is normally employed as the current collector on which the catalyst layer is coated. The typically employed electrochemical cell is the conventional three-electrode cell (Figure 35). In addition, a motor to control the electrode rotating rate is included in the set-up. Equally in CV and LSV experiments, the cell is composed by the catalyst-coated disk-working electrode, the counter electrode, and the reference electrode such as a normal hydrogen electrode (NHE), reversible hydrogen electrode (RHE), or saturated calomel electrode (SCE). For measuring catalyst surface-cyclic voltammograms, pure N_2 or Ar gas will be used to de-aerate the electrolyte solution and for ORR measurement, either pure oxygen or air is purged [189].

Figure 35. Schematic of the three-electrode cell for RDE measurement from Pine Instrument. Adapted from [189].

To study the ORR kinetics catalyzed by the catalyst, the RDE current-potential curves are normally recorded at different electrode rotating rates when the electrolyte solution is saturated with O_2 or air. The current-potential curves obtained in RDE experiments are shown in Figure 36a.

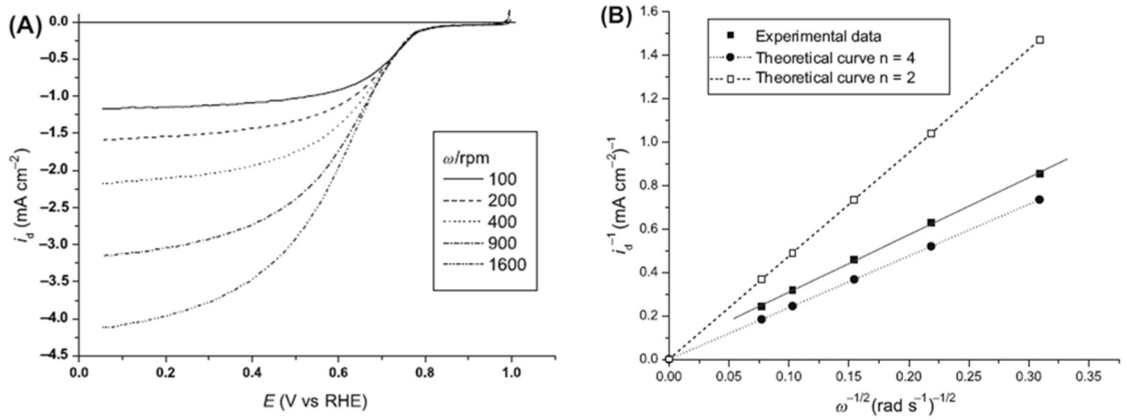

Figure 36. (A) Current-potential curves for ORR on a Fe-N/C-coated GC electrode (0.5 M H_2SO_4, scan rate: 5 mV s^{-1}). (B) Koutecky-Levich plots on a Fe-N/C coated GC electrode. The current data were taken at 0.1 V (vs RHE) from (A). Adapted from [190].

By means of the Koutecky-Levich theory and analyses of the current-potential curves, the ORR exchange current density, the electron-transfer coefficient, and the overall electron transfer number can be determined. The plots of the reciprocal of RDE current density (i_d) vs the reciprocal of square root of rotation rate ($\omega^{-1/2}$) can be drawn at different electrode potentials (as shown in Figure 36b).

For the electrochemical experiments within this thesis, a glassy carbon (GC) electrode with a geometric area (A) of 0.196 cm^2 was used as an underlying substrate. The electrode was prepared by mounting the GC disc (GC-20SS, Tokai Carbon, Japan) into a Teflon® holder and then the GC electrode surface was polished before use with 1.0 and 0.3 μm alumina slurries (Buehler). The surface of the GC electrode was cleaned by sonication in Milli-Q water (Millipore, Inc.) and 2-propanol for 5 min in each solvent. For coating the GC electrode with the catalyst materials, 2 mg of the corresponding nanomaterial were dispersed in 1 mL of 2-propanol, followed by sonication for 1 h. After the sonication, 10 × 2 μL of the catalyst ink was pipetted onto the polished GC surface. After solvent evaporation in air, 0.2 mg cm^{-2} catalyst loading was obtained. Prior to electrochemical measurements, the electrodes were carefully

rinsed with Milli-Q water. For clarification, the catalyst-coated GC electrodes are designated as the underlying material (GC) followed by the catalyst material.

For comparison purposes, the Pt/C catalyst coated GC electrode was also used. The commercial 20 wt% Pt catalyst supported on Vulcan carbon XC-72 was acquired from E-TEK, Inc. (Framingham, MA, USA) and dispersed in 2-propanol. The GC electrode was coated with Pt/C ink in a similar manner to the other studied nanomaterials, resulting in a Pt loading of 40 μg cm^{-2}.

The electrochemical measurements were carried out in an Ar-saturated (99.999%, AGA) or O_2-saturated (99.999%, AGA) aqueous solution using the cyclic voltammetry (CV), linear sweep voltammetry (LSV) and rotating disc electrode (RDE) methods described above. Three different electrolyte solutions were used:

i) 0.1 M KOH (pH = 13) (p.a. quality, Merck),
ii) 0.1 M phosphate buffer solution (PBS) (pH = 7) containing 0.1 M $NaClO_4$ (pro analysi, Merck) and
iii) 0.5 M H_2SO_4 (pH = 0.3) (96% Suprapur®, Merck).

The buffer solution was prepared from Na_2HPO_4 (puriss p.a., Fluka) and KH_2PO_4 (pro analysi, Merck). The electrochemical experiments were performed with an Autolab potentiostat/galvanostat PGSTAT128N (Metrohm Autolab, The Netherlands) controlled with Nova 2.1 software. A three-compartment electrochemical cell with Pt wire as a counter electrode and a saturated calomel electrode (SCE) as a reference electrode was used. For the RDE measurements, an EDI101 rotator and a CTV101 speed control unit (Radiometer) were employed. The following electrode rotation rates (ω) were used for RDE experiments: 360, 610, 960, 1900, 3100 and 4600 rpm. All the presented RDE polarization curves are recorded in the cathodic direction. All the potentials mentioned in this study are referenced to the reversible hydrogen electrode (RHE). For the conversion of potential values from vs. SCE to *vs.* RHE, the following equation $E_{RHE} = E_{SCE} + 0.241\ V + 0.059 \times pH$ was used.

In the following section the characterization of the produced SiOC electrodes as parts of bioelectrochemical systems (BES) is described. BES setups used to characterize the performance of the produced SiOC electrode and electrocatalysts materials within this thesis are introduced. The experiments were carried out in cooperation with the Indian Institute of Technology (IIT), Kharagpur – India (topic 3.4.1 and 3.4.2) under supervision of Dr. Makarand M. Ghangrekar with strong support of Gourav Dhar Bhowmick and Helmholtz-Zentrum für Umweltforschung (UFZ), Leipzig – Germany (topic 3.4.3) under supervision of PD Dr. Falk Harnisch and with strong support of Dr. Rodrigo Quejigo and started during the research stays.

3.4 Bioelectrochemical Characterization

3.4.1 BES Configuration

3.4.1.1 Aqueous Cathode Clayware-based MFC

Batch-operated aqueous cathode laboratory MFCs were used in order to enable performance comparison of as-synthesized tape-cast SiOC-based electrodes (as anode material, topic 3.1.1.1) with the commercially available carbon felt (Panex 35, Zoltek Corporation), used as received. The anodic chamber of MFCs was made up of a low cost baked clayware ceramic cylinder [191] with a total working volume of 85 ml. The cylinder served as an anodic chamber and the wall material of the cylinder (0.5 cm thick) worked as a separator. The PDC-based materials developed, with a total projected surface area of 36 cm^2 and a thickness of 0.25 cm, were used as anode and placed in the inner part of the clayware cylinder. As a current collector for ORR, carbon felt (Panex 35, Zoltek Corporation) was wrapped on the outer surface of the cylinder and aerated tap water was used as catholyte. The electrical connection between the electrodes was made with concealed copper wire, while the potential drop was measured through an external resistance of 100 Ω. A schematic representation of the MFC is shown in Figure 37 and the four experimental setups are illustrated in the Appendix (Fig. A.1.1).

A volume of 15 ml of anaerobic sludge collected from the bottom of a septic tank (volatile suspended solids of 19.9 g l^{-1} and total suspended solids of 30.2 g l^{-1}) and heat-treated (100 °C for 15 min) was added as inoculum in the anodic chamber of all the MFCs. Synthetic wastewater containing sucrose as the carbon source with a chemical oxygen demand (COD) of 3000 mg l^{-1} and pH adjusted to 7.4 was used as anolyte.

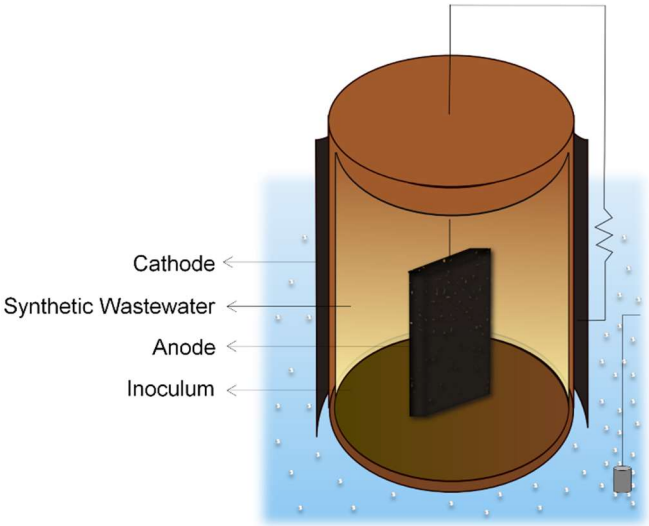

Figure 37. MFC setup representation and its components. Adapted from [149].

A sucrose medium containing sucrose (900 mg), $NaHCO_3$ (1500 mg); NH_4Cl (318 mg); $CaCl_2.2H_2O$ (250 mg); $MgSO_4.7H_2O$ (64 mg); K_2HPO_4 (27 mg); and KH_2PO_4 (9 mg) was used in preparing synthetic wastewater with around 3 g of COD l^{-1} [192]. In addition, trace metals were added as $FeSO_4.6H_2O$ (10.00 mg l^{-1}); $NiSO_4.6H_2O$ (0.50 mg l^{-1}), $MnCl_2.4H_2O$ (0.50 mg l^{-1}), $ZnSO_4.7H_2O$ (0.106 mg l^{-1}); H_3BO_3 (0.106 mg l^{-1}); $CoCl_2.6H_2O$ (50 µg l^{-1}), $(NH_4)_6Mo_7O_{24}.4H_2O$ (50 µg l^{-1}) and $CuSO_4.5H_2O$ (4.5 µg l^{-1}) [193]. All the MFCs were operated for 45 days under fed-batch condition at room temperature (28 – 32 °C) with the fresh feeding of the anolyte after every second day.

To evaluate the MFC performance of the produced SiOC electrocatalysts materials (topic 3.1.2) the same MFC configuration described above was used. However, only the electrocatalyst material PDC-Co-N was considered and discussed in Chapter VI. The study was conducted using carbon felt (Panex 35, Zoltek Corporation) with an ink (ink preparation Appendix A.4) of activated carbon (Vulcan AC XC 72, Cabot) as control, PDC-Co-N supported on AC and 10 wt% Pt supported on AC powder coated carbon felt. A catalyst loading rate of 2 mg cm^{-2} and cathode areas of 113 (control) and 133 cm^2 (Pt and PDC-Co-N) were applied.

3.4.1.2 Two-chambered MFC

Batch-operated two chambered laboratory MFCs were used in order to study the performance of the synthesized sandwiched SiOC-carbon-based composite electrodes (as anode material, topic 3.1.1.2). Each chamber had a working volume of 35 ml and the four experimental setups are shown in Figure 38.

The performance was compared to commercial graphite felt (CGT Carbon GmbH), single graphite felt and PDC material pyrolyzed at 1300 °C under argon. The projected surface

area of the materials varied from about 15 to 25 cm^2. As separator, pre-treated Nafion (Fuel Cell Store) membrane was used while carbon felt (Panex 35, Zoltek Corporation) was applied as cathode. The electrical connection between the electrodes was made with concealed copper wire, while the potential drop was measured through an external resistance of 100 Ω.

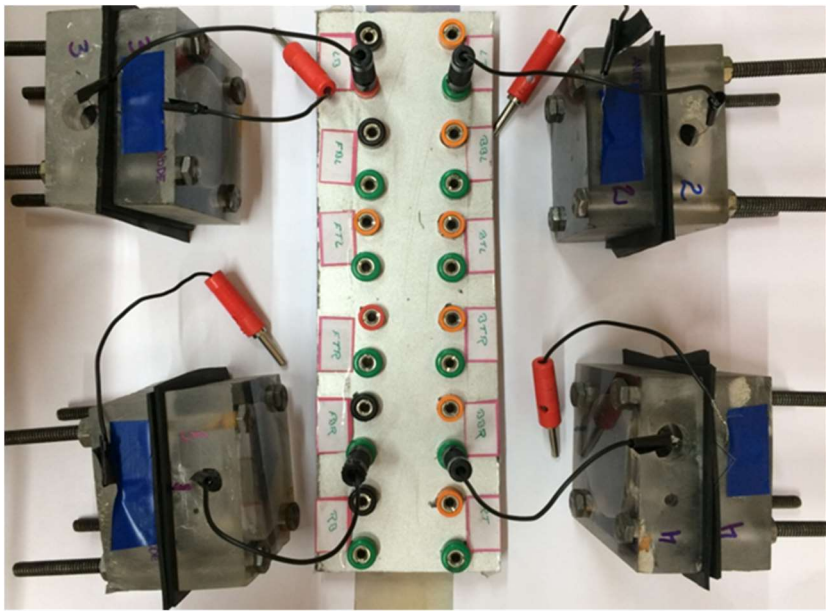

Figure 38. Two chambered laboratory MFCs setups.

Synthetic wastewater containing sucrose as the carbon source with a COD of 3000 mg l^{-1} and pH adjusted to 7.4 was used as anolyte with the same composition described in the MFC configuration of the topic 3.4.1.1, while aerated distilled water was used as catholyte. Furthermore, a volume of 5 ml of anaerobic sludge was added as inoculum in the anodic chambers. All the MFCs were operated for 45 days under the fed-batch condition at room temperature (28 – 32 °C) with the fresh feeding of the anolyte after every two days.

3.4.1.3 Three-electrode Setup

An additional study of the impact of SiOC-based porous anode materials (topic 3.1.1.1) properties on anodic electroactive microbial biofilm and current generation was carried out in a three-electrode setup described in [194] and similar to the one shown in Figure 39. However, in this experiment, a single-neck reactor was used. The SiOC-based materials were used as working electrodes, Ag/AgCl (SE11 Sensortechnik Meinsberg, Germany) as a reference electrode and graphite rod (CP-Handels-GmbH) as a counter electrode. For this study, Ag/AgCl (sat. KCl) electrode, being +0.197 V vs. standard hydrogen electrode (SHE) was used. The working electrodes were operated chronoamperometrically at +0.2 V under pontentiostatic control (MPG BioLogic Science Instruments, Claix, France).

Three varieties of SiOC-materials were studied, each in triplicate, resulting in nine individual reactors running in parallel. Artificial wastewater based in acetate was prepared according to [195] and as a microbial inoculum source, a secondary electroactive biofilm containing mostly *Geobacter* was used [194]. The temperature during the entire course of the study was maintained at 33 °C (Incubator Hood TH 15, Edmund Bühler GmbH, Germany).

The identification of the electrochemically active anodic biofilms was assessed by the increase in current flow, being expressed as current density normalized to the projected surface area of the anode (j_{GSA}, A m^{-2}). The projected surface area was calculated considering the measured height, width and depth of the produced 3D electrode materials with values varying from 20 to 25 cm^2. Further cyclic voltammetry (CV) analysis over the course of eight feeding cycles (~30 days) was performed. The developed biofilms were additionally investigated by SEM as described in topic 3.2.1.

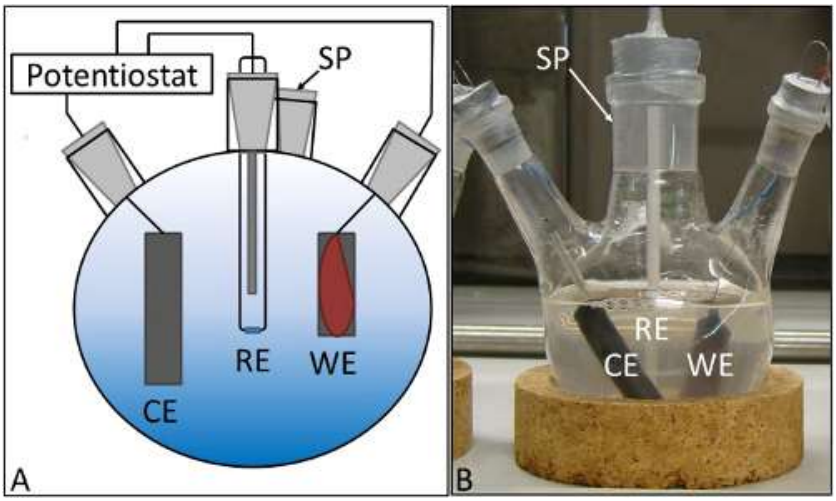

Figure 39. Three electrode setup. (A) Scheme, (B) photograph of reactor; CE = counter electrode, RE = reference electrode, WE = working electrode with electroactive microbial biofilm, SP = sampling port. Adapted from [194].

3.4.2 Electrochemical Measurements and Analysis

The potential difference and current generated by the MFCs were monitored using a digital multimeter with data acquisition unit (Agilent Technologies, Malaysia) and power was calculated according to the following equation:

$$P = I \times V$$

Where P is power (W), I is current (A), and V is acquired voltage (V). Anodic and cathodic potentials were measured using Ag/AgCl reference electrode (CH Instruments, Inc.,

RE-5B; +0.197 V vs. a standard hydrogen electrode, SHE). After the MFCs attained a stable potential, polarization was performed by monitoring the voltage output across various external resistances, ranging from 10 kΩ to 5 Ω, using a resistance box (GEC 05 R decade Resistance Box, Renown Systems, Kolkata, India). The voltage was recorded after every 30 min and the data was collected with the help of a data acquisition unit. Power density values were normalized to the exposed surface area of the anode materials, which gave an idea about the maximum power density it can yield. This study was also followed to obtain the relationship between the voltage and current, expressed as IV curves. The internal resistance of the MFC was calculated from the slope of the linear portion of the polarization plot (voltage $vs.$ current).

Normalized Energy Recovery (NER) was estimated according to Ge et al. [196] and expressed in two units; based on the volume of wastewater treated and amount of organic matter removal, in terms of COD, over the time (kWh m^{-3} and kWh kg COD^{-1}, respectively). The relation is shown in the following equations.

$$NERv\ \left[\frac{kWh}{m^3}\right] = \frac{P}{wastewater\ volume}$$

$$NERr\ \left[\frac{kWh}{kg\ COD}\right] = \frac{P}{\Delta\ COD\ x\ wastewater\ volume}$$

Total and soluble COD were analyzed for samples collected from anodic chamber of the MFC at a regular interval according to Standard Methods [197]. The coulombic efficiency (CE) was estimated by integrating the measured current relative to the theoretical current according to the following equation [42].

$$CE\ [\%] = \frac{M_s \int_0^t I\ dt}{F b_{es} V_{an} \Delta COD}$$

where, M_s is the molecular weight of substrate (g mol^{-1}), ΔCOD is the change in substrate concentration over a batch cycle (g L^{-1}), V_{an} is the anodic chamber liquid volume (L), F is Faraday's constant (96485 C mol^{-1}) and b_{es} is the generated electrons during each mol of substrate oxidation (mol of e^- per mol of $substrate^{-1}$).

Any evidence of leaching of metal ions from the electrodes to the electrolyte during the operation of MFC was investigated using SOLAAR S Series atomic absorption spectrometer (AAS, Thermo Fisher Scientific, USA) according to the method described in Standard Methods [197].

Chapter IV. Functional Properties of Tape-cast SiOC-based Porous Ceramic Electrode Materials

This chapter contains the results and discussion of characterized functional properties concerning the tape-cast SiOC-based electrode materials described in Chapter III (topic 3.1.1). Properties regarding structural and electrical characteristics as well as biocompatibility, in means of bacterial adhesion, are considered for bioengineering applications as BES. Parts of the following chapter have been published in the Journal of Materials Science, 54 (2019) 6471–6487 (DOI: 10.1007/s10853-018-03309-3) [147].

4.1 Macrostructure and Surface Characterization

SiOC-based electrodes materials were produced by tape-casting technique with dimensions varying from 10 x 10 x 1.5 mm and scaled-up till 50 x 50 x 5 mm. The green tapes were stable and easy to cut. The pyrolyzed tapes presented the so-called black glass look and appropriate handling stability. In this work, ca. 17 wt% azodicarboxiamide was used as a foaming agent to induce the formation of pores [131]. Additionally, the pore sizes could be adjusted by applying different pyrolysis temperatures. The foaming agent decomposes around 200 °C and leaves cavities behind in the matrix producing porous materials. With regard to compensating the shrinkage and weight loss of the tapes during the ceramic conversion of polymers, ca. 8 wt% $MoSi_2$ was used as filler based in the optimized amount of previous studies [131].

The resulting macrostructure was investigated by SEM, and the pyrolyzed electrode materials are shown in Figure 40. Figure 40a illustrates the graphite-containing material pyrolyzed at 500 °C, which presents smaller pores due to an incomplete polymer-to-ceramic conversion. This incomplete conversion results in hybrid materials with pronounced microporosity [118], which is why a similar structure is observed for the material pyrolyzed at 600 °C. Above 600 °C, amorphous ceramics are obtained, the microporosity collapses, and the macropore formation is pronounced providing chemical and mechanical stability [18, 198]. Figure 40b shows the graphite-containing material pyrolyzed at 1000 °C where bigger pores can be observed. Similar structure was found for the material pyrolyzed at 1200 °C. In general, the SEM analysis revealed pores sizes in the range of 0.5–40 μm for all pyrolyzed electrode materials. When the pyrolysis is carried out above 1400 °C and under N_2 atmosphere, different phases like SiC-Si_3N_4-Si_2N_2O can be built [199]. Figure 40c shows the graphite-containing

material pyrolyzed at 1500 °C for which a structural change and the formation of Si_3N_4 whiskers (left side) were found.

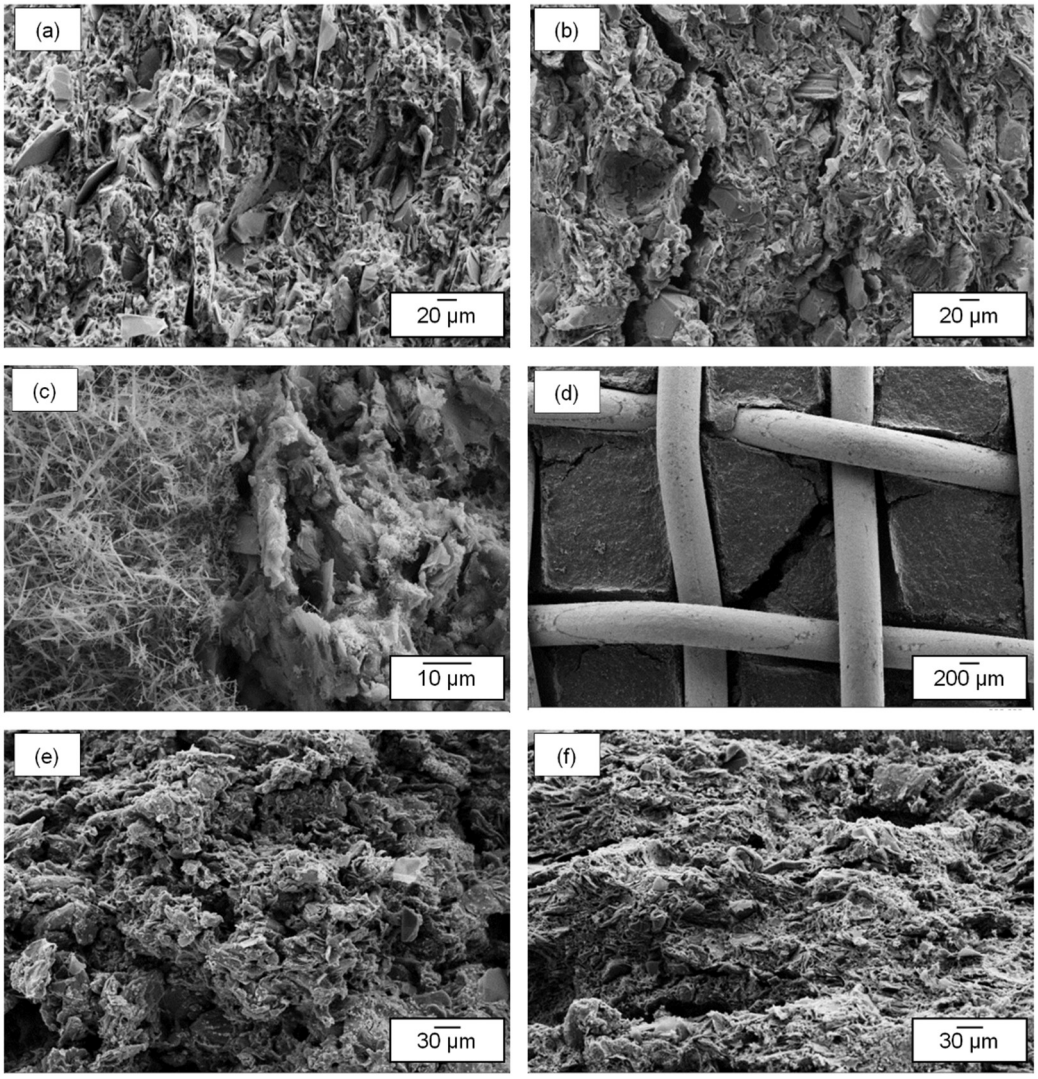

Figure 40. SEM images of the pyrolyzed electrode materials at 500, 1000, 1500 °C (a, b, c), materials integrated with SS grids (d) and Co/Ni-containing materials (e, f). Adapted from [147].

In metallic grid-containing materials, SS and Cu grids were integrated on the surface of the PDC matrix after the tape-casting step. Figure 40d shows the SS grid-integrated graphite-containing material with a grid aperture of 1.20 mm and a wire diameter of 0.4 mm. A few cracks were observed in the matrix which is the result of different thermal expansion coefficients of metal grids and ceramic matrix. A similar behavior was observed for the Cu grid-integrated material. In general, the introduction of metal particles influences pyrolytic conversion, stabilization of phases, as well as material properties [200]. For the metal-

containing materials, metal salts were used as sources of Co and Ni particles. By metal ions reduction during pyrolysis, metal nanoparticles could be generated within the SiOC matrix [135]. The metal content after pyrolysis at 1000 °C was calculated on the basis of thermogravimetric measurements (Fig. A.2.1), resulting in an amount of 2.88 and 1.69 wt% for Co- and Ni-containing materials, respectively. In Figure 40e, f, the morphology of Co and Ni-graphite-containing materials are shown. The Co/Ni-containing materials show a rough surface and a pore arrangement which differs from the metal-free material pyrolyzed at 1000 °C (Figure 40b) confirming the influence of metal presence on the near net shape of the material. Bacteria sizes can range from 200 nm to 750 µm [201], though in BES their sizes are typically 0.5–5.0 µm in length. The resulting structure of all the synthesized materials provides a suitable size for accommodating bacteria as well as the feasibility of nutrients access through the pores and internal colonization.

Pore size and their distribution are important parameters that influence physical properties of porous materials and also determine reaction/active sites in electrochemical applications. In order to characterize the micro–meso–macroporosity of the materials synthesized, nitrogen adsorption/desorption isotherms were recorded and mercury intrusion porosimetry was applied. The isotherms and corresponding SSAs are shown in Figure 41.

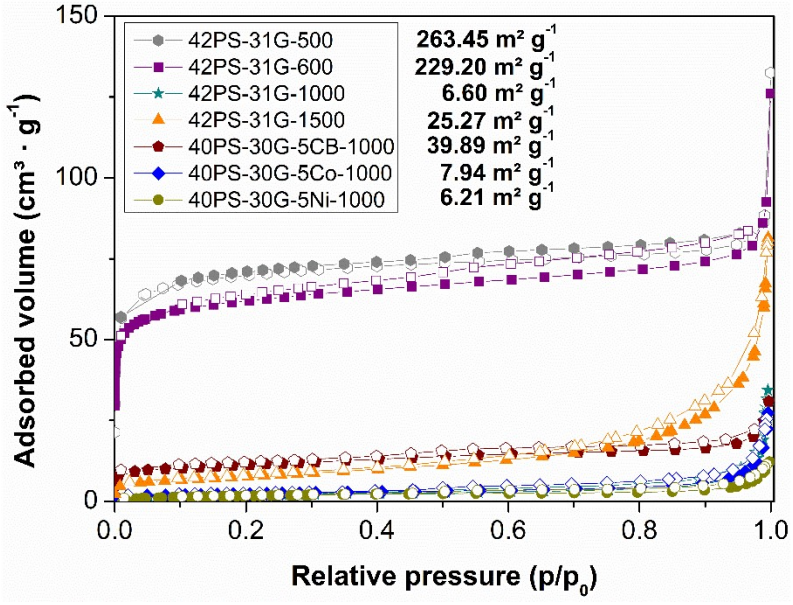

Figure 41. Nitrogen adsorption–desorption isotherms and SSA of pyrolyzed electrode materials with carbon-based conductive fillers and metal particles. Adapted from [147].

For the electrode materials pyrolyzed at 500 and 600 °C, the isotherms are classified as type I [202] which characterizes micropores (pore diameter < 2 nm) [203] filled at low relative pressures. These micropores are generated during the partial polymer-to-ceramic conversion

upon pyrolysis between 400 and 800 °C [23, 204, 205], as transient porosity and resulting in higher specific surface areas (230–265 $m^2 g^{-1}$). For the materials pyrolyzed at 1000 °C, type IV isotherms [202] (Fig. A.2.2) were observed, which are typical for mesoporous materials (pore diameter 2–50 nm) [203], and show an increase in volume adsorbed at higher relative pressures as well as a hysteresis loop. With increasing pyrolysis temperature, SSAs decrease which is related to the collapse of micropores [23]. As a result, the materials pyrolyzed above 600 °C present lower SSAs of 6–40 $m^2 g^{-1}$.

The isotherm of the material pyrolyzed at 1200 °C was also classified as type IV (Fig. A.2.3). For the material pyrolyzed at 1500 °C, type II isotherm (Fig. A.2.3) was observed, which is correlated to macroporous (pore diameter > 50 nm) [203] or nonporous materials. At this temperature, an increase in specific surface area up to 25 $m^2 g^{-1}$ was observed which can be referred to small gaseous molecules released and simultaneous generation of pores during carbothermal reduction process [206]. Since the graphite (KS75) used in this work has a low SSA of 7 $m^2 g^{-1}$, the porosity was mainly influenced by the pyrolytic conversion of the silsesquioxanes into ceramics.

For the carbon black-containing material, an increase in surface area was observed which is related to the microporosity of the carbon-based filler, which possesses an SSA of 44.80 $m^2 g^{-1}$. For the Co/Ni-containing materials, the type IV isotherms were also observed (Figure 41, Fig. A.2.2), as for the graphite-containing material pyrolyzed at 1000 °C and SSAs were not significantly affected by the formation and presence of metal particles. As expected, the SSAs of graphite-containing materials without and with grids (SS/Cu) pyrolyzed at 1000 °C are similar. This can be attributed to the integration of the grids which do not influence the micro–mesoporosity of the SiOC matrix.

The SSAs of the SiOC-based electrode materials (6.21–263.45 $m^2 g^{-1}$) are relatively higher compared to a carbon felt characterized in this work (0.032 $m^2 g^{-1}$) and thus can impact the BES performance by enhancing electrode kinetics. Moreover, the Co/Ni-containing materials could offer reactive sites influencing the electrocatalytic activity toward the oxygen reduction reaction (ORR) that takes place at cathode electrodes in BES.

Figure 42 shows mercury intrusion results performed for graphite-containing materials pyrolyzed at different temperatures and graphite-carbon black as well as Co/Ni-containing materials pyrolyzed at 1000 °C. The material pyrolyzed at 500 °C possesses a broad distribution with the main diameters around 0.1 and 1 μm. For the material pyrolyzed at 600 °C, a bimodal distribution and a decrease in relative volume of mesopores was observed. At 1000 °C, an even broader distribution was found, and an increase in relative volume of macropores was observed. The pronounced macroporosity results from the collapse of pores due to the increase in pyrolysis temperature applied. The total porosity of materials pyrolyzed in the range of 500–1000 °C was not significantly affected by the temperature and remains around 34%. For the materials pyrolyzed at 1200 °C and 1500 °C, a similar trend of bimodal distribution and a comparatively narrow region of main diameter between 0.1 and 1 μm were observed. However, the total porosity of 52.02 and 59.09% was increased, compared to the materials pyrolyzed at 1000 °C and below. The change in porosity is due to the phase separation process of SiOC and further carbothermal reduction in silica with free carbon that occurs at higher pyrolysis temperatures (>1200 °C). At these temperatures, nanocrystallites of SiC and Si_3N_4 are produced with the evolution of gaseous species (i.e., SiO, CO and CO_2) [199, 207, 208].

Concerning the graphite-carbon black-containing material, a trimodal distribution was observed with an increase in the relative volume of mesopores. The open porosity was not influenced by the incorporation of this carbon-based filler. For the Co/Ni-containing materials, the formation of Co and Ni particles led to a shift of the pores in the macropore region with diameters larger than 1 μm. An increase in the relative volume of mesopores compared to the graphite-containing material pyrolyzed at 1000 °C (metal-free) was also observed. Based on thermogravimetric measurements (Fig. A.2.1), Ni and Co particles catalyze the decomposition process during the pyrolytic conversion and, hence, influence the pore size distribution.

Overall, the synthesized materials pyrolyzed at temperatures up to 600 °C show micro-/mesoporous structures, while materials pyrolyzed at higher temperatures show meso-/macropores. Due to the tailorable porosity achieved, the electrode materials developed can play different roles in providing an optimized porous structure to accommodate bacteria cells as anode electrodes. From the cathode side perspective, the open pores developed can influence in the oxygen transport to the catalyst for the ORR.

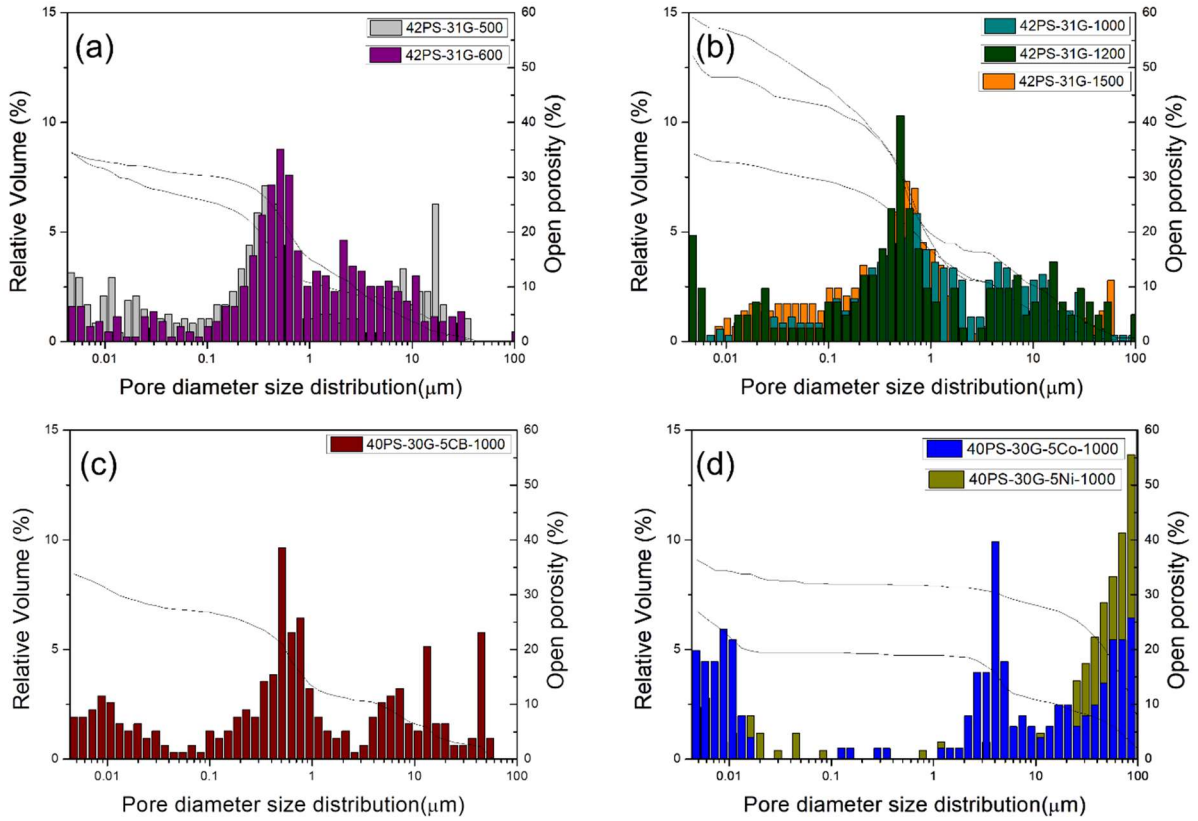

Figure 42. Relative pore volume, pore size distribution and open porosity of pyrolyzed electrode materials with carbon-based conductive fillers (a–c) and metal particles (d). Adapted from [147].

Surface characteristics are a determining parameter on material–surface interactions regarding adsorption or adhesion in chemical separation processes and coatings [54, 209, 210]. Adsorption capacities of solvent vapors of different polarity, polar (water) and nonpolar (n-heptane), were investigated in the interest of determining the hydrophilicity and hydrophobicity of the materials synthesized. The materials were compared with regard to ratios of water to n-heptane vapor adsorption. A ratio higher than 1 indicates a higher affinity for water and hence a hydrophilic behavior. The uptakes were related to SSA values and are presented in Figure 43. The surface wettability was also investigated, and the water contact angle values are displayed in Figure 43 (right y-axis).

Overall, the materials adsorbed more water vapor than n-heptane, indicating a higher affinity to polar vapors and by that demonstrating a hydrophilic behavior of the surface. The hydrophilicity (the ratio of water/n-heptane vapor adsorbed) greatly increased with the increase in pyrolysis temperature which can be explained by the decomposition of the methyl and phenyl

moieties during the pyrolytic conversion of MK and H44 and the evolution of porosity [20]. A pronounced increase in hydrophilicity was seen for the pyrolyzed material at 1200 °C. This increase can be referred to the consumption of free carbon due to the start of carbothermal reduction at this temperature. For the graphite-containing material pyrolyzed at 1500 °C, the decrease in hydrophilicity is correlated with the formation of Si_3N_4. Besides, due to increased open porosity (59.09%), the contact angle measurement of this material could not be performed, because the water was soaked in.

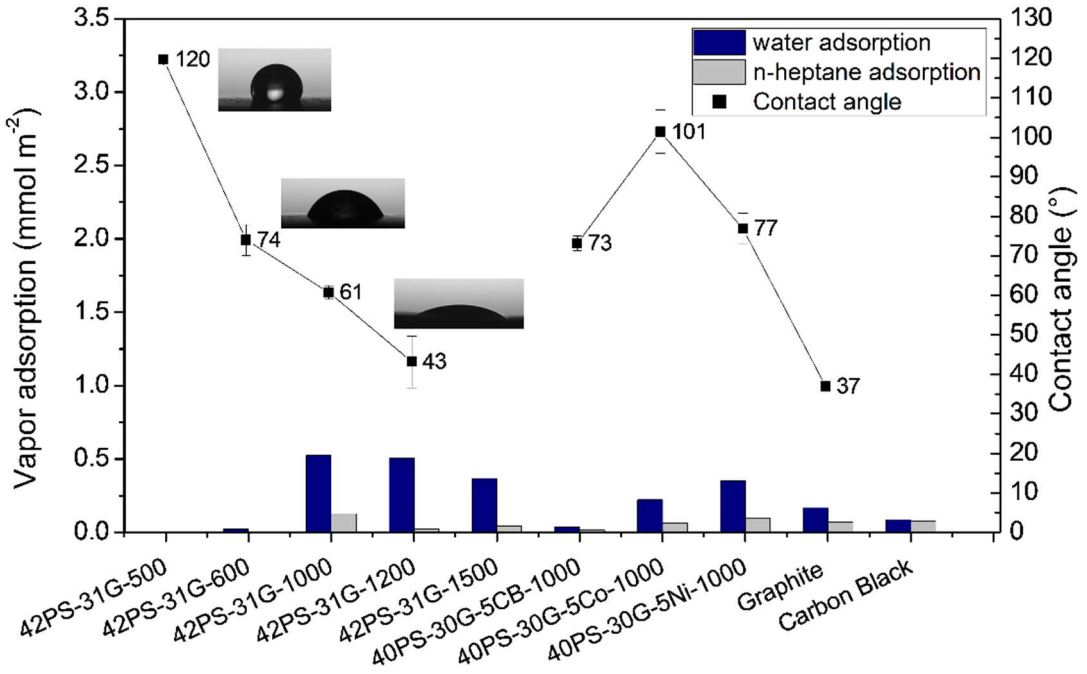

Figure 43. Water and n-heptane max. vapor adsorption related to SSA (columns) and contact angle (black markers) of the pyrolyzed electrodes containing graphite, carbon black and Co/Ni particles and single carbon fillers. Adapted from [147].

Regarding the graphite-carbon black-containing material, a decrease in hydrophilicity was observed, when compared to the graphite-containing material pyrolyzed at 1000 °C, which is connected to the hydrophobic nature of carbon black. Therefore, the increase in total carbon content in the material together with a decrease in hydrophilic silica content led to the decrease in hydrophilicity.

For Co/Ni-containing materials, a slight reduction in hydrophilicity was found. As surface characteristics for the materials integrated with grids (SS/Cu), the value was considered the same as the graphite-containing materials pyrolyzed at 1000 °C. The additional contact

angle measurements of water droplets show the gradual increase in wettability with increasing pyrolysis temperature by the decrease in the contact angle values. For the graphite-carbon black- and Ni-containing materials, a hydrophilic behavior was also confirmed by the contact angle (73.2° and 76.9°), whereas for the Co-containing material hydrophobicity (101.4°) was observed.

In the final result, the surface characteristics of the synthesized materials could be mainly tailored by the pyrolysis temperature applied, making them suitable for different applications that require hydrophilic materials. Regarding bioelectrochemical applications, the tailorability of hydrophilicity of the materials developed can improve surface interactions to enable the growth of anodic electroactive biofilms in BES [211, 212]. In terms of cathode configurations in BES, aqueous-based cathode with dissolved oxygen in the electrolyte and air-based cathode with direct air diffusion are usually applied [213]. A balanced three-phase boundary (liquid, air and solid) is required to provide oxygen transfer, protons migration and flow of electrons maintaining the performance. In order to minimize water filling in the pores in air cathodes, hydrophobic materials are preferable, thus preventing flooding [214]. Therefore, in this context, the choice is limited to the materials developed which presented lower degree of hydrophilicity.

4.2 Electrical Properties

By EIS method, the electrical conductivity [$\sigma_{AC}(\omega)$] values of the SiOC-based electrode materials were determined using the following equation.

$$\sigma_{AC}(\omega) = (L/A)\, x\, (1/R)$$

where L and A represent the thickness and the cross-sectional area of the material, respectively, and R is the impedance measured. The direct current (DC) conductivity was calculated from conductance spectrums and according to Jonscher's power-law behaviour [215], which describes the frequency dependence to alternating current (AC) conductivity by the following equation.

$$\sigma_{AC}(\omega) = \sigma_{DC} + A\omega^{n}$$

where σ_{DC} and σ_{AC} are the DC and AC conductivities of the materials, respectively, A is a pre-exponential constant, ω is the angular frequency and n is the frequency exponent, with $0 < n < 1$. The DC conductivity values of the electrode material measured at room temperature are shown in Figure 44a in comparison with a commercial carbon felt. Values of DC conductivity of two materials prepared without any incorporation of conductive materials and pyrolyzed at 600 and 1000 °C are additionally displayed in Figure 44a. The comparison of SiOC-materials free of conductive phases with graphite-containing ones pyrolyzed at 600 and 1000 °C shows an increase in DC conductivity by ~14 and 10 orders of magnitude, respectively. The materials without conductive phases behave like an insulator. The conduction mechanism in SiOC was found to be based on the intrinsic conductivity of turbostratic carbon (formation above 800 °C) [129]. For the materials without incorporated conductive phases, the conduction is based on the bandgap of turbostratic carbon, which gives very low conductivity values [136].

The lack of conduction of the materials in this work was, in a first step, overcome by the use of graphite powder based on loads used in [131] and by changes of the pyrolysis temperature. Comparing the graphite-containing materials pyrolyzed at 500 and 1500 °C (0.044 S cm^{-1} and 0.190 S cm^{-1}), the conductivity values increase by ~ 1 order of magnitude. Here, since the composition of the materials was kept identical, the electrical conductivity of the SiOC-derived materials is mainly dominated by pyrolysis temperatures applied during the polymer–ceramic conversion. In the temperature range between 700 and 1400 °C, an excess of carbon precipitates forming an interpercolating network that results in a transition from an insulator to a semiconductor [129, 216]. Regarding the combination of graphite and addition of carbon black, an increase of ~ 1.8-fold in DC conductivity was found. The enhanced conductivity is related to the higher amount of carbon due to its incorporation.

For the materials with integrated metallic grids, an increase of ~ 1.7-fold in conductivity was found for the Cu-integrated material when compared to the graphite-containing material pyrolyzed at 1000 °C which is due to the low electron resistivity of the metal (Cu). In contrast to Cu-integrated material, SS-integrated material did not show a significant improvement in electrical conductivity without degrading the conductivity compared to the materials without the grid. This can be explained by the fact that stainless steel alloys do not form a crystal lattice where the outer shell electrons are shared and easily move through the lattice (as in copper, silver and gold) and by that, the resistance of electron flow is increased compared to Cu-based materials. The best improvement in electron conductivity could be achieved by incorporation of Co and Ni particles.

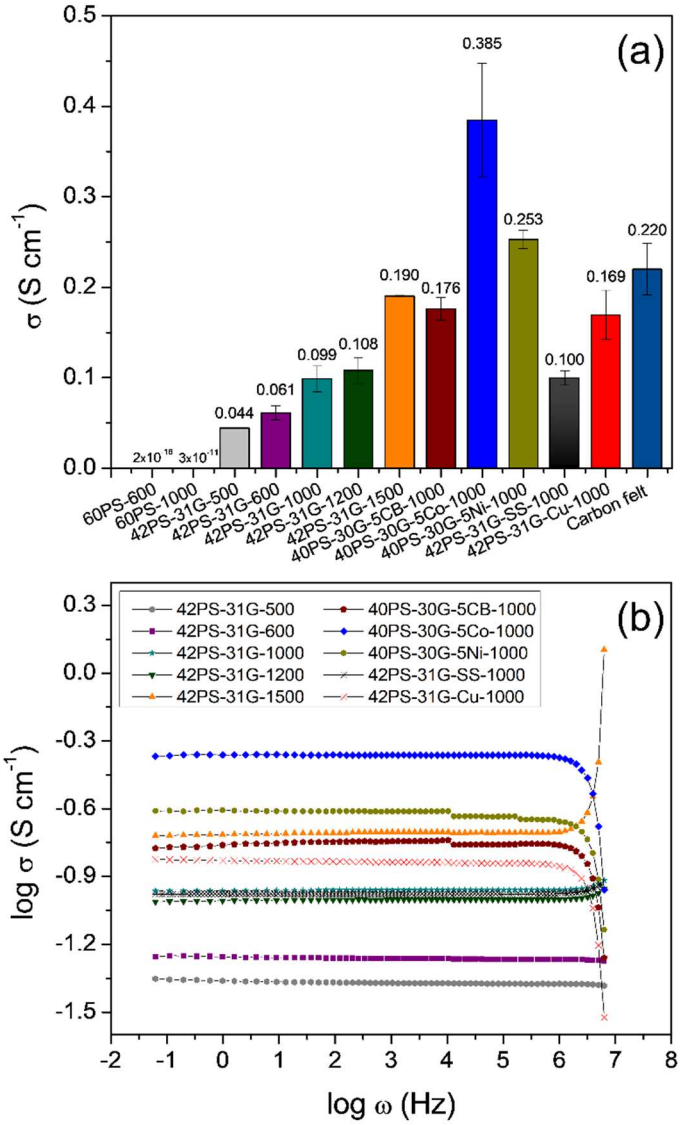

Figure 44. Electrical conductivity values obtained by impedance analyzer (a) and conductance spectra at room temperature of the electrode materials prepared (b). Adapted from [147].

Comparing with the DC conductivity of graphite-containing material (0.099 S cm^{-1}), an increase up to four-fold (0.253 S cm^{-1} for Ni and 0.385 S cm^{-1} for Co) was obtained with a metal content of less than 2–3wt%, as calculated by thermogravimetric analysis. Within the pore structure of the Co/Ni-containing materials, carbon nanotube (CNT) formation could be identified by SEM and TEM analysis, as shown in Figure 45 for Co-containing material. Metal particles were found either fixed to the matrix and/or also along the length of the tubes formed. The known mechanism of CNT formation describes pores as catalytic microreactors while CNTs emanate from individual metal particles on the ceramic material [129, 135]. The in situ

formation of CNTs can also be addressed to the further enhancement of DC conductivity due to the high conductivity of this carbon species.

The DC conductivity of a carbon felt usually used as a commercial electrode material in BES was also measured for comparison reasons. The DC conductivity values of most of the materials are substantially close to the carbon felt value measured (0.22 S cm^{-1}), and for the Co/Ni-containing materials, even higher conductivity values were observed. The sufficient electrical conductivity demonstrated supports the applicability of the new electrode materials in the area of BES.

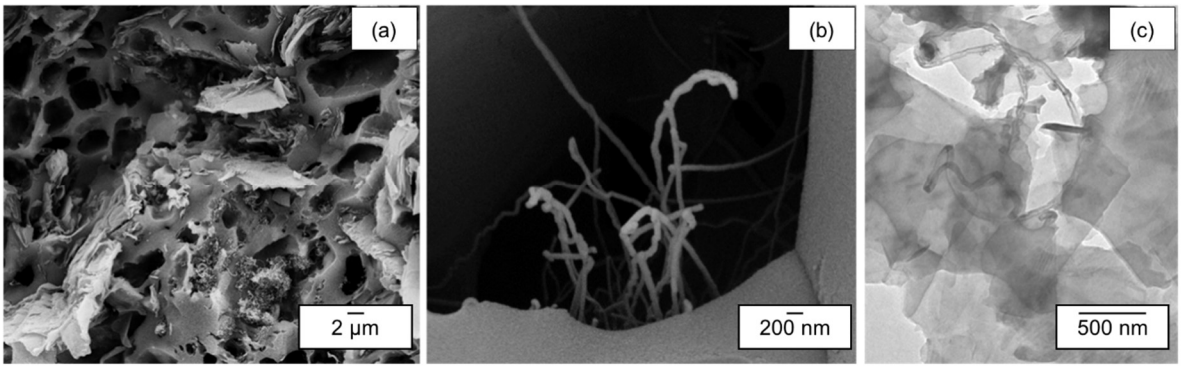

Figure 45. SEM (a, b) and TEM (c) images confirming the carbon nanotubes formation in the Co-containing electrode material prepared. Adapted from [147].

Even though the electron transfer mechanisms discussed in BES are related to the microorganisms, in order to understand the transport behavior of these materials, frequency dependence studies of AC conductivity were performed. Figure 44b shows the frequency dependences of conductivity measured at 25 °C for the prepared materials, and the individual plots are additionally presented in Fig. A.2.4 and Fig. A.2.5.

Regarding the graphite-containing electrode materials pyrolyzed at temperatures from 500 °C to 1500 °C, two main behaviors were observed. From the conductance spectrum of the materials pyrolyzed at 500 and 600 °C (Fig. A.2.4), a conductivity–frequency dependence is shown, where σ decreases with the increase in frequency. The conductivity dependence of frequency can be associated to the low carbon content and low percolation network degree of SiOC-based materials at these pyrolysis temperatures.

For the graphite-containing materials pyrolyzed at 1000, 1200 and 1500 °C, a similar tendency was observed. Through the conductance spectrum shown in Fig. A.2.4, a slight increase of σ is observed at lower frequency range, followed by a frequency-independent

behaviour in the mid-ranges and frequency dispersion at higher frequency range [217]. The independence of frequency at lower mid-frequencies is related to the corresponding DC conductivity of the material and the dispersion at higher frequencies suggesting a hopping conduction mechanism for these materials [217, 218].

For the metallic grids/metal-containing materials, as well as, the carbon black-incorporated material, two distinct behaviors were found and are displayed at Fig. A.2.4 and Fig. A.2.5. The SS-integrated electrode material follows the trend of the materials pyrolyzed at 1000–1500 °C, indicating hopping mechanism. The Cu-integrated, Co/Ni- and the graphite-carbon black-containing materials possess frequency-independent behavior in the lower range of frequency whereas at higher frequency conductivities decreases monotonically with frequency. The decrease of σ_{AC} at higher frequencies is related to the change of conduction mechanism from hopping to metal-like conduction, as well as, enhancement of the skin effect (electric current flow through the ‘‘skin’’ of the conductor) [219, 220].

4.3 Chemical Stability

With regard to a first impression about the stability of the materials synthesized, neutral conditions and a period of four weeks were chosen as parameters based on the BES environment. The variation of the weight of the dry materials over the period is shown in Figure 46.

In summary, the materials presented a weight loss/increase lower than 5%, except for the Co-containing material which showed a weight loss of ~ 10%. With the increase in pyrolysis temperature applied (600–1500 ºC), a decrease in weight loss is observed. This trend can be associated with the partial decomposition and elimination of organic moieties from the preceramic precursors during pyrolysis, which starts at 400 ºC and is not complete until 600 ºC [18, 118]. Due to the higher degree of organic load of the polymeric precursors at temperatures below 700 ºC, the susceptibility of the materials toward disintegration is higher.

Pyrolysis above 800 ºC consolidates the amorphous structure of the SiOC-materials, and beyond 1000 ºC, the transition to the crystalline phase, followed by phase separation, starts [18]. As a result of the rearrangement of the structure during the heat treatment, the stability is enhanced what is in agreement with the results obtained. The increase in weight loss for the graphite-carbon black-containing material compared to the graphite-containing pyrolyzed at

1000 ºC can be correlated to the higher amount of carbon. This makes the material more susceptible to chemical reactions.

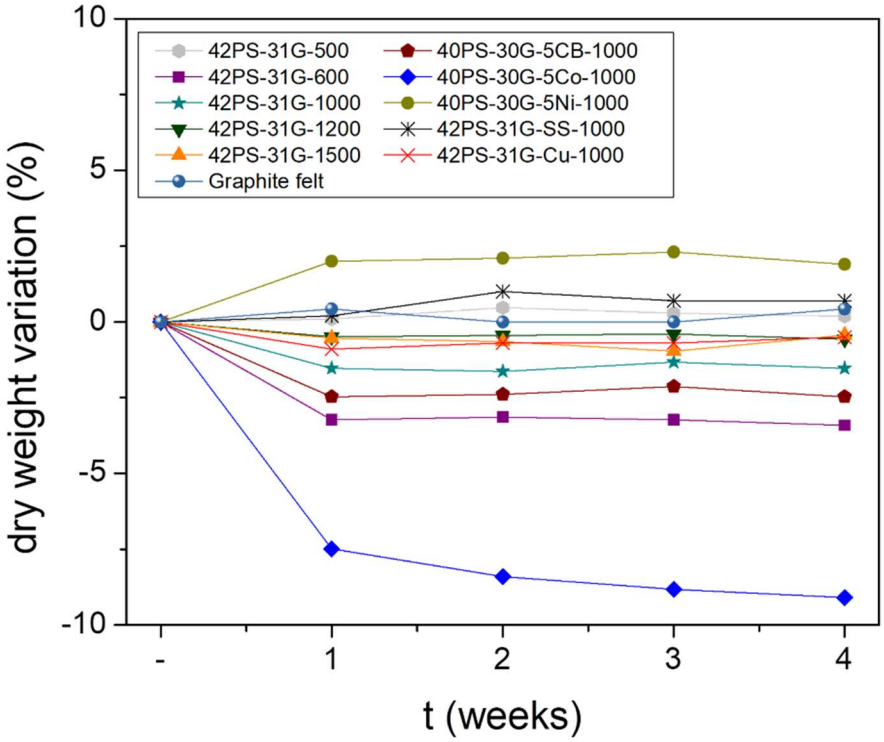

Figure 46. Chemical stability tests in phosphate buffer solution (pH 7) over a period of 4 weeks. Adapted from [147].

The increase in weight, more pronounced for the Ni-containing material, can be accounted to the formation of passive layer (oxide) on the surface exposed. The pronounced increase in weight loss for the Co-containing material can be associated to the change in the built of the structure, affected by the metal incorporation, resulting in larger pores and higher accessibility of the liquid media to allow disintegration. Additionally, leaching of intermediate products formed from thermal decomposition of $CoCl_2$ can be addressed to the higher weight loss.

4.4 Biofilm Development

The development of a biofilm is a complex multi-step process which leads to the formation of a microbial community adhered to the surface [52]. Biofilms play an important role in nature and recently also in bioelectrochemical technology. *B. cereus* and *E. coli* were used as model bacteria to assess adhesion (2 h) and biofilm formation (24 h) on the SiOC-based surfaces (Figure 47). It was possible to observe that most of the surfaces allowed adhesion in

the first 2 h, except for the Cu grid-containing material using *E. coli*. The number of cells further increases with the 24-h incubation time ($P<0.05$). Therefore, biofilm formation was observed for all materials. In addition, the surfaces show higher bacterial adhesion and biofilm formation with *E. coli*.

With regard to the physicochemical properties of the materials obtained by distinct pyrolysis temperature applied (500, 600 and 1000), this seems to have a negligible impact on bacterial adhesion and biofilm formation ($P>0.05$). Regarding the additional conductive materials, a decrease was observed for metal-based materials, with pronounced reduction for the Cu grid-containing material with both microorganisms ($P<0.05$).

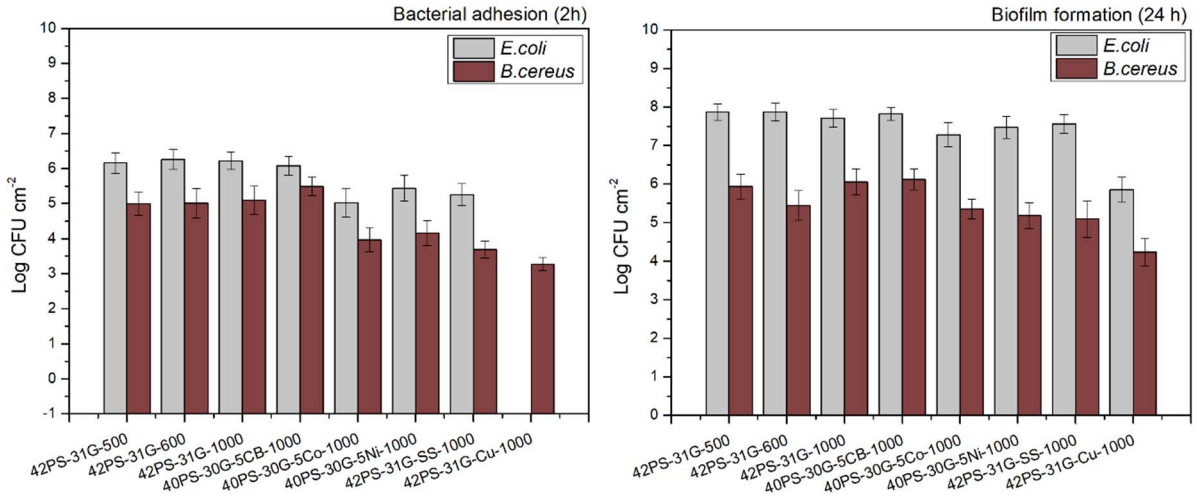

Figure 47. *B. cereus* and *E. coli* adhesion (2 h) and biofilm formation (24 h) on the SiOC-based electrode materials. The error bars represent the standard deviations from three independent experiments. Adapted from [147].

Previous studies reported the use of Ni and Co nanoparticles to prevent bacterial attachment [221, 222]. In this work, a slight reduction is also observed for the Co/Ni-containing materials even though the metal content incorporated is low and not all the particles are exposed on the surface. For the SS/Cu grid-containing materials similarly to Sharifahmadian et al., the bacterial viability was reduced on Cu surfaces while SS did not present antibacterial properties [223]. Nevertheless, the antibacterial activity of cooper is known [224] and low bacterial adhesion was already expected.

Although metal electrodes have been considered in BES research, stability concerns during the operation such as passivating oxide layer formation, oxidative dissolution and metal

ions released upon oxidation still limit the operative potential window [62]. Adverse effects on biofilm formation due to copper corrosion and toxicity have also been described by Zhu and Logan [225].

In this study, pure cultures of distinct gram-positive and gram-negative microorganisms were used. Although the BES operates with these two gram types, mixed culture is the reality in wastewater treatments. Besides, factors such as pH, temperature, shear stress and wastewater composition were not considered in this initial assessment. Therefore, further studies using mixed culture bacteria and considering some of these factors may provide a fine-tuning in the manufacture of SiOC-based electrode materials for BES.

Chapter V. Application of SiOC-based Polymer derived-ceramic Porous Anodes in Microbial Fuel Cells

This chapter contains the results and discussion of characterized physical properties and MFC performance concerning the SiOC electrode materials described in Chapter III (topic 3.1.1). Properties regarding structural and electrical characteristics as well as biocompatibility, in means of biofilm development, are considered. The MFC performance is discussed through current and power densities as well as COD removal determining the wastewater treatment efficiency (methods described in topic 3.4). Parts of the following chapter have been published in Biochemical Engineering Journal 148 (2019) 29-36 (DOI: 10.1016/j.bej.2019.04.004) [149]. This chapter is also supplemented with added unpublished results.

5.1 Tape-cast SiOC-based Anode Materials

SiOC-based anode materials were produced by tape casting technique with dimensions of 40 × 40 × 2.5 mm and pyrolyzed under nitrogen environment at 1000 °C. In order to compensate the shrinkage and weight loss of the tapes during the ceramic conversion of polymers, *ca.* 8 wt% $MoSi_2$ was used as filler based on previous studies [131]. In addition, azodicarboxiamide was used as a foaming agent to induce the formation of pores, due to its ability of introducing macro- and open porosity in the structure [226, 227]. The resulting morphology of the as-prepared materials was investigated by SEM and the micrographs of the pyrolyzed anode materials are shown in Figure 48. The PDC-Graphite, PDC-G-Carbon Black and PDC-G-Nickel materials pyrolyzed at 1000 °C are shown in Figure 48a–c, respectively. Figure 48d shows the morphology of the non-treated carbon felt used as a control. From the SEM images, macropores ranging from 0.5–40 μm could be identified, which are suitable in size for accommodating bacteria, since their sizes are in the range of 200 nm to 750 μm [201]. It is also visible, because of the materials development possess, a completely distinct morphology was found compared to the carbon fibers arrangement of carbon felt. While comparing the PDC-based materials among themselves, a similar macrostructure is observed, indicating that the incorporation of carbon black or nickel particles formation is not significantly affecting the macrostructure of the PDC matrix.

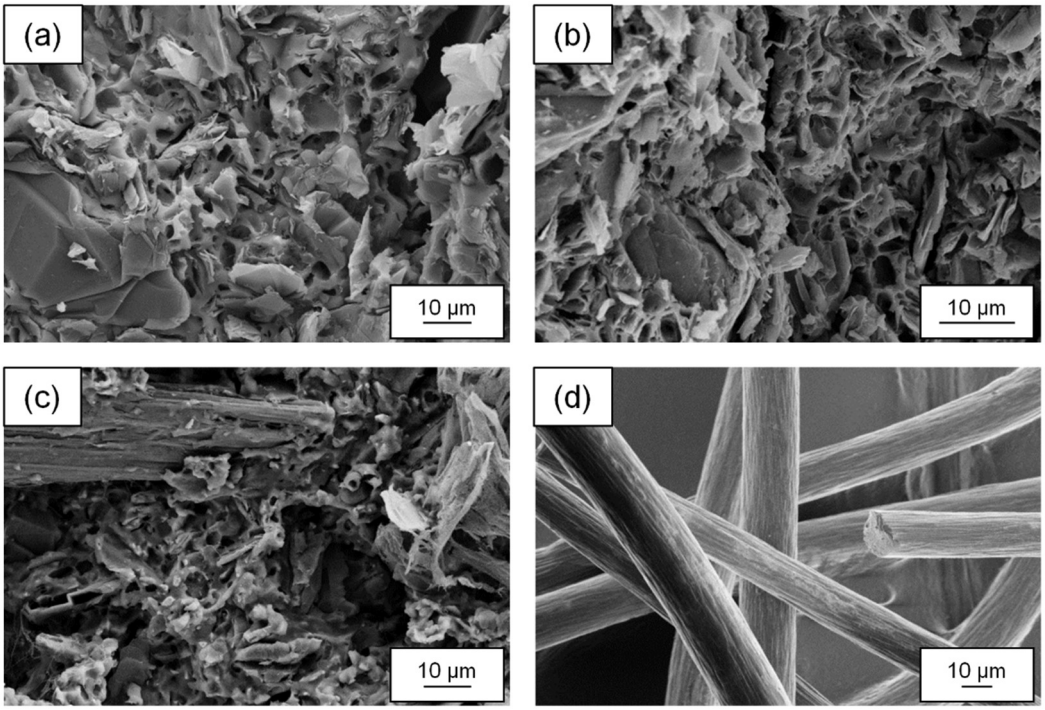

Figure 48. SEM images of the pyrolyzed PDC-Graphite, PDC-G-Carbon Black and PDC-G-Nickel anode materials (a, b, and c respectively) at 1000 °C and commercial carbon felt (d). Adapted from [149].

The interior structures were further analyzed in terms of BET specific surface areas and surface characteristics. Figure 49a represents the nitrogen adsorption-desorption isotherms, respective SSAs and the adsorption capacities of water and n-heptane related to SSA in combination with water contact angle measurements. As shown in Figure 49a, PDC-G-Carbon Black, exhibited isotherms type I, that characterize micropores (pore diameter < 2 nm) filled at low relative pressures, resulting in higher specific surface areas. For PDC-Graphite and PDC-G-Nickel, isotherms type IV were observed, which is associated with mesoporous materials (pore diameter 2–50 nm) [202, 203]. The PDC-based anode materials exhibited SSAs as high as 6.52–39.89 $m^2\ g^{-1}$, which was much higher as compared to the carbon felt (0.032 $m^2\ g^{-1}$) used as a control. The higher SSAs of the PDC-based anode materials can provide more sites for reactions, enhancing electrode kinetics and hence improve the performance of MFC.

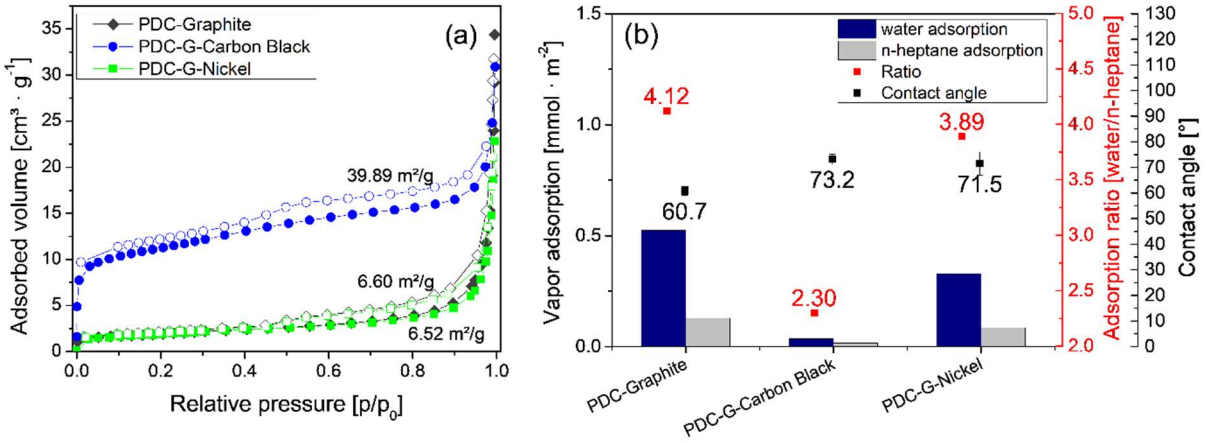

Figure 49. Nitrogen adsorption-desorption isotherms and respective BET specific surface areas (a), water and n-heptane adsorption at 25 °C, the water/n-heptane ratio (red markers) and contact angle (black markers) of the pyrolyzed anodes prepared (b). Adapted from [149].

Since the hydrophobic/hydrophilic properties of a surface can affect the anodic biofilm formation, as well as the generated current intensity [211], surface characteristics and water contact angles of the synthesized anode materials were characterized (Figure 49b). For the characterization of vapor adsorption, the materials are correlated with regard to ratios of water to n-heptane vapor adsorption, where a ratio higher than 1 indicates hydrophilicity. Materials which adsorbed more water vapor than n-heptane, indicate a higher affinity to polar vapors and hence hydrophilic surface characteristics. The additional water contact angle (WCA) measurements (Figure 49b, black markers) also confirmed the hydrophilic behavior of the PDC-based anode surfaces and hydrophobic behavior of carbon felt (WCA=112°). The hydrophilic behavior of these PDC-based materials is related to the decomposition of methyl and phenyl moieties as a result of the pyrolysis temperature applied (1000 °C) [20]. The materials differ in the degree of hydrophilicity, evaluated by the vapor uptake ratio (water/n-heptane), and PDC-G-Carbon Black showed the lower hydrophilicity, which is mainly due to the higher carbon content on its composition.

The hydrophilicity was found to be beneficial to bacterial adherence [211], which demonstrates an advantage of PDC materials when compared to hydrophobic carbon materials. This positive effect on the performance of MFC is also supported by Chang et al. and Zhao et al., while using carbon-based surface-modified electrodes [228, 229]. The relevance of hydrophilic surfaces is attributed to favorable biosorption of bacteria on the surface of electrodes providing a more suitable environment for bacterial growth [228, 229].

In order to evaluate the stability of the anodes, a preliminary study of dry weight variation in a phosphate buffer solution (PBS, pH 7), at room temperature over a period of 4 weeks was performed. For this test, a material with a higher amount of $NiCl_2$ in the composition (5 wt%) was considered. The materials revealed appropriate stability, with weight loss/increase lower than 3% (Fig. A.3.1). The increased weight for the PDC-G-Ni material can be accounted to the formation of a passive layer (oxide) on the exposed surface.

5.1.1 Electrical Performance of MFC

Applicability and performance of the novel anode materials based on PDC were evaluated in terms of power production. The presence of active exo-electrogenic bacteria in mixed anaerobic consortia was endorsed by the fact that all the four MFCs started showing voltage from the very first day after its start-up. Thus, reduced time for anodic acclimatization was observed for all the MFCs. After the initial start-up duration of 13–15 days, stable performance in terms of electrical output and organic matter removal was observed for the next 15 cycles for better replication of datasets. The measured electrical conductivity by EIS and anode's parameters during the stable operation of the MFC are summarized in Table 4.

Table 4. Electrical conductivity measured by impedance and anode parameters during the operation of the MFCs.

Anode material	**PDC- Graphite**	**PDC-G-Carbon Black**	**PDC-G-Nickel**	**Carbon Felt**
Electrical conductivity [$S \cdot cm^{-1}$]	0.099	0.176	0.102	0.761
Maximum OV [mV]	162	231	21	220
Maximum OCV[mV]	789	824	239	811
Anode potential [mV]	-421	-439	-12	-447
Maximum power density [$mW \cdot m^{-2}$]	144	211	30	111
Maximum current density [$mA \cdot m^{-2}$]	447	542	288	277
Internal resistance [Ω]	217	165	286	373

The average operating voltage (OV) of 219 ± 15 mV was achieved under the steady-state operating condition and over an external resistance of 100 Ω for MFC with PDC-G-Carbon Black as anode. This value was comparably higher than the values obtained by the MFC with PDC-Graphite (150 ± 15 mV), the MFC with PDC-G-Nickel (18 ± 7 mV) and the control MFC with carbon felt (213 ± 7 mV). In addition, the pH of the anolyte was adjusted to about 7.4, whereas in the catholyte the pH ranged between 7.5 and 8.0 for the entire course of the study.

Figure 50a-b represents the power generation results according to IV curves and polarization curves. Power generation normalized to the volume of the MFC is additionally displayed in Fig. A.3.2. The polarization data showed that low activation loss was observed and the total internal resistance of MFC with PDC-G-Carbon Black was found to be 165 Ω, comparably lower than MFC with the PDC-Graphite anode (217 Ω), MFC with PDC-G-Nickel (286 Ω) and the control MFC with carbon felt (373 Ω). Besides, the MFC operated with PDC-G-Carbon Black as anode could generate a maximum power density of 211 mW m^{-2}, which was 46.5%, 603.3% and 90.1% higher compared to that of MFC with PDC-Graphite anode (144 mW m^{-2}), MFC with PDC-G-Nickel (30 mW m^{-2}) and the control MFC with carbon felt (111 mW m^{-2}), respectively (Figure 50, Table 4).

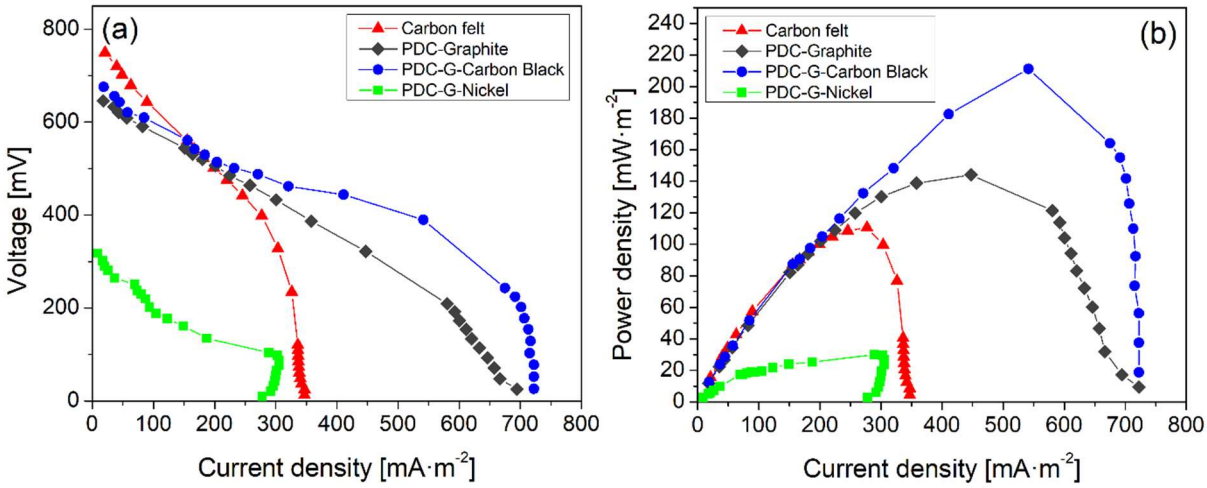

Figure 50. Polarization curves (a) and power density versus current density curves (b) of the MFCs with PDC-based anodes and carbon felt normalized to the projected anode area. Adapted from [149].

Based on the results obtained, it may be concluded that the MFC with the anode PDC-G-Carbon Black had higher electron transfer efficiency with reduced ohmic resistance, due to which it could generate higher power production as compared to the other three MFCs by recovering additional coulombs. A two-fold increase in the maximum current density and maximum power density was achieved by the anode PDC-G-Carbon Black compared to commercial carbon felt reveals a significant improvement in the performance of MFC. This improved performance can be related to the porous structure, hydrophilic surface and highest SSA characterized in this PDC-based anode material. The lower power production of the MFC with PDC-G-Nickel can be attributed to the leaching of nickel over time during operation of

MFC. The AAS results further confirmed the supposition by giving a positive test result (0.9 ± 0.1 μg l^{-1}) for the presence of nickel in the anolyte of MFC, over any course of time.

During the continuous operation of the MFC, fatty acids are produced while organic matter degradation and fermentation processes, which results in electrolyte acidification. The acidic conditions could gradually lead to the dissolution of nickel from the electrode. The solution with leached Ni(II) from the PDC-G-Nickel acts as electron acceptor in the anode chamber and reduces down to pure Ni(0) with a redox potential of -0.25 V (equation bellow), because of this the power production was compromised for this MFC.

Ni^{2+} (aq) + $2e^-$ → Ni° (s)

On the other hand, the carbon nanotubes formation at this particular Ni-containing material (Fig. A.3.3) could have been, in a certain level, toxic to the exoelectrogenic bacteria used in this study and inhibit the growth of biomass [230], which further decreases the performance of MFC.

Although the control MFC with graphite felt showed higher electrical conductivity value than the PDC-based anodes, the improved performance achieved suggests that the contribution of porosity and surface properties of the materials plays a crucial role in the biofilm development, influencing the overall power production. The performance obtained by the PDC-G-Carbon Black is in the range of previous studies conducted using 3D-electrode materials for Bioelectrochemical Systems (Table 5).

Table 5. Comparison of power densities resulted from 3D electrodes in BES.

BES configuration	**Electrode material**	**Inoculum**	**Power Density [mW m^{-2}]**	**Reference**
SC-MFC/Pt-air cathode	Granule activated carbon	Wastewater	245	Jiang et al., 2009 [231]
Marine benthic MFC	MWCNTs/MnO_2 modified GP	*	110	Fu et al., 2014 [232]
DC-MFC/biocathode	CNT/chitosan modified CP	Anaerobic sludge	189	Liu et al., 2011 [233]
DC-MFC/ferricyanide	CNT in-situ growth	Wastewater	20	Mink et al., 2012 [234]
SC-MFC/air-cathode	MWCNTs modified CP	Anaerobic sludge	290	Sun et al., 2010 [235]
SC-MFC	Stainless steel	Marine Sediments	23	Dumas et al., 2007 [236]
SC-MFC/aqueous cathode	PDC-G-Carbon Black	Anaerobic sludge	211	**This work**

BES: Bioelectrochemical Systems, SC-MFC: Single-chamber MFC, DC-MFC: Double-chamber MFC; MWCNTs: Multi-walled carbon nanotubes; CNT: Carbon nanotube; GP: Planar graphite; CP: Carbon paper; PDC: Polymer-derived ceramic; G: Graphite.

5.1.2 Wastewater Treatment in MFC

In order to analyze the performance of electricity generation focusing on energy, maximum NER was estimated (Figure 51a). The maximum NER_v in the MFC with PDC-G-Carbon Black was found to be substantially enhanced, with a value of 0.43 kW h m^{-3}, which was around 95.4% higher than the MFC with carbon felt as control (0.22 kW h m^{-3}), and 48.3%, 616.7% higher than the MFC with PDC-Graphite (0.29 kW h m^{-3}) and PDC-G-Nickel (0.06 kW h m^{-3}), respectively. For the maximum NER_r, a similar trend was observed, however, it differs in the percentage of enhancement. The MFC with PDC-G-Carbon Black anode showed the highest NER_r of 0.26 kW h kg COD^{-1}, which was 100% higher than the MFC using carbon felt as control anode (0.13 kW h kg COD^{-1}). Additionally, an increase of 52.9% and 420.0% was found for the MFCs with PDC-Graphite (0.17 kW h kg COD^{-1}) and PDC-G-Nickel (0.05 kW h kg COD^{-1}), when compared to PDC-G-Carbon Black (0.26 kW h kg COD^{-1}).

Bi-functional property of MFC as an efficient system for the treatment of wastewater and simultaneous bio-energy production has been documented extensively [237]. Wastewater treatment efficiency, mostly comprises of removal efficiency of COD, was monitored for 15 fed-batch cycles with each cycle having a reaction time of 2 days. The COD removal efficiencies of 86.3 ± 0.7%, 83.3 ± 1.9%, 60.0 ± 2.5% and 85.4 ± 0.7% were found in MFC with PDC-Graphite, MFC with PDC-G-Carbon Black, MFC with PDC-G-Nickel and the control MFC with carbon felt, respectively (Figure 51b). Except for the Ni-containing material, all the COD removal rates were comparable with the values reported for clayware based MFCs in the literature [238, 239].

The CE was estimated to further evaluate the accountability of PDC-based anode materials for MFC applications. The CE values are a passive index of correlation between the total current output from the MFCs and the COD removal values, which reflect the overall performance of the MFCs. The MFC with PDC-G-Carbon Black showed a CE of 22.04 ± 1.16%, which was higher than that obtained from the MFC with PDC-graphite (14.55 ± 1.73%) and control MFC with graphite felt (21.01 ± 0.70%) and almost 7 times higher than the MFC with PDC-G-Nickel (3.01 ± 0.81%; Figure 51c).

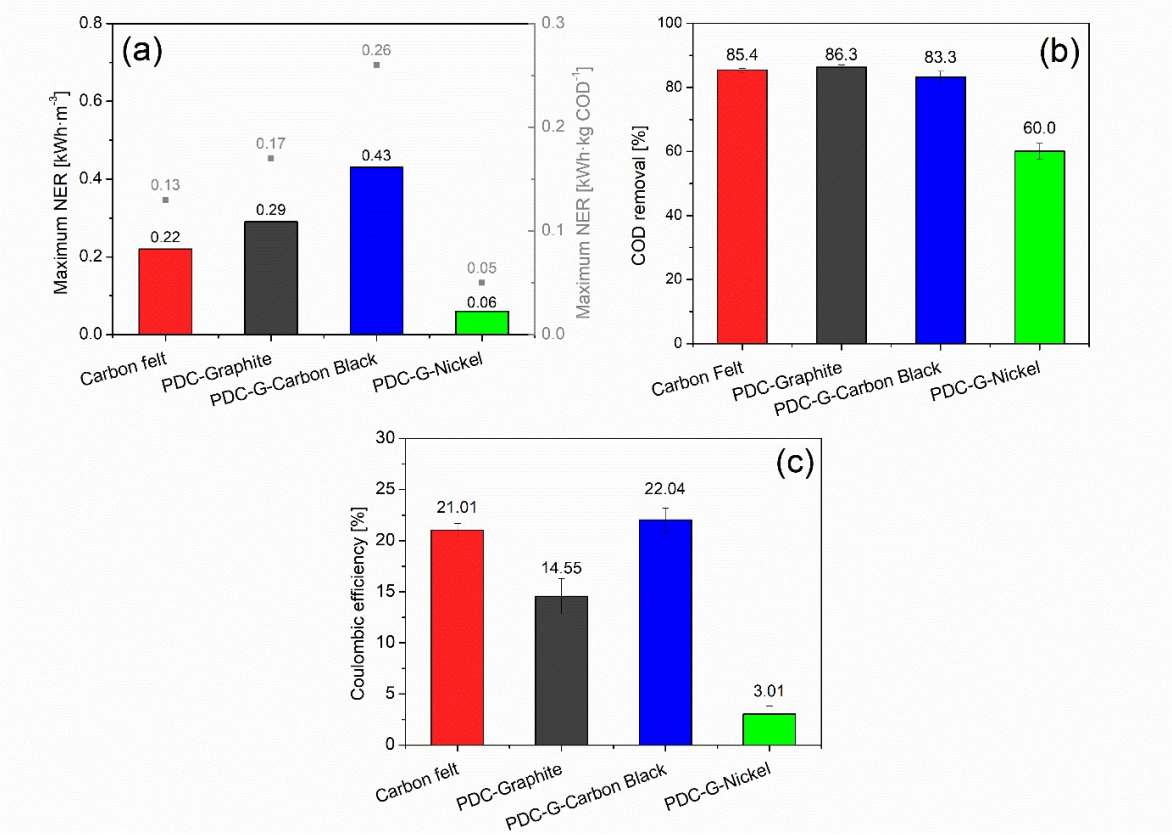

Figure 51. Maximum NER (a), COD removal rate (b), coulombic efficiency (c) of the MFCs with PDC-based anodes and carbon felt. Adapted from [149].

Thus, the applicability of PDC-G- Carbon Black as a better alternative anode material for MFC is established with promising sustainable wastewater treatment capability along with the benefit of tapping the maximum available energy reserve from wastewater.

5.1.3 Biofilm on Anode Surfaces

The increase in current and power generation can be associated with an electrochemically active biofilm formed on solid electrodes. To confirm and evaluate the biofilm formation on the anode materials, the materials were observed under a digital microscope and SEM after 45 days of operation. Figure 52 demonstrates the biofilm growth on the surfaces, confirming the biocompatibility of PDC-based materials to allow bacterial attachment.

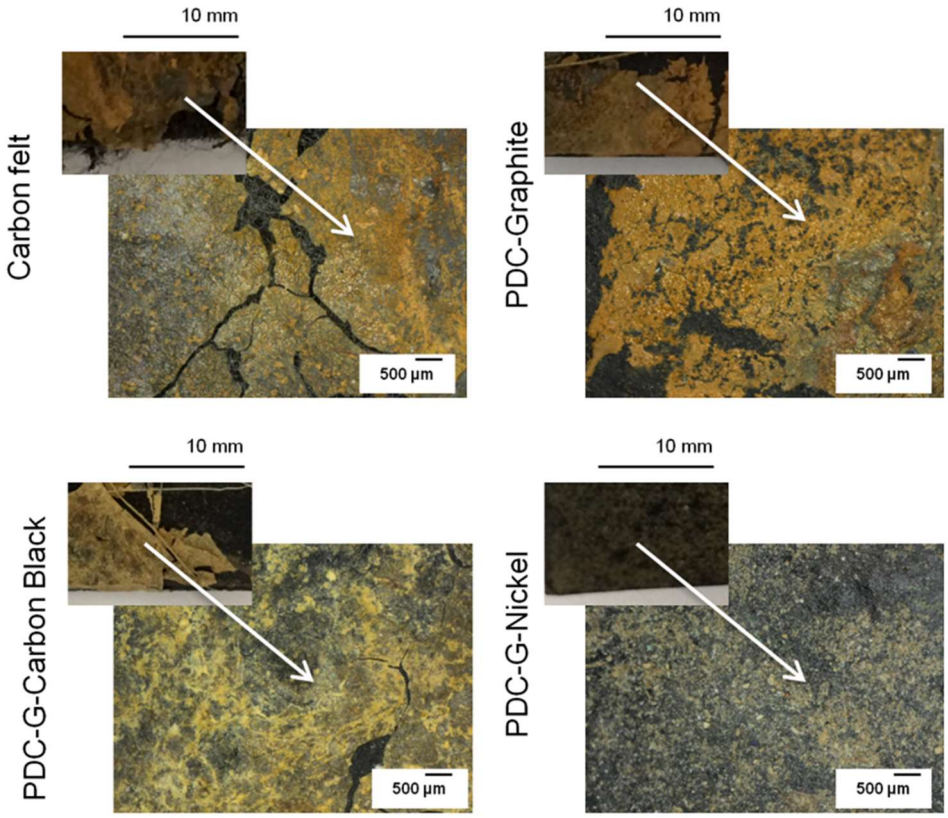

Figure 52. Digital images of biofilm on carbon felt and PDC-based anodes after 45 days of MFC performance. Adapted from [149].

A distinctive biofilm formation was observed in the images of each material. Especially for the Ni-containing one, that shows a poor biofilm formation and presented a lower power performance compared to the other PDC-based materials and carbon felt. From the SEM images (Fig. A.3.4), it was further confirmed that the meso-macroporous structure of the PDC-anode materials provided an available surface for bacterial growth, superior to the carbon felt structure. Dense colonization was also observed and distributed on cracks. Furthermore, short, rod-shaped bacteria attached could also be visualized.

5.2 Sandwiched SiOC-carbon-based Composite Anode Materials

5.2.1 Surface and Electrical Characterization

SiOC-based composite anode materials were produced by tape casting technique with dimensions varying from 10 × 10 mm to 30 × 30 mm. The materials were further pyrolyzed under nitrogen and argon environment at temperatures of 1000 to 1500 °C. The composite structure was developed in order to improve electron transport, prevent carbon felt corrosion and adjustment in porosity; through the combination of carbon felt and layers of polymer-derived ceramics (PDC) in a sandwiched structure (Figure 53). Additionally, the developed structure should also facilitate the wire connection of the electrode in the setup through the flexible carbon felt part.

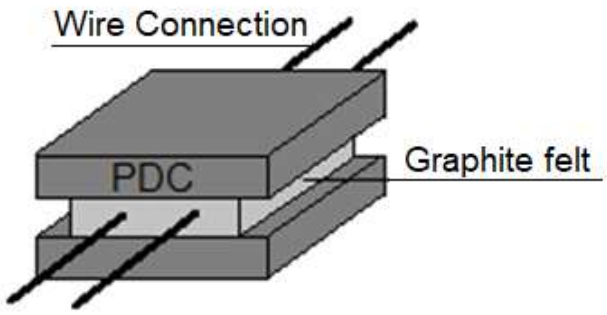

Figure 53. Schematic representation of the composite sandwich structure.

The resulting morphology of the composite layers composed of PDC and carbon felt was investigated by SEM and the micrographs of the pyrolyzed materials are shown in Figure 54 and Figure 55.

Comparing the morphology of the PDC layers in Figure 54a, b and Figure 54d, e, quite similar porous structures are observed with irregular shaped pores. Though, when analyzing the structure of the materials pyrolyzed at 1500 °C (Figure 54c and Figure 5f), a rearrangement in porosity is distinguishable for both atmospheres. Under nitrogen, the formation of whiskers of Si_3N_4 is presented, as a result of the reactive nitrogen atmosphere when the pyrolysis is carried out above 1400 °C [199]. In case of argon, mainly the SiC formation without whisker formation is observed as is expected. The rearrangement in porosity also led to a decrease in mechanical stability, perceived when the materials were manually handled.

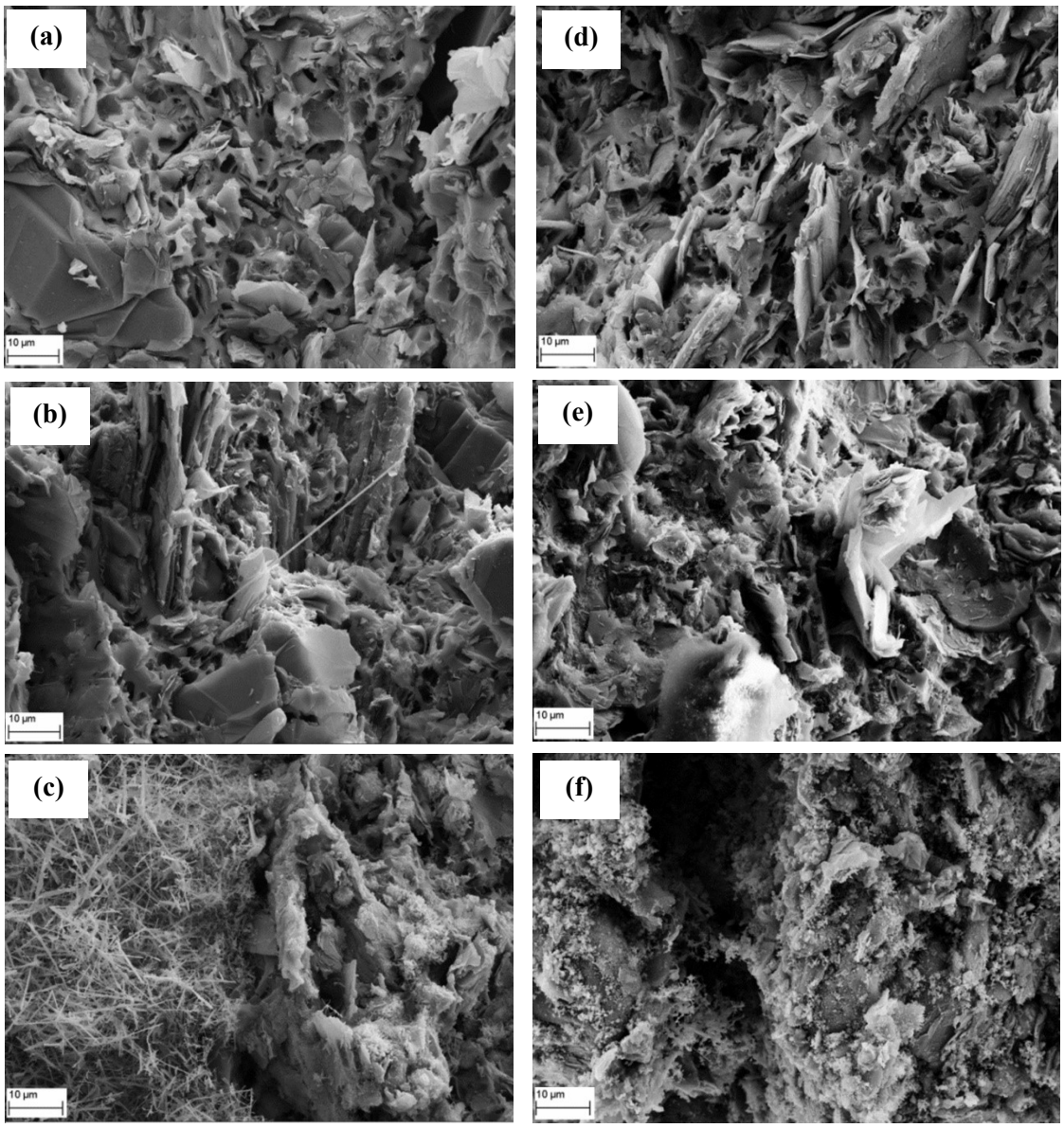

Figure 54. Morphology of the samples 42PS-31G-1000, 42PS-31G-1300, and 42PS-31G-1500 pyrolyzed under nitrogen (a, b, c) and argon (d, e, f) respectively (scale bar 10 µm).

With regard to the pyrolyzed carbon felt layers shown is Figure 55, no significant change of the carbon fiber structure was observed for pyrolysis temperatures of 1000 and 1300 °C. However, applying pyrolysis temperatures of 1500 °C, led to some defects/deterioration of the fibers for CF-1500-N2 (Figure 55c), while CF-1500-Ar (Figure 55f) presented some crystalline formations in the fibers structure.

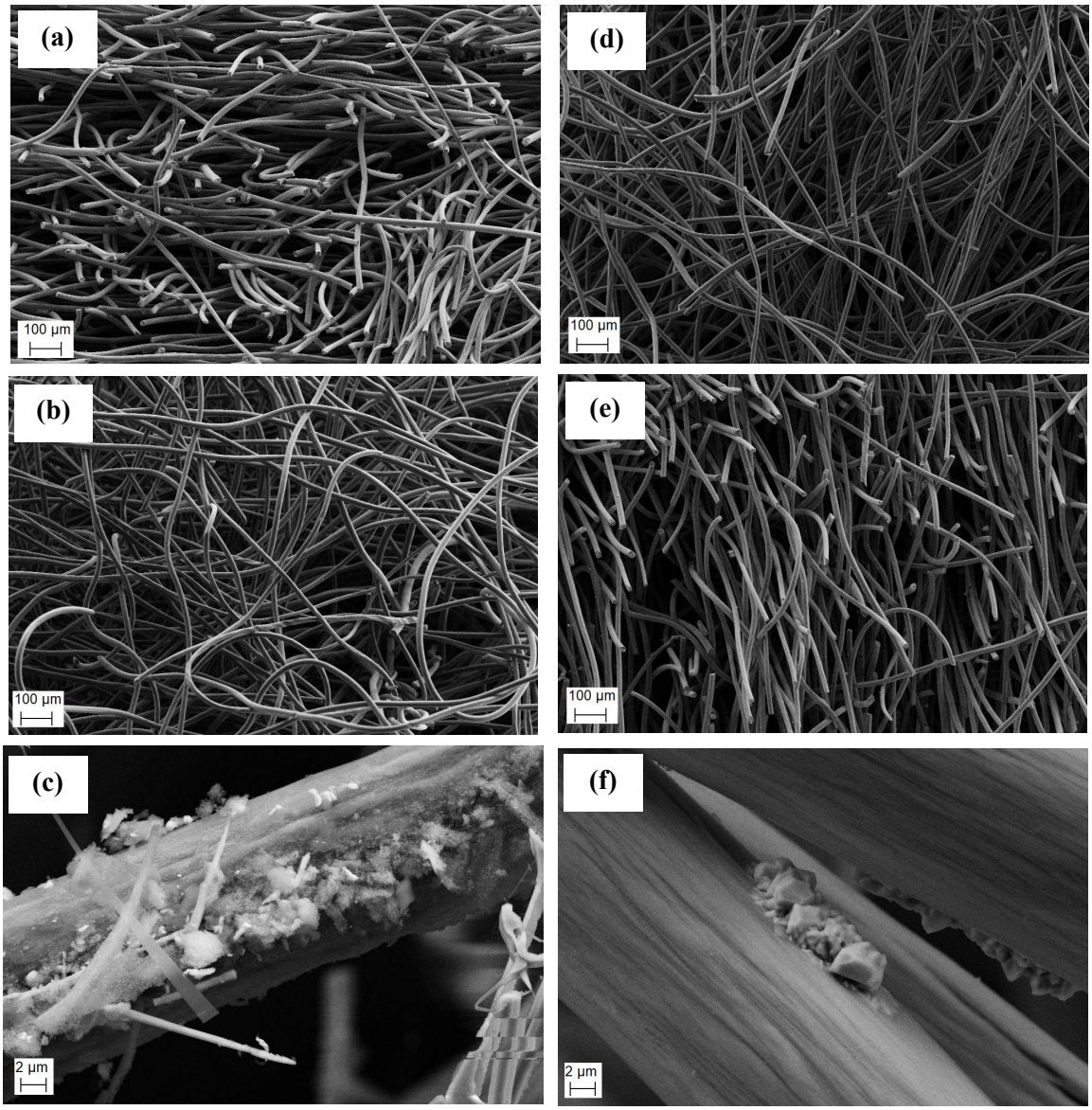

Figure 55. Morphology of the samples CF-1000, CF-1300, and CF-1500 pyrolyzed under nitrogen (a, b, c) and argon (d, e, f), respectively. Scale bar a,b,d, e: 100 µm and c, f: 2 µm.

To further investigate the phase transformation depending on pyrolysis conditions and the formations on the carbon felt fibers, the pyrolyzed carbon felt samples were analyzed by XRD technique. The XRD patterns are shown in Figure 56. According to literature, the diffraction peaks located at 26.4° and 43.5° correspond to the (002) and (100) planes of carbon and the broadening suggests the presence of an amorphous carbon phase and the graphitic nature of the felt [240, 241].

Comparing the pyrolysis temperatures applied, it can be seen that the positions of diffraction peaks of the pyrolyzed carbon felt hardly change but a decrease in diffraction intensity is observed for temperatures of 1500 °C. These results demonstrate that structural defects are introduced on the samples pyrolyzed at 1500 °C, more pronounced under a nitrogen atmosphere. The weakened intensity of diffraction peaks is attributed to the formation of small crystalline structures (under argon) and fibers (under nitrogen), also confirmed by the observation of the SEM images.

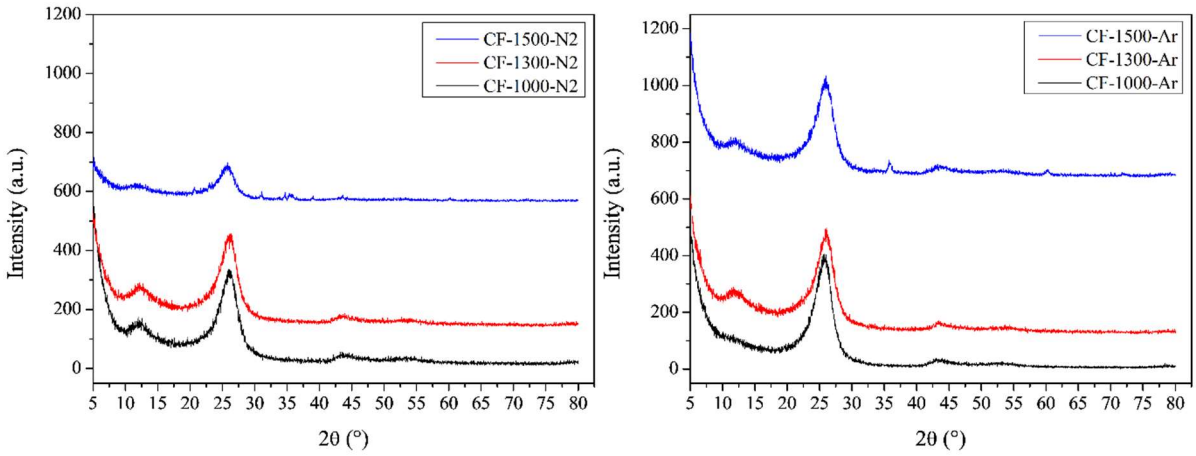

Figure 56. XRD spectrum of carbon felt materials pyrolyzed under nitrogen and argon atmosphere.

Regarding the characterization of porosity related to the PDC layers, nitrogen adsorption/desorption isotherms were recorded and mercury intrusion porosimetry was applied. The obtained isotherms for the materials pyrolyzed under nitrogen and argon atmosphere are shown in Figure 57. The material 42PS-31G-1000-N2 presented an isotherm type IV according to the IUPAC classification, supporting the presence of mesopores, while for the remaining materials a typical type II isotherm, characterizing the macroporosity was observed [203].

SSAs ranging from 7 to 27 $m^2\ g^{-1}$ were characterized for the PDC layer (Table 6), with a decrease related to the increase of pyrolysis temperatures. The decrease is associated with the collapse of smaller pores and increased macroporosity [23].

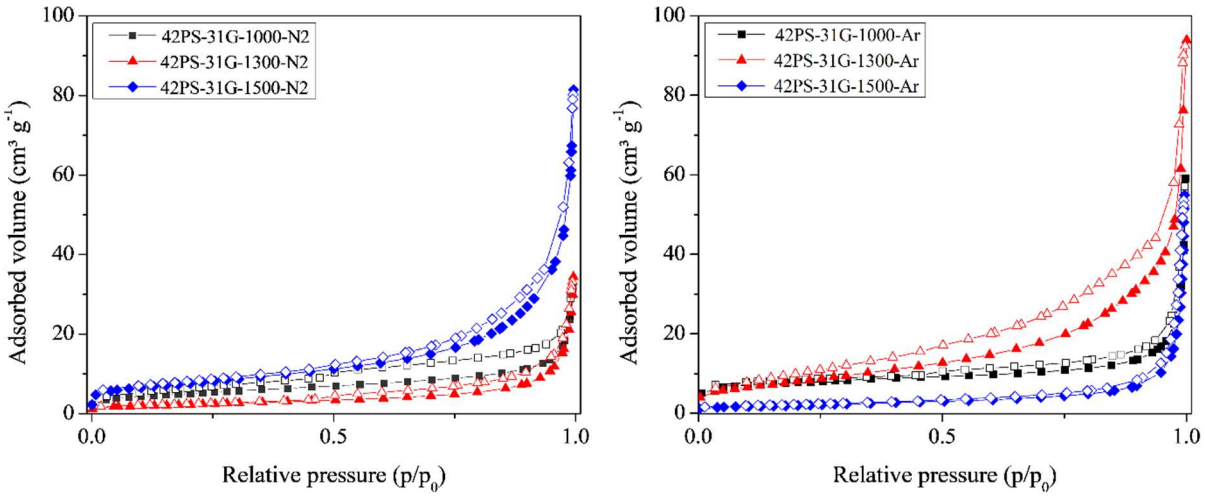

Figure 57. Nitrogen adsorption isotherms for the PDC layer pyrolyzed under nitrogen and argon.

The results obtained by mercury intrusion technique (Fig. A. 3.5) permit to classify the pores of the materials pyrolyzed under nitrogen and argon atmosphere as macroporous with an additional low amount of mesopores. Furthermore, the open porosity increases (Table 6) with the increase of the pyrolysis temperature, what is related to the pronounced macroporosity developed at higher temperatures and the rearrangement of the structure at temperatures above 1200 °C [206, 208]. Concerning MFC application, a range of macroporous is an advantage regarding the biofilm adhesion due to the bacteria sizes as well to avoid clogging.

The measured electrical conductivity values of the synthesized materials are shown in Figure 58, starting with pure carbon felt and PDC, followed by the composite structures. A carbon felt without any thermal treatment is also included in the values (s. Carbon felt*). For the pure carbon felt pyrolyzed at different temperatures, the values range from 0.3 to 0.9 S cm^{-1}. In addition, an increase in electrical conductivity up to 1300 °C and a decrease for the samples pyrolyzed at 1500 °C for both atmospheres can be perceived. The decrease in electrical conductivity can be related to a degradation of the carbon fibers with temperature that can alter the material properties [242].

For the PDC layers, values range from 0.01 to 0.2 S cm^{-1}. Again, the electrical conductivity of the PDC layers likewise increases with the increase of the pyrolysis temperature. The increase of conductivity in the PDC layer can be related to the percolation of an excess of carbon and the change of the structure (sp^3/sp^2) [243].

Table 6. SSA and open porosity of the PDC-layers pyrolyzed under nitrogen and argon.

PDC layer	SSA (m^2/g)	Open porosity (%)
42PS-31G-1000-N2	6.60	28.24
42PS-31G-1300-N2	7.69	29.73
42PS-31G-1500-N2	25.27	59.09
42PS-31G-1000-Ar	27.11	31.31
42PS-31G-1300-Ar	20.66	43.74
42PS-31G-1500-Ar	7.04	63.79

Furthermore, the formation of the insulator Si_3N_4 due to the reactive nitrogen atmosphere at higher temperatures, explains the decrease in conductivity for 42PS-31G-1500-N2. On the other hand, the formation of SiC, which has semiconductor property, leads to an increase in electron conductivity for the samples 42PS-31G-1500-Ar.

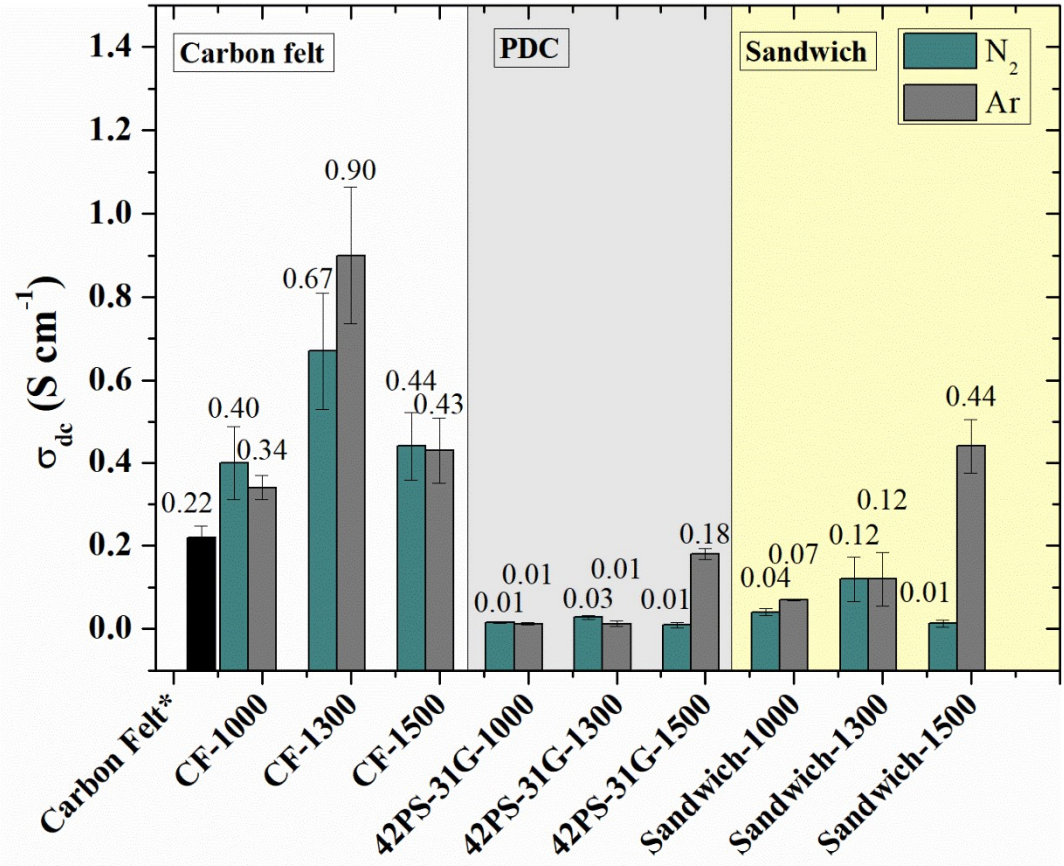

Figure 58. Electrical conductivity values of the single carbon felt, and PDC, composite materials pyrolyzed under nitrogen and argon.

From the values, it is possible to conclude that the electrical conductivity of carbon felt is higher than the electrical conductivity of polymer-derived ceramics, even when the carbon felt is not pyrolyzed (~ 0.22 S cm^{-1}), what was already expected due to the semiconductor behavior of PDCs at this range of temperature.

The electrical conductivity of the sandwich composite materials range from 0.01 to 0.13 S cm^{-1}, meaning intermediate electrical conductivity values compared to the values of PDC and carbon felt. In general, the electrical conductivity of the sandwich samples increases with the increase of the pyrolysis temperature and the values vary with the change of pyrolysis atmosphere.

5.2.2 MFC Performance and Wastewater Treatment

In order to study the MFC performance of the developed structures, four MFC setups (described in Topic 3.4.1.2) were initiated and evaluated over a period of 45 days in the Civil Engineering Department at IIT Kharagpur. The anode materials considered for this experiment were the non-heat treated carbon felt (MFC-1), pure carbon felt and PDC materials pyrolyzed under argon at 1300 ºC (MFC-2 and MFC-3) and the sandwich structure (MFC-4) pyrolyzed under argon at 1300 °C. These pyrolysis conditions were chosen according to the characterized properties, considering electrical conductivity, SSA and appropriate mechanical stability. Even though, the material Sandwich-1500-Ar showed higher electrical conductivity, the mechanical stability was not sufficient.

After 10 days of the initial start-up of the MFCs, a stable performance in terms of electrical output, as well as organic matter removal, was observed. The average operating voltage (OV) and open circuit voltage (OCV) of 166 ± 4 mV and 622 ± 5 mV were achieved under steady-state operating condition for MFC-4 (Composite-1300-Ar as anode), which were comparably higher than the values obtained for MFC-2 (109 ± 3 mV and 578 ± 6 mV), MFC-3 (125 ± 2 mV and 579 ± 11 mV) and control MFC-1 (79 ± 3 mV and 540 ± 9 mV).

The polarization data is shown in Figure 59. The maximum current density (733 mA m^{-2}) and the maximum power density (194 mW m^{-2}) was observed for the developed composite structure (MFC-4) and show a three-fold increase in terms of current and power density compared to commercial carbon felt (MFC-1; 304 mA m^{-2}, 67 mW m^{-2}), respectively. Superior coulombic efficiency of 40% than carbon felt (22%) was achieved and a COD removal efficiency of about 87% was demonstrated for the composite structure (Figure 60).

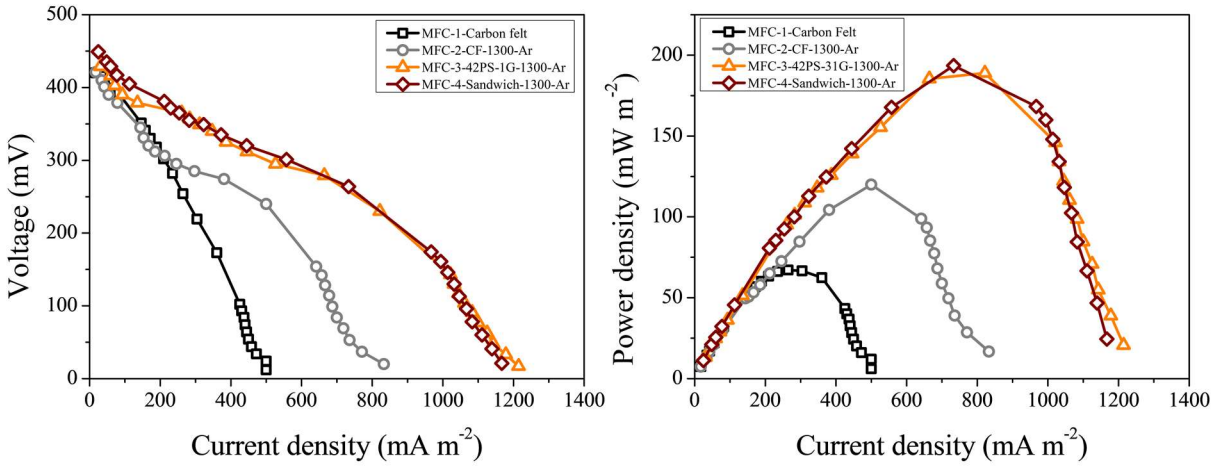

Figure 59. Current-voltage (IV) curves and polarization curves of the MFCs, normalized to the projected anode areas.

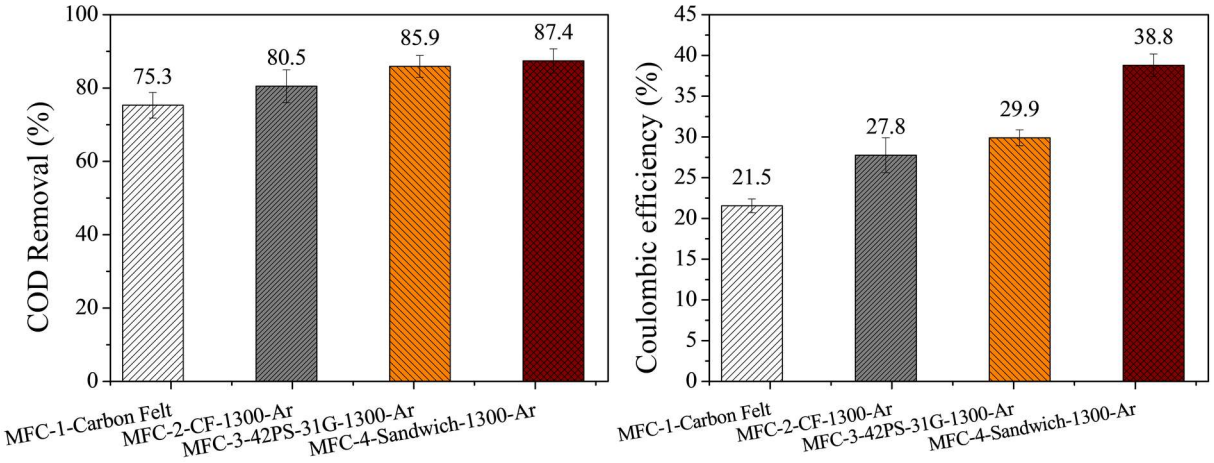

Figure 60. COD removal rate and coulombic efficiency of the MFCs.

The improved performance compared to the commercial carbon felt, reveals the potential of the synthesized SiOC-carbon-based composite anode material in MFCs. Even though the power density results shown similar maximum power density compared to MFC-3, the COD removal and CE results confirms the prospective of the sandwich structure. The results can be attributed to the adjustment in porosity and a hydrophilic PDC surface (contact angle measurements, Figure A.3.6) exposed as well as the gain of the combination of best quality of the graphite felt and PDC components.

5.3 The Impact of SiOC-based Porous Anode Materials Properties on Current Generation in BES

Silicon oxycarbide (SiOC)-based anode materials with distinct surface properties were synthesized. The study started with the approach of varying pyrolysis conditions in terms of temperatures (500 and 1000 °C) to adjust porosity and surface characteristics. The materials are denoted as E1: PDC-500, E2: PDC-1000 and E3: PDC-CB-1000. Its composition is described in Topic 3.1.1, Table 1. Properties such as specific surface area (SSA), roughness, and hydrophobicity/hydrophilicity were characterized and are presented in Figure 61. The characterization method used for roughness determination is described in Appendix A.3.

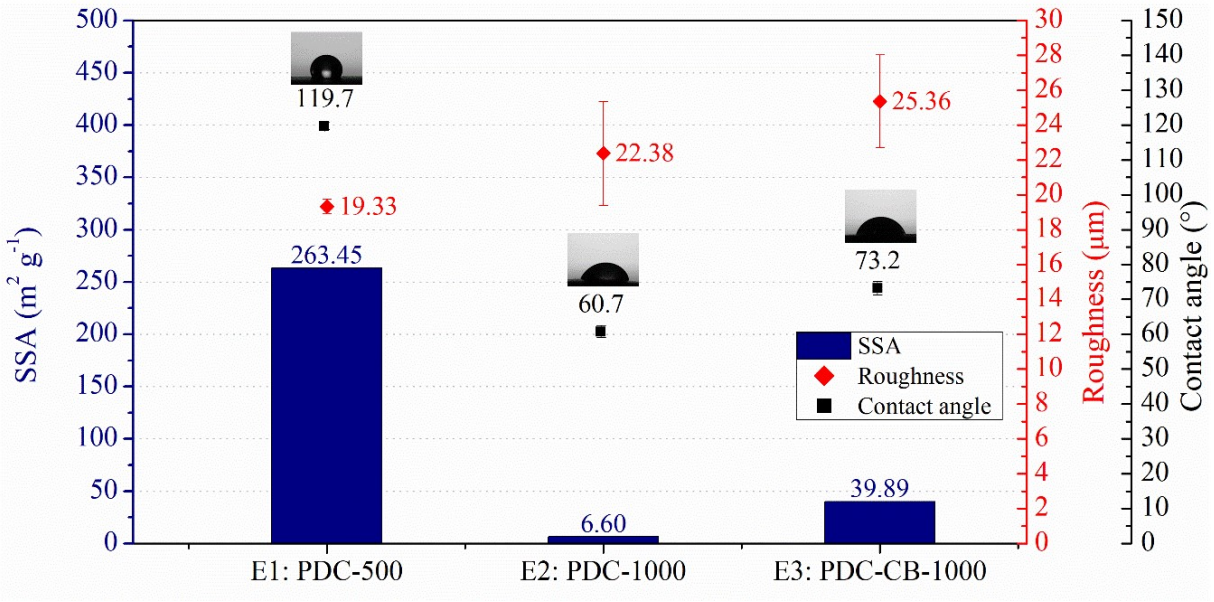

Figure 61. SSA (blue columns), roughness (red markers) and contact angle (black markers) of the SiOC-based anodes.

Anode materials with SSAs ranging from 6.60 to 263. 45 $m^2 g^{-1}$, contact angles varying from 60 to 119° and surface roughness (Ra) of 19 to 25 µm were observed. The electrical conductivity values range from 0.04 to 0.18 S cm^{-1}. The developed materials were tested (three independent replicates) as working electrodes in a three-electrode setup (described at topic 3.4.3 and performed by Dr. Jose Rodrigo Quejigo).

According to the bioelectrochemical characterization (Figure 62), the current densities increased over time and range between 3 to 5 A m^{-2} for the last batch cycle, i.e. after 30 days. The performance follows the order E3 > E2 > E1. To correlate bioelectrochemical data with electrode surface properties, as an initial observation the hydrophilicity plays a major role since the hydrophobic material showed the lowest performance. However, when materials in the same range of hydrophilicity are used (E2 and E3), the current production was influenced by the SSA, which the material with higher SSA (E3) presented the best result. The surface roughness appears to not strongly influence the results as also reported in the literature [244], where only structures above 20 µm presented a measurable effect.

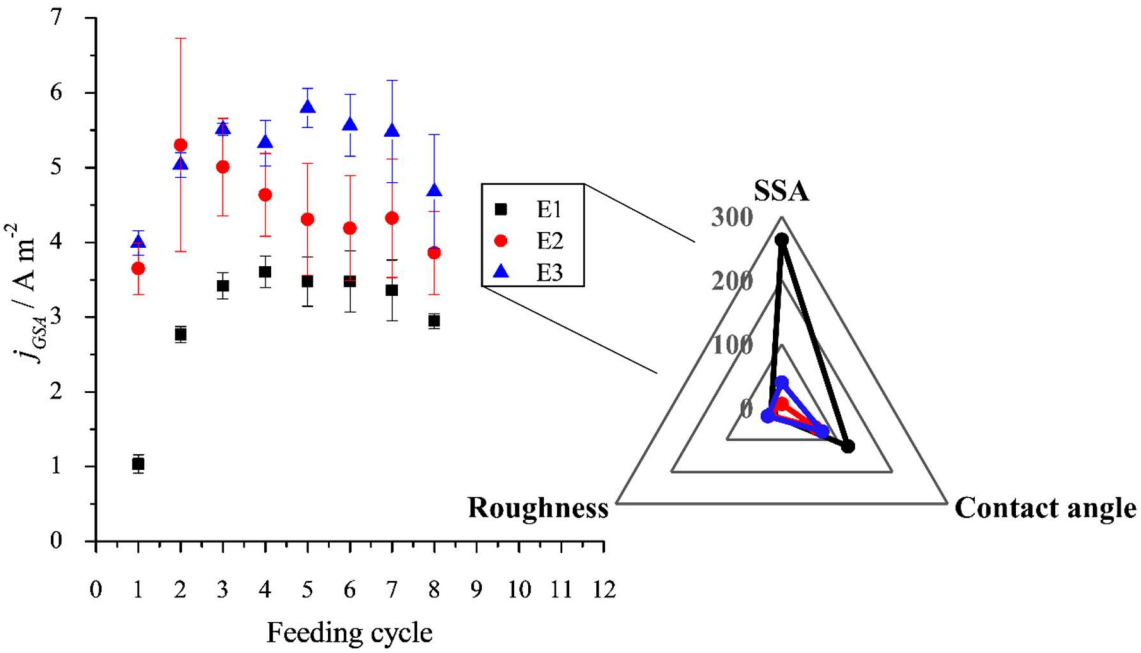

Figure 62. Maximum current density during chronoamperometry at 0.2 V vs. Ag/AgCl sat. KCl at eight different feeding cycles and radar plot describing the distinct surface properties of the three anode materials.

It can also be seen from the CV analysis shown in Figure 63 the biofilm evolution comparing the abiotic CV (before bacteria inoculation, black line) with the colored lines representing the progressive feeding cycles after microbial colonization. The capacitive behavior also follows the order E3 > E2 > E1, which can be additionally attributed to the particular electrical properties of the materials (E3: 0.18 S cm^{-1}, E2: 0.10 S cm^{-1} and E1: 0.04 S cm^{-1}). Thus, only for E1 the typical s-shaped CV curve for the turn-over conditions, as e.g. reported by Fricke et al. [245] was observed.

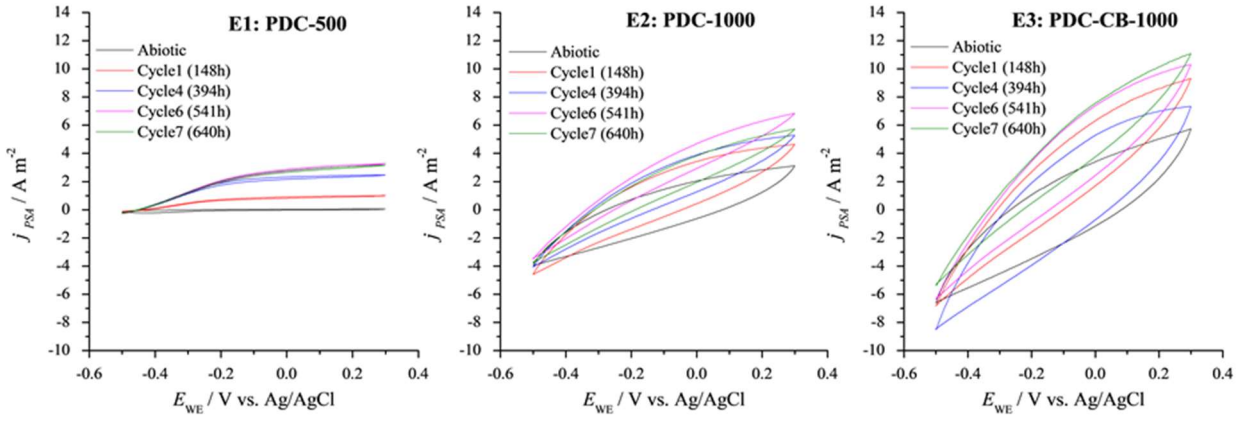

Figure 63. Cyclic Voltammetry on anodes at different feeding cycles (scan rate: 1 mV s^{-1}).

Regarding the biofilm, a uniform and dense reddish colored biofilm was formed in all surfaces characterized by optical images (Figure A. 3. 7) and SEM analysis, in the UFZ and University of Bremen, respectively. The reddish color supports the dominance of *Geobacter* species in the biofilms nonetheless microbial community analysis is still being carried out to further confirmation. Biofilm layers of 20-30 µm thickness could be observed during SEM analysis (Figure 64).

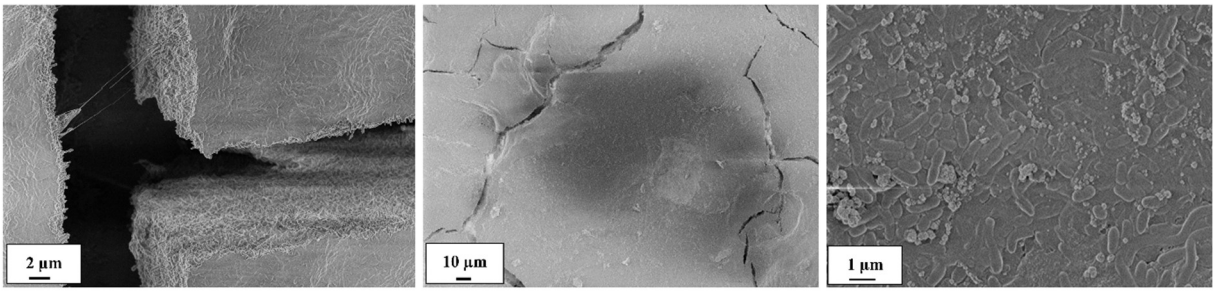

Figure 64. SEM images of the biofilm developed in E2.

The distinct bioelectrochemical performance reveals the material influence on anodic electroactive microbial biofilm and current generation, therefore highlighting the potential of adjusting surface properties in SiOC-based electrode materials to improve performance in BES.

Chapter VI. Polymer-derived Co/Ni–SiOC(N) Ceramic Electrocatalysts for Oxygen Reduction Reaction in Fuel Cells

This chapter contains the results and discussion of characterized physical properties concerning the Co/Ni-SiOC(N) electrocatalyst materials described in Chapter III (topic 3.1.2). Properties regarding structural and electrical characteristics are considered as well as chemical composition. ORR studies of the catalysts in alkaline, neutral and acid media are discussed. Furthermore, the ORR activity of the PDC-Co–N catalyst is highlighted and its MFC performance is also included. Parts of the following chapter have been published in Catalysis Science & Technology, 9 (2019) 854-866 (DOI: 10.1039/C8CY02207K) [148]. This chapter is also supplemented with added unpublished results.

6.1 Physical Characterization of SiOC(N)-based Electrocatalysts

Figure 65 summarizes the SEM micrographs (50 000× magnification) of the different SiOC materials tested in this work. Ball-milling is used to grind the ceramic material in order to reduce the particle size of the material and the SEM results show that ball-milling for 4 h at 350 rpm refined the SiOC ceramic material into powder with particle sizes smaller than 20 μm (see Figure 65a). The doping of the materials with Ni, Co and N has no visible effect on the structure of the SiOC powder (see Figure 65b–f) as expected.

Nitrogen adsorption–desorption measurements were performed in order to characterize the porosity and BET SSA of the PDC-based materials (Figure 66). According to the IUPAC classification, all the materials reveal type IV isotherms with a hysteresis loop close in shape to a type H3, indicating the presence of mesopores (pore diameter 2–50 nm) [203]. The type H3 loop is often linked with plate-like particles or slit-shaped pores [159, 246], which was also supported by the SEM images (Figure 65). The presence of mesopores enhances mass transport and access of active sites and is thus essential for the ORR performance.

The size distribution of mesopores obtained by the Barrett–Joyner–Halenda (BJH) method is shown in Figure 66b. Table 7 summarizes the pore characteristics of the PDC materials. The materials exhibit a broad pore size distribution (Figure 66b) and an increase in pore volume and pore size (Table 7) for the N-doped catalysts compared to the pristine materials. The SSA values for the pristine materials are in the range of 6–8 $m^2\ g^{-1}$ and are attributed to the rather high pyrolysis temperature of 1000 °C, at which the collapse of

micropores occurs during the polymer-to-ceramic conversion [23]. A slight increase in SSA is observed for the Co-containing material.

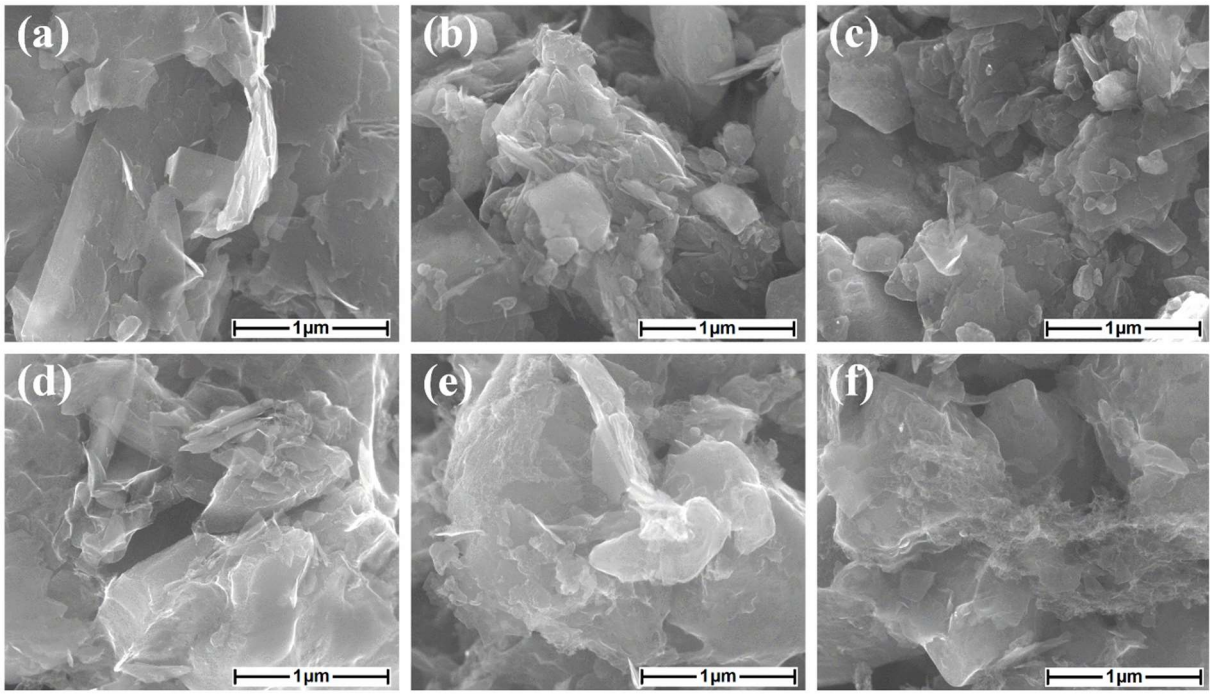

Figure 65. SEM images (50 000× magnification, scale bar: 1 µm) of (a) PDC, (b) PDC-Ni, (c) PDC-Co, (d) PDC–N, (e) PDC-Ni–N, and (f) PDC-Co–N catalyst materials on the glassy carbon electrode. Adapted from [148].

The SSA increases significantly for the N-doped materials and could offer more adsorption and reactive sites, influencing the enhancement of electrocatalytic activity.

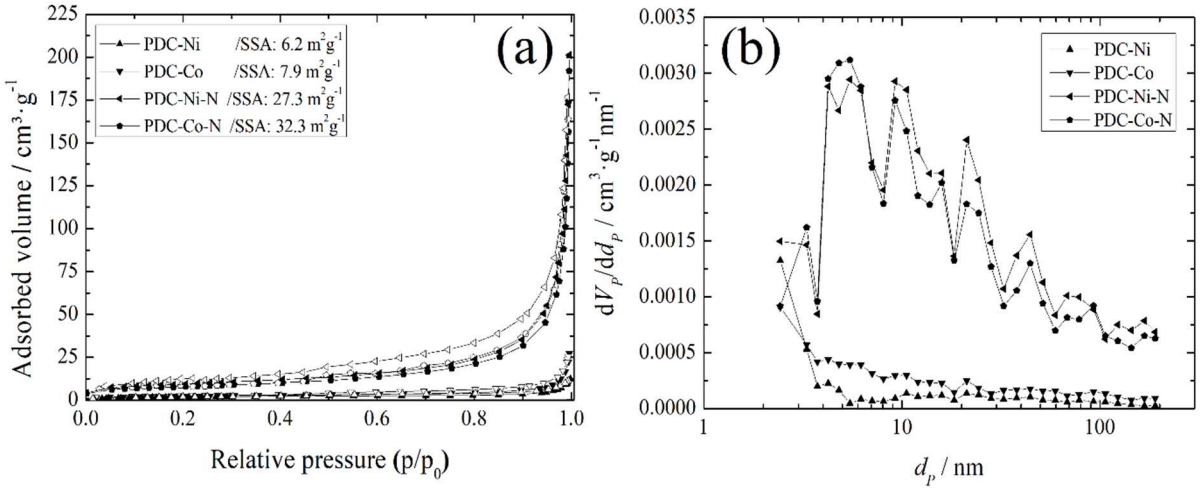

Figure 66. Nitrogen adsorption–desorption isotherms, respective specific surface areas (a), and Barrett–Joyner–Halenda (BJH) pore size distribution plot (b) of the PDC-Ni, PDC-Co, PDC-Ni–N and PDC-Co–N materials. Adapted from [148].

Table 7. Pore characteristics and electrical conductivities of the PDC-based electrocatalysts.

Catalyst material	BET SSA ($m^2 g^{-1}$)	Pore volume ($cm^3 g^{-1}$)	Average pore size (nm)	σ ($S cm^{-1}$)
PDC	6.6	3.1×10^{-2}	18.8	0.039
PDC-Ni	6.2	1.4×10^{-2}	9.2	0.063
PDC-Co	7.9	2.9×10^{-2}	14.5	0.085
PDC-N	9.1	8.0×10^{-2}	35.2	0.030
PDC-Ni-N	32.3	0.21	25.7	0.030
PDC-Co-N	27.3	0.18	26.2	0.031

Figure 67 shows the XRD patterns of the studied Ni/Co-containing pristine and N-doped PDC electrocatalyst materials. After pyrolysis at 1000 °C, polysiloxane derived ceramics are normally amorphous SiOC [18]. The diffraction patterns of all the materials reflect similar main peaks. The identified peaks at (2θ) 22.6°, 30.1°, 39.7°, 44.6°, 46.2°, 57.4°, 62.5°, 66.2°, 72.2°, 75.5°, 76.7°, and 85.6° are attributed to the filler molybdenum disilicide (PDF 041-0612) and the peaks at 26.5°, 42.4°, 44.6°, 54.6°, 77.5°, and 83.7° to carbon (graphite 2H, PDF 01-089-7213) with preserved crystalline phases after pyrolysis. Furthermore, the peaks at 2θ, 39.7°, 41.8°, 45.6°, and 85.5° and those at 44.6°, 51.4°, and 75.8° refer to a small amount of metallic Ni (PDF 01-089-7129) and Co (PDF 01-089-4307), respectively. In addition, the peaks at 39.7° and 72.1° evidence the initial crystallization of silicon nitride Si_3N_4 (PDF 00-005-0659) and those at 45.6° of cobalt silicide CoSi, as a product of the reaction between Co particles and the SiOC matrix (PDF 03-065-3296).

The TEM images of the Ni or Co-containing materials are shown in the insets of Figure 67. The Ni and Co metallic particles could be observed and present different sizes varying from 7 to 40 nm for Ni and from 2 to 14 nm for Co. For the N-doped materials, smaller particles were visualised with mean values of about 5 nm.

The electrical conductivity values of the PDC-based materials measured at room temperature are additionally shown in Table 7. The values vary from 0.03 to 0.09 S cm^{-1} suggesting a semiconductor behaviour [18]. A decrease in conductivity is found for the N-doped materials and can be correlated with the increased pore size and increased porosity which tends to lower the electrical conductivity in accordance with previous observations [247].

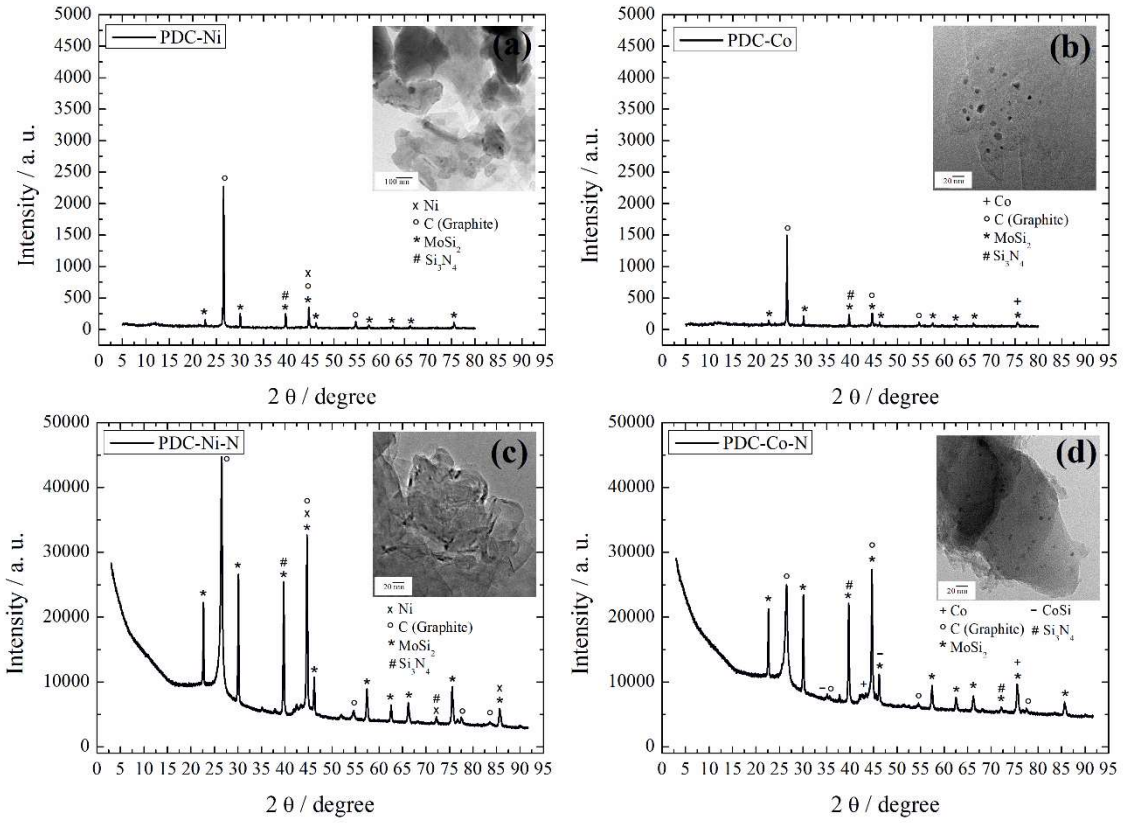

Figure 67. XRD patterns of the PDC-Ni (a), PDC-Co (b), PDC-Ni–N (c) and PDC-Co–N (d) materials and their respective TEM images (insets). Adapted from [148].

Figure 68 presents the XPS survey spectra of the studied materials. In all cases, the XPS peaks of O1s, C1s, Si2s, and Si2p corresponding to O, C and Si can be observed, as expected for SiOC-based materials [248]. The detection of nitrogen (N1s) further confirmed the successful N-doping of the PDC-based catalysts. However, the intensity of the XPS peaks for Co and Ni (Figure 68c–f) is so low that these are rather difficult to distinguish in the XPS wide scan spectra. This is a relatively common phenomenon and has been previously observed in studies on carbon nanomaterial based ORR catalysts with low Co loading [249-251].

In the present work, the content of transition metals (Co or Ni) resulting from the thermal decomposition of cobalt$_{(II)}$ and nickel$_{(II)}$ chloride was calculated to be less than 3 wt% in the PDC matrix. The contents of different elements in the catalyst materials calculated from the high-resolution XPS spectra and SEM–EDX data are presented in Table A.4.1. According to the SEM–EDX data, the chemical composition of the ceramic catalysts does not significantly vary, presenting $ca.$ 7 at% Si, 20 at% O and 68 at% C as a result of the polysiloxane conversion into ceramics and an additional amount of the carbon source used. The nitrogen content ($ca.$ 2 at%) present on the pristine materials corresponds to the residual amount of the pore-forming

agent azodicarboxamide, due to incomplete decomposition after heat treatment at 1000 °C (data not shown). Furthermore, the increase in the nitrogen content to $ca.$ 6 at% was observed for all the N-doped materials, confirming successful doping using DCDA. Regarding Co/Ni, a content of $ca.$ 0.3 at% was observed for all the transition metal-containing catalyst materials (see Table Table A.4.1).

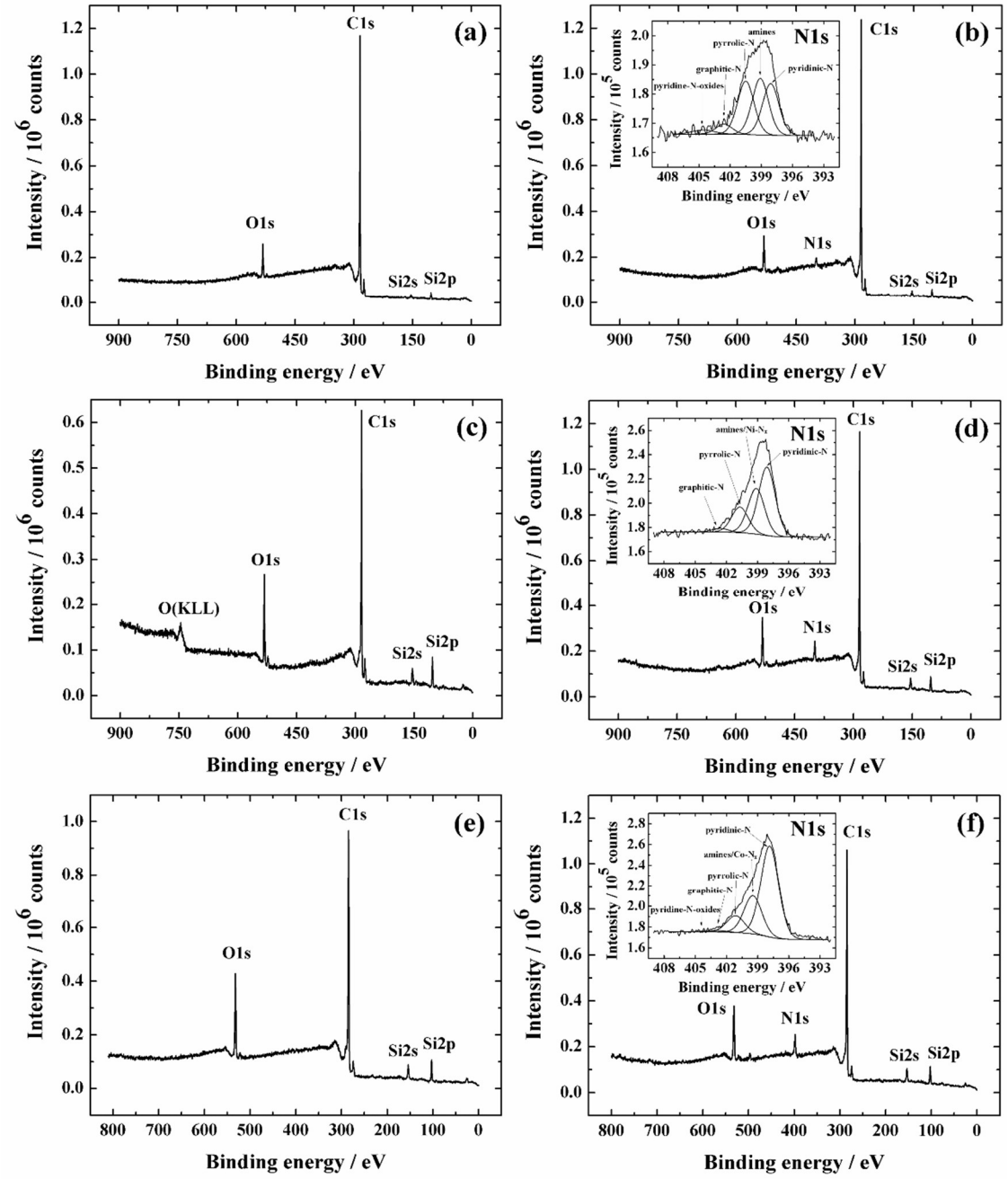

Figure 68. XPS survey spectra of (a) PDC, (b) PDC–N, (c) PDC-Ni, (d) PDC-Ni–N, (e) PDC-Co, and (f) PDC-Co–N catalyst materials on the glassy carbon electrode. The insets in b, d, and f show the high-resolution XPS spectra in the N1s region. Adapted from [148].

The C1s, O1s and Si2p representative core-level XPS spectra of the PDC-Co and PDC-Co–N materials are also presented in Figure A.4.1. The main C-signal identified in C1s can be attributed to the free carbon (284 eV) [248]. Low intensity C-signals from 286 to 289 eV correspond to carbon oxygenated groups or C–N and those at 283 eV to C–Si bonds [248, 252]. The O1s spectra reveal a broad peak with a peak energy of about 533 eV indicating the presence of Si–O bonds and a low intensity peak at 536 eV typical of C–O bonds [253]. The Si2p spectra exhibit signals from 102 to 103 eV, corresponding to Si–O–C bonds and the Si–O bond, respectively [254]. It is possible that these signals also mask the Si–C and Si–N signals, due to the high % of SiOC and SiO_2 in the Si2p spectra. The core-level XPS spectra collected in the Co2p region for PDC-Co and PDC-Co–N catalysts are shown in Figure 69.

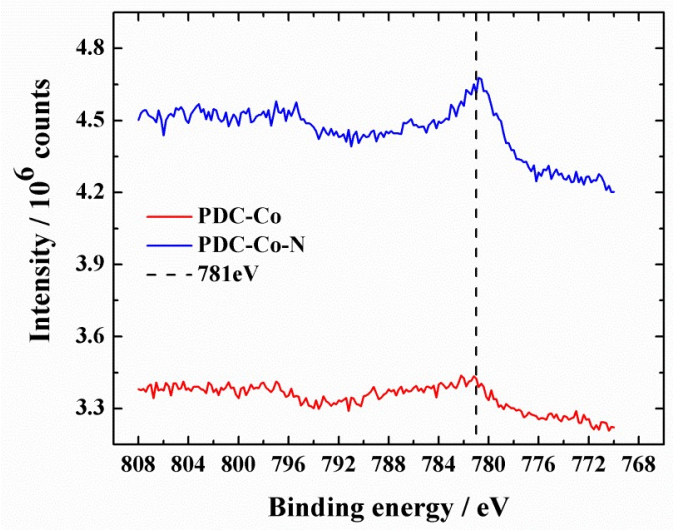

Figure 69. XPS high resolution spectra in the Co2p region for PDC-Co and PDC-Co-N catalyst material on the glassy carbon electrode. Adapted from [148].

The clear difference between these two XPS spectra is the considerably higher amount of Co photoelectrons recorded at *ca.* 781 eV in the case of PDC-Co–N compared to PDC-Co. According to the literature [251, 255-258], the corresponding peak at *ca.* 781–782 eV conforms to Co–N_x, which indicates that a considerable amount of Co could be coordinated to nitrogen in the case of PDC-Co–N compared to the material that has not been pyrolyzed in the presence of the nitrogen source (PDC-Co). The deconvoluted N1s XPS spectra of the nitrogen-doped catalysts are presented in the insets of Figure 68b, d and f and the relative content (%) of different nitrogen species is given in Table 8.

Table 8. Relative content (%) of different nitrogen species determined for the N-functionalized catalyst materials from deconvoluted N1s XPS peaks shown in Figure 68b, d and f.

Catalyst material	Pyridinic-N	Amines / Me-N_x	Pyrrolic-N	Graphitic-N	Pyridine-N-oxide
PDC-N	29	32	30	6	3
PDC-Ni-N	48	32	18	3	-
PDC-Co-N	61	26	11	1	1

In the case of the PDC–N material, the content of pyridinic-N, amines and pyrrolic-N is very similar (around 30%). The N1s peak of amines could also correspond to the nitrile groups because of the possible disappearance of amine groups during high-temperature heat-treatment [259]. Likewise, the N1s peaks of pyridinic-N could also be assigned to N–Si bonds [260, 261]. In the case of both transition metal (Co and Ni) and nitrogen co-doped catalysts, the suppression of the pyridine-N-oxide peak has also been noticed in our previous work with carbon aerogel-based catalysts [259]. In the comparison of PDC-Ni–N with the PDC–N material, the relative decrease in pyrrolic-N and increase in pyridinic-N are pronounced. A very similar tendency has been observed for pyrolyzed N-doped carbon and nickel nitride composite materials and this could correspond to the conversion of the nitrogen species among each other during pyrolysis [262].

PDC-Co–N is the catalyst with the highest N content (7 at%) studied in the present work (see Table A.4.1). According to the literature, Co could act as a booster for increasing nitrogen content by creating more nitrogen moieties that are electrocatalytically active towards the ORR from initial nitrogen sources [263]. This could be the explanation for the highest total content of N, lower content of pyrrolic-N and higher content of pyridinic-N in PDC-Co–N compared to those in the PDC-Ni–N catalyst (see Table 8). In addition to pyridinic-N, Co–N_x contributes at a very similar binding energy value of $ca.$ 399 eV to the N1s XPS spectra [258]. Also, the presence of Co–Nx species [258, 264] is most likely detected in the Co2p region (see Figure 69).

6.2 ORR Studies in Alkaline, Neutral and Acid Media

6.2.1 Cyclic Voltammetry and Linear Sweep Voltammetry Studies

The electrochemical behaviour of the catalyst materials was studied in three different aqueous solutions: i) 0.1 M KOH (pH = 13), ii) 0.1 M PBS containing 0.1 M $NaClO_4$ (pH = 7), and iii) 0.5 M H_2SO_4 (pH = 0.3). Figure 70 presents the cyclic voltammograms (CVs) of the bare and nanomaterial-coated GC electrodes recorded in Ar-saturated electrolyte solutions. The electrodes were cycled until a reproducible CV was obtained. The baseline current density in the studied potential range for all the catalyst material coated GC electrodes is significantly higher compared to that of the bare GC electrode. This is a typical CV behaviour of electrodes coated with high-area electrochemically active carbon nanomaterials (e.g. graphene, multi-walled carbon nanotubes) due to the higher electrical double layer capacitance compared to the polished GC electrode [265, 266].

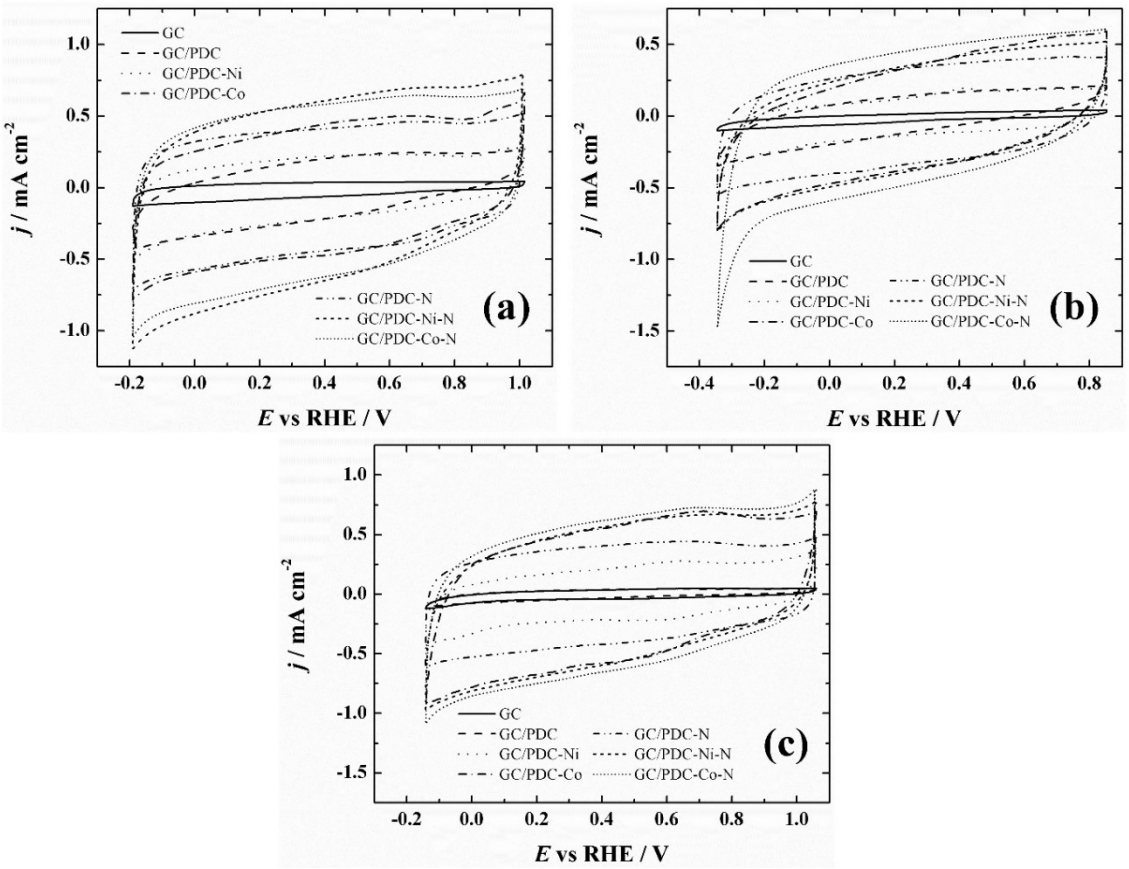

Figure 70. CV of bare glassy carbon and GC electrodes coated with different PDC-based catalyst materials recorded in Ar-saturated 0.1 M KOH (pH = 13) (a), 0.1 M PBS containing 0.1 M $NaClO_4$ (pH = 7) (b) and 0.5 M H_2SO_4 (pH = 0.3) (c) at ν = 100 mV s^{-1}. Adapted from [148].

In Figure 71 the linear sweep voltammograms (LSVs) of the studied electrodes in O_2-saturated solutions are presented in an analogous layout to CVs in Figure 70. In all the solutions, the catalyst coated electrodes show higher ORR current density compared to the GC electrode. According to the ORR peak potential, the most positive value is always obtained in the case of GC/PDC-Co–N, which indicates that this catalyst is superior for the ORR compared to the other studied materials. However, the baseline current density seems to add a significant contribution to the LSV current density values. Therefore, the ORR was also studied under hydrodynamic conditions using the RDE method for more accurate evaluation of the ORR performance of the different catalyst materials.

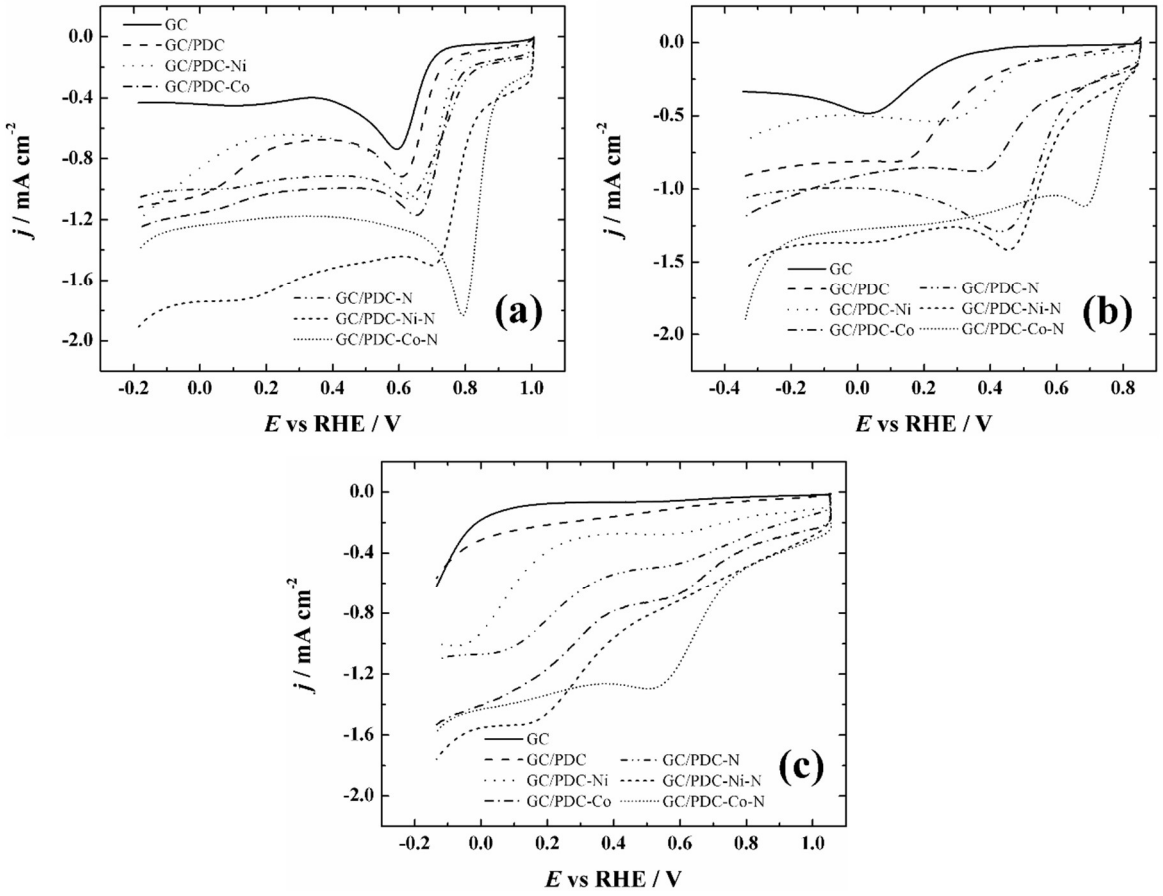

Figure 71. LSV for oxygen reduction on bare glassy carbon and GC electrodes coated with different PDC-based catalyst materials recorded in O_2-saturated 0.1 M KOH (pH = 13) (a), 0.1 M PBS containing 0.1 M $NaClO_4$ (pH = 7) (b) and 0.5 M H_2SO_4 (pH = 0.3) (c) at ν = 100 mV s^{-1}. Adapted from [148].

6.2.2 RDE Studies of ORR and Koutecky–Levich Analysis

In Figure 72a, c and e, the baseline-corrected RDE voltammetry curves of the catalysts recorded at 1900 rpm in solutions with different pH values are presented. Also, the RDE polarisation curves obtained with the commercial Pt/C catalyst are included for comparison purposes. Various parameters describing the ORR performance of the studied catalysts (e.g. onset potential (E_{onset}), half-wave potential ($E_{1/2}$), and O_2 reduction current density at −0.2 V) derived from the RDE polarisation curves are presented in Table 9. According to these results, the commercial Pt/C catalyst is superior compared to all of the other non-noble metal catalysts studied in the present work.

In the case of the PDC-based catalyst materials, the order of the ORR activity of the catalysts is similar to that observed in the case of LSVs in all the studied media. The pristine PDC material exhibited the lowest ORR performance, which could be explained by the absence of nitrogen and/or transition metal centres (see Figure 68a) responsible for high ORR activity. After the catalysts were pyrolyzed in the presence of DCDA, the E_{onset} and O_2 reduction current density have remarkably improved due to the presence of nitrogen-containing groups (see Figure 68b). A similar tendency has been observed in our previous works with different carbon-based catalysts before and after pyrolysis with DCDA [151, 267, 268].

Besides, the porous structure composed of mesopores, the increased pore sizes and specific surface areas of the N-doped materials suggest improved accessibility of active sites and lower mass-transfer limitations. Both the metal-doped catalyst coated electrodes (GC/PDC-Ni and GC/PDC-Co) exhibit higher ORR activity compared to the GC/PDC electrode indicating the positive impact of transition metals on the ORR performance, in line with previous observations [269].

Specifically, GC/PDC-Co shows better ORR activity than GC/PDC-Ni. A similar result has been obtained by Abdelwahab et al. in the case of Ni and Co-doped carbon aerogels [270]. After pyrolysis of PDC-Ni in the presence of DCDA, the resulting catalyst material coated electrode (GC/PDC-Ni–N) shows a rather similar ORR activity to that of GC/PDC-N, but much lower ORR performance than the Co-containing catalyst.

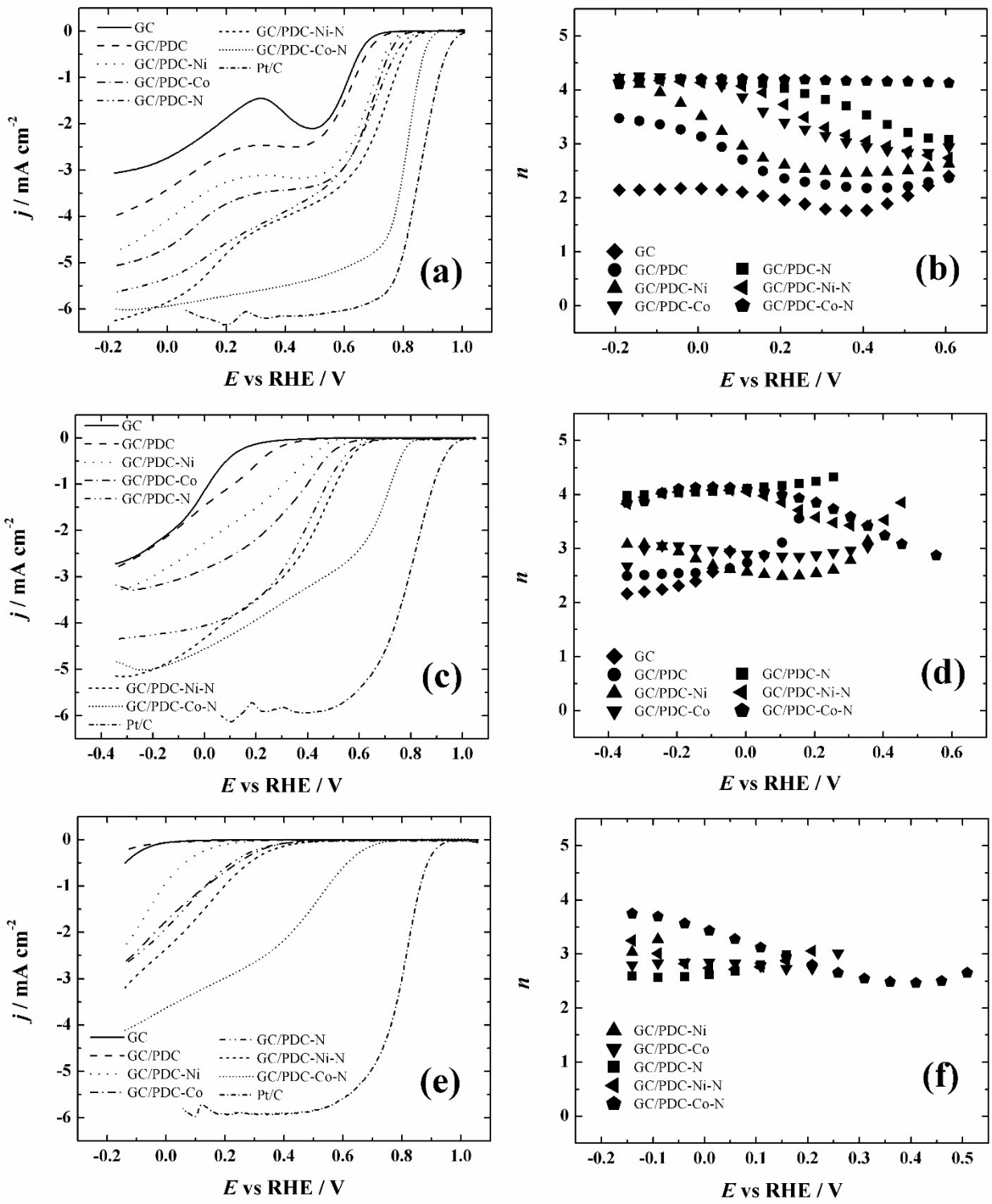

Figure 72. RDE voltammetry curves for O_2 reduction on different electrodes in O_2-saturated 0.1 M KOH (pH = 13) (a), 0.1 M PBS containing 0.1 M $NaClO_4$ (pH = 7) (c) and 0.5 M H_2SO_4 (pH = 0.3) (e) (ω: 1900 rpm, ν = 10 mV s^{-1}). The potential dependence of the number of electrons transferred per O_2 molecule calculated using the Koutecky–Levich equation from the corresponding RDE data (b, d and f). Adapted from [148].

From that, we can assume that Ni does not form as many metal coordinated centres (Me–N_x) during high-temperature pyrolysis or the ORR activity of Ni–N_x is lower than that of its Co–N_x counterpart. This is also supported by the study of Liu et al. [271], where the influence of different metal dopants was explored in nitrogen-doped carbon xerogels: the E_{onset} value in 0.5 M H_2SO_4 solution for the Ni-doped and metal-free catalyst coated electrodes was very similar, while the Co-doped catalyst exhibited significantly higher electrocatalytic activity towards the ORR [271].

Regarding the different media studied, a superior ORR performance was observed in alkaline media for all the materials. This result can be attributed to the change in active sites and their interaction with oxygen. This influence on ORR performance is supported by Wan et al., where the effect of pH was studied on nitrogen-doped ordered mesoporous carbon [272].

Table 9. The ORR onset potential (E_{onset}), half-wave potential ($E_{1/2}$) and O_2 reduction current density at −0.2 V (j) for different electrodes in O_2-saturated aqueous solutions. The data is derived from the RDE polarisation curves presented in Figures 72a, c, e. Experiments were carried out using ω = 1900 rpm and ν = 10 mV s^{-1}. All the potentials are given with respect to the RHE.

Catalyst	E_{onset}[a] (V)	$E_{1/2}$[a] (V)	j[a] (mA cm^{-2})	E_{onset}[b] (V)	E_{onset}[c] (V)
GC	0.70	0.58	−3.1	0.22	−0.03
GC/PDC	0.73	0.56	−4.0	0.34	−0.05
GC/PDC-Ni	0.78	0.63	−4.7	0.48	0.20
GC/PDC-Co	0.80	0.64	−5.1	0.55	0.38
GC/PDC-N	0.83	0.61	−5.7	0.62	0.38
GC/PDC-Ni-N	0.85	0.62	−6.3	0.63	0.43
GC/PDC-Co-N	0.90	0.80	−6.0	0.79	0.71
Pt/C	0.99	0.86	-	0.97	0.93

[a]Data obtained in 0.1 M KOH (pH = 13) (see Fig. 72a)
[b]Data obtained in 0.1 M PBS containing 0.1 M $NaClO_4$ (pH = 7) (see Fig. 72c)
[c]Data obtained in 0.5 M H_2SO_4 (pH = 0.3) (see Fig. 72e)

For the evaluation of the number of electrons (n) transferred per O_2 molecule from the RDE data of the different electrodes studied in the present work, the Koutecky–Levich (K–L) equation was used [273],

$$\frac{1}{j} = \frac{1}{j_k} + \frac{1}{j_d} = -\frac{1}{nFkc_{O_2}^b} - \frac{1}{0.62nFD_{O_2}^{2/3}v^{-1/6}c_{O_2}^b\omega^{1/2}}$$

where j is the measured ORR current density at a specific potential E, j_k and j_d are the kinetic and diffusion-limited current densities, respectively, k is the electrochemical rate constant for O_2 reduction at a specific potential E, F is the Faraday constant (96 485 C mol^{-1}), ω is the rotation rate of the electrode, $c_{O_2}^b$ is the concentration of oxygen in the bulk ($c_{O_2}^b$ in 0.5 M H_2SO_4 is 1.13×10^{-6} mol cm^{-3},88 while in 0.1 M PBS and 0.1 M KOH it is 1.2×10^{-6} mol cm^{-3}) [274], D_{O_2} is the diffusion coefficient of oxygen (D_{O_2} in 0.1 M KOH is 1.9×10^{-5} cm^2 s^{-1} [274], while in 0.5 M H_2SO_4 and 0.1 M PBS it is 1.8×10^{-5} cm^2 s^{-1}) [275, 276], and v is the kinematic viscosity of the electrolyte solution (0.01 cm^2 s^{-1}) [277].

The calculated n values for the different electrodes are presented in Figure 72b, d and f. All the electrodes exhibit a n value between 2 and 4 in the studied potential ranges. As stated earlier, the 2-electron reduction corresponds to peroxide formation and the 4-electron process to the reduction of O_2 to water. Compared to the other electrodes, GC/PDC-Co–N indicates the highest n value in all the studied solutions. This is an expected result because the cobalt ion coordinated to nitrogen in the form of Co–N_x plays an important role in the 4-electron reduction of O_2 [264]. According to this, GC/PDC-Co–N is the most attractive ORR electrocatalyst for use at the low-temperature fuel cell and MFC cathode.

6.3 The ORR Activity of the PDC-Co–N Catalyst

Since the PDC-Co–N electrode exhibited the highest ORR activity compared to the other studied materials, the following discussion is therefore mainly focused on the PDC-Co–N catalyst. Figure 73 depicts the RDE polarization curves for O_2 reduction in 0.1 M KOH at different rotation rates and the K–L plots derived from the corresponding RDE data on the GC/PDC-Co–N electrode. The diffusion-controlled O_2 reduction is achieved at relatively low overpotentials as the K–L lines already coincide from $ca.$ 0.4 V and the extrapolated K–L lines pass the origin of the axis. For comparison, the RDE polarization curves at different electrode rotation rates and the corresponding K–L plots for GC/PDC-Co–N obtained in neutral and acidic media are shown in Figure A.4.2. The current plateau of diffusion controlled O_2 reduction

is not as well developed as that in alkaline medium (Figure 73a) and therefore, the extrapolated K–L lines pass the origin at relatively higher overpotentials compared to the RDE results obtained in 0.1 M KOH.

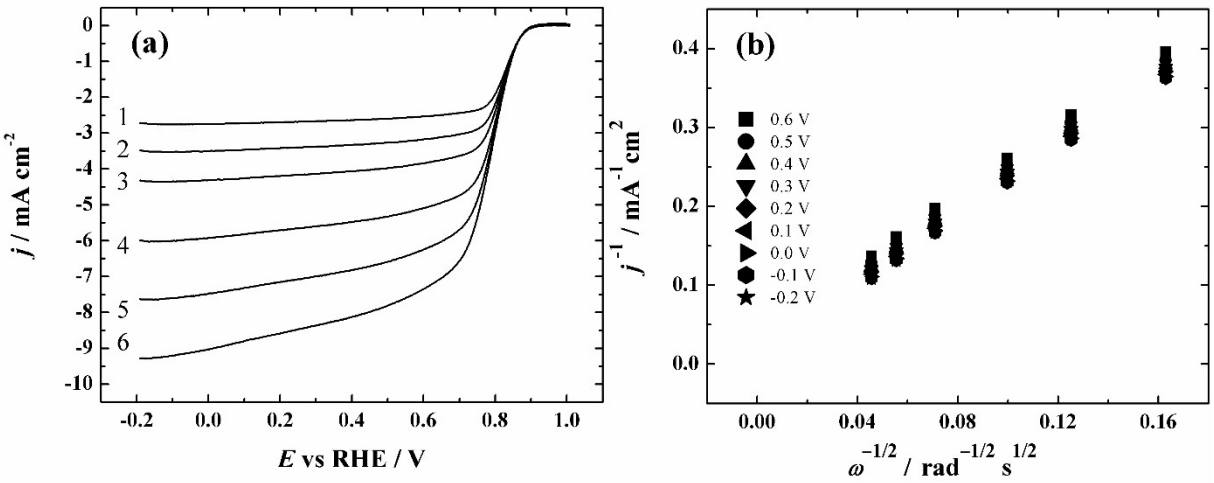

Figure 73. RDE voltammetry curves for oxygen reduction on the GC/PDC-Co–N electrode in O_2-saturated 0.1 M KOH (pH = 13) (ω: 1-360; 2-610; 3-960; 4-1900; 5-3100; 6-4600 rpm, ν = 10 mV s^{-1}) (a), Koutecky–Levich plots for O_2 reduction in 0.1 M KOH derived from the RDE data shown in Figure 73a (b). Adapted from [148].

For potential application of PDC-Co–N as a fuel cell cathode catalyst, the long-term stability should be assessed. For this reason, an accelerated aging test was performed by cycling the catalyst coated electrode for 10 000 cycles between 0.6 and 1.0 V $vs.$ RHE. The testing was carried out with GC/PDC-Co–N and Pt/C electrodes in alkaline solution and the obtained RDE polarization curves are presented in Figure 74. The $E_{1/2}$ is about 34 mV more negative and the current density at 0.05 V has decreased by 6% after the potential cycling in the case of the Pt/C electrode. Meanwhile, the corresponding values for GC/PDC-Co–N are 4 mV and less than 1%, respectively. These differences imply that the durability of the PDC-Co–N catalyst in an alkaline environment is remarkably higher compared to that of Pt/C.

There are a number of ORR studies describing Co-containing carbon based catalysts doped with nitrogen by pyrolysis. A comparison of the ORR performance with similar catalysts reported in the literature is presented in Table A.4.2. In the present work, an E_{onset} of 0.90 V and $E_{1/2}$ of 0.80 V were determined for GC/PDC-Co–N in 0.1 M KOH at 1900 rpm (see Table 9). For comparison, several more negative E_{onset} values have been reported for Co and nitrogen-containing catalysts in alkaline solution [251, 278], while very similar E_{onset} and $E_{1/2}$ values were obtained in the case of Co-containing nitrogen-doped carbon aerogels in our earlier work

[259]. Also, higher E_{onset} values can be found in some studies [151, 256, 258, 264], and the highest value has been obtained in the case of cobalt nanocrystals grown using nitrogen-doped graphene nanoparticles (1.06 V) [279].

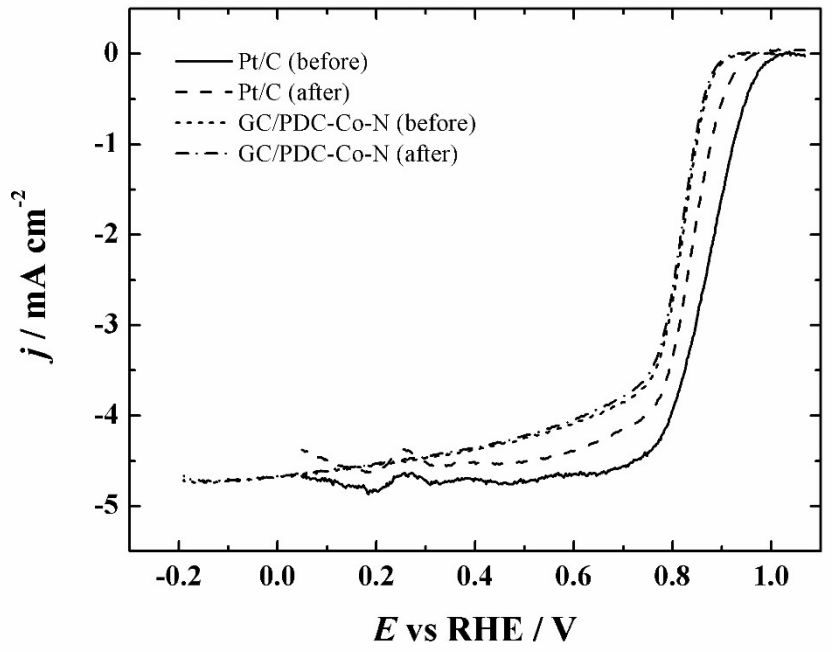

Figure 74. RDE voltammetry curves for oxygen reduction on GC/PDC-Co–N and Pt/C catalysts in O_2-saturated 0.1 M KOH recorded before and after 10 000 cycles between 0.6 and 1 V in Ar-saturated 0.1 M KOH (ω= 960 rpm, ν = 10 mV s^{-1}). Adapted from [148].

In neutral solutions, E_{onset} values of 0.59 V and 0.55 V (*vs.* RHE) have been reported for a NiCo-doped C–N nanocomposite in 0.5 M KNO_3 [280] and for a square-like nano cobalt oxide anchored on N-doped graphene catalyst in PBS (pH = 7) [281], respectively. The latter catalyst was also studied for application in MFCs [281]. In the present work, a considerably more positive value of 0.79 V (see Table 9 and Fig. 72c and A.4.2a) was obtained, which makes the PDC-Co–N catalyst also attractive for use under MFC conditions. In 0.5 M H_2SO_4, higher E_{onset} values than herein have been reported for materials pyrolyzed with DCDA [258, 282]. For example, Tang and Ng achieved a more positive E_{onset} value (0.90 V) for the Co- and N-codoped carbon catalyst prepared by pyrolysis of aniline and $Co(NO_3)_2$ for MFC studies [283]. Nevertheless, considering previous information, the PDC-Co–N catalyst is comparable to the most active ORR catalysts of its type.

Most of the electrocatalytic activity of the catalyst probably originates from the highly active Co–N_x species [251, 256, 258, 259, 264, 282]; their presence on PDC-Co–N was also supported by the XPS studies herein (see section 6.1). However, according to the XPS data, there is a considerably higher amount of N than Co in the PDC-Co–N catalyst (see Table A.4.1) and this refers to the presence of metal-free nitrogen functionalities. In works describing Co-containing carbon-based ORR catalysts modified via pyrolysis with DCDA or other N precursors, one of the most active nitrogen species towards the ORR is proposed to be pyridinic-N [258, 259, 263, 264, 281]. The relevance of having pyridinic-N moieties is attributed to its nitrogen bonding with two carbons on the edge plane that gives rise to a structure with localized lone electron pairs and improved electron-donating ability [284].

In the present study, the highest content of total nitrogen (see Table A.4.1) together with the highest relative content of pyridinic-N (see Table 8) was detected for PDC-Co–N amongst all the studied catalysts. In addition, the importance of pyridinic-N for the ORR has also been emphasized in studies regarding carbon-based Co- and N-codoped ORR catalysts for application in MFCs [191, 281, 283]. Besides, previous studies regarding Si-containing carbon materials have suggested that the presence of Si could improve the ORR activity, due to changes in the charge distribution and in the chemisorption mode of O_2 [285, 286]. Also, the contribution to the enhanced ORR performance by the high surface area, confirmed by N_2 adsorption and CV experiments (see section 6.2.1), of the catalyst material must be considered [256, 283].

Considering all these findings, the PDC-Co–N material seems to be an active ORR electrocatalyst and therefore attractive for fuel cell applications.

6.4 The MFC Performance of PDC-Co-N Catalyst

In order to study the MFC performance of the PDC-Co-N catalyst, MFC performance tests were carried out in the Civil Engineering Department of IIT Kharagpur. The materials considered for this experiment were plain carbon felt, carbon felt coated with PDC-Co-N and coated with Pt.

When a stable performance in terms of electrical output and organic matter removal, was reached the data were considered. The average operating voltage (OV) and open circuit voltage (OCV) of 146 ± 19 mV and 525 ± 33 mV were achieved under steady-state operating condition for the PDC-Co-N-Carbon felt, which were slightly higher than the values obtained for plain carbon felt (119 ± 10 mV and 522 ± 22 mV) and lower than the ones obtained with Pt (174 ± 12 mV and 559 ± 27 mV).

Regarding the polarization data shown in Figure 75, a maximum current density of 61 mA m^{-2} and maximum power density of 25 mW m^{-2} was observed for the PDC-Co-N catalyst material. The obtained performance was comparably higher compared to the carbon felt used as control (99 mA m^{-2}, 22 mW m^{-2}) and slightly inferior to Pt (105 mA m^{-2}, 29 mW m^{-2}). In terms of wastewater treatment, COD removal efficiency of about 89% was demonstrated for the PDC-Co-N catalyst, while 75% and 90% was achieved by carbon felt and Pt-carbon felt, respectively.

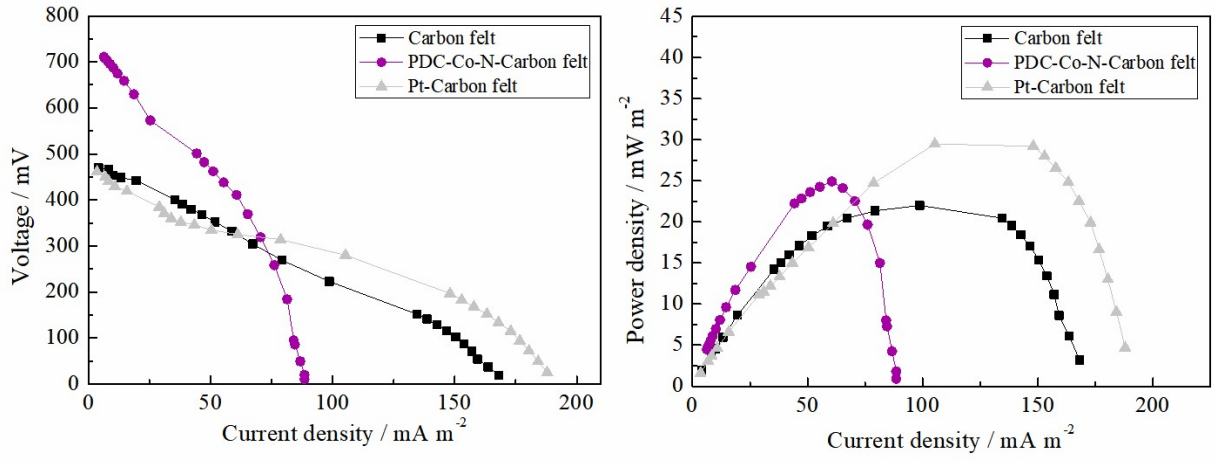

Figure 75. Polarization and power curves of the MFCs, normalized to the cathode areas.

The results presented confirm the applicability of PDC-Co-N catalyst as a novel catalyst material to be considered in MFC application especially considering the high price of Pt-based catalysts.

Chapter VII. Conclusion

7. Conclusion

7.1 SiOC-based electrode materials manufacturing and functional properties

SiOC-based electrodes were synthesized based on poly(silsesquioxanes) containing carbon- and metal-based conductive materials by the polymer-derived ceramics route. Tape casting was used in the manufacturing followed by pyrolysis at temperatures varying from 500 to 1500 °C, under argon and nitrogen atmosphere. The influence of pyrolysis temperature and incorporation of conductive materials on functional properties and electrical conductivity was assessed and discussed. Furthermore, this study provides the first investigation of biofilm development on SiOC-based ceramic surfaces with *Escherichia coli* and *Bacillus cereus*. The electrical conductivity of SiOC-materials increases by ~1 order of magnitude with change in pyrolysis temperature from 500 to 1500 °C. Electrical conductivity values ranging from 0.100 to 0.385 S cm^{-1} were achieved by the carbon- and metal-based materials used with values comparable to a usual used BES electrode material. The AC conductivity studies revealed hopping conduction mechanism and metal-like conduction due to the incorporation of distinct conductive phases. Acceptable chemical stability in medium conditions over 4 weeks was observed. The biofilm studies revealed adhesion in the first 2 h for most of the surfaces, with a decrease in adhesion and biofilm formation when metal-based materials (Co, Ni or Cu) were introduced. Furthermore, the tailorability of porosity from the micro–meso to meso–macro range and adjustment in hydrophilicity for these materials was also suggested to provide optimized interaction of the biofilm during the BES operation.

In addition, composite electrode materials were produced through the combination of carbon felt and layers of polymer-derived ceramics (PDC) in a sandwiched structure. The PDC layers were exposed in order to allow adjustment in porosity and surface characteristics and additionally, a decrease in corrosion of the graphite felt material. Moreover, the developed structure also intended to facilitate the wire connection of the electrode in the setup through the flexible carbon felt layer. Sandwich structures in the meso-macroporous range with SSAs from 6.60 to 27.11 $m^2 g^{-1}$ and hydrophilic surfaces were developed with electrical conductivity values (0.01 to 0.44 S cm^{-1}) intermediate to the PDC and carbon felt range.

Lastly, the flexibility in thickness and sizes, according to the bioreactor sizes, is additionally offered by the tape-casting technique used during the processing of the electrode materials.

7.2 BES performance using SiOC-based electrode materials

The SiOC-based electrodes prepared in this work, by the polymer-derived ceramics route, were applied in MFC technology for the first time. For the initial study, three materials were considered using poly(methyl silsesquioxane) and poly(methyl phenyl silsesquioxane) as precursors while incorporating carbonaceous fillers (graphite and carbon black) and metal precursor ($NiCl_2$). The developed electrodes were used as anodes and tested in MFC with aqueous cathode configuration using a low-cost clayware cylinder as the anodic chamber. The electrodes allowed bacterial attachment and showed a performance compared to a commercially available carbon felt, resulting in a two-fold increase in power density (211 and 111 mW m^{-2}, respectively). In terms of wastewater treatment efficiency, a chemical oxygen demand removal of about 85% was achieved. The highest performance, obtained by the PDC-G-Carbon Black, was also compared to previous studies in bio-electrochemical systems, confirming its applicability as novel anode material.

Furthermore, performance tests of the developed composite materials were carried out in a two-chamber MFC setup. The sandwich structures were used as anodes and its performance was compared to a commercial carbon felt, a pyrolyzed carbon felt and PDC material. Maximum power density of 194 mW m^{-2} was observed for the developed composite structure showing a three-fold increase compared to commercial carbon felt (67 mW m^{-2}). Coulombic efficiency of 40% was achieved and a COD removal efficiency about 87% was demonstrated. The improved performance of the PDC-based anodes was attributed to its porous structure, hydrophilic surface, and high electrical conductivity.

Besides, the impact of surface properties on performance was investigated in a bioelectrochemical system. For this study, tape-cast SiOC-based materials with distinct SSAs, surface characteristics and roughness were considered. The performance tests were evaluated in terms of current density progression normalized to the projected surface area of the electrodes and CV analysis. According to the results, the correlation of bioelectrochemical performance with studied electrode surface properties was that hydrophilicity plays a major role followed by SSA. Whereas roughness in the obtained range is most likely not critical.

7.3 SiOC(N)-based electrocatalyst materials

Co/Ni–SiOC-based pristine and nitrogen doped electrocatalysts were proposed as a new class of catalysts for the ORR. The ORR kinetics was investigated in acid, neutral and alkaline media using the RDE technique. XPS and SEM–EDX results confirmed the successful N-

doping of the PDC-based catalyst materials with DCDA. Both Co/Ni and nitrogen introduction to the PDC material exhibit positive effects on the ORR performance compared to the metal/nitrogen-free PDC-based materials. The Koutecky–Levich analysis yielded electron transfer numbers between 2 and 4, with the highest value for the PDC-Co–N catalyst. The results showed that PDC-Co–N catalyst possesses a superior electrocatalytic activity for the ORR compared to the other materials in all the studied media. The revealed performance is attributed to the higher amount of pyridinic-N and Co–Nx centers. According to the stability testing results, the ORR performance of the PDC-Co–N catalyst remains almost unchanged after 10 000 CV cycles and its durability is superior as compared to the commercial Pt/C.

Furthermore, the MFC performance of the most promising electrocatalyts (PDC-Co-N) was investigated in MFC with aqueous cathode configuration. Maximum power density of 25 mW m^{-2} was observed for the PDC-Co-N catalyst material, which was comparably higher to the carbon felt used as control (22 mW m^{-2}) though, inferior to Pt (29 mW m^{-2}).

To conclude, the studies and results presented in this thesis confirmed the applicability of the proposed SiOC-based porous materials as novel electrode as well as catalyst material to be considered in BES.

Chapter VIII. Outlook

8. Outlook

This study provides the first findings for SiOC-based ceramic materials to be considered in future material development as promising electrodes for MFC technology. Although the materials synthesized in this study already meet most of the required properties for appropriate performance, other ideas for further investigations and improvements are suggested.

In terms of porous structures and surface characteristics for anode materials, a meso-macroporous range is desired, which is a suitable pore size for accommodating bacteria, since their sizes are on the range of 0.2 to 750 µm, and hydrophilic surfaces are preferable for bacterial attachment. Macroporous structures, which can be prepared by a few methods such as partial sintering, replica method, sacrificial template methods, direct foaming method, and additive methods were not explored in this work. One interesting method which could be favorable to this application is the use of freeze casting method. The advantages of this method for MFC include the feasibility of producing macroporous structures with pore sizes ranging from 20 to 200 µm, with additionally high permeability (for substrate transport) and easy surface characteristics adjustment by functionalization and pyrolysis conditions.

Besides, the nitrogen doping studied only for the electrocatalyst materials could be extended to the anode material to further beneficial electron conductivity and biocompatibility enhancement. Likewise, the surface modification with functional groups was not addressed in this study. Positively charged functional groups at the anode surface can enable and influence the interaction between the negatively charged bacteria cell wall via electrostatic interactions, representing an interesting study direction to be considered.

In terms of structures developed, after the composite sandwich structure approach, experiments with infiltrated samples were initiated. The materials consisted of carbon felt pieces which were dipped into the starting mixture of polymer-derived ceramic. However, this structure presented many cracks and unsuitable attachment of the PDC coating after pyrolysis. Further adjustments related to the viscosity of the PDC mixture and the pyrolysis heating/cooling rates, can promote a better infiltration and minimization of cracks.

With regard to experimental methods and setups, biofilm studies for longer time and with electroactive microorganism (*e.g., Shewanella oneidensis* and *Geobacter*) could expand the understanding of biofilm development on SiOC-based ceramic surfaces related to BES. In the context of real size applications, the promising properties of SiOC-based ceramics such as

high mechanical and chemical stability, and low-cost precursor materials meet the challenges in upscaling the setups and may possibly be considered.

Finally, it should be kept in mind that MFCs are a complex system of parameters and some fundamental processes like the anodic electron transfer mechanism are still not understood completely. Therefore, an understanding of each processes in parallel is crucial.

Chapter IX. References

References

[1] B.E. Logan, K. Rabaey, Conversion of Wastes into Bioelectricity and Chemicals by Using Microbial Electrochemical Technologies, Science, 337 (2012) 686.

[2] A. Janicek, Y. Fan, H. Liu, Design of microbial fuel cells for practical application: a review and analysis of scale-up studies, Biofuels, 5 (2014) 79-92.

[3] V.B. Oliveira, M. Simoes, L.F. Melo, A.M.F.R. Pinto, Overview on the developments of microbial fuel cells, Biochemical Engineering Journal, 73 (2013) 53-64.

[4] K. Shimizu, L. Sepunaru, R.G. Compton, Innovative catalyst design for the oxygen reduction reaction for fuel cells, Chemical Science, 7 (2016) 3364-3369.

[5] A. ElMekawy, H.M. Hegab, X. Dominguez-Benetton, D. Pant, Internal resistance of microfluidic microbial fuel cell: Challenges and potential opportunities, Bioresource Technol, 142 (2013) 672-682.

[6] C. Santoro, C. Arbizzani, B. Erable, I. Ieropoulos, Microbial fuel cells: From fundamentals to applications. A review, J Power Sources, 356 (2017) 225-244.

[7] A. Mehdinia, E. Ziaei, A. Jabbari, Multi-walled carbon nanotube/SnO2 nanocomposite: a novel anode material for microbial fuel cells, Electrochim Acta, 130 (2014) 512-518.

[8] M.H. Zhou, M.L. Chi, J.M. Luo, H.H. He, T. Jin, An overview of electrode materials in microbial fuel cells, J Power Sources, 196 (2011) 4427-4435.

[9] H.T. Chou, H.J. Lee, C.Y. Lee, N.H. Tai, H.Y. Chang, Highly durable anodes of microbial fuel cells using a reduced graphene oxide/carbon nanotube-coated scaffold, Bioresource Technol, 169 (2014) 532-536.

[10] Y. Hindatu, M.S.M. Annuar, A.M. Gumel, Mini-review: Anode modification for improved performance of microbial fuel cell, Renewable and Sustainable Energy Reviews, 73 (2017) 236-248.

[11] H. Yuan, L. Deng, Y. Chen, Y. Yuan, MnO2/Polypyrrole/MnO2 multi-walled-nanotube-modified anode for high-performance microbial fuel cells, Electrochim Acta, 196 (2016) 280-285.

[12] R. Thorne, H. Hu, K. Schneider, P. Bombelli, A. Fisher, L.M. Peter, A. Dent, P.J. Cameron, Porous ceramic anode materials for photo-microbial fuel cells, Journal of Materials Chemistry, 21 (2011) 18055-18060.

[13] J. Winfield, I. Gajda, J. Greenman, I. Ieropoulos, A review into the use of ceramics in microbial fuel cells, Bioresource Technol, 215 (2016) 296-303.

[14] I.M. Jimenez, J. Greenman, I. Ieropoulos, Electricity and catholyte production from ceramic MFCs treating urine, Int J Hydrogen Energ, 42 (2017) 1791-1799.

[15] V. Yousefi, D. Mohebbi-Kalhori, A. Samimi, Ceramic-based microbial fuel cells (MFCs): A review, Int J Hydrogen Energ, 42 (2017) 1672-1690.

[16] D. Hidalgo, T. Tommasi, V. Cauda, S. Porro, A. Chiodoni, K. Bejtka, B. Ruggeri, Streamlining of commercial Berl saddles: A new material to improve the performance of microbial fuel cells, Energy, 71 (2014) 615-623.

[17] D. Massazza, R. Parra, J.P. Busalmen, H.E. Romeo, New ceramic electrodes allow reaching the target current density in bioelectrochemical systems, Energ Environ Sci, 8 (2015) 2707-2712.

[18] P. Colombo, G. Mera, R. Riedel, G.D. Soraru, Polymer-Derived Ceramics: 40 Years of Research and Innovation in Advanced Ceramics, J Am Ceram Soc, 93 (2010) 1805-1837.

[19] E. Ionescu, H.J. Kleebe, R. Riedel, Silicon-containing polymer-derived ceramic nanocomposites (PDC-NCs): preparative approaches and properties, Chem Soc Rev, 41 (2012) 5032-5052.

[20] T. Prenzel, M. Wilhelm, K. Rezwan, Pyrolyzed polysiloxane membranes with tailorable hydrophobicity, porosity and high specific surface area, Micropor Mesopor Mat, 169 (2013) 160-167.

[21] M.S. Kolathodi, L. David, M.A. Abass, G. Singh, Polysiloxane-functionalized graphene oxide paper: pyrolysis and performance as a Li-ion battery and supercapacitor electrode, Rsc Adv, 6 (2016) 74323-74331.

[22] P. Moni, M. Wilhelm, K. Rezwan, The influence of carbon nanotubes and graphene oxide sheets on the morphology, porosity, surface characteristics and thermal and electrical properties of polysiloxane derived ceramics, Rsc Adv, 7 (2017) 37559-37567.

[23] M. Wilhelm, M. Adam, M. Baumer, G. Grathwohl, Synthesis and properties of porous hybrid materials containing metallic nanoparticles, Adv Eng Mater, 10 (2008) 241-245.

[24] C. Harms, M. Adam, K.A. Soliman, M. Wilhelm, L.A. Kibler, T. Jacob, G. Grathwohl, New Electrocatalysts with Pyrolyzed Siloxane Matrix, Electrocatalysis-Us, 5 (2014) 301-309.

[25] A. Karakuscu, A. Ponzoni, P.R. Aravind, G. Sberveglieri, G.D. Soraru, Gas Sensing Behavior of Mesoporous SiOC Glasses, J Am Ceram Soc, 96 (2013) 2366-2369.

[26] V.S. Pradeep, D.G. Ayana, M. Graczyk-Zajac, G.D. Soraru, R. Riedel, High Rate Capability of SiOC Ceramic Aerogels with Tailored Porosity as Anode Materials for Li-ion Batteries, Electrochim Acta, 157 (2015) 41-45.

[27] B.E. Logan, K. Rabaey, Conversion of Wastes into Bioelectricity and Chemicals by Using Microbial Electrochemical Technologies, Science, 337 (2012) 686-690.

[28] B.E. Logan, Exoelectrogenic bacteria that power microbial fuel cells, Nat Rev Microbiol, 7 (2009) 375-381.

[29] X.X. Cao, X. Huang, P. Liang, K. Xiao, Y.J. Zhou, X.Y. Zhang, B.E. Logan, A New Method for Water Desalination Using Microbial Desalination Cells, Environ Sci Technol, 43 (2009) 7148-7152.

[30] C. Donovan, A. Dewan, D. Heo, H. Beyenal, Batteryless, Wireless Sensor Powered by a Sediment Microbial Fuel Cell, Environ Sci Technol, 42 (2008) 8591-8596.

[31] M.C. Potter, Electrical effects accompanying the decomposition of organic compounds, P R Soc Lond B-Conta, 84 (1911) 260-276.

[32] K. Lewis, Symposium on bioelectrochemistry of microorganisms. IV. Biochemical fuel cells, Bacteriological reviews, 30 (1966) 101-113.

[33] B.E. Logan, J.M. Regan, Microbial fuel cells--challenges and applications, Environ Sci Technol, 40 (2006) 5172-5180.

[34] K. Rabaey, W. Verstraete, Microbial fuel cells: novel biotechnology for energy generation, Trends Biotechnol, 23 (2005) 291-298.

[35] S.A. Cheng, H. Liu, B.E. Logan, Optimization of air cathode used in one-chamber microbial fuel cells., Abstr Pap Am Chem S, 228 (2004) U639-U639.

[36] A.S. Galushko, A.G. Ivanova, M.S. Masalovich, O.A. Zagrebelnyy, G.G. Panova, I.Y. Kruchinina, O.A. Shilova, An Overview of the Functional Ceramic and Composite Materials for Microbiological Fuel Cells, J Ceram Sci Technol, 8 (2017) 433-453.

[37] H. Rismani-Yazdi, S.M. Carver, A.D. Christy, I.H. Tuovinen, Cathodic limitations in microbial fuel cells: An overview, J Power Sources, 180 (2008) 683-694.

[38] R. Kumar, L. Singh, A.W. Zularisam, F.I. Hai, Microbial fuel cell is emerging as a versatile technology: a review on its possible applications, challenges and strategies to improve the performances, Int J Energ Res, 42 (2018) 369-394.

[39] M.H. Do, H.H. Ngo, W.S. Guo, Y. Liu, S.W. Chang, D.D. Nguyen, L.D. Nghiem, B.J. Ni, Challenges in the application of microbial fuel cells to wastewater treatment and energy production: A mini review, Sci Total Environ, 639 (2018) 910-920.

[40] M. Aghababaie, M. Farhadian, A. Jeihanipour, D. Biria, Effective factors on the performance of microbial fuel cells in wastewater treatment – a review, Environmental Technology Reviews, 4 (2015) 71-89.

[41] M. Sharma, S. Bajracharya, S. Gildemyn, S.A. Patil, Y. Alvarez-Gallego, D. Pant, K. Rabaey, X. Dominguez-Benetton, A critical revisit of the key parameters used to describe microbial electrochemical systems, Electrochim Acta, 140 (2014) 191-208.

[42] B.E. Logan, B. Hamelers, R.A. Rozendal, U. Schrorder, J. Keller, S. Freguia, P. Aelterman, W. Verstraete, K. Rabaey, Microbial fuel cells: Methodology and technology, Environmental Science & Technology, 40 (2006) 5181-5192.

[43] A.J. Bard, Electrochemical methods : fundamentals and applications / Allen J. Bard, Larry R. Faulkner, Wiley, New York, 1980.

[44] L.S. Clesceri, A.E. Greenberg, A.D. Eaton, Standard Methods for the Examination of Water and Wastewater, 20th Edition, APHA American Public Health Association1998.

[45] Z. Ge, J. Li, L. Xiao, Y.R. Tong, Z. He, Recovery of Electrical Energy in Microbial Fuel Cells, Environ Sci Tech Let, 1 (2014) 137-141.

[46] J. Azeredo, N.F. Azevedo, R. Briandet, N. Cerca, T. Coenye, A.R. Costa, M. Desvaux, G. Di Bonaventura, M. Hebraud, Z. Jaglic, M. Kacaniova, S. Knochel, A. Lourenco, F. Mergulhao, R.L. Meyer, G. Nychas, M. Simoes, O. Tresse, C. Sternberg, Critical review on biofilm methods, Crit Rev Microbiol, 43 (2017) 313-351.

[47] A. Nandy, P.P. Kundu, Chapter 3 - Configurations of Microbial Fuel Cells, in: P.P. Kundu, K. Dutta (Eds.) Progress and Recent Trends in Microbial Fuel Cells, Elsevier2018, pp. 25-45.

[48] G.T. Sun, A. Thygesen, M.T. Ale, M. Mensah, F.W. Poulsen, A.S. Meyer, The significance of the initiation process parameters and reactor design for maximizing the efficiency of microbial fuel cells, Appl Microbiol Biot, 98 (2014) 2415-2427.

[49] U. Kumari, R. Shankar, P. Mondal, Chapter 8 - Electrodes for Microbial Fuel Cells, in: P.P. Kundu, K. Dutta (Eds.) Progress and Recent Trends in Microbial Fuel Cells, Elsevier2018, pp. 125-141.

[50] Y. Qiao, C.M. Li, S.J. Bao, Q.L. Bao, Carbon nanotube/polyaniline composite as anode material for microbial fuel cells, J Power Sources, 170 (2007) 79-84.

[51] Y. Wang, B. Li, L. Zeng, D. Cui, X. Xiang, W. Li, Polyaniline/mesoporous tungsten trioxide composite as anode electrocatalyst for high-performance microbial fuel cells, Biosensors and Bioelectronics, 41 (2013) 582-588.

[52] R. Bos, H.C. van der Mei, H.J. Busscher, Physico-chemistry of initial microbial adhesive interactions--its mechanisms and methods for study, FEMS Microbiol Rev, 23 (1999) 179-230.

[53] K. Guo, A. Prévoteau, S.A. Patil, K. Rabaey, Engineering electrodes for microbial electrocatalysis, Current Opinion in Biotechnology, 33 (2015) 149-156.

[54] F. Song, H. Koo, D. Ren, Effects of Material Properties on Bacterial Adhesion and Biofilm Formation, J Dent Res, 94 (2015) 1027-1034.

[55] B.E. Logan, Scaling up microbial fuel cells and other bioelectrochemical systems, Appl Microbiol Biot, 85 (2010) 1665-1671.

[56] A. Sarapuu, E. Kibena-Põldsepp, M. Borghei, K. Tammeveski, Electrocatalysis of oxygen reduction on heteroatom-doped nanocarbons and transition metal–nitrogen–carbon catalysts for alkaline membrane fuel cells, Journal of Materials Chemistry A, 6 (2018) 776-804.

[57] H. Yuan, Y. Hou, I.M. Abu-Reesh, J. Chen, Z. He, Oxygen reduction reaction catalysts used in microbial fuel cells for energy-efficient wastewater treatment: a review, Materials Horizons, 3 (2016) 382-401.

[58] B.E. Logan, Microbial Fuel Cells, Wiley2008.

[59] J. Cha, S. Choi, H. Yu, H. Kim, C. Kim, Directly applicable microbial fuel cells in aeration tank for wastewater treatment, Bioelectrochemistry, 78 (2010) 72-79.

[60] B. Logan, S. Cheng, V. Watson, G. Estadt, Graphite Fiber Brush Anodes for Increased Power Production in Air-Cathode Microbial Fuel Cells, Environmental Science & Technology, 41 (2007) 3341-3346.

[61] S. Chen, G. He, Q. Liu, F. Harnisch, Y. Zhou, Y. Chen, M. Hanif, S. Wang, X. Peng, H. Hou, U. Schröder, Layered corrugated electrode macrostructures boost microbial bioelectrocatalysis, Energ Environ Sci, 5 (2012) 9769-9772.

[62] A. Baudler, I. Schmidt, M. Langner, A. Greiner, U. Schroder, Does it have to be carbon? Metal anodes in microbial fuel cells and related bioelectrochemical systems, Energ Environ Sci, 8 (2015) 2048-2055.

[63] H.-F. Cui, L. Du, P.-B. Guo, B. Zhu, J.H.T. Luong, Controlled modification of carbon nanotubes and polyaniline on macroporous graphite felt for high-performance microbial fuel cell anode, J Power Sources, 283 (2015) 46-53.

[64] S.Q. Ci, Z.H. Wen, J.H. Chen, Z. He, Decorating anode with bamboo-like nitrogen-doped carbon nanotubes for microbial fuel cells, Electrochem Commun, 14 (2012) 71-74.

[65] C. Erbay, G. Yang, P. de Figueiredo, R. Sadr, C.H. Yu, A. Han, Three-dimensional porous carbon nanotube sponges for high-performance anodes of microbial fuel cells, J Power Sources, 298 (2015) 177-183.

[66] J.X. Hou, Z.L. Liu, S.Q. Yang, Y. Zhou, Three-dimensional macroporous anodes based on stainless steel fiber felt for high-performance microbial fuel cells, J Power Sources, 258 (2014) 204-209.

[67] C. Erbay, X. Pu, W. Choi, M.J. Choi, Y. Ryu, H.J. Hou, F.R. Lin, P. de Figueiredo, C. Yu, A. Han, Control of geometrical properties of carbon nanotube electrodes towards high-performance microbial fuel cells, J Power Sources, 280 (2015) 347-354.

[68] J.M. Sonawane, A. Yadav, P.C. Ghosh, S.B. Adeloju, Recent advances in the development and utilization of modern anode materials for high performance microbial fuel cells, Biosensors and Bioelectronics, 90 (2017) 558-576.

[69] J. Hou, Z. Liu, S. Yang, Y. Zhou, Three-dimensional macroporous anodes based on stainless steel fiber felt for high-performance microbial fuel cells, J Power Sources, 258 (2014) 204-209.

[70] X. Liu, W. Wu, Z. Gu, Poly (3,4-ethylenedioxythiophene) promotes direct electron transfer at the interface between Shewanella loihica and the anode in a microbial fuel cell, J Power Sources, 277 (2015) 110-115.

[71] S.H. Roh, H.G. Woo, Carbon Nanotube Composite Electrode Coated with Polypyrrole for Microbial Fuel Cell Application, J Nanosci Nanotechno, 15 (2015) 484-487.

[72] K.-B. Pu, Q. Ma, W.-F. Cai, Q.-Y. Chen, Y.-H. Wang, F.-J. Li, Polypyrrole modified stainless steel as high performance anode of microbial fuel cell, Biochemical Engineering Journal, 132 (2018) 255-261.

[73] Z. Gao, W. Yang, J. Wang, B. Wang, Z. Li, Q. Liu, M. Zhang, L. Liu, A New Partially Reduced Graphene Oxide Nanosheet/Polyaniline Nanowafer Hybrid as Supercapacitor Electrode Material, Energ Fuel, 27 (2013) 568-575.

[74] T. Yin, Z.Y. Lin, L. Su, C.W. Yuan, D.G. Fu, Preparation of Vertically Oriented TiO2 Nanosheets Modified Carbon Paper Electrode and Its Enhancement to the Performance of MFCs, Acs Appl Mater Inter, 7 (2015) 400-408.

[75] J. Tang, Y. Yuan, T. Liu, S. Zhou, High-capacity carbon-coated titanium dioxide core–shell nanoparticles modified three dimensional anodes for improved energy output in microbial fuel cells, J Power Sources, 274 (2015) 170-176.

[76] I.H. Park, M. Christy, P. Kim, K.S. Nahm, Enhanced electrical contact of microbes using Fe3O4/CNT nanocomposite anode in mediator-less microbial fuel cell, Biosensors and Bioelectronics, 58 (2014) 75-80.

[77] S. Zhou, J. Tang, Y. Yuan, Conduction-band edge dependence of carbon-coated hematite stimulated extracellular electron transfer of Shewanella oneidensis in bioelectrochemical systems, Bioelectrochemistry, 102 (2015) 29-34.

[78] L. Dai, Y. Xue, L. Qu, H.-J. Choi, J.-B. Baek, Metal-Free Catalysts for Oxygen Reduction Reaction, Chemical Reviews, 115 (2015) 4823-4892.

[79] F. Jaouen, E. Proietti, M. Lefèvre, R. Chenitz, J.-P. Dodelet, G. Wu, H.T. Chung, C.M. Johnston, P. Zelenay, Recent advances in non-precious metal catalysis for oxygen-reduction reaction in polymer electrolyte fuel cells, Energ Environ Sci, 4 (2011) 114-130.

[80] G. Wu, A. Santandreu, W. Kellogg, S. Gupta, O. Ogoke, H. Zhang, H.-L. Wang, L. Dai, Carbon nanocomposite catalysts for oxygen reduction and evolution reactions: From nitrogen doping to transition-metal addition, Nano Energy, 29 (2016) 83-110.

[81] S. Oh, B. Min, B.E. Logan, Cathode Performance as a Factor in Electricity Generation in Microbial Fuel Cells, Environmental Science & Technology, 38 (2004) 4900-4904.

[82] Z.J. Wang, C.L. Cao, Y. Zheng, S.L. Chen, F. Zhao, Abiotic Oxygen Reduction Reaction Catalysts Used in Microbial Fuel Cells, Chemelectrochem, 1 (2014) 1813-1821.

[83] V.J. Watson, C. Nieto Delgado, B.E. Logan, Influence of Chemical and Physical Properties of Activated Carbon Powders on Oxygen Reduction and Microbial Fuel Cell Performance, Environmental Science & Technology, 47 (2013) 6704-6710.

[84] Y. Ahn, I. Ivanov, T.C. Nagaiah, A. Bordoloi, B.E. Logan, Mesoporous nitrogen-rich carbon materials as cathode catalysts in microbial fuel cells, J Power Sources, 269 (2014) 212-215.

[85] X. Zhang, X. Xia, I. Ivanov, X. Huang, B.E. Logan, Enhanced Activated Carbon Cathode Performance for Microbial Fuel Cell by Blending Carbon Black, Environmental Science & Technology, 48 (2014) 2075-2081.

[86] K.P. Gong, F. Du, Z.H. Xia, M. Durstock, L.M. Dai, Nitrogen-Doped Carbon Nanotube Arrays with High Electrocatalytic Activity for Oxygen Reduction, Science, 323 (2009) 760-764.

[87] Y.-R. He, F. Du, Y.-X. Huang, L.-M. Dai, W.-W. Li, H.-Q. Yu, Preparation of microvillus-like nitrogen-doped carbon nanotubes as the cathode of a microbial fuel cell, Journal of Materials Chemistry A, 4 (2016) 1632-1636.

[88] L. Feng, L. Yang, Z. Huang, J. Luo, M. Li, D. Wang, Y. Chen, Enhancing Electrocatalytic Oxygen Reduction on Nitrogen-Doped Graphene by Active Sites Implantation, Scientific Reports, 3 (2013) 3306.

[89] Z. Fu, L. Yan, K. Li, B. Ge, L. Pu, X. Zhang, The performance and mechanism of modified activated carbon air cathode by non-stoichiometric nano Fe3O4 in the microbial fuel cell, Biosensors and Bioelectronics, 74 (2015) 989-995.

[90] Y. Chen, Z. Lv, J. Xu, D. Peng, Y. Liu, J. Chen, X. Sun, C. Feng, C. Wei, Stainless steel mesh coated with MnO2/carbon nanotube and polymethylphenyl siloxane as low-cost and high-performance microbial fuel cell cathode materials, J Power Sources, 201 (2012) 136-141.

[91] Q. Wen, S. Wang, J. Yan, L. Cong, Z. Pan, Y. Ren, Z. Fan, MnO2–graphene hybrid as an alternative cathodic catalyst to platinum in microbial fuel cells, J Power Sources, 216 (2012) 187-191.

[92] Y. Hou, H. Yuan, Z. Wen, S. Cui, X. Guo, Z. He, J. Chen, Nitrogen-doped graphene/CoNi alloy encased within bamboo-like carbon nanotube hybrids as cathode catalysts in microbial fuel cells, J Power Sources, 307 (2016) 561-568.

[93] F. Zhao, F. Harnisch, U. Schröder, F. Scholz, P. Bogdanoff, I. Herrmann, Challenges and Constraints of Using Oxygen Cathodes in Microbial Fuel Cells, Environmental Science & Technology, 40 (2006) 5193-5199.

[94] F. Zhao, F. Harnisch, U. Schröder, F. Scholz, P. Bogdanoff, I. Herrmann, Application of pyrolysed iron(II) phthalocyanine and CoTMPP based oxygen reduction catalysts as cathode materials in microbial fuel cells, Electrochemistry Communications, 7 (2005) 1405-1410.

[95] L. Deng, M. Zhou, C. Liu, L. Liu, C. Liu, S. Dong, Development of high performance of Co/Fe/N/CNT nanocatalyst for oxygen reduction in microbial fuel cells, Talanta, 81 (2010) 444-448.

[96] B. Li, X. Zhou, X. Wang, B. Liu, B. Li, Hybrid binuclear-cobalt-phthalocyanine as oxygen reduction reaction catalyst in single chamber microbial fuel cells, J Power Sources, 272 (2014) 320-327.

[97] Y. Zhao, K. Watanabe, K. Hashimoto, Self-Supporting Oxygen Reduction Electrocatalysts Made from a Nitrogen-Rich Network Polymer, J Am Chem Soc, 134 (2012) 19528-19531.

[98] Z.H. Wen, S.Q. Ci, F. Zhang, X.L. Feng, S.M. Cui, S. Mao, S.L. Luo, Z. He, J.H. Chen, Nitrogen-Enriched Core-Shell Structured Fe/Fe3C-C Nanorods as Advanced Electrocatalysts for Oxygen Reduction Reaction, Adv Mater, 24 (2012) 1399-1404.

[99] H.L. Tang, S.C. Cai, S.L. Xie, Z.B. Wang, Y.X. Tong, M. Pan, X.H. Lu, Metal-Organic-Framework-Derived Dual Metal- and Nitrogen-Doped Carbon as Efficient and Robust Oxygen Reduction Reaction Catalysts for Microbial Fuel Cells, Adv Sci, 3 (2016).

[100] L. Zeng, L. Zhang, W. Li, S. Zhao, J. Lei, Z. Zhou, Molybdenum carbide as anodic catalyst for microbial fuel cell based on Klebsiella pneumoniae, Biosensors and Bioelectronics, 25 (2010) 2696-2700.

[101] A. Mehdinia, E. Ziaei, A. Jabbari, Facile microwave-assisted synthesized reduced graphene oxide/tin oxide nanocomposite and using as anode material of microbial fuel cell to improve power generation, Int J Hydrogen Energ, 39 (2014) 10724-10730.

[102] Y. Yin, G. Huang, N. Zhou, Y. Liu, L. Zhang, Increasing power generation of microbial fuel cells with a nano-CeO2 modified anode, Energy Sources, Part A: Recovery, Utilization, and Environmental Effects, 38 (2016) 1212-1218.

[103] Z. Lv, D. Xie, X. Yue, C. Feng, C. Wei, Ruthenium oxide-coated carbon felt electrode: A highly active anode for microbial fuel cell applications, J Power Sources, 210 (2012) 26-31.

[104] W. Chen, Z.H. Liu, G. Su, Y.B. Fu, X.R. Zai, C.Y. Zhou, J. Wang, Composite-modified anode by MnO2/polypyrrole in marine benthic microbial fuel cells and its electrochemical performance, Int J Energ Res, 41 (2017) 845-853.

[105] P. Narayanaswamy Venkatesan, S. Dharmalingam, Synthesis and characterization of Pt, Pt–Fe/TiO2 cathode catalysts and its evaluation in microbial fuel cell, Materials for Renewable and Sustainable Energy, 5 (2016) 11.

[106] L. Zhang, C. Liu, L. Zhuang, W. Li, S. Zhou, J. Zhang, Manganese dioxide as an alternative cathodic catalyst to platinum in microbial fuel cells, Biosensors and Bioelectronics, 24 (2009) 2825-2829.

[107] M.T. Noori, M.M. Ghangrekar, C.K. Mukherjee, V2O5 microflower decorated cathode for enhancing power generation in air-cathode microbial fuel cell treating fish market wastewater, Int J Hydrogen Energ, 41 (2016) 3638-3645.

[108] J. Ahmed, H.J. Kim, S. Kim, Embedded cobalt oxide nano particles on carbon could potentially improve oxygen reduction activity of cobalt phthalocyanine and its application in microbial fuel cells, Rsc Adv, 4 (2014) 44065-44072.

[109] B. Mecheri, A. Iannaci, A. D'Epifanio, A. Mauri, S. Licoccia, Carbon-Supported Zirconium Oxide as a Cathode for Microbial Fuel Cell Applications, ChemPlusChem, 81 (2016) 80-85.

[110] E. Ionescu, Polymer-Derived Ceramics, Ceramics Science and Technology.

[111] F.W. Ainger, J.M. Herbert, The Preparation of Phosphorus-Nitrogen Compounds as Non-Porous Solids, Angew Chem Int Edit, 71 (1959) 653-653.

[112] P.G.a.P. Chantrell, P., Inorganic Polymers and Ceramics, in: P.P.A. Press (Ed.) Special Ceramics, New York, 1965, pp. 87-103.

[113] S. Yajima, J. Hayashi, M. Omori, Continuous Silicon-Carbide Fiber of High-Tensile Strength, Chem Lett, (1975) 931-934.

[114] S. Yajima, Y. Hasegawa, K. Okamura, T. Matsuzawa, Development of High-Tensile Strength Silicon-Carbide Fiber Using an Organosilicon Polymer Precursor, Nature, 273 (1978) 525-527.

[115] E. Bernardo, L. Fiocco, G. Parcianello, E. Storti, P. Colombo, Advanced Ceramics from Preceramic Polymers Modified at the Nano-Scale: A Review, Materials, 7 (2014) 1927-1956.

[116] S. Bernard, K. Fiaty, D. Cornu, P. Miele, P. Laurent, Kinetic Modeling of the Polymer-Derived Ceramics Route: Investigation of the Thermal Decomposition Kinetics of Poly[B-(methylamino)borazine] Precursors into Boron Nitride, The Journal of Physical Chemistry B, 110 (2006) 9048-9060.

[117] G. Mera, M. Gallei, S. Bernard, E. Ionescu, Ceramic Nanocomposites from Tailor-Made Preceramic Polymers, Nanomaterials-Basel, 5 (2015) 468-540.

[118] M. Wilhelm, C. Soltmann, D. Koch, G. Grathwohl, Ceramers - functional materials for adsorption techniques, J Eur Ceram Soc, 25 (2005) 271-276.

[119] R.M.d. Rocha, P. Greil, J.C. Bressiani, A.H.d.A. Bressiani, Complex-shaped ceramic composites obtained by machining compact polymer-filler mixtures, Materials Research, 8 (2005) 191-196.

[120] P. Greil, Polymer derived engineering ceramics, Adv Eng Mater, 2 (2000) 339-348.

[121] G. Parcianello, Advanced ceramics from preceramic polymers and fillers, Università degli Studi di Padova, Padova, Italy, 2012, pp. 186.

[122] Y.D. Blum, K.B. Schwartz, R.M. Laine, Preceramic Polymer Pyrolysis .1. Pyrolytic Properties of Polysilazanes, J Mater Sci, 24 (1989) 1707-1718.

[123] P. Greil, Active-Filler-Controlled Pyrolysis of Preceramic Polymers, J Am Ceram Soc, 78 (1995) 835-848.

[124] V. Belot, R.J.P. Corriu, D. Leclercq, P.H. Mutin, A. Vioux, Thermal redistribution reactions in crosslinked polysiloxanes, Journal of Polymer Science Part A: Polymer Chemistry, 30 (1992) 613-623.

[125] G.D. Sorarù, L. Pederiva, J. Latournerie, R. Raj, Pyrolysis Kinetics for the Conversion of a Polymer into an Amorphous Silicon Oxycarbide Ceramic, J Am Ceram Soc, 85 (2002) 2181-2187.

[126] M. Narisawa, Silicone Resin Applications for Ceramic Precursors and Composites, Materials, 3 (2010) 3518-3536.

[127] B.V.M. Kumar, Y.W. Kim, Processing of polysiloxane-derived porous ceramics: a review, Sci Technol Adv Mat, 11 (2010).

[128] P. Colombo, Conventional and novel processing methods for cellular ceramics, Philosophical Transactions of the Royal Society A: Mathematical, Physical and Engineering Sciences, 364 (2006) 109-124.

[129] J. Cordelair, P. Greil, Electrical conductivity measurements as a microprobe for structure transitions in polysiloxane derived Si–O–C ceramics, J Eur Ceram Soc, 20 (2000) 1947-1957.

[130] P. Colombo, T. Gambaryan-Roisman, M. Scheffler, P. Buhler, P. Greil, Conductive ceramic foams from preceramic polymers, J Am Ceram Soc, 84 (2001) 2265-2268.

[131] J.F. Drillet, M. Adam, S. Barg, A. Herter, D. Koch, V.M. Schmidt, M. Wilhelm, Development of a Novel Zinc/Air Fuel Cell with a Zn Foam Anode, a PVA/KOH Membrane and a MnO2/SiOC-based Air Cathode, Ecs Transactions, 28 (2010) 13-24.

[132] J. Cordelair, P. Greil, Electrical Characterization of Polymethylsiloxane/MoSi2-Derived Composite Ceramics, J Am Ceram Soc, 84 (2001) 2256-2259.

[133] K.J. Kim, J.-H. Eom, T.Y. Koh, Y.-W. Kim, W.-S. Seo, Effects of carbon addition on the electrical properties of bulk silicon-oxycarbide ceramics, J Eur Ceram Soc, 36 (2016) 2705-2711.

[134] K. Lu, D. Erb, M. Liu, Thermal stability and electrical conductivity of carbon-enriched silicon oxycarbide, Journal of Materials Chemistry C, 4 (2016) 1829-1837.

[135] M. Scheffler, P. Greil, A. Berger, E. Pippel, J. Woltersdorf, Nickel-catalyzed in situ formation of carbon nanotubes and turbostratic carbon in polymer-derived ceramics, Mater Chem Phys, 84 (2004) 131-139.

[136] K. Lu, D. Erb, M.Y. Liu, Phase transformation, oxidation stability, and electrical conductivity of TiO2-polysiloxane derived ceramics, J Mater Sci, 51 (2016) 10166-10177.

[137] B.E. Conway, Electrochemical Supercapacitors: Scientific Fundamentals and Technological Applications, Springer US2013.

[138] M.W. Verbrugge, P. Liu, Microstructural analysis and mathematical modeling of electric double-layer supercapacitors, J Electrochem Soc, 152 (2005) D79-D87.

[139] M.A. Abass, A.A. Syed, C. Gervais, G. Singh, Synthesis and electrochemical performance of a polymer-derived silicon oxycarbide/boron nitride nanotube composite, Rsc Adv, 7 (2017) 21576-21584.

[140] R. Bhandavat, G. Singh, Stable and Efficient Li-Ion Battery Anodes Prepared from Polymer-Derived Silicon Oxycarbide–Carbon Nanotube Shell/Core Composites, The Journal of Physical Chemistry C, 117 (2013) 11899-11905.

[141] A.M. Wilson, G. Zank, K. Eguchi, W. Xing, J.R. Dahn, Pyrolysed silicon-containing polymers as high capacity anodes for lithium-ion batteries, J Power Sources, 68 (1997) 195-200.

[142] P. Moni, W.F. Chaves, M. Wilhelm, K. Rezwan, Polysiloxane microspheres encapsulated in carbon allotropes: A promising material for supercapacitor and carbon dioxide capture, Journal of Colloid and Interface Science, 542 (2019) 91-101.

[143] R. Harshe, C. Balan, R. Riedel, Amorphous Si(Al)OC ceramic from polysiloxanes: bulk ceramic processing, crystallization behavior and applications, J Eur Ceram Soc, 24 (2004) 3471-3482.

[144] M. Adam, M. Wilhelm, G. Grathwohl, Polysiloxane derived hybrid ceramics with nanodispersed Pt, Micropor Mesopor Mat, 151 (2012) 195-200.

[145] M. Wojcik-Bania, A. Krowiak, J. Strzezik, M. Hasik, Pt supported on cross-linked poly(vinylsiloxanes) and SiCO ceramics - new materials for catalytic applications, Mater Design, 96 (2016) 171-179.

[146] M. Schubert, M. Wilhelm, S. Bragulla, C.H. Sun, S. Neumann, T.M. Gesing, P. Pfeifer, K. Rezwan, M. Baumer, The Influence of the Pyrolysis Temperature on the Material Properties of Cobalt and Nickel Containing Precursor Derived Ceramics and their Catalytic Use for CO2 Methanation and Fischer-Tropsch Synthesis, Catal Lett, 147 (2017) 472-482.

[147] T.C.D.E. Silva, V.F. Kettermann, C. Pereira, M. Simoes, M. Wilhelm, K. Rezwan, Novel tape-cast SiOC-based porous ceramic electrode materials for potential application in bioelectrochemical systems, J Mater Sci, 54 (2019) 6471-6487.

[148] T. Canuto de Almeida e Silva, M. Mooste, E. Kibena-Põldsepp, L. Matisen, M. Merisalu, M. Kook, V. Sammelselg, K. Tammeveski, M. Wilhelm, K. Rezwan, Polymer-derived Co/Ni–SiOC(N) ceramic electrocatalysts for oxygen reduction reaction in fuel cells, Catalysis Science & Technology, 9 (2019) 854-866.

[149] T. Canuto de Almeida e Silva, G.D. Bhowmick, M.M. Ghangrekar, M. Wilhelm, K. Rezwan, SiOC-based polymer derived-ceramic porous anodes for microbial fuel cells, Biochemical Engineering Journal, 148 (2019) 29-36.

[150] F. Schlüter, J. Meyer, M. Wilhelm, K. Rezwan, Hierarchical emulsion based hybrid ceramics synthesized with different siloxane precursor and with embedded nickel nanoparticles, Colloids and Surfaces A: Physicochemical and Engineering Aspects, 492 (2016) 160-169.

[151] S. Ratso, I. Kruusenberg, M. Käärik, M. Kook, R. Saar, M. Pärs, J. Leis, K. Tammeveski, Highly efficient nitrogen-doped carbide-derived carbon materials for oxygen reduction reaction in alkaline media, Carbon, 113 (2017) 159-169.

[152] K.D. Vernon-Parry, Scanning electron microscopy: an introduction, III-Vs Review, 13 (2000) 40-44.

[153] N. Instruments, Scanning Electron Microscopy, n. d. .

https://www.nanoscience.com/techniques/scanning-electron-microscopy/#, Access date April 22,2019

[154] J. Rouquerol, D. Avnir, C.W. Fairbridge, D.H. Everett, J.H. Haynes, N. Pernicone, J.D.F. Ramsay, K.S.W. Sing, K.K. Unger, Recommendations for the Characterization of Porous Solids, Pure Appl Chem, 66 (1994) 1739-1758.

[155] K. Sing, The use of nitrogen adsorption for the characterisation of porous materials, Colloid Surface A, 187 (2001) 3-9.

[156] M. Wang, G.N. Pande, L.W. Kong, Y.T. Feng, Comparison of Pore-Size Distribution of Soils Obtained by Different Methods, Int J Geomech, 17 (2017).

[157] K.S.W. Sing, D.H. Everett, R.A.W. Haul, L. Moscou, R.A. Pierotti, J. Rouquérol, T. Siemieniewska, Reporting Physisorption Data for Gas/Solid Systems With Special Reference to the Determination of Surface Area and Porosity.

[158] K.S.W. Sing, R.T. Williams, Physisorption hysteresis loops and the characterization of nanoporous materials, Adsorpt Sci Technol, 22 (2004) 773-782.

[159] M. Kruk, M. Jaroniec, Gas adsorption characterization of ordered organic-inorganic nanocomposite materials, Chem Mater, 13 (2001) 3169-3183.

[160] S. Brunauer, P.H. Emmett, E. Teller, Adsorption of Gases in Multimolecular Layers, J Am Chem Soc, 60 (1938) 309-319.

[161] R. Haul, S. J. Gregg, K. S. W. Sing: Adsorption, Surface Area and Porosity. 2. Auflage, Academic Press, London 1982. 303 Seiten, Preis: $ 49.50, Berichte der Bunsengesellschaft für physikalische Chemie, 86 (1982) 957-957.

[162] H. Giesche, Mercury Porosimetry: A General (Practical) Overview, Particle & Particle Systems Characterization, 23 (2006) 9-19.

[163] P.V.v.W.G. GMBH, Mercury Intrusion Porosimetry.

https://www.porotec.de/en/porosity/mercury_intrusion_porosimetry.html, Access date May 25, 2019

[164] H. Salmang, R. Telle, H. Scholze, Keramik, Springer Berlin Heidelberg2006.

[165] J.C. Echeverría, M.T. Morera, C. Mazkiarán, J.J. Garrido, Characterization of the porous structure of soils: adsorption of nitrogen (77 K) and carbon dioxide (273 K), and mercury porosimetry, European Journal of Soil Science, 50 (1999) 497-503.

[166] A.B. Abell, K.L. Willis, D.A. Lange, Mercury Intrusion Porosimetry and Image Analysis of Cement-Based Materials, Journal of Colloid and Interface Science, 211 (1999) 39-44.

[167] A.A. Bunaciu, E.g. Udriştioiu, H.Y. Aboul-Enein, X-Ray Diffraction: Instrumentation and Applications, Critical Reviews in Analytical Chemistry, 45 (2015) 289-299.

[168] T.F. Scientific, What is X-Ray Photoelectron Spectroscopy (XPS)?, n. d. .

https://xpssimplified.com/whatisxps.php, Access date April 23,2019

[169] P. Electronics, XPS / ESCA, n. d. . https://www.phi.com/surface-analysis-techniques/xps-esca.html, Access date April 23, 2019

[170] K. Analytical, X-ray Photoelectron Spectroscopy (XPS), n. d. .

https://www.kratos.com/applications/techniques/x-ray-photoelectron-spectroscopy, Access date April 23, 2019

[171] S. Kabir, K. Artyushkova, A. Serov, B. Kiefer, P. Atanassov, Binding energy shifts for nitrogen-containing graphene-based electrocatalysts – experiments and DFT calculations, Surface and Interface Analysis, 48 (2016) 293-300.

[172] K. Artyushkova, I. Matanovic, B. Halevi, P. Atanassov, Oxygen Binding to Active Sites of Fe–N–C ORR Electrocatalysts Observed by Ambient-Pressure XPS, The Journal of Physical Chemistry C, 121 (2017) 2836-2843.

[173] T. Prenzel, T.L.M. Guedes, F. Schluter, M. Wilhelm, K. Rezwan, Tailoring surfaces of hybrid ceramics for gas adsorption - From alkanes to CO2, Sep Purif Technol, 129 (2014) 80-89.

[174] B. Tylkowski, I. Tsibranska, Overview of main techniques used for membrane characterization, 2014.

[175] D. Instruments, Sessile drop method - Optical determination of the contact angle, n. d. .

https://www.dataphysics-instruments.com/knowledge/understanding-interfaces/sessile-drop-method/, Access date April 24, 2019

[176] H. Jiang, F. Müller-Plathe, A.Z. Panagiotopoulos, Contact angles from Young's equation in molecular dynamics simulations, The Journal of Chemical Physics, 147 (2017) 084708.

[177] M. Simoes, S. Cleto, M.O. Pereira, M.J. Vieira, Influence of biofilm composition on the resistance to detachment, Water Sci Technol, 55 (2007) 473-480.

[178] M. Lemos, I. Gomes, F. Mergulhao, L. Melo, M. Simoes, The effects of surface type on the removal of Bacillus cereus and Pseudomonas fluorescens single and dual species biofilms, Food Bioprod Process, 93 (2015) 234-241.

[179] A. Meireles, C. Ferreira, L. Melo, M. Simoes, Comparative stability and efficacy of selected chlorine-based biocides against Escherichia coli in planktonic and biofilm states, Food Res Int, 102 (2017) 511-518.

[180] M.A. Islam, B. Ethiraj, C.K. Cheng, A. Yousuf, M.M.R. Khan, Electrogenic and Antimethanogenic Properties of Bacillus cereus for Enhanced Power Generation in Anaerobic Sludge-Driven Microbial Fuel Cells, Energ Fuel, 31 (2017) 6132-6139.

[181] Y.L. Wu, X.L. Zhang, S.H. Li, X.Y. Lv, Y. Cheng, X.M. Wang, Microbial biofuel cell operating effectively through carbon nanotube blended with gold-titania nanocomposites modified electrode, Electrochim Acta, 109 (2013) 328-332.

[182] A. Mehdinia, E. Ziaei, A. Jabbari, Facile microwave-assisted synthesized reduced graphene oxide/tin oxide nanocomposite and using as anode material of microbial fuel cell to improve power generation, Int J Hydrogen Energ, 39 (2014) 10724-10730.

[183] J. Malheiro, I. Gomes, A. Borges, M.M.S.M. Bastos, J.Y. Maillard, F. Borges, M. Simoes, Phytochemical profiling as a solution to palliate disinfectant limitations, Biofouling, 32 (2016) 1007-1016.

[184] Z. He, F. Mansfeld, Exploring the use of electrochemical impedance spectroscopy (EIS) in microbial fuel cell studies, Energ Environ Sci, 2 (2009) 215-219.

[185] E. Barsoukov, J.R. Macdonald, Impedance Spectroscopy: Theory, Experiment, and Applications, Wiley2005.

[186] N. Elgrishi, K.J. Rountree, B.D. McCarthy, E.S. Rountree, T.T. Eisenhart, J.L. Dempsey, A Practical Beginner's Guide to Cyclic Voltammetry, Journal of Chemical Education, 95 (2018) 197-206.

[187] C.G. Zoski, Handbook of Electrochemistry, Elsevier Science2007.

[188] U.o. Cambridge, Linear Sweep and Cyclic Voltametry: The Principles.

https://www.ceb.cam.ac.uk/research/groups/rg-eme/Edu/linear-sweep-and-cyclic-voltametry-the principles Access date May 20, 2019

[189] C. Du, Q. Tan, G. Yin, J. Zhang, 5 - Rotating Disk Electrode Method, in: W. Xing, G. Yin, J. Zhang (Eds.) Rotating Electrode Methods and Oxygen Reduction Electrocatalysts, Elsevier, Amsterdam, 2014, pp. 171-198.

[190] C.W.B. Bezerra, L. Zhang, K. Lee, H. Liu, J. Zhang, Z. Shi, A.L.B. Marques, E.P. Marques, S. Wu, J. Zhang, Novel carbon-supported Fe-N electrocatalysts synthesized through heat treatment of iron tripyridyl triazine complexes for the PEM fuel cell oxygen reduction reaction, Electrochim Acta, 53 (2008) 7703-7710.

[191] K.K. Türk, I. Kruusenberg, E. Kibena-Põldsepp, G.D. Bhowmick, M. Kook, K. Tammeveski, L. Matisen, M. Merisalu, V. Sammelselg, M.M. Ghangrekar, A. Mitra, R. Banerjee, Novel multi walled carbon nanotube based nitrogen impregnated Co and Fe cathode catalysts for improved microbial fuel cell performance, Int J Hydrogen Energ, 43 (2018) 23027-23035.

[192] G.S. Jadhav, M.M. Ghangrekar, Performance of microbial fuel cell subjected to variation in pH, temperature, external load and substrate concentration, Bioresour Technol, 100 (2009) 717-723.

[193] M.M. Ghangrekar, S.R. Asolekar, S.G. Joshi, Characteristics of sludge developed under different loading conditions during UASB reactor start-up and granulation, Water Res, 39 (2005) 1123-1133.

[194] C. Gimkiewicz, F. Harnisch, Waste Water Derived Electroactive Microbial Biofilms: Growth, Maintenance, and Basic Characterization, Jove-J Vis Exp, (2013).

[195] J.R. Kim, B. Min, B.E. Logan, Evaluation of procedures to acclimate a microbial fuel cell for electricity production, Appl Microbiol Biotechnol, 68 (2005) 23-30.

[196] Z. Ge, J. Li, L. Xiao, Y. Tong, Z. He, Recovery of Electrical Energy in Microbial Fuel Cells, Environ Sci Tech Let, 1 (2014) 137-141.

[197] APHA, Standard Methods for the Examination of Water and Wastewater, 20th Edition, APHA American Public Health Association, Washington, DC, USA, 1998.

[198] M. Adam, C. Vakifahmetoglu, P. Colombo, M. Wilhelm, G. Grathwohl, Polysiloxane- Derived Ceramics Containing Nanowires with Catalytically Active Tips, J Am Ceram Soc, 97 (2014) 959-966.

[199] P. Colombo, M.O. Abdirashid, M. Guglielmi, L.M.D. Esposti, L. Agostini, Preparation of Ceramic Composites by Active-Ftller-Controlled-Polymer-Pyrolysis, MRS Proceedings, 346 (1994) 403.

[200] P. Greil, Near Net Shape Manufacturing of Polymer Derived Ceramics, J Eur Ceram Soc, 18 (1998) 1905-1914.

[201] S.W. Lee, B.Y. Jeon, D.H. Park, Effect of bacterial cell size on electricity generation in a single-compartmented microbial fuel cell, Biotechnol Lett, 32 (2010) 483-487.

[202] S. Brunauer, L.S. Deming, W.E. Deming, E. Teller, On a theory of the van der Waals adsorption of gases, J Am Chem Soc, 62 (1940) 1723-1732.

[203] D.H. Everett, Manual of Symbols and Terminology for Physicochemical Quantities and Units, Appendix II: Definitions, Terminology and Symbols in Colloid and Surface Chemistry, Pure Appl Chem, 1972, pp. 577.

[204] P. Colombo, Engineering porosity in polymer-derived ceramics, J Eur Ceram Soc, 28 (2008) 1389-1395.

[205] H. Schmidt, D. Koch, G. Grathwohl, P. Colombo, Micro-/macroporous ceramics from preceramic precursors, J Am Ceram Soc, 84 (2001) 2252-2255.

[206] L.Q. Duan, Q.S. Ma, Effect of pyrolysis temperature on the pore structure evolution of polysiloxane-derived ceramics, Ceram Int, 38 (2012) 2667-2671.

[207] H. Brequel, J. Parmentier, G.D. Soraru, L. Schiffini, S. Enzo, Study of the phase separation in amorphous silicon oxycarbide glasses under heat treatment, Nanostruct Mater, 11 (1999) 721-731.

[208] X.H. Zhang, J.X. Gao, C.Q. Hong, J.C. Han, W.B. Han, Observation of SiC nanodots and nanowires in situ growth in SiOC ceramics, Crystengcomm, 15 (2013) 7803-7807.

[209] Z.B. Zhao, S.S. An, H.J. Xie, X.L. Han, F.H. Wang, Y. Jiang, The Relationship between the Hydrophilicity and Surface Chemical Composition Microphase Separation Structure of Multicomponent Silicone Hydrogels, J Phys Chem B, 119 (2015) 9780-9786.

[210] T. Matsuda, S. Ito, Surface Coating of Hydrophilic-Hydrophobic Block-Copolymers on a Poly(Acrylonitrile) Hemodialyzer Reduces Platelet-Adhesion and Its Transmembrane Stimulation, Biomaterials, 15 (1994) 417-422.

[211] K. Guo, S. Freguia, P.G. Dennis, X. Chen, B.C. Donose, J. Keller, J.J. Gooding, K. Rabaey, Effects of Surface Charge and Hydrophobicity on Anodic Biofilm Formation, Community Composition, and Current Generation in Bioelectrochemical Systems, Environmental Science & Technology, 47 (2013) 7563-7570.

[212] C. Santoro, M. Guilizzoni, J.P.C. Baena, U. Pasaogullari, A. Casalegno, B. Li, S. Babanova, K. Artyushkova, P. Atanassov, The effects of carbon electrode surface properties on bacteria attachment and start up time of microbial fuel cells, Carbon, 67 (2014) 128-139.

[213] S. Bajracharya, A. ElMekawy, S. Srikanth, D. Pant, Cathodes for Microbial Fuel Cells, Microbial Electrochemical and Fuel Cells: Fundamentals and Applications, Woodhead Publishing2015, pp. 179-213.

[214] A.D. Li, M. Han, S.H. Chan, N.T. Nguyen, Effects of hydrophobicity of the cathode catalyst layer on the performance of a PEM fuel cell, Electrochim Acta, 55 (2010) 2706-2711.

[215] A.K. Jonscher, Universal Dielectric Response, Nature, 267 (1977) 673-679.

[216] M. Monthioux, O. Delverdier, Thermal behavior of (organosilicon) polymer-derived ceramics. V: Main facts and trends, J Eur Ceram Soc, 16 (1996) 721-737.

[217] M. Prabu, S. Selvasekarapandian, M.V. Reddy, B.V.R. Chowdari, Impedance studies on the 5-V cathode material, LiCoPO4, J Solid State Electr, 16 (2012) 1833-1839.

[218] J.C. Dyre, T.B. Schroder, Universality of ac conduction in disordered solids, Rev Mod Phys, 72 (2000) 873-892.

[219] X.A. Wang, Z.C. Shi, M. Chen, R.H. Fan, K.L. Yan, K. Sun, S.B. Pan, M.X. Yu, Tunable Electromagnetic Properties in Co/Al2O3 Cermets Prepared by Wet Chemical Method, J Am Ceram Soc, 97 (2014) 3223-3229.

[220] Z.D. Zhang, C.B. Cheng, X. Han, Percolative cobalt/silicon nitride composites with tunable negative electromagnetic parameters, Rsc Adv, 6 (2016) 82478-82483.

[221] Y.A. Syed Khadar, A. Balamurugan, V.P. Devarajan, R. Subramanian, S. Dinesh Kumar, Synthesis, characterization and antibacterial activity of cobalt doped cerium oxide (CeO2:Co) nanoparticles by using hydrothermal method, Journal of Materials Research and Technology, (2018).

[222] M. Vahedi, N. Hosseini-Jazani, S. Yousefi, M. Ghahremani, Evaluation of anti-bacterial effects of nickel nanoparticles on biofilm production by Staphylococcus epidermidis, Iran J Microbiol, 9 (2017) 160-168.

[223] O. Sharifahmadian, H.R. Salimijazi, M.H. Fathi, J. Mostaghimi, L. Pershin, Relationship between surface properties and antibacterial behavior of wire arc spray copper coatings, Surf Coat Tech, 233 (2013) 74-79.

[224] G. Grass, C. Rensing, M. Solioz, Metallic Copper as an Antimicrobial Surface, Appl Environ Microb, 77 (2011) 1541-1547.

[225] X.P. Zhu, B.E. Logan, Copper anode corrosion affects power generation in microbial fuel cells, J Chem Technol Biot, 89 (2014) 471-474.

[226] M. Fukushima, P. Colombo, Silicon carbide-based foams from direct blowing of polycarbosilane, J Eur Ceram Soc, 32 (2012) 503-510.

[227] A. Idesaki, P. Colombo, Synthesis of a Ni-Containing Porous SiOC Material From Polyphenylmethylsiloxane by a Direct Foaming Technique, Adv Eng Mater, 14 (2012) 1116-1122.

[228] S.-H. Chang, J.-S. Liou, J.-L. Liu, Y.-F. Chiu, C.-H. Xu, B.-Y. Chen, J.-Z. Chen, Feasibility study of surface-modified carbon cloth electrodes using atmospheric pressure plasma jets for microbial fuel cells, J Power Sources, 336 (2016) 99-106.

[229] Y. Zhao, Y. Ma, T. Li, Z. Dong, Y. Wang, Modification of carbon felt anodes using double-oxidant HNO3/H2O2 for application in microbial fuel cells, Rsc Adv, 8 (2018) 2059-2064.

[230] A. Magrez, S. Kasas, V. Salicio, N. Pasquier, J.W. Seo, M. Celio, S. Catsicas, B. Schwaller, L. Forró, Cellular Toxicity of Carbon-Based Nanomaterials, Nano Letters, 6 (2006) 1121-1125.

[231] D. Jiang, B. Li, Granular activated carbon single-chamber microbial fuel cells (GAC-SCMFCs): A design suitable for large-scale wastewater treatment processes, Biochemical Engineering Journal, 47 (2009) 31-37.

[232] Y. Fu, J. Yu, Y. Zhang, Y. Meng, Graphite coated with manganese oxide/multiwall carbon nanotubes composites as anodes in marine benthic microbial fuel cells, Applied Surface Science, 317 (2014) 84-89.

[233] X.-W. Liu, X.-F. Sun, Y.-X. Huang, G.-P. Sheng, S.-G. Wang, H.-Q. Yu, Carbon nanotube/chitosan nanocomposite as a biocompatible biocathode material to enhance the electricity generation of a microbial fuel cell, Energ Environ Sci, 4 (2011) 1422-1427.

[234] J.E. Mink, J.P. Rojas, B.E. Logan, M.M. Hussain, Vertically Grown Multiwalled Carbon Nanotube Anode and Nickel Silicide Integrated High Performance Microsized (1.25 μL) Microbial Fuel Cell, Nano Letters, 12 (2012) 791-795.

[235] J.-J. Sun, H.-Z. Zhao, Q.-Z. Yang, J. Song, A. Xue, A novel layer-by-layer self-assembled carbon nanotube-based anode: Preparation, characterization, and application in microbial fuel cell, Electrochim Acta, 55 (2010) 3041-3047.

[236] C. Dumas, A. Mollica, D. Féron, R. Basséguy, L. Etcheverry, A. Bergel, Marine microbial fuel cell: Use of stainless steel electrodes as anode and cathode materials, Electrochim Acta, 53 (2007) 468-473.

[237] Z. Du, H. Li, T. Gu, A state of the art review on microbial fuel cells: A promising technology for wastewater treatment and bioenergy, Biotechnology Advances, 25 (2007) 464-482.

[238] D.A. Jadhav, A.N. Ghadge, M.M. Ghangrekar, Simultaneous organic matter removal and disinfection of wastewater with enhanced power generation in microbial fuel cell, Bioresource Technol, 163 (2014) 328-334.

[239] A.N. Ghadge, D.A. Jadhav, H. Pradhan, M.M. Ghangrekar, Enhancing waste activated sludge digestion and power production using hypochlorite as catholyte in clayware microbial fuel cell, Bioresource Technol, 182 (2015) 225-231.

[240] L. Yue, W. Li, F. Sun, L. Zhao, L. Xing, Highly hydroxylated carbon fibres as electrode materials of all-vanadium redox flow battery, Carbon, 48 (2010) 3079-3090.

[241] W. Li, J. Liu, C. Yan, Multi-walled carbon nanotubes used as an electrode reaction catalyst for VO2+/VO2+ for a vanadium redox flow battery, Carbon, 49 (2011) 3463-3470.

[242] H.R. Jiang, M.C. Wu, Y.X. Ren, W. Shyy, T.S. Zhao, Towards a uniform distribution of zinc in the negative electrode for zinc bromine flow batteries, Appl Energ, 213 (2018) 366-374.

[243] K. Wang, B. Ma, X. Li, Y. Wang, L. An, Effect of Pyrolysis Temperature on the Structure and Conduction of Polymer-Derived SiC, J Am Ceram Soc, 97 (2014) 2135-2138.

[244] M. Pierra, M. Golozar, X. Zhang, A. Prévoteau, M. De Volder, D. Reynaerts, K. Rabaey, Growth and current production of mixed culture anodic biofilms remain unaffected by sub-microscale surface roughness, Bioelectrochemistry, 122 (2018) 213-220.

[245] K. Fricke, F. Harnisch, U. Schröder, On the use of cyclic voltammetry for the study of anodic electron transfer in microbial fuel cells, Energ Environ Sci, 1 (2008) 144-147.

[246] Z.A. ALOthman, A Review: Fundamental Aspects of Silicate Mesoporous Materials, Materials, 5 (2012) 2874-2902.

[247] G. Zhao, T.S. Zhao, J. Xu, Z. Lin, X. Yan, Impact of pore size of ordered mesoporous carbon FDU-15-supported platinum catalysts on oxygen reduction reaction, Int J Hydrogen Energ, 42 (2017) 3325-3334.

[248] X.D. Zhang, X.X. Huang, G.W. Wen, X. Geng, J.D. Zhu, T. Zhang, H.W. Bai, Novel SiOC nanocomposites for high-yield preparation of ultra-large-scale SiC nanowires, Nanotechnology, 21 (2010).

[249] K.-K. Türk, I. Kruusenberg, J. Mondal, P. Rauwel, J. Kozlova, L. Matisen, V. Sammelselg, K. Tammeveski, Oxygen electroreduction on MN4-macrocycle modified graphene/multi-walled carbon nanotube composites, Journal of Electroanalytical Chemistry, 756 (2015) 69-76.

[250] Q. Cheng, L. Yang, L. Zou, Z. Zou, C. Chen, Z. Hu, H. Yang, Single Cobalt Atom and N Codoped Carbon Nanofibers as Highly Durable Electrocatalyst for Oxygen Reduction Reaction, ACS Catalysis, 7 (2017) 6864-6871.

[251] Y. Qian, Z. Liu, H. Zhang, P. Wu, C. Cai, Active Site Structures in Nitrogen-Doped Carbon-Supported Cobalt Catalysts for the Oxygen Reduction Reaction, Acs Appl Mater Inter, 8 (2016) 32875-32886.

[252] Z. Luo, S. Lim, Z. Tian, J. Shang, L. Lai, B. MacDonald, C. Fu, Z. Shen, T. Yu, J. Lin, Pyridinic N doped graphene: synthesis, electronic structure, and electrocatalytic property, Journal of Materials Chemistry, 21 (2011) 8038-8044.

[253] D.M.K. Abro, P. Dablé, F. Cortés-Salazar, V. Amstutz, H. Girault, Characterization of Surface State of Inert Particles: Case of Si and SiC, pp. 62-72-62-72.

[254] S. Roualdes, R. Berjoan, J. Durand, 29Si NMR and Si2p XPS correlation in polysiloxane membranes prepared by plasma enhanced chemical vapor deposition, Sep Purif Technol, 25 (2001) 391-397.

[255] A. Zhu, P. Tan, L. Qiao, Y. Liu, Y. Ma, X. Xiong, J. Pan, Multiple active components, synergistically driven cobalt and nitrogen Co-doped porous carbon as high-performance oxygen reduction electrocatalyst, Inorganic Chemistry Frontiers, 4 (2017) 1748-1756.

[256] T. Sun, L. Xu, S. Li, W. Chai, Y. Huang, Y. Yan, J. Chen, Cobalt-nitrogen-doped ordered macro-/mesoporous carbon for highly efficient oxygen reduction reaction, Applied Catalysis B: Environmental, 193 (2016) 1-8.

[257] K. Liu, S. Kattel, V. Mao, G. Wang, Electrochemical and Computational Study of Oxygen Reduction Reaction on Nonprecious Transition Metal/Nitrogen Doped Carbon Nanofibers in Acid Medium, The Journal of Physical Chemistry C, 120 (2016) 1586-1596.

[258] Q. Zhao, Q. Ma, F. Pan, J. Guo, J. Zhang, Facile synthesis of N-doped carbon nanosheet-encased cobalt nanoparticles as efficient oxygen reduction catalysts in alkaline and acidic media, Ionics, 22 (2016) 2203-2212.

[259] A. Sarapuu, L. Samolberg, K. Kreek, M. Koel, L. Matisen, K. Tammeveski, Cobalt- and iron-containing nitrogen-doped carbon aerogels as non-precious metal catalysts for electrochemical reduction of oxygen, Journal of Electroanalytical Chemistry, 746 (2015) 9-17.

[260] V.L. Nguyen, N.B. Laidani, G.D. Soraru, N-doped polymer-derived Si(N)OC: The role of the N-containing precursor, J Mater Res, 30 (2015) 770-781.

[261] K. Yamamoto, Y. Koga, S. Fujiwara, XPS studies of amorphous SiCN thin films prepared by nitrogen ion-assisted pulsed-laser deposition of SiC target, Diam Relat Mater, 10 (2001) 1921-1926.

[262] S.H. Gage, D.A. Ruddy, S. Pylypenko, R.M. Richards, Deep eutectic solvent approach towards nickel/nickel nitride nanocomposites, Catalysis Today, 306 (2018) 9-15.

[263] H.-S. Oh, H. Kim, The role of transition metals in non-precious nitrogen-modified carbon-based electrocatalysts for oxygen reduction reaction, J Power Sources, 212 (2012) 220-225.

[264] R. Zhang, L. Liu, J. Zhang, W. Wang, F. Ma, R. Li, L. Gao, Fabrication of the pyrolyzing carbon-supported cobalt–dicyandiamide electrocatalysts and study on the active sites and mechanism for oxygen reduction in alkaline electrolyte, J Solid State Electr, 19 (2015) 1695-1707.

[265] M. Mooste, E. Kibena-Põldsepp, L. Matisen, K. Tammeveski, Oxygen Reduction on Anthraquinone Diazonium Compound Derivatised Multi-walled Carbon Nanotube and Graphene Based Electrodes, Electroanalysis, 29 (2017) 548-558.

[266] M. Mooste, E. Kibena-Põldsepp, B.D. Ossonon, D. Bélanger, K. Tammeveski, Oxygen reduction on graphene sheets functionalised by anthraquinone diazonium compound during electrochemical exfoliation of graphite, Electrochim Acta, 267 (2018) 246-254.

[267] M. Vikkisk, I. Kruusenberg, U. Joost, E. Shulga, I. Kink, K. Tammeveski, Electrocatalytic oxygen reduction on nitrogen-doped graphene in alkaline media, Applied Catalysis B: Environmental, 147 (2014) 369-376.

[268] R. Sibul, E. Kibena-Põldsepp, S. Ratso, M. Kook, M. Käärik, M. Merisalu, P. Paiste, J. Leis, V. Sammelselg, K. Tammeveski, Nitrogen-doped carbon-based electrocatalysts synthesised by ball-milling, Electrochem Commun, 93 (2018) 39-43.

[269] N. Gavrilov, M. Momčilović, A.S. Dobrota, D.M. Stanković, B. Jokić, B. Babić, N.V. Skorodumova, S.V. Mentus, I.A. Pašti, A study of ordered mesoporous carbon doped with Co and Ni as a catalyst of oxygen reduction reaction in both alkaline and acidic media, Surface and Coatings Technology, 349 (2018) 511-521.

[270] A. Abdelwahab, J. Castelo-Quibén, J.F. Vivo-Vilches, M. Pérez-Cadenas, F.J. Maldonado-Hódar, F. Carrasco-Marín, A.F. Pérez-Cadenas, Electrodes Based on Carbon Aerogels Partially Graphitized by Doping with Transition Metals for Oxygen Reduction Reaction, Nanomaterials (Basel), 8 (2018) 266.

[271] S. Liu, C. Deng, L. Yao, H. Zhong, H. Zhang, The key role of metal dopants in nitrogen-doped carbon xerogel for oxygen reduction reaction, J Power Sources, 269 (2014) 225-235.

[272] K. Wan, Z.P. Yu, X.H. Li, M.Y. Liu, G. Yang, J.H. Piao, Z.X. Liang, pH Effect on Electrochemistry of Nitrogen-Doped Carbon Catalyst for Oxygen Reduction Reaction, Acs Catalysis, 5 (2015) 4325-4332.

[273] A.J. Bard, L.R. Faulkner, Electrochemical Methods: Fundamentals and Applications, 2nd Edition, Wiley Textbooks2000.

[274] R.E. Davis, G.L. Horvath, C.W. Tobias, The solubility and diffusion coefficient of oxygen in potassium hydroxide solutions, Electrochim Acta, 12 (1967) 287-297.

[275] S. Gottesfeld, I.D. Raistrick, S. Srinivasan, Oxygen Reduction Kinetics on a Platinum Rde Coated with a Recast Nafion1 Film, J Electrochem Soc, 134 (1987) 1455-1462.

[276] F. King, C.D. Litke, Y. Tang, Effect of interfacial pH on the reduction of oxygen on copper in neutral NaClO4 solution, Journal of Electroanalytical Chemistry, 384 (1995) 105-113.

[277] D.R. Lide, CRC Handbook of Chemistry and Physics, 82nd Edition, Taylor & Francis2001.

[278] Y. Hao, Z. Lu, G. Zhang, Z. Chang, L. Luo, X. Sun, Cobalt-Embedded Nitrogen-Doped Carbon Nanotubes as High-Performance Bifunctional Oxygen Catalysts, Energy Technology, 5 (2017) 1265-1271.

[279] L.-B. Lv, T.-N. Ye, L.-H. Gong, K.-X. Wang, J. Su, X.-H. Li, J.-S. Chen, Anchoring Cobalt Nanocrystals through the Plane of Graphene: Highly Integrated Electrocatalyst for Oxygen Reduction Reaction, Chem Mater, 27 (2015) 544-549.

[280] Z. Deng, Q. Yi, G. Li, Y. Chen, X. Yang, H. Nie, NiCo-doped C-N nano-composites for cathodic catalysts of Zn-air batteries in neutral media, Electrochim Acta, 279 (2018) 1-9.

[281] C. Cao, L. Wei, M. Su, G. Wang, J. Shen, Enhanced power generation using nano cobalt oxide anchored nitrogen-decorated reduced graphene oxide as a high-performance air-cathode electrocatalyst in biofuel cells, Rsc Adv, 6 (2016) 52556-52563.

[282] S. Ratso, I. Kruusenberg, A. Sarapuu, M. Kook, P. Rauwel, R. Saar, J. Aruväli, K. Tammeveski, Electrocatalysis of oxygen reduction on iron- and cobalt-containing nitrogen-doped carbon nanotubes in acid media, Electrochim Acta, 218 (2016) 303-310.

[283] X. Tang, H.Y. Ng, Cobalt and nitrogen-doped carbon catalysts for enhanced oxygen reduction and power production in microbial fuel cells, Electrochim Acta, 247 (2017) 193-199.

[284] G. Liu, X. Li, P. Ganesan, B.N. Popov, Development of non-precious metal oxygen-reduction catalysts for PEM fuel cells based on N-doped ordered porous carbon, Applied Catalysis B: Environmental, 93 (2009) 156-165.

[285] Z. Liu, X. Fu, M. Li, F. Wang, Q. Wang, G. Kang, F. Peng, Novel silicon-doped, silicon and nitrogen-codoped carbon nanomaterials with high activity for the oxygen reduction reaction in alkaline medium, Journal of Materials Chemistry A, 3 (2015) 3289-3293.

[286] S.C. Abbas, K. Ding, Q. Liu, Y. Huang, Y. Bu, J. Wu, J. Lv, M.A. Ghausi, Y. Wang, Si–C–F decorated porous carbon materials: A new class of electrocatalysts for the oxygen reduction reaction, Journal of Materials Chemistry A, 4 (2016) 7924-7929.

Appendix

A.1 Supporting information for Chapter 3

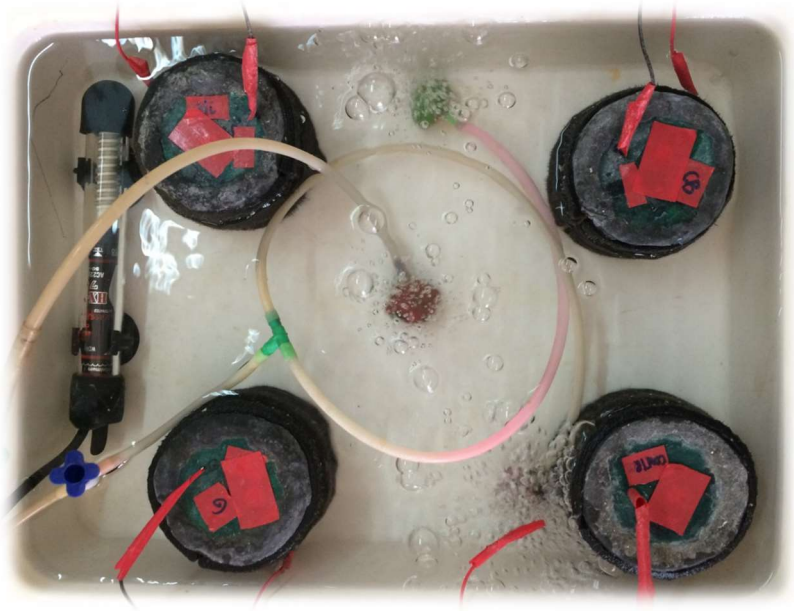

Figure A.1.1 Experimental setup of the four MFCs working with the different anodes.

A.2 Supporting information for Chapter 4

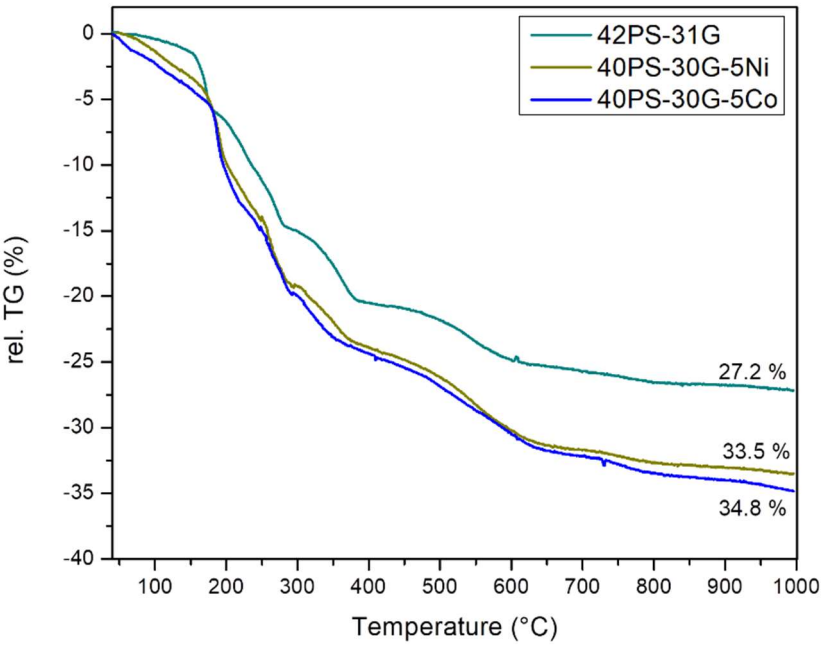

Figure A.2.1 Thermogravimetric analysis (TGA) of cross-linked graphite- and graphite-Co/Ni-containing electrode materials.

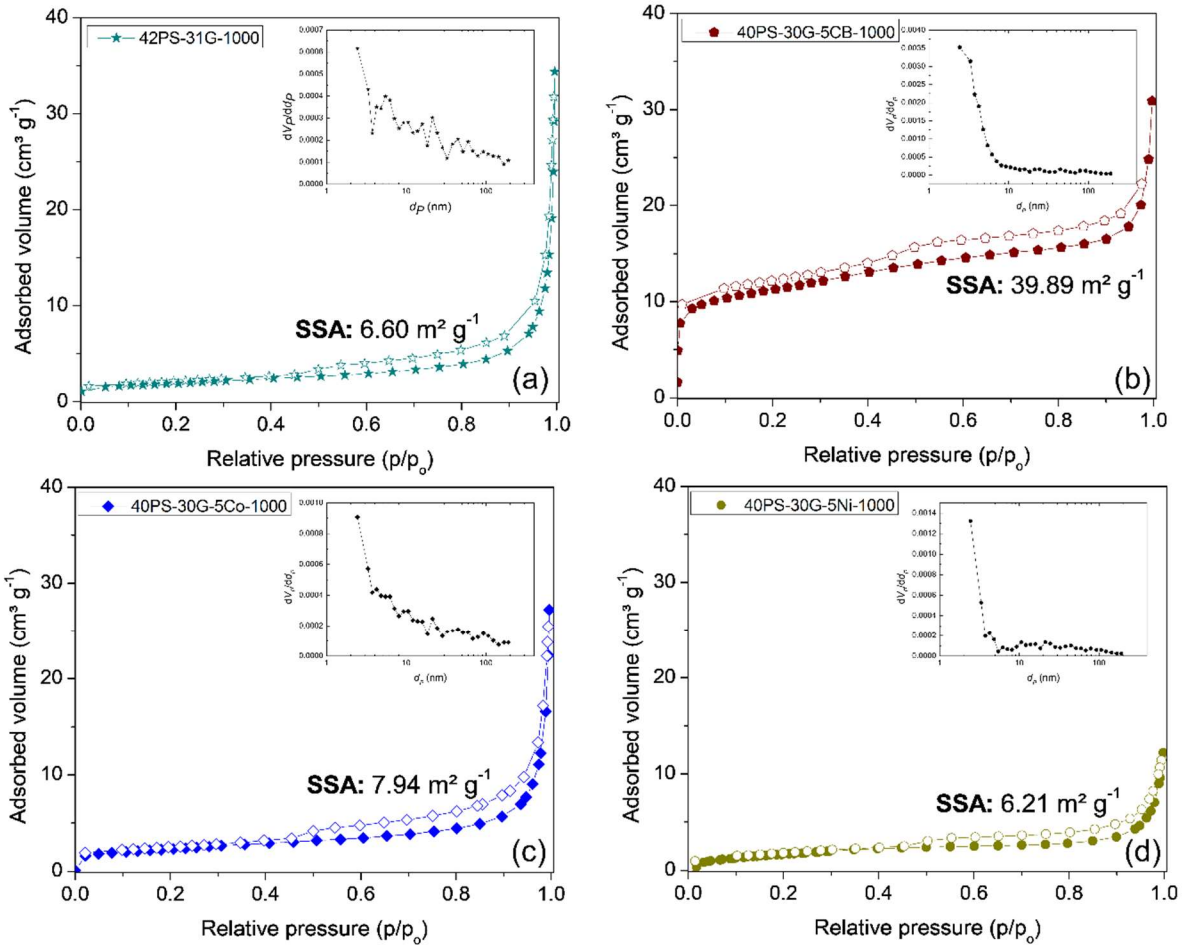

Figure A.2.2 Nitrogen adsorption-desorption isotherms, SSAs and pore size distribution of carbon-based fillers- (a, b) and Co/Ni-containing (c, d) electrode materials pyrolyzed at 1000 °C.

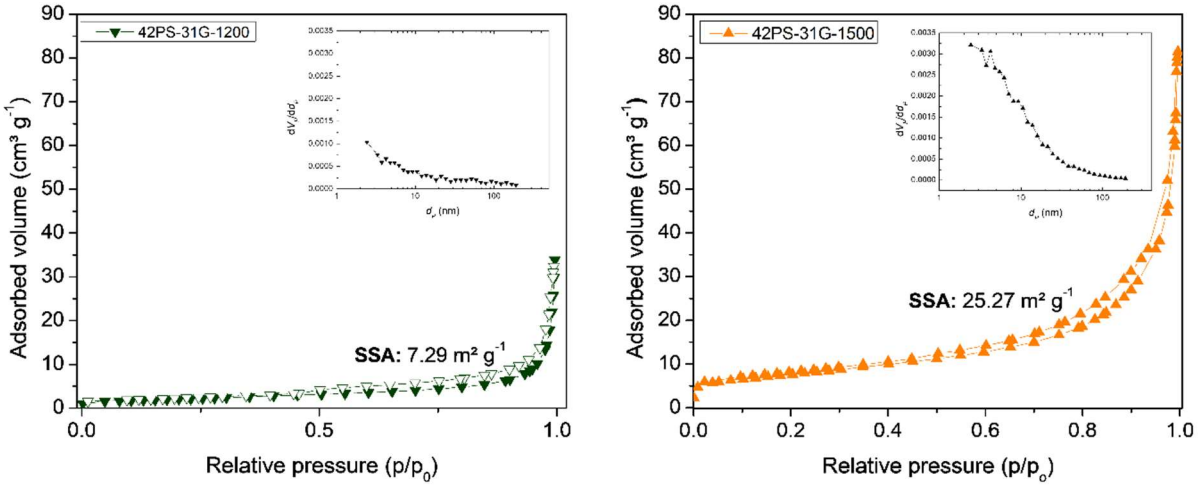

Figure A.2.3 Nitrogen adsorption-desorption isotherms, SSAs and pore size distribution of graphite-containing electrode materials pyrolyzed at 1200 °C and 1500 °C.

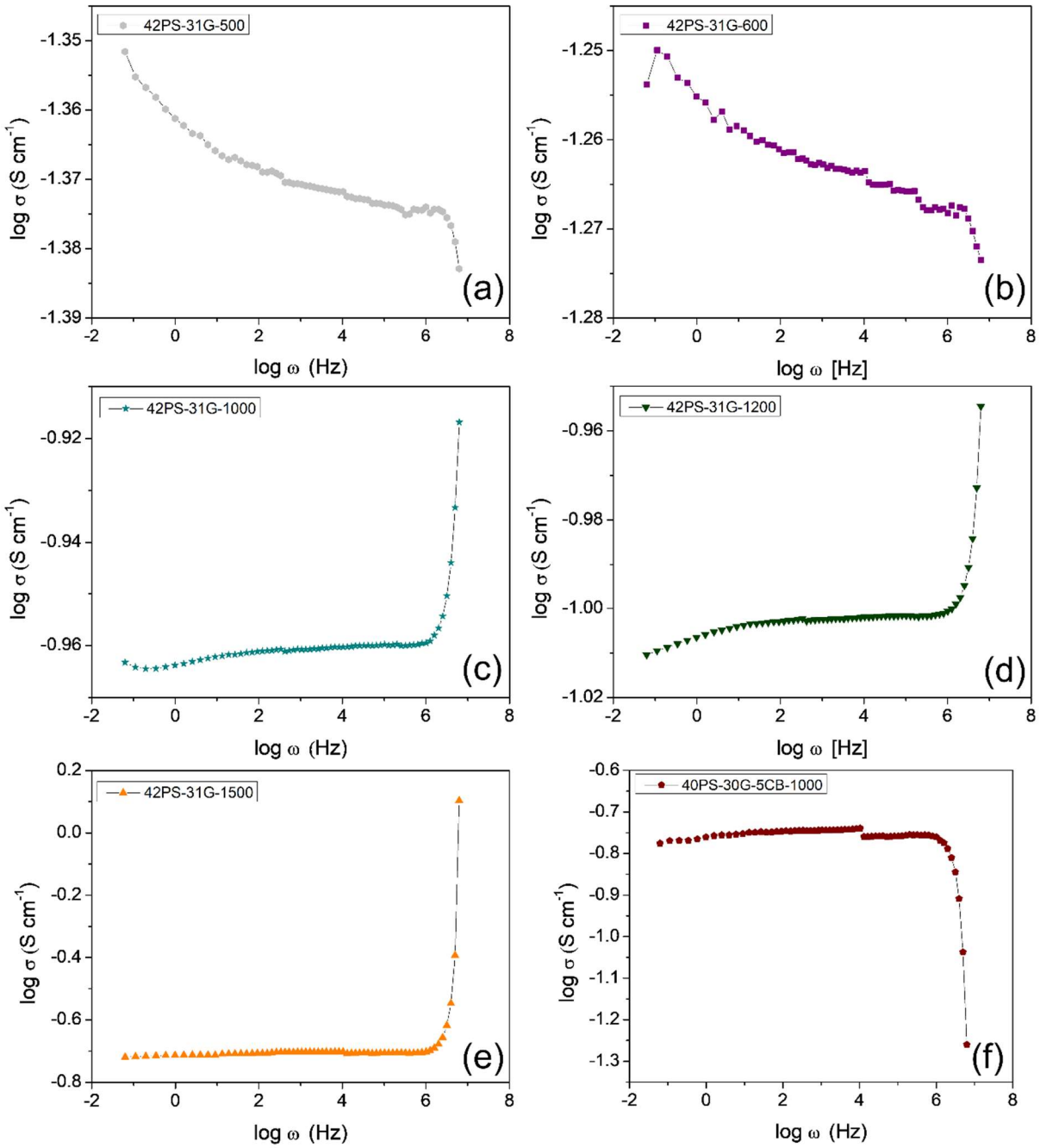

Figure A.2.4 Conductance spectra recorded at room temperature for graphite-containing materials pyrolyzed at 500, 600, 1000, 1200, 1500 °C (a-e) and graphite-carbon black-containing electrode pyrolyzed at 1000 °C (f).

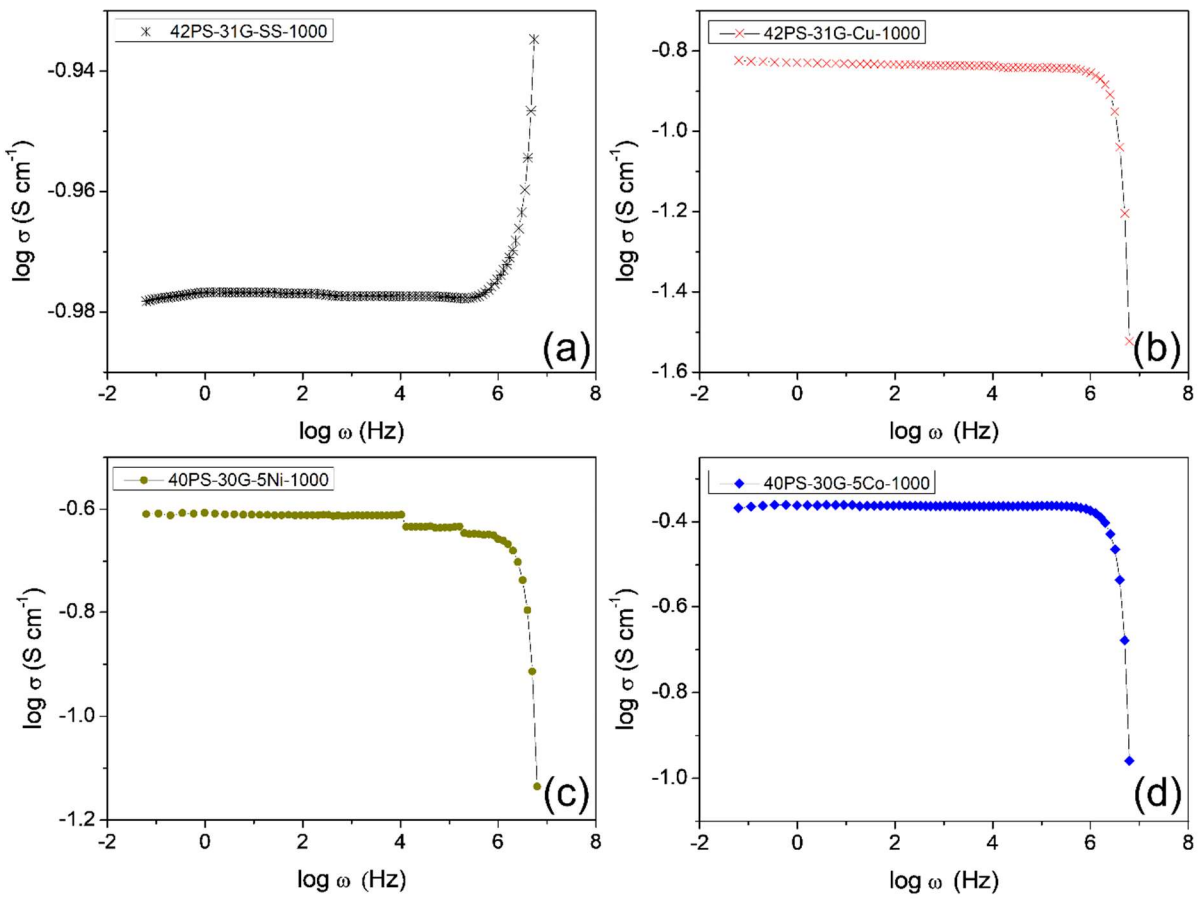

Figure A.2.5 Conductance spectra recorded at room temperature for electrodes with integrated SS/Cu metallic grids (a, b) and Co/Ni-containing electrodes (c, d) pyrolyzed at 1000 °C.

A.3 Supporting information for Chapter 5

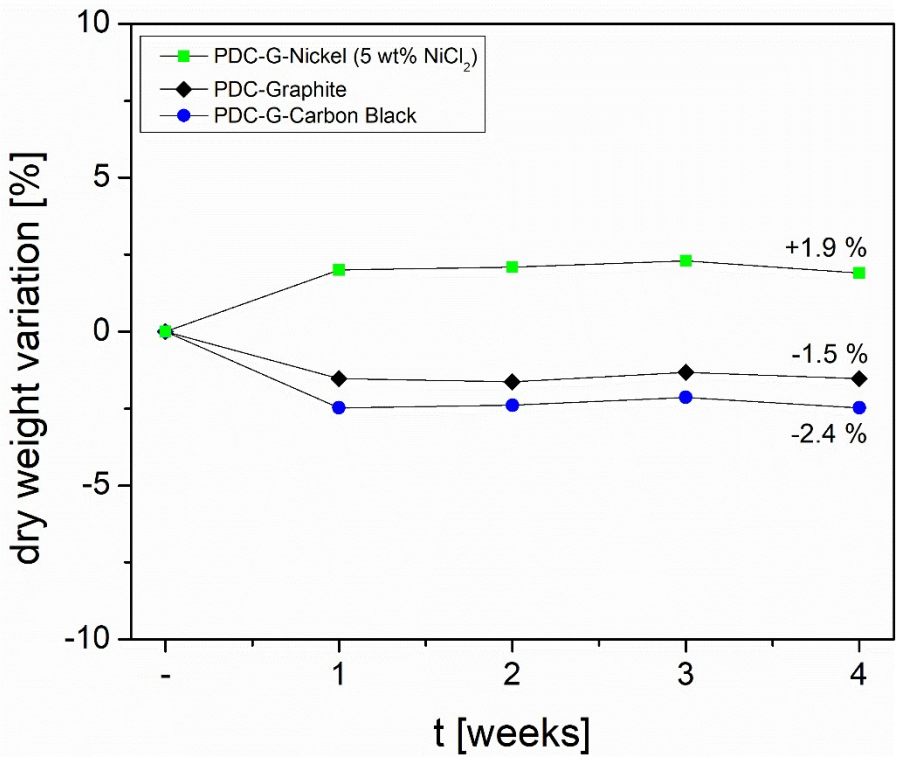

Figure A.3.1. Chemical stability tests in phosphate buffer solution (pH 7) of the PDC-based anode materials.

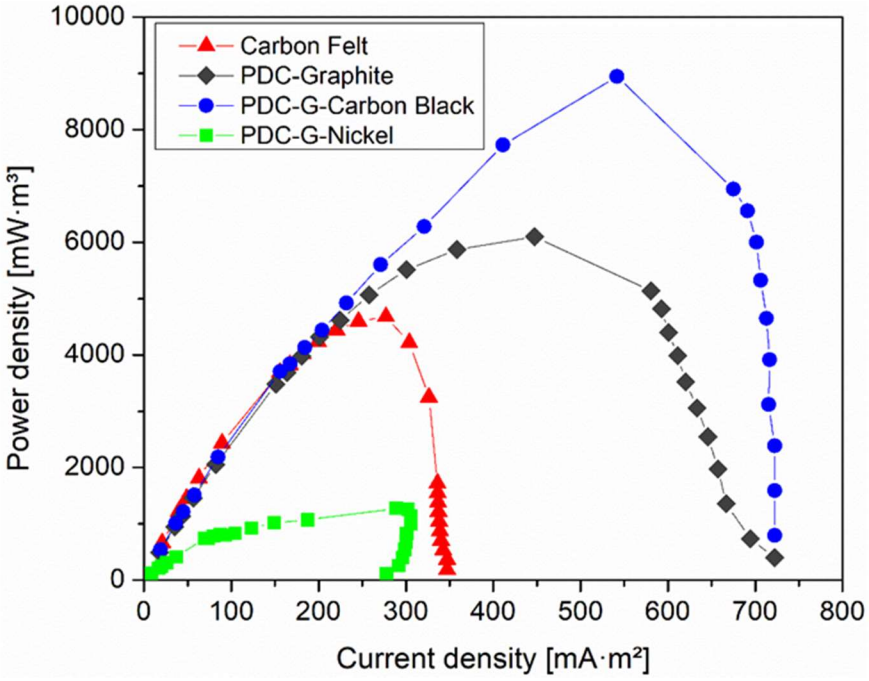

Figure A.3.2 Polarization curves of the PDC-based anodes and carbon felt normalized to the volume of the MFC.

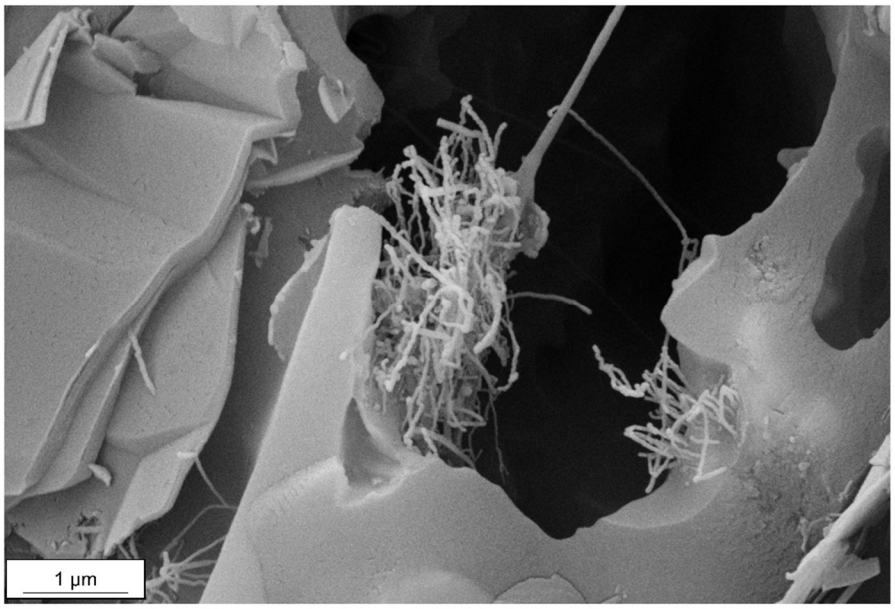

Figure A.3.3. Carbon nanotubes formation in the PDC-G-Nickel anode material.

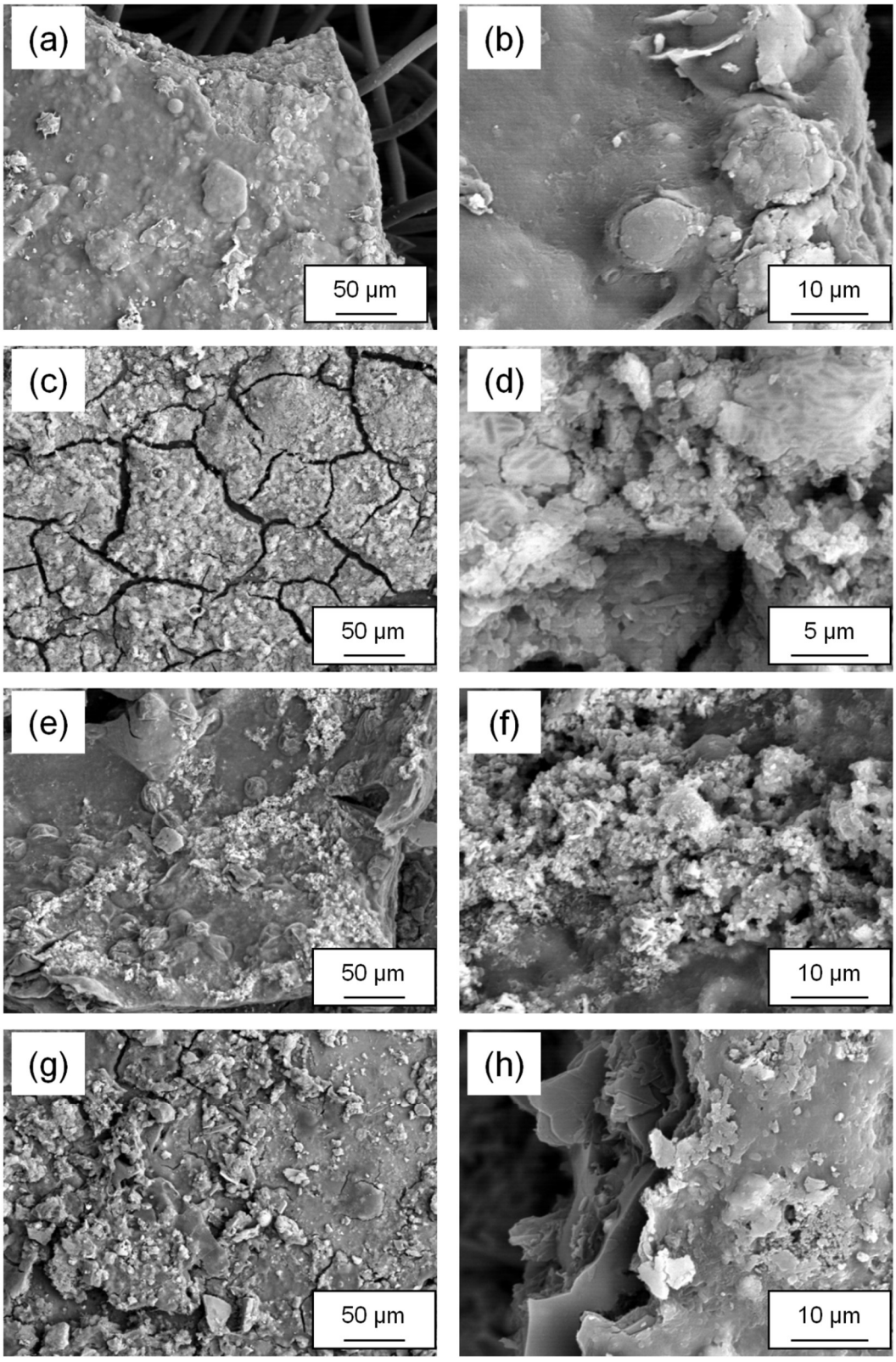

Figure A.3.4. SEM images of the biofilm formed on the carbon felt (a, b), PDC-Graphite (c, d), PDC-G-Carbon Black (e, f) and PDC-G-Nickel (g, h) anodes.

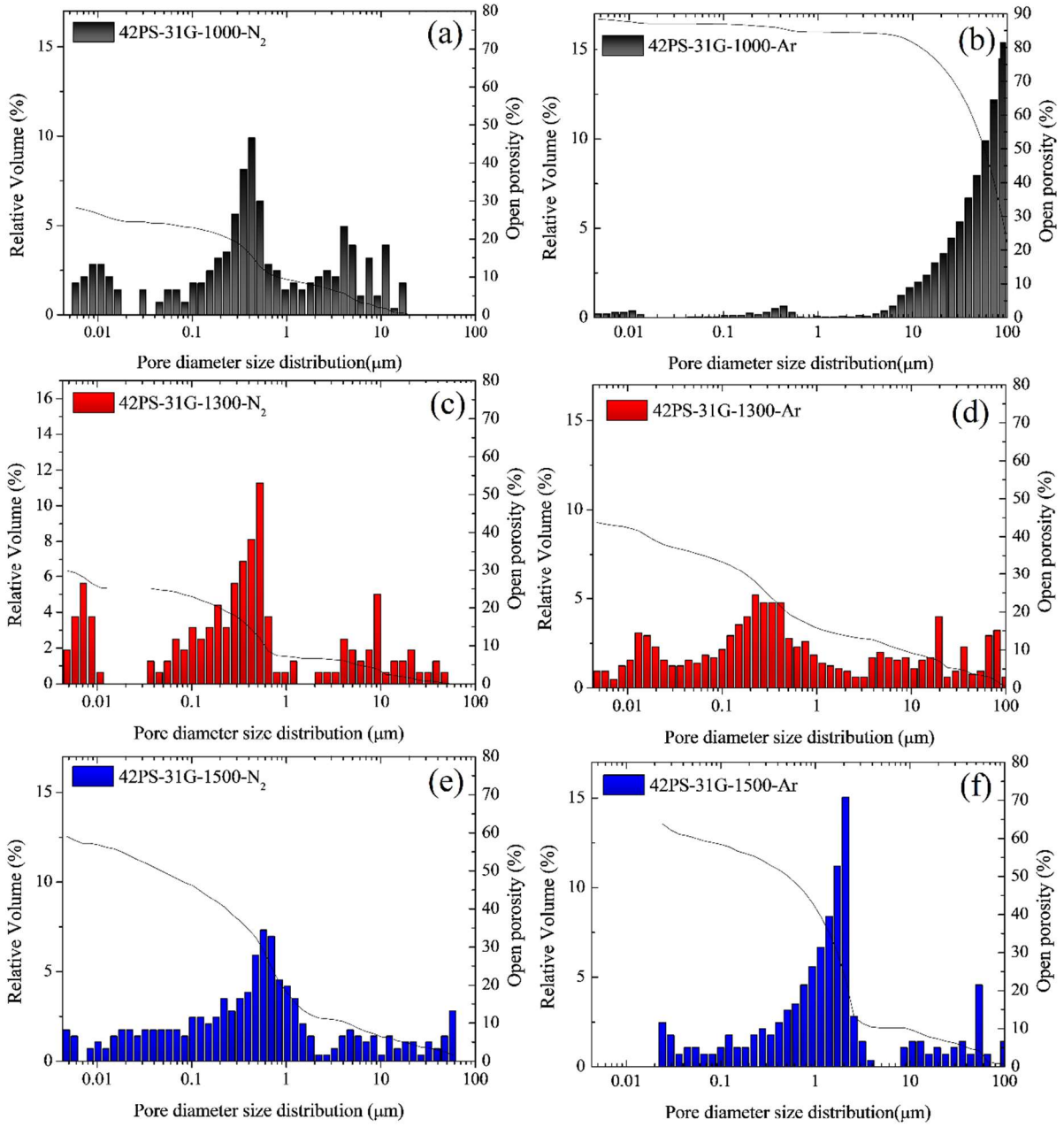

Figure A.3.5. Relative pore volume, pore size distribution and open porosity of pyrolyzed PDC layers under nitrogen (a, c, e) and argon (b, d, f).

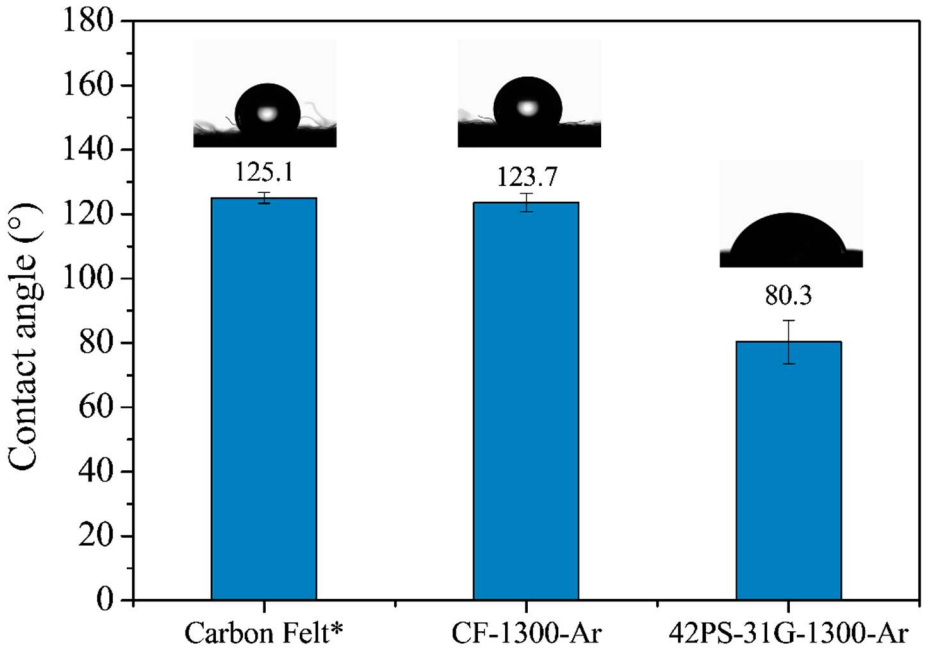

Figure A.3.6. Contact angle of non-pyrolyzed carbon felt, pyrolyzed carbon felt and PDC layer (argon, 1300 °C).

Roughness characterization

The materials were quantitatively evaluated with a profilometer (Sensorfar PLμ2300) and software (SensoMap Plus 5.0) with respect to Ra (average roughness). Five different regions were evaluated in each specimen and the final value is the arithmetic mean among them. During the data acquisition, all experimental parameters, i.e. voltage, magnification, were kept constant.

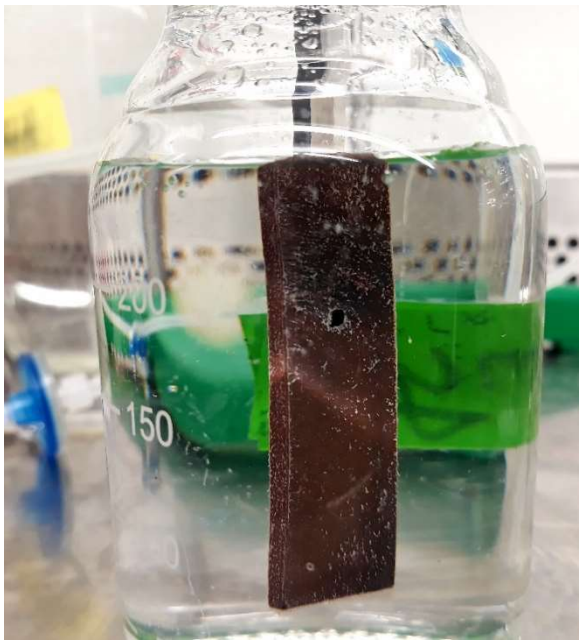

Figure A.3.7. Image of the reddish biofilm formed on the SiOC-based anodes.

A.4 Supporting information for Chapter 6

Table A.4.1. Elemental composition (at.%) determined from EDX and XPS analysis of the PDC-based electrocatalysts, respectively.

Electrocatalyst	Si	O	C	N	Mo	Ni	Co
EDX results							
PDC	6.4	23.7	67.5	2.3	0.1	-	-
PDC-Ni	5.5	20.3	71.1	2.4	0.3	0.3	-
PDC-Co	6.7	21.0	69.1	2.1	0.4	-	0.4
PDC-N	9.5	22.2	60.9	7.0	0.1	-	-
PDC-Ni-N	5.3	18.1	70.1	5.8	0.3	0.1	-
PDC-Co-N	6.6	15.6	70.7	6.0	0.3	-	0.3
XPS results							
PDC	3.3	8.1	88.6	-	-	-	-
PDC-Ni	9.3	11.2	79.3	-	-	0.2	-
PDC-Co	7.2	13.7	78.9	-	-	-	0.2
PDC-N	2.8	7.3	87.1	2.8	-	-	-
PDC-Ni-N	5.7	8.4	80.6	5.1	-	0.2	-
PDC-Co-N	6.9	10.2	75.7	7.0	-	-	0.2

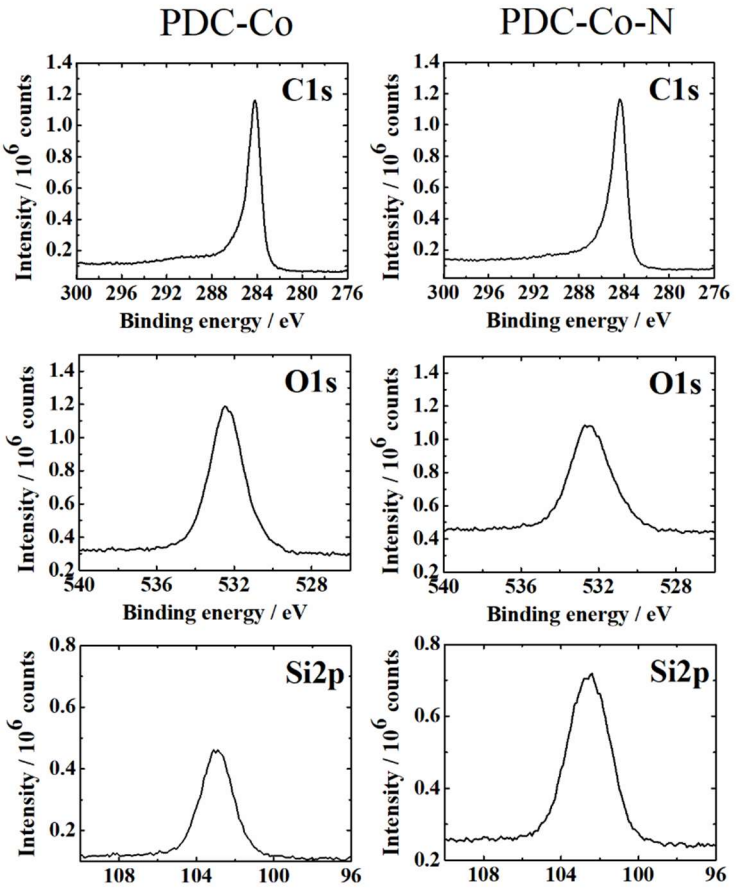

Figure A.4.1. XPS high resolution spectra in the C1s, O1s and Si2p regions for PDC-Co and PDC-Co-N catalyst material on the glassy carbon electrode.

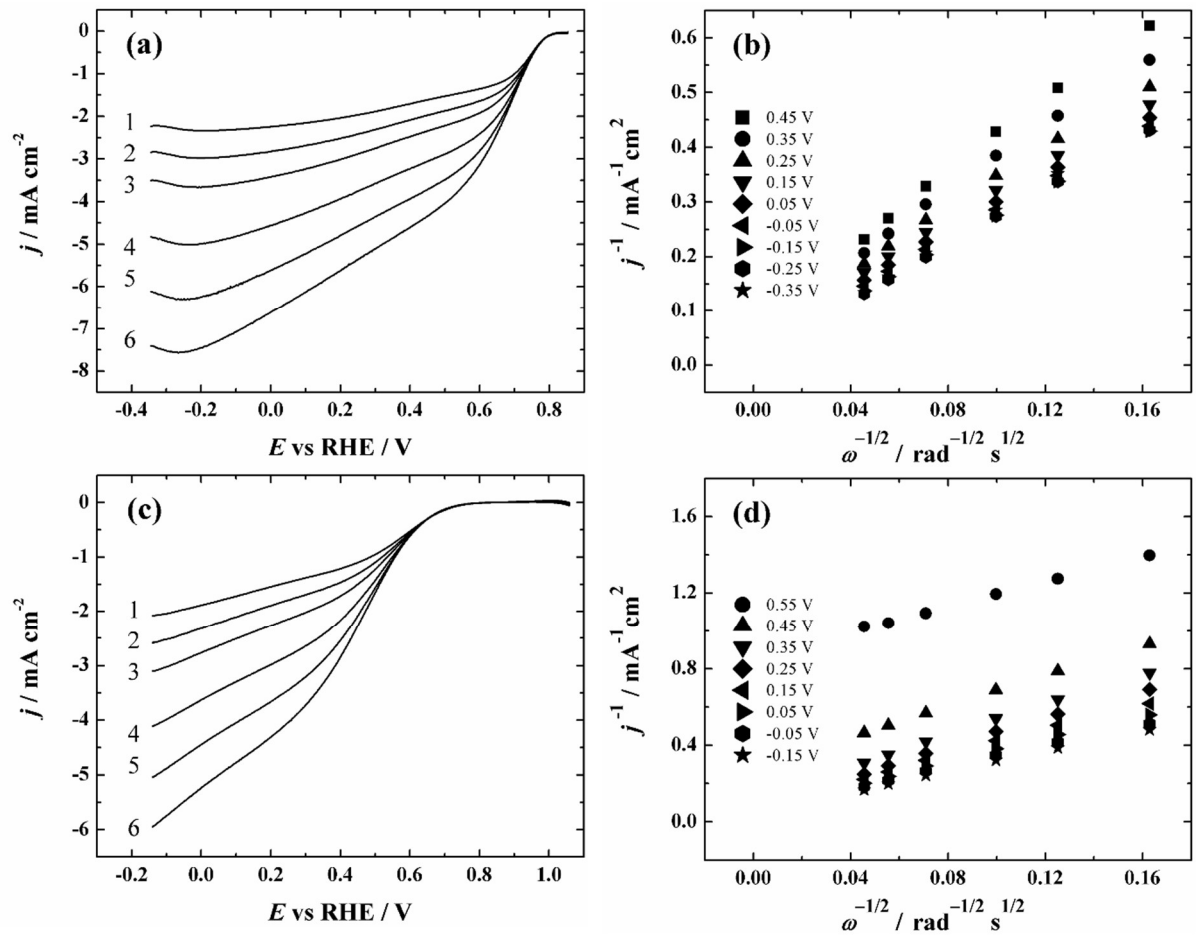

Figure A.4.2 RDE voltammetry curves for oxygen reduction on GC/PDC-Co-N electrode in O_2-saturated 0.1 M PBS containing 0.1 M $NaClO_4$ (pH = 7) (a) and 0.5 M H_2SO_4 (pH = 0.3) (c) (ω: *1*-360; *2*-610; *3*-960; *4*-1900; *5*-3100; *6*-4600 rpm, v = 10 mV s^{-1}). Koutecky-Levich plots for O_2 reduction in 0.1 M PBS containing 0.1 M $NaClO_4$ (pH = 7) (b) and 0.5 M H_2SO_4 (d) derived from the RDE data shown in Fig. A.4.2a and A.4.2c, respectively.

Table A.4.2 Comparison of the ORR onset potential (E_{onset}), half-wave potential ($E_{1/2}$) and electron transfer number (n) in O_2-saturated 0.1 M KOH for different Co- and N-codoped catalyst materials prepared by pyrolysis. All the potentials are given with respect to the RHE.

Catalyst material (and preparation procedure)	**Catalyst loading (mg cm^{-2})**	E_{onset} **(V)**	$E_{1/2}$ **(V)**	***n***	**Ref**
GC/PDC-Co-N (Polymer-derived Co-SiOC ceramic nanomaterial sonicated along with DCDA and further pyrolysed at 800 °C in N_2 flow.)	0.2	0.90	0.80	4	This work
Co@NCNT-700 (Synthesized via one-step pyrolysis of $CoCl_2{\times}6H_2O$ and DCDA.)	0.2	0.89	-	3.9	1
Co_{15}-N-C800 (Pyrolysis of 1-ethyl-3-methyl-imidazolium dicyanamide and $Co(NO_3)_2$, later purification by refluxing in 2M H_2SO_4 solution.)	0.49	0.97	0.82	4	2
Co-NCA (Sol–gel polymerisation of organic precursors, followed by insertion of Co by ion exchange and subsequent carbonisation.)	0.2	0.91	0.80	4	3
Co-N-OMMC-0.6 (Dual-templating synthesis in a one-pot controllable procedure by the use of silica colloidal crystal (opal) as a macroporous mold and copolymer as a mesoporous template.)	0.22	-	0.83	3.9	4
Co/N/CDC (Synthesised via pyrolysis of titanium carbide derived carbon, DCDA and $CoCl_2$.)	0.1	0.96	-	4	5
$Co_{0.2}$–$N_{2.35}$/$C_{0.25}$–800 (DCDA and $Co(OAc)_2{\times}4H_2O$ mixed, then C-material (BP2000, Cabot) was added and the mixture pyrolysed for 2 h under N_2 flow.)	-	0.93	-	4	6
NCN-Co-0.1 (Corn starch, DCDA and $Co(OAc)_2{\times}4H_2O$ were dissolved in water and after drying pyrolysed in Ar flow.)	0.28	0.93	0.82	4	7
CoNPs@NG ($CoCl_2$, glucose and DCDA heated to 1000° C and held at that temperature for 1 h under N_2 flow.)	0.25	1.06	1.01	4	8
Co/N/MWCNT-1 (Pyrolysis of $CoCl_2$, DCDA and MWCNTs at 800°C under inert conditions.)	0.1	0.96	0.84	4	9
Co/N-C-800 (Solution of $Co(Ac)_2$, dopamine hydrochloride and NH_4OH was mixed and stirred. Firstly, hydrothermal reaction in autoclave, after that carbonisation at 800°C under Ar flow.)	0.25	0.83	-	4	10
Co-NCNT/NrGO-800 (Graphene oxide (GO), $CoCl_2{\times}6\ H_2O$ and melamine were mixed, stirred	0.14	0.91	0.82	3.9	11

and dried. The resulting solid was ground and calcined in two steps (550 and 800 °C) in N_2 flow.)					
$NiCo_2O_4$-rGO ($NiCo_2O_4$ nanocrystals grown on reduced GO sheets through polyol process together with a thermal annealing at 300 °C in air.)	0.4	0.88	-	3.8	12
Co/N-HCOs ($Co(CH_3COO)_2 \times 4H_2O$ was added to 2,6-bis(benzimidazol-2-yl)pyridine solution in ethanol. Formed yellow precipitate was washed, dried and heat-treated at 800 °C in N_2 atmosphere.)	0.27	0.92	0.81	4	13
Co@C-NCNTs (N-doped carbon nanotubes decorated with carbon-coated Co nanoparticles prepared by carbonisation at 800 °C and subsequent leaching in HF solution for 12 h.)	0.2	0.86	0.80	4	14
Co–N/Co–O@N–C (N-C prepared by pyrolysis at 900 °C in N_2 flow from copolymers. N-doped hollow carbon microspheres with cobalt nitrate and N-C heated at 300 °C for 1 h in air.)	0.2	0.93	-	4	15
Co-N/G 600 (Hydrothermal process using 2,4,6-triaminopyrimidine, GO and cobalt (II) acetate at 180 °C. Subsequent carbonisation in N_2 atmosphere at 600 °C.)	0.24	0.85	0.76	4	16
Co@C-N-120-900 (D-glucose and cobalt acetate tetrahydrate were added into the g-C_3N_4 (prepared from urea) solution, further hydrothermal treatment 120 °C, final calcination at 900 °C in Ar flow.)	0.2	0.96	0.85	4	17
Co-N/CNFs (Electrospun material from polyacrylonitrile, 4-dimethylaminopyridine and cobalt acetate solution in dimethylformamide. Material stabilised at 250 °C in air, after that pyrolysed in N_2 atmosphere at 950 °C.)	0.2	0.92	0.82	4	18
Co–N-pCNs (Polymerisable ionic liquid $[HVim]NO_3$ was mixed with the ethanol solution of $Co(NO_3)_2$, then dried and pyrolysed at 600 °C in N_2 flow, later treated in 0.5 M HNO_3.)	0.26	0.96	0.80	3.9	19
Co-NGX 900 (Cobalt acetate, urea, melamine and formaldehyde were added to aqueous dispersion of GO and stirred. Firstly, hydrothermal treatment in autoclave and subsequent pyrolysis at 900 °C in Ar atmosphere.)	0.28	0.97	0.84	4	20
N/Co/CMK-3 plate (The solution in water of ordered mesoporous carbon (CMK-3) and	0.14	0.88	0.77	3.9	21

$Co(NO_3)_2$ was ultrasonicated and dried. Further, the material was pyrolysed under NH_3 at 800 °C.)					

References

1. Y. C. Hao, Z. Y. Lu, G. X. Zhang, Z. Chang, L. Luo and X. M. Sun, *Energy Technol-GER*, 2017, **5**, 1265-1271.
2. Y. D. Qian, Z. Liu, H. Zhang, P. Wu and C. X. Cai, *ACS Appl. Mater. Interfaces*, 2016, **8**, 32875-32886.
3. A. Sarapuu, L. Samolberg, K. Kreek, M. Koel, L. Matisen and K. Tammeveski, *J. Electroanal. Chem.*, 2015, **746**, 9-17.
1. Y. C. Hao, Z. Y. Lu, G. X. Zhang, Z. Chang, L. Luo and X. M. Sun, *Energy Technol-GER*, 2017, **5**, 1265-1271.
2. Y. D. Qian, Z. Liu, H. Zhang, P. Wu and C. X. Cai, *ACS Appl. Mater. Interfaces*, 2016, **8**, 32875-32886.
3. A. Sarapuu, K. Kreek, K. Kisand, M. Kook, M. Uibu, M. Koel and K. Tammeveski, *Electrochim. Acta*, 2017, **230**, 81-88.
4. T. T. Sun, L. B. Xu, S. Y. Li, W. X. Chai, Y. Huang, Y. S. Yan and J. F. Chen, *Appl. Catal., B*, 2016, **193**, 1-8.
5. S. Ratso, I. Kruusenberg, M. Kaarik, M. Kook, L. Puust, R. Saar, J. Leis and K. Tammeveski, *J. Power Sources*, 2018, **375**, 233-243.
6. R. Zhang, L. Liu, J. Zhang, W. Y. Wang, F. Ma, R. F. Li and L. Z. Gao, *J. Solid State Electrochem.*, 2015, **19**, 1695-1707.
7. Q. P. Zhao, Q. Ma, F. P. Pan, J. H. Guo and J. Y. Zhang, *Ionics*, 2016, **22**, 2203-2212.
8. L. B. Lv, T. N. Ye, L. H. Gong, K. X. Wang, J. Su, X. H. Li and J. S. Chen, *Chem. Mater.*, 2015, **27**, 544-549.
9. I. Kruusenberg, D. Ramani, S. Ratso, U. Joost, R. Saar, P. Rauwel, A. Kannan and K. Tammeveski, *Chemelectrochem*, 2016, **3**, 1455-1465.
10. Y. H. Su, Y. H. Zhu, H. L. Jiang, J. H. Shen, X. L. Yang, W. J. Zou, J. D. Chen and C. Z. Li, *Nanoscale*, 2014, **6**, 15080-15089.
11. C. T. Wei, H. J. Wang, K. Eid, J. Kim, J. H. Kim, Z. A. Alothman, Y. Yamauchi and L. Wang, *Chem. Eur. J.*, 2017, **23**, 637-643.
12. G. Q. Zhang, B. Y. Xia, X. Wang and X. W. Lou, *Adv. Mater.*, 2014, **26**, 2408-2412.
13. S. J. Chao, Z. Y. Bai, Q. Cui, H. Y. Yan, K. Wang and L. Yang, *Carbon*, 2015, **82**, 77-86.
14. R. Li, X. Z. Wang, Y. F. Dong, X. Pan, X. G. Liu, Z. B. Zhao and J. S. Qiu, *Carbon*, 2018, **132**, 580-588.
15. K. J. Lee, D. Y. Shin, A. Byeon, A. Lim, Y. S. Jo, A. Begley, D. H. Lim, Y. E. Sung, H. S. Park, K. H. Chae, S. W. Nam, K. Y. Lee and J. Y. Kim, *Nanoscale*, 2017, **9**, 15846-15855.
16. Q. Wang, W. H. Hu and Y. M. Huang, *Int. J. Hydrog. Energy*, 2017, **42**, 5899-5907.
17. A. Q. Zhu, P. F. Tan, L. Qiao, Y. J. Liu, Y. Ma, X. Xiong and J. Pan, *Inorg. Chem. Front.*, 2017, **4**, 1748-1756.
18. Q. Q. Cheng, L. J. Yang, L. L. Zou, Z. Q. Zou, C. Chen, Z. Hu and H. Yang, *ACS Catal.*, 2017, **7**, 6864-6871.
19. J. Gao, N. Ma, Y. M. Zheng, J. F. Zhang, J. Z. Gui, C. K. Guo, H. Q. An, X. Y. Tan, Z. Yin and D. Ma, *Chemcatchem*, 2017, **9**, 1601-1609.
20. D. L. Yu and X. Q. He, *J. Appl. Electrochem.*, 2017, **47**, 13-23.
21. V. M. Bau, X. J. Bo and L. P. Guo, *J. Energy Chem.*, 2017, **26**, 63-71.

Preparation of catalyst ink

The catalyst inks were prepared according to Bhowmick et al. [1], using the synthesized PDC-Co-N catalyst and Pt/C as a benchmark ORR catalyst at loading rate of 2 mg cm^{-2} of the cathodic surface area with activated carbon (AC Vulcan XC 72, Cabot Corporation, USA) as the carbon base material. The ink solution of the control contained only AC without any catalyst. Nafion® 117 (DuPont, USA) was used as binder and acetone as solvent. The catalyst inks were sprayed on the exposed side of the carbon felts using N_2 gas at 0.5 bar of applied pressure to ensure uniform concentration.

1. G.D. Bhowmick, Md.T. Noori, I. Das, B. Neethu, M.M. Ghangrekar, A. Mitra, Bismuth doped TiO_2 as an excellent photocathode catalyst to enhance the performance of microbial fuel cell, Int J Hydrogen Energ, 43 (2018) 7501-7510.

List of Supervised Students

In the dissertation the results from the supervision of the following student's works are included.

- **Internship**, "Investigation of the mixture of conductive fillers for the preparation of materials based on polysiloxanes", **Luiz Pedro Xavier Carvalho**, Metallurgic and Materials Engineering, Federal University of Minas Gerais (UFMG), Brazil.
  Supervision period: Oct.2015 - Feb.2016

- **Bachelor Thesis and Internship**, "Polysiloxanes based electrodes with metal particles and grids as anode materials for MFC Technology" **Viviane Kettermann Fernandes**, Materials Engineering, Federal University of Santa Catarina (UFSC), Brazil.
  Supervision period: May.2016 – Dec.2016

- **Bachelor Thesis and Internship**, "Macroporous SiOC-carbon-based composite as anodes for MFC technology" **Fernanda Tavares Luiz**, Materials Engineering, Federal University of Santa Catarina (UFSC), Brazil.
  Supervision period: Apr.2017 – Oct.2017

Curriculum Vitae

Surname	Canuto de Almeida e Silva
Name	Thamires
Date / Place of Birth	2 January, 1991 – Maceió, Brazil
Nationality	Brazilian

Education

08.2015- Present	Ph.D Student Advanced Ceramics Group, University of Bremen Bremen, Germany
07.2014	Diploma in Chemical Engineering Federal University of Espírito Santo (UFES) São Mateus, Brazil
12.2007	High School Centro Educacional Casa do Estudante Aracruz, Brazil

Positions and Work/Research Experience

05.2015- 07.2015	Environmental Licensing Coordinator of Urban Activities Municipal Department of the Environment (SEMAM) Aracruz, Brazil
05.2014- 07.2014	Intern - International Association for the Exchange of Students for Technical Experience (IAESTE) Program Advanced Ceramics Group, University of Bremen Bremen, Germany
09.2013- 03.2014	Intern Department of Lift and Flow Petróleo Brasileiro S.A., Petrobras São Mateus, Brazil
09.2012- 08.2013	Tutor Laboratory of General and Analytical Chemistry Federal University of Espírito Santo (UFES) São Mateus, Brazil

06.2011- 06.2012	Scholarship Student, undergraduate research entitled "Development of new macadamia products" Federal University of Espírito Santo (UFES) São Mateus, Brazil
05.2010- 05.2011	Scholarship Student, undergraduate research entitled "Improvement of harvesting and processing of cultivated freshwater prawn (*Macrobrachium Rosenbergii*)" Federal University of Espírito Santo (UFES) São Mateus, Brazil

Additional qualifications

Portuguese	Mother tongue
English	Fluent
German	Intermediary
Spanish	Intermediary
Software	Microsoft Office, OriginLab, Aspen HYSIS

List of Publications

Canuto de Almeida e Silva, T., Bhowmick, G. D., Ghangrekar, M. M., Wilhelm, M., Rezwan, K. **SiOC-based polymer derived-ceramic porous anodes for microbial fuel cells**, Biochemical Engineering Journal, 148, 29-36, (2019) DOI: 10.1016/j.bej.2019.04.004

Canuto de Almeida e Silva, T., Fernandes Kettermann, V., Pereira, C., Simões, M., Wilhelm, M., Rezwan, K. **Novel tape-cast SiOC-based porous ceramic electrode materials for potential application in bioelectrochemical systems**, Journal of Materials Science, 54, 6471–6487 (2019) DOI: 10.1007/s10853-018-03309-3

Canuto de Almeida e Silva, T., Mooste, M., Kibena-Põldsepp, E., Matisen, L., Merisalu, M., Kook, M., Sammelselg, V., Tammeveski, K., Wilhelm, M., Rezwan, K. **Polymer-derived Co/Ni–SiOC(N) ceramic electrocatalysts for oxygen reduction reaction in fuel cells**, Catalysis Science & Technology, 9, 854-866, (2019) DOI: 10.1039/C8CY02207K

dos Reis, G. S., Wilhelm, M., Silva, T. C., Rezwan, K., Sampaio, C. H., Lima, E. C., de Souza, S. M. A. G. U. **The use of design of experiments for the evaluation of the production of surface rich activated carbon from sewage sludge via microwave and conventional pyrolysis**, Applied Thermal Engineering, 93, 590-597, (2016) DOI: https://doi.org/10.1016/j.applthermaleng.2015.09.035

Silva, T. C. A., Arrieche, L. S., Sartori, D. J. M. **Development of new macadamia products**, Journal of Chemistry and Chemical Engineering, 7, 698-710, (2013).

List of Presentations and Research Stays

List of Oral and Poster Presentations

- **Thamires Canuto de Almeida e Silva**, New polysiloxanes-based anode materials for Microbial Fuel Cells (MFCs), 6th International Conference on Functional Electroceramics and Polymers (ICEP 2017), IIT Kharagpur, India, February 20-22 2017, **oral presentation.**

- **Thamires Canuto de Almeida e Silva**, Polysiloxanes-based anode materials for Microbial Fuel Cells (MFCs), 6th General Meeting of the International Society for Microbial Electrochemistry and Technology (ISMET6 2017), Lisbon, Portugal, October 03-06 2017, **poster presentation.**

- **Thamires Canuto de Almeida e Silva**, Novel polysiloxane-based anode materials for Microbial Fuel Cells (MFCs), INDO-EU Workshop, IIT Kharagpur, India, February 2-3 2018, **oral presentation.**

- **Thamires Canuto de Almeida e Silva,** Gourav Dhar Bhowmick, Makarand Madhao Ghangrekar, Michaela Wilhelm and Kurosch Rezwan**,** Macroporous SiOC-Carbon-based Composite as Anodes for Microbial Fuel Cell Technology, 5th International Conference on Chemical Materials and Process (ICCMP 2019), Bangkok, Thailand, May 1-3, **oral presentation.**

  ***Best Presentation Award**

  The presentation has been selected as the best one of the 5th International Conference on Chemical Materials and Process.

List of Research Stays

- Department of Civil Engineering, **Indian Institute of Technology**, Kharagpur, India Period: 10th February to 05th March 2017.
- Department of Civil Engineering, **Indian Institute of Technology**, Kharagpur, India Period: 4th to 10th February 2018.
- Department Environmental Microbiology, **Zentrum für Umweltforschung** (UFZ), Leipzig, Germany - Period: 9th to 12th October 2018.